ABSTRACT

Title of Dissertation: ANALOG QUANTUM SIMULATION AND QUANTUM MANY-BODY DYNAMICS IN ATOMIC, MOLECULAR AND OPTICAL SYSTEMS

Fangli Liu
Doctor of Philosophy, 2021

Dissertation Directed by: Professor Alexey V. Gorshkov
Department of Physics

In recent decades, the rapid development of quantum technologies has led to a new era of programmable platforms, enabling the realizations of quantum simulation and quantum computation. This dissertation is motivated by recent experimental progress on controlling individual quantum degrees of freedom in systems such as trapped ions and Rydberg atom arrays. By tailoring the interactions in these quantum systems, we study analog quantum simulations of various physical phenomena, including non-equilibrium quantum dynamics and nontrivial topological physics.

In the first part of the dissertation, we study slow quantum many-body dynamics in trapped-ion systems and Rydberg atom arrays. We first show that either the long-range interactions or an additional symmetry-breaking field can give rise to a confining potential. Such a potential can couple domain wall quasiparticles into mesonic or baryonic bound states. These confined quasiparticles strongly suppress the quantum information dynamics and lead to slow thermalization. In the

limit of strict domain-wall confinement, the full Hilbert space is fragmented into exponentially many disconnected subspaces. Furthermore, we demonstrate that thermalization can be halted by quantum engineering a uniformly increasing field in the trapped-ion quantum simulator.

The second part of the dissertation focuses on topologically relevant phenomena in quantum simulators. We first study the effect of experimentally relevant disorder in 2D Rydberg atom arrays. We find that there are three distinct localization regimes due to the presence of nontrivial topological bands. We further study the non-equilibrium dynamics of Abelian anyons in a one-dimensional system. We show that the interplay of anyonic statistics and interactions can give rise to spatially asymmetric quantum dynamics. Finally, we use Nielsen's geometric approach to quantify circuit complexity in topological models. We find that the circuit complexities of ground states and non-equilibrium steady states both exhibit nonanalytical behavior at topological transition points.

ANALOG QUANTUM SIMULATION AND QUANTUM MANY-BODY DYNAMICS IN ATOMIC, MOLECULAR AND OPTICAL SYSTEMS

by

Fangli Liu

Dissertation submitted to the Faculty of the Graduate School of the
University of Maryland, College Park in partial fulfillment
of the requirements for the degree of
Doctor of Philosophy
2021

Advisory Committee:
Professor Steven L. Rolston, Chair
Professor Alexey V. Gorshkov, Advisor
Professor Xiaodi Wu, Dean's Representative
Professor Zohreh Davoudi
Professor Christopher Monroe

Acknowledgments

The 'Acknowledgements' section in a dissertation differs from academic papers in that it gives people the chance to express gratitude to persons rather than funding resources. So I will take this chance here to thank the people who have helped me to get to this point, in particular those who have made the most direct impact on my graduate study and life.

First and foremost, I would like to thank my advisor Alexey Gorshkov for his support over these years. I am so lucky to have had the chance to work with him since my first day of graduate school. Alexey has not only given me the greatest freedom to choose projects that I am interested in but also offered me the strongest support in every possible way (e.g. giving valuable academic advice and helping build multiple collaborations). His enthusiasm towards research and life has greatly inspired and encouraged me in countless situations.

I have also been fortunate to have had the chance to learn from and collaborate with Professor Christopher Monore. I greatly enjoyed the discussions on trapped ions with Chris and all the other QSim members, including Guido Pagano, Jiehang Zhang, William Morong, Lei Feng, Wen-Lin Tan, Patrick Becker, Kate Collins, Arinjoy De, Harvey Kaplan, and Antonios Kyprianidis. Many parts of this dissertation would not have been possible without the fruitful collaboration and their hard work.

Special thanks go to Guido, who led me on a lab tour that started my journey in trapped-ion quantum simulation. I am also indebted to Guido, Patrick, Will, and Chris for their kind help during my job search.

Besides Alexey and Chris, I would also like to thank other faculty members, including Professor Steven L. Rolston, Professor Xiaodi Wu, and Professor Zohreh Davoudi, for serving on the committee of this dissertation.

Many other professors, postdocs, and graduate students have also been crucial in helping me get to where I am today, including Dong-Ling Deng, Thomas Iadecola, Zhe-Xuan Gong, Paraj Titum, Rex Lundgren, Zhi-Cheng Yang, Seth Whitsitt, Przemyslaw Bienias, and James Garrison. I have also benefitted from discussions with Mohammad Hafezi, Zohreh Davoudi, Brian Swingle, Maissam Barkeshli, Guanyu Zhu, Xiaopeng Li, Jon Curtis, Jeremy Young, Christopher Baldwin, Lucas Brady, Luis Pedro García-Pintos, Yaroslav Kharkov, Oles Shtanko, Aniruddha Bapat, Su-Kuan Chu, Abhinav Deshpande, Andrew Guo, Minh Tran, and Yidan Wang.

I also would like to thank some of my friends outside of my graduate studies. My life in graduate school would not be fun without them, including but not limited to Ying Han, Peizhi Du, Xunnong Xu, Christopher Flower, Yiming Cai, Xingyao Wu, Ruizhi Pan, Shukai Ma, Qixin Yang, Zexun Lin, Bin Cao, Yongbin Feng, Haoquan Fan, Yuchen Yue, and Daiwei Zhu.

Finally, I would like to thank my parents and my elder brother for their support and selfless love.

Table of Contents

List of Tables

List of Figures

Citations to Previously Published Work

Much of this dissertation has appeared in papers already published. Here we outline those publications, with additional citations to related papers whose text does not appear here.

- Chapter 2: "Confined Quasiparticle Dynamics in Long-Range Interacting Quantum Spin Chains," F. Liu, R. Lundgren, P. Titum, G. Pagano, J. Zhang, C. Monroe, and A. V. Gorshkov, Phys. Rev. Lett. 122, 150601, 2019.
  - Further work related to string breaking in short-range and long-range interacting quantum spin chains is also presented in "Real-Time Dynamics of String Breaking in Quantum Spin Chains," R. Verdel, F. Liu, S. Whitsitt, A. V. Gorshkov, and M. Heyl, Phys. Rev. B 102, 014308, 2020.
- Chapter 3: "Observation of Domain Wall Confinement and Dynamics in a Quantum Simulator," W. L. Tan, P. Becker, F. Liu, G. Pagano, K. S. Collins, A. De, L. Feng, H. B. Kaplan, A. Kyprianidis, R. Lundgren, W. Morong, S. Whitsitt, A. V. Gorshkov, C. Monroe, arXiv:1912.11117, Nat. Phys. 2021.
- Chapter 4: "Realizing and Probing Baryonic Excitations in Rydberg Atom Arrays," F. Liu, S. Whitsitt, P. Bienias, R. Lundgren, A. V. Gorshkov, arXiv:2007.07258.
- Chapter 5: "Hilbert-Space Fragmentation from Strict Confinement," Z.-C. Yang, F. Liu, A. V. Gorshkov, T. Iadecola, Phys. Rev. Lett. 124, 207602, 2020.

- Chapter 6: "Observation of Stark Many-Body Localization without Disorder," W. Morong, F. Liu, P. Becker, K. S. Collins, L. Feng, A. Kyprianidis, G. Pagano, T. You, A. V. Gorshkov, C. Monroe, arXiv:2102.07250.

  - Further work related to preparing low-energy quantum many-body states with trapped ions is also presented in "Quantum Approximate Optimization of the Long-Range Ising Model with a Trapped-Ion Quantum Simulator," G. Pagano, A. Bapat, P. Becker, K. S. Collins, A. De, P. W. Hess, H. B. Kaplan, A. Kyprianidis, W. L. Tan, C. Baldwin, L. T. Brady, A. Deshpande, F. Liu, S. Jordan, A. V. Gorshkov, C. Monroe, PNAS 117, 25396, 2020.

- Chapter 7: "Localization and Criticality in Antiblockaded 2D Rydberg Atom Arrays," F. Liu, Z.-C. Yang, P. Bienias, T. Iadecola, A. V. Gorshkov, arXiv:2012.03946.

- Chapter 8: "Asymmetric Particle Transport and Light-Cone Dynamics Induced by Anyonic Statistics," F. Liu, J. R. Garrison, D.-L. Deng, Z.-X. Gong, A. V. Gorshkov, Phys. Rev. Lett. 121, 250404, 2018.

- Chapter 9: "Circuit Complexity Across a Topological Phase Transition," F. Liu, S. Whitsitt, J. B. Curtis, R. Lundgren, P. Titum, Z.-C. Yang, J. R. Garrison, and A. V. Gorshkov, Phys. Rev. Research 2, 013323, 2020.

  - Further work related to using momentum space entanglement to characterize quantum information dynamics is also presented in "Momentum-

Space Entanglement after a Quench in One-Dimensional Disordered Fermionic Systems," R. Lundgren, F. Liu, P. Laurell, G. A. Fiete, Phys. Rev. B 100, 241108, 2019.

Chapter 1: Introduction

1.1 Motivation

Since the beginning of the 20th century, the theory of quantum mechanics has had enormous success in explaining and predicting the properties of the microscopic world. In contrast with classical mechanics, quantum mechanics makes predictions of probabilities instead of certainties. More counterintuitively, quantum mechanics allows an object to be in a superposition of two or more states at once, and allows a group of particles to be connected instantaneously via entanglement. In the past thirty years, enormous progress has been made in harnessing these unusual quantum effects to achieve a variety of new quantum technologies.

While we do not normally encounter quantum mechanical effects in everyday life[1], a great number of real-world devices and applications are indeed built upon the principles of quantum mechanics. For instance, modern semiconductor-based electronics rely on the band structure of solid materials, which is a quantum phenomenon at the basic level. The very ability to manipulate the electrical properties is based on the fact that we understand their quantum mechanical nature. Another

[1]This is because quantum systems lose their coherence quickly by interacting with the environment

important example is magnetic resonance imaging, for which the central process—nuclear magnetic resonance—is also fundamentally quantum mechanical [1].

At the frontier of quantum physics research, an important motivation for harnessing quantum effects is to build a practical quantum computer [2,3]. A quantum computer is a device that performs computing based on basic quantum mechanical principles. Such a computer is completely different from binary digital electronic computers, as the fundamental building block of a quantum computer—a quantum bit—can be in both states (0 and 1) at the same time using the property of quantum superposition. Large-scale quantum computers could potentially solve certain problems, such as integer factorization [4,5] and unstructured database search [6], much more quickly than classical computers. Since quantum effects are very fragile, it is crucial to isolate a quantum system from its environment when performing quantum computing. Due to their high-quality isolation from the environment, atomic, molecular, and optical (AMO) systems provide perfect platforms for engineering quantum bits and performing quantum computation. Still, the realization of scalable and universal quantum computation is challenging due to the requirement of extensive and precise control.

Quantum simulators, on the other hand, can be regarded as restricted quantum computers, with operations that may not be universal but instead may be tailored to a particular quantum physical model under study [7,8]. The idea of the quantum simulation was first proposed by Richard Feynman about 40 years ago [9]. The direct motivation for building quantum simulators comes from the fact that the complexity of simulating quantum systems using classical resources scales exponentially with

the number of quantum particles. For instance, to simulate the full wavefunction dynamics of N spin-1/2 quantum particles, it is required to keep track of (at least) 2^N complex amplitudes. Even the most powerful classical computers that exist in the world are not able to simulate the full wave-function dynamics associated with more than a few hundred of such spins. The approach suggested by Feynman is, instead, building synthetic quantum systems in a physical laboratory that can directly implement models of practical interest (or models motivated by theoretical studies). The appealing feature of this approach is the tunability of these synthetic quantum systems.

While we are waiting for the realization of a large-scale useful quantum computer, analog quantum simulation has already been demonstrated experimentally and has shed light on various quantum many-body problems. Different from universal quantum computation, we do not generally need the information of the complete many-body wavefunction when doing quantum simulation. Instead, quantum observables, such as particle densities and correlation functions, are sufficient to tell the essential physical properties that we are interested in.

The progress in programmable quantum simulation is driven greatly by the dramatic improvement of quantum technologies in the past few decades. Quantum control of individual quantum objects has been achieved in platforms such as trapped ions [10, 11], Rydberg atoms trapped by optical tweezers [12, 13], photonic systems [14, 15], and superconducting qubit systems [16, 17]. It has been reported that the number of interacting quantum particles in both trapped-ion [18] and Rydberg-atom systems [13] has gone beyond the simulating capability of classical computers.

Quantum simulators have provided insights to broad physical problems including topological phases of matter [19–21], quantum magnetism [22, 23], non-equilibrium quantum many-body dynamics [13, 18], and quantum critically [24, 25]. In this dissertation, we will mainly focus on two quantum simulation platforms: trapped ion systems and Rydberg atom arrays. We will show that due to the great controllability and isolation from the environment, these two programmable platforms are excellent for simulating various physical phenomena. We will focus on non-equilibrium quantum many-body dynamics and topological physics that are natural to realize and probe in the two systems. It is worth pointing out that the two systems are also among the most promising platforms for realizing scalable quantum computers [12, 26].

The remainder of this chapter is structured as follows: The next two sections provide introductory discussions of analog quantum many-body Hamiltonians that arise in trapped-ion and Rydberg atom systems, while the final section provides an outline (or abstract) for the remaining chapters. Motivations and background information for various physical phenomena are presented in the 'Introduction' section of each subsequent chapter. In the final chapter, we give summaries of previous chapters and point out several potential research directions based on our studies.

1.2 Trapped ions

Trapped-ion quantum system is one of the most promising quantum computation platforms that allow for both large-scale analog quantum simulation and

digital quantum computation, exploiting a native qubit platform with outstanding coherence properties [7, 10, 11]. In such a system, quantum gates can be applied to subsets of qubits, while global addressing allows the realization of effective long-range tunable Ising Hamiltonians, adiabatic ramping, fast quenches, and Floquet drives [7, 27]. One particular advantage of the trapped-ion computation platform is the full connectivity of two-qubit gates, which can be exploited to design efficient quantum circuits. Long coherent lifetimes [28] and the high fidelities of single and two-qubit gates have been demonstrated in trapped ions [29].

Here we briefly review the analog quantum many-body Hamiltonian that appears naturally in trapped-ion quantum simulators. More details about the experimental systems are presented in Appendix B and Appendix D. Excellent reviews of trapped ion quantum simulations can be found in Refs. [7, 30].

The experimental system in question consists of a chain of ions, with pseudospin states $|\uparrow_x\rangle$ and $|\downarrow_x\rangle$ encoded in their hyperfine ground-state levels. The atomic ions are confined with electromagnetic fields supplied by nearby electrodes. There are two types of ion traps: the linear radio-frequency trap (Paul trap) [31] and the Penning trap [32]. This dissertation presents results that use the Paul trap. The effective analog quantum many-body Hamiltonian studied in this dissertation essentially has two ingredients. The first is the long-range spin-spin interaction term described by

$$H_1 = \sum_{j<j'} J_{jj'} \sigma_j^x \sigma_{j'}^x, \tag{1.1}$$

where σ_j^x is a Pauli operator acting on site j. $J_{i,j} \approx J_0/|i-j|^\alpha$ is the approximately-

power-law long-range Ising coupling between spins i and j with tunable exponent α. Such long-range spin-spin interactions are mediated by global laser beams that couple the spin and motional degrees of freedom using the Mølmer-Sørensen scheme [33].

The second is the transverse field that is described by

$$H_2 = \sum_{j=1}^{N} B_i \sigma_j^z, \tag{1.2}$$

where B_i is a tunable transverse field. Such a field can be generated by a global offset of two Raman lasers [7], or by tightly-focused beams creating programmable effective fields at each ion [34].

The key feature of this platform is its high degree of controllability. Specifically, one can use tightly-focused beams to initialize spins to any desired product state. Moreover, Eq. (1.1) and Eq. (1.2) can be turned on and off both simultaneously and separately. Furthermore, one can measure local or non-local observables in an arbitrary basis by collecting state-dependent fluorescent photons using a CCD camera. Due to these advantages, we are able to study novel quantum many-body dynamics governed by the analog long-range interacting Hamiltonian ($H = H_1 + H_2$) in this dissertation.

1.3 Rydberg atom arrays

Programmable Rydberg quantum simulators have attracted great interest recently because they can provide insights into strongly correlated quantum sys-

tems [13], and enable studies of new phases of matter [35]. These systems can also form building blocks for the eventual realization of quantum information processors [36], which could ultimately lead to computational systems that outperform existing computers based on classical approaches.

Rydberg atoms are atoms whose valence electron(s) has been excited to large principal quantum numbers n [12]. There are two important properties when Rydberg atoms are in these highly excited states. First, the lifetime of a Rydberg state is much longer than that of the low-lying states. Second, the dipole moment is extremely large since the valance electron is generally far from the nucleus and core electrons [37]. When Rydberg atoms are close to each other, the interactions (due to the large dipole moment) between atoms are so strong that the simultaneous excitations of two Rydberg atoms is greatly suppressed. This is the so-called Rydberg blockade, an essential mechanism that enables simulating strongly correlated quantum many-body systems and performing quantum computation using Rydberg atoms [12, 38].

In recent years, the techniques to assemble arrays of individual neutral Rydberg atoms trapped in optical microtraps have been greatly developed. Rydberg atom arrays in 1D, 2D and 3D have been demonstrated experimentally [39–41]. The analog quantum many-body Hamiltonian given by such arrays can be described by

$$H_{\mathrm{Ryd}} = \sum_i \frac{\Omega_i}{2} X_i - \sum_i \Delta_i n_i + \sum_{i \neq j} V_{|i-j|} n_i n_j. \tag{1.3}$$

Here, $|r_i\rangle$ ($|g_i\rangle$) denotes the Rydberg (ground) state for atom at site i, $X_i = |g_i\rangle\langle r_i| +$

$|r_i\rangle\langle g_i|$, $n_i = |r_i\rangle\langle r_i|$, Ω_i and Δ_i are the Rabi frequencies and detunings respectively, and $V_{|i-j|}$ describes the interaction between atoms in the Rydberg state at sites i and j. The interactions decay strongly with distance, with the scaling $V_r \propto 1/r^6$.

Recent experiments have studied the quantum many-body dynamics governed by this Hamiltonian with homogeneous parameters [13], giving insight into phenomena such as quantum many-body scars [42, 43], exotic quantum criticality [44–46], and the quantum Kibble-Zurek mechanism [47]. In this dissertation, we will study quantum simulation of novel confined quasiparticles, topological properties of a subspace within the full Hilbert space, and quantum dynamics governed by the above Hamiltonian.

1.4 Outline of dissertation

- Chapter 2: "Confined Quasiparticle Dynamics in Long-Range Interacting Quantum Spin Chains," presents a study of quasiparticle excitation and quench dynamics of the one-dimensional transverse-field Ising model with power-law ($1/r^\alpha$) interactions. We find that long-range interactions give rise to a confining potential, which couples pairs of domain walls (kinks) into bound quasiparticles, analogous to mesonic states in high-energy physics. We illustrate that these quasiparticle states can lead to slow thermalization of one-point observables for certain initial states. This study is readily applicable to current trapped-ion experiments.

- Chapter 3: "Observation of Domain Wall Confinement and Dynamics in a

Quantum Simulator," reports the first observation of magnetic domain wall confinement in interacting spin chains with a trapped-ion quantum simulator. By measuring how correlations spread, we show that confinement can dramatically suppress information propagation and thermalization in such many-body systems. We are able to quantitatively determine the excitation energy of domain wall bound states from non-equilibrium quench dynamics. Furthermore, we study the number of domain wall excitations created for different quench parameters in a regime that is difficult to model with classical computers.

- Chapter 4: "Realizing and Probing Baryonic Excitations in Rydberg Atom Arrays," proposes a realization of mesonic and baryonic quasiparticle excitations in Rydberg atom arrays with programmable interactions. By engineering a $\mathbb{Z}_3$-translational-symmetry breaking field on top of the Rydberg-blockaded Hamiltonian, we show that different types of defects experience confinement, and as a consequence form mesonic or baryonic quasiparticle excitations. We show that the confined quasiparticle spectrum can limit quantum information spreading in this system. This proposal is readily applicable to current Rydberg experiments.

- Chapter 5: "Hilbert-Space Fragmentation from Strict Confinement," presents the study of one-dimensional spin-1/2 models in which strict confinement of Ising domain walls leads to the fragmentation of Hilbert space into exponentially many disconnected subspaces. Remarkably, while some connected components of the Hilbert space thermalize, others are integrable by Bethe

ansatz.

- Chapter 6: "Observation of Stark Many-Body Localization without Disorder," reports the realization of Stark MBL in a trapped-ion quantum simulator and demonstrates its key properties: halting of thermalization and slow propagation of correlations. Tailoring the interactions between ionic spins in an effective field gradient, we directly observe their microscopic equilibration for a variety of initial states, and we apply single-site control to measure correlations between separate regions of the spin chain.

- Chapter 7: "Localization and Criticality in Antiblockaded 2D Rydberg Atom Arrays," presents the study of the effect of experimentally relevant positional disorder on Rydberg atoms trapped in a 2D square lattice under anti-blockade (facilitation) conditions. We show that the facilitation conditions lead the connectivity graph of a particular subspace of the full Hilbert space to form a 2D Lieb lattice, which features a singular flat band. Remarkably, we find three distinct regimes as the disorder strength is varied: a critical regime, a delocalized but nonergodic regime, and a regime with a disorder-induced flat band.

- Chapter 8: "Asymmetric Particle Transport and Light-Cone Dynamics Induced by Anyonic Statistics," presents the study of the non-equilibrium dynamics of Abelian anyons in a one-dimensional system. We find that the interplay of anyonic statistics and interactions gives rise to spatially asymmetric particle transport together with a novel dynamical symmetry that depends

on the anyonic statistical angle and the sign of the interactions.

- Chapter 9: "Circuit Complexity Across a Topological Phase Transition," uses Nielsen's geometric approach to quantify the circuit complexity in a one-dimensional Kitaev chain across a topological phase transition. We find that the circuit complexities of both the ground states and nonequilibrium steady states of the Kitaev model exhibit nonanalytical behaviors at the critical points, and thus can be used to detect both equilibrium and dynamical topological phase transitions.

Chapter 2: Confined Quasiparticle Dynamics in Long-Range Interacting Quantum Spin Chains

2.1 Introduction

Long-range interacting quantum systems occur naturally in numerous quantum simulators [12, 48–56]. A paradigmatic model considers interactions decaying with distance r as a power law $1/r^{\alpha}$. This describes the interaction term in trapped-ion spin systems [18, 49, 57–60], polar molecules [61–64], magnetic atoms [51, 65, 66], and Rydberg atoms [12, 48, 67, 68]. One remarkable consequence of long-range interactions is the breakdown of locality, where quantum information, bounded by linear 'light cones' in short-range interacting systems [69], can propagate super-ballistically or even instantaneously [70–76]. The non-local propagation of quantum correlations in 1D systems has been observed in trapped-ion experiments [58, 59]. Moreover, 1D long-range interacting quantum systems can host novel physics that is absent in their short-range counterparts, such as continuous symmetry breaking [77, 78].

Recently, it has been shown that confinement–which has origins in high-energy physics–has dramatic signatures in the quantum quench dynamics of short-range interacting spin chains [79]. Owing to confinement, quarks cannot be directly observed

in nature as they form mesons and baryons due to strong interactions [80, 81]. An archetypal model with analogous confinement effects in quantum many-body systems is the 1D short-range interacting Ising model with both transverse and longitudinal fields [82–87]. For a vanishing longitudinal field, domain-wall quasiparticles propagate freely and map out light-cone spreading of quantum information [86–89]. As first proposed by McCoy and Wu [90–92], a non-zero longitudinal field induces an attractive linear potential between two domain walls and confines them into mesonic quasiparticles. Recently, Kormos et al. investigated global quenches in this system and showed that the non-equilibrium dynamics can be used to probe the confined quasiparticle excitations [79].

In this Chapter, we study the non-equilibrium dynamics of the long-range interacting transverse-field Ising model *without a longitudinal field* after a global quantum quench. We find that long-range interactions introduce an effective attractive force between a pair of domain walls, thus confining them into a bound state, analogous to the meson in high-energy physics. We calculate time-dependent order parameters and connected correlation functions, both of which feature clear signatures of confined quasiparticle excitations [86, 87]. The masses of these bound quasiparticles–the energy gaps relative to the ground state–can be directly extracted from the Fourier spectrum of time-dependent order parameters [79, 86, 87]. We introduce a two-kink model to explicitly show that the confining potential comes from long-range interactions. This effective model also gives good predictions for the quasiparticles' masses and their dispersion relations. Furthermore, we study the effect of confined quasiparticles on the thermalization of different initial states.

We find that for certain initial states, one-point observables exhibit slow thermalization [86, 87, 93, 94], which might help protect ordered phases in the prethermal region [95–97].

We note that our study is in agreement with the general mechanism of global quantum quenches, first formulated in Refs. [86, 87, 89] for short-range interacting systems, and demonstrates that the general theory developed in Refs. [86, 87, 89] holds for systems with long-range interactions. Our work is well within the reach of current trapped-ion experiments [18] and other atomic, molecular, and optical (AMO) experimental platforms [12, 13, 55].

2.2 The model

Let us consider a quantum spin chain with long-range interactions, described by the following Hamiltonian,

$$H = -\sum_{i<j}^{L} \frac{J}{r_{ij}^{\alpha}} \sigma_i^z \sigma_j^z - B \sum_{i=1}^{L} \sigma_i^x, \tag{2.1}$$

where σ_i^{μ} are the Pauli matrices on site i, L is the system size, r_{ij} is the distance between sites i and j (nearest-neighbor spacing is set to 1), J sets the overall energy scale (set to 1), B is a global transverse field, and α describes the power-law decay of long-range interactions. In this work, we consider periodic boundary conditions unless otherwise specified ($r_{ij} = \min(|i-j|, L-|i-j|)$).

In the nearest-neighbor interacting limit ($\alpha \to \infty$), H is exactly solvable via a Jordan-Wigner mapping to spinless fermions. It exhibits a phase transition at

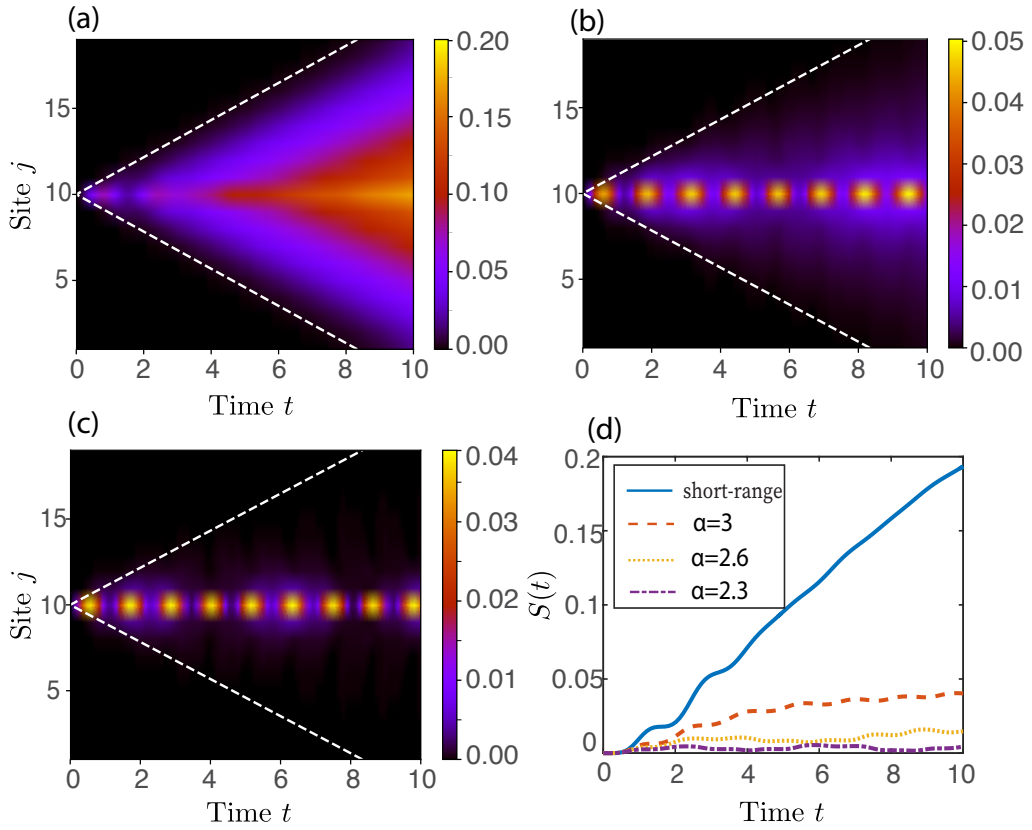

Figure 2.1: (a)-(c) $\langle \sigma_j^z \sigma_k^z \rangle_c$, and (d) $S_A(t)$ versus t after a quantum quench with initial state $|\Psi_0\rangle$. $L = 19$, $k = 10$, and $B = 0.27$. (a) Short-range interacting case ($\alpha \to \infty$), (b) $\alpha = 2.6$, (c) $\alpha = 2.3$. The dashed white lines illustrate the maximal velocity, $4B$, of freely propagating domain walls in the short-range interacting case [79]. (d) $S_A(t)$ for various α.

$B = 1$, which separates the ferromagnetic and paramagnetic regions [98]. The phase transition persists for long-range interactions, while the critical value of B increases [99–102]. In trapped-ion experiments, the range of the exponent can be tuned within $0 < \alpha < 3$ by changing the detuning of the applied optical fields from phonon sidebands. We restrict the numerics to $\alpha > 1$ in order to ensure a well-behaved thermodynamic limit (the case of $\alpha \in [0, 1]$ will be discussed later). Several experiments have investigated the real-time dynamics of the above model (or closely related models), including dynamical phase transitions [18,103], the non-local propagation of correlations [58, 59], time crystals [95], and many-body localization [60].

2.3 Quench dynamics

We first study the quench dynamics of the above model. We focus on an initial state with all spins polarized in the z direction, $|\Psi_0\rangle = |...\uparrow\uparrow\uparrow...\rangle$, which is easily preparable in trapped-ion experiments [18]. The system is allowed to evolve under the Hamiltonian (2.1). This is equivalent to a global quantum quench from zero to finite B [18, 86, 87]. In order to explore the physics of domain walls, we focus on quantum quenches within the ferromagnetic phase [88, 104]. We mention that similar features persist when the initial state is chosen as the ground state of Eq. (2.1) with finite B in the ferromagnetic region.

We use the Krylov-space method to simulate the quench dynamics of our system [105,106]. Figs. 2.1(a)-(c) show the equal-time connected correlation functions,

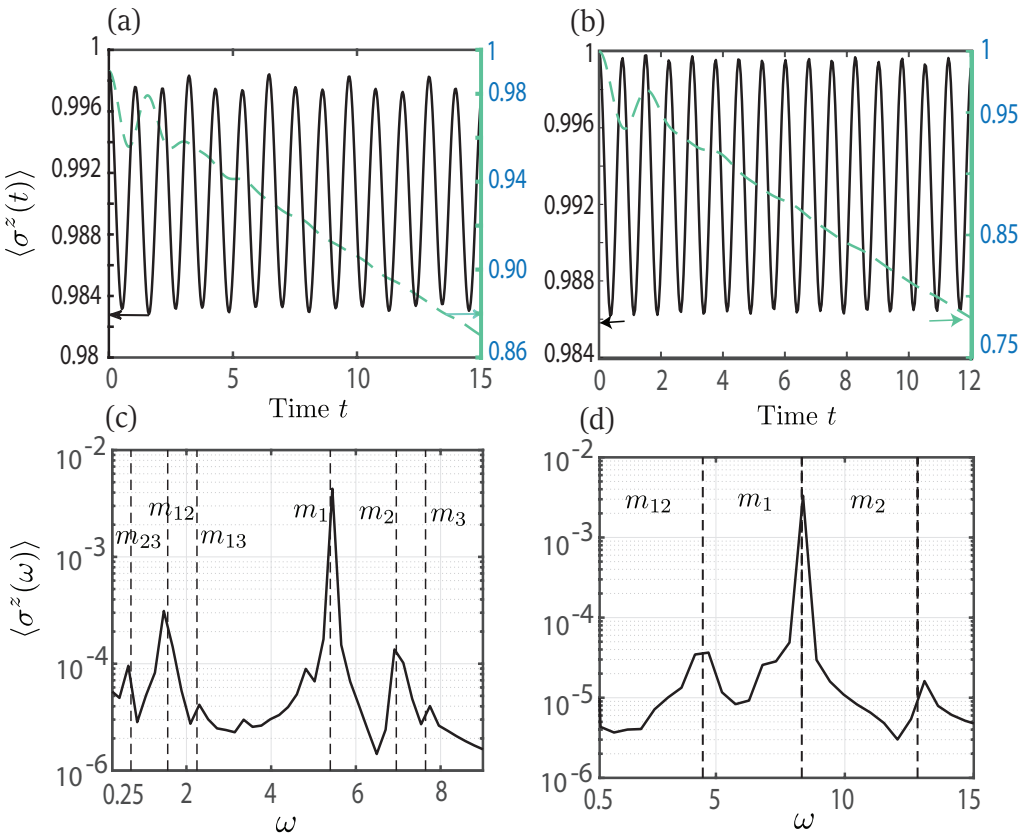

Figure 2.2: (a)-(b) $\langle\sigma^z(t)\rangle$ (black line) versus time after quenching to (a) $\alpha = 2.3, B = 0.27$, (b) $\alpha = 1.4, B = 0.35$ for $L = 20$. The dashed green lines show $\langle\sigma^z(t)\rangle$ for the short-range model (same B). (c)-(d) Fourier spectrum of $\langle\sigma^z(t)\rangle$ for the long-range case in (a) and (b), respectively. The largest time for the Fourier transform is $t = 30$ and 12 for (c) and (d), respectively. The parameters in (b,d) are accessible in current trapped-ion experiments [18]. The dashed lines show the mesonic masses (m_i) and their differences ($m_{ij} \equiv m_j - m_i$) calculated using the two-kink model.

$\langle\sigma_j^z(t)\sigma_k^z(t)\rangle_c = \langle\sigma_j^z(t)\sigma_k^z(t)\rangle - \langle\sigma_j^z(t)\rangle\langle\sigma_k^z(t)\rangle$, after the sudden quench (k indicates the central lattice site). In the short-range interacting limit [Fig. 2.1(a)], we recover the exactly solvable case, where correlations spread with a velocity ($4B$) equal to twice the maximal speed of free domain-walls [79,88,89]. Increasing the Ising interaction range (decreasing α) strongly suppresses the magnitude of $\langle\sigma_j^z(t)\sigma_k^z(t)\rangle_c$, as shown in Figs. 2.1(b) and 2.1(c). One can also see the oscillatory behaviour of correlations [Figs. 2.1(b) and 2.1(c)], similar to that of Ref. [79]. However, we emphasize that the light-cone spreading of correlations is always present [79,89], though it may have a different velocity depending on the quasiparticles in the system [89]. The actual extent of the light cone becomes clearer by zooming in on the 'black' regions of Figs. 2.1(b) and 2.1(c) (see Appendix A). This result is in agreement with the general mechanism of global quantum quenches first derived in Ref. [89].

The propagating quasiparticles produced by the quench map out the light-cone spreading of correlations [89] and lead to the growth of entanglement entropy [79]. Fig. 2.1(d) shows the growth of entanglement entropy, $S_A(t) = -\mathrm{Tr}[\rho_A(t)\ln(\rho_A(t))]$, where $\rho_A(t)$ is the reduced density matrix of one half of the chain, for various α. As one can see, the entanglement entropy growth for smaller α is much slower than the short-range case (linear growth) [73]. This is because the propagating quasiparticles have smaller velocities for longer-range interactions (see Appendix A).

We plot time-dependent order parameters $\langle\sigma^z(t)\rangle = \frac{1}{L}\sum_i\langle\sigma_i^z(t)\rangle$ in Figs. 2.2(a) and (b) [1]. Different from the rapid exponential decay of the magnetization for

[1]For Fig. 2.2(b), we use parameters and probing time relevant to current trapped-ion experiments [18,58,59]

the short-range case, $\langle\sigma^z(t)\rangle$ exhibits periodic oscillations with almost no decay [86,87,107–109] in the time window shown here. We emphasize that the qualitative change in dynamics is caused by the long-range interactions, not by an additional longitudinal field as in the short-range interacting case [79]. The Fourier spectrum of $\langle\sigma^z(t)\rangle$ illustrates that the oscillations are associated with multiple frequencies [Figs. 2.2(c) and 2.2(d)]. As we will see, these frequencies coincide with the masses (and their differences) of quasiparticles [86,87].

2.4 Two-kink model and bound states

To understand the quasiparticles in our system, we use a two-kink model to perturbatively study the low-energy excitations of Eq. (2.1). The two-kink model has been used to phenomenologically study excitations in short-range interacting quasi-1D compounds [82,110]. The idea is to restrict the Hilbert-space to two domain-wall states [see inset of Fig. 2.3(a)], where regions of different magnetization are separated by the two domain walls. The projected model is expected to work well when B is much smaller than J [79].

The Hilbert space of the projected model is spanned by states of n down-spins (clustered together), represented as: $|j,n\rangle = |...\uparrow\uparrow\downarrow_j\downarrow ... \downarrow\downarrow_{(j+n-1)}\uparrow\uparrow ...\rangle$, where j is the starting position of the cluster. The projected Hamiltonian, $\mathcal{H} = \mathcal{P}H\mathcal{P}$ ($\mathcal{P}$ denotes the projection operator to the two-domain-wall subspace), acts on $|j,n\rangle$ as

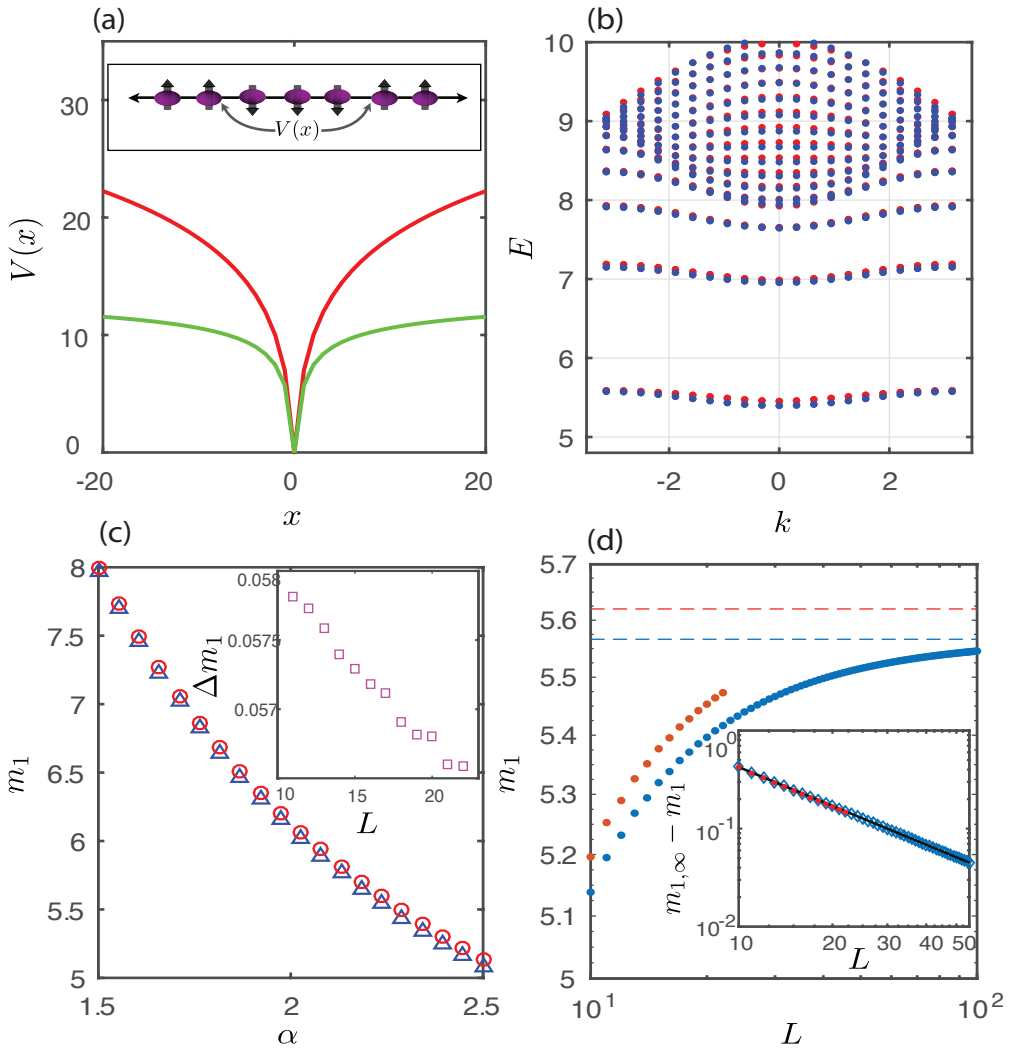

Figure 2.3: (a) Potential energy as a function of distance x between the two domain walls ($n = |x|$). Red line: $\alpha = 1.9$; green line: $\alpha = 2.3$. Inset: typical spin configuration of two-domain-wall states. (b)-(d) Comparison of two-kink model (blue) and ED results (red). (b) Energy spectrum. Parameters: $\alpha = 2.3, B = 0.27$, $L = 20$. (c) m_1 versus α with parameters $B = 0.27$ and $L = 22$. Inset: Difference of m_1 between the two methods, Δm_1, versus L. (d) m_1 versus L (same parameters as (b)). The dashed lines are $m_{1,\infty}$. The inset shows $m_{1,\infty} - m_1$ versus system size. The black line shows the fitting of the two-kink model's data to $(1/L)^\beta$, with $\beta = 1.315$. ED data has similar scaling with $\beta = 1.34$. $m_{1,\infty}$ is chosen as 5.56 (5.62) for the two-kink model (ED).

follows,

$$\begin{aligned}\mathcal{H}\,|j,n\rangle =& V(n)\,|j,n\rangle - B[|j,n+1\rangle + |j,n-1\rangle \\ &+ |j+1,n+1\rangle + |j-1,n+1\rangle].\end{aligned} \tag{2.2}$$

Here, we have defined the potential energy as $V(n) = \langle j,n|\mathcal{H}|j,n\rangle - \langle\Psi_0|\mathcal{H}|\Psi_0\rangle$. Utilizing translational invariance, we transform the two-domain-wall state into momentum basis, $|k,n\rangle = \frac{1}{\sqrt{L}}\sum_{j=1}^{L}\exp(-ikj - ikn/2)\,|j,n\rangle$, which gives

$$\begin{aligned}\mathcal{H} = \sum_{k,n} V(n)|k,n\rangle\langle k,n| - 2B\cos\frac{k}{2}|k,n\rangle\langle k,n+1| \\ - 2B\cos\frac{k}{2}|k,n\rangle\langle k,n-1|.\end{aligned} \tag{2.3}$$

For $L\to\infty$, the potential energy of a two-domain-wall spin configuration is

$$V(n) = 4n\zeta(\alpha)J - 4J\sum_{1\le l<n}\sum_{1\le r\le l}\frac{1}{r^{\alpha}}, \tag{2.4}$$

where $\zeta(\alpha) = \sum_{z=1}^{\infty}\frac{1}{z^{\alpha}}$ denotes the Riemann zeta function. As plotted in Fig. 2.3(a), $V(n)$ *increases* with the distance between domain walls. For the short-range model studied in Ref. [79], the confining potential is due to an additional on-site longitudinal magnetic field. In our case, the confining potential is intrinsically generated by the long-range interactions.

The picture now becomes clear: the long-range Ising interaction gives rise to an effective potential, which *increases* with separation between the two domain walls, while the transverse magnetic field acts as kinetic energy for domain walls (changing

the size of the cluster). Therefore, a pair of domain walls, each of which is free quasiparticle in the short-range limit, become bounded together when α decreases. Note that $V(n)$ has an upper bound when $\alpha > 2$, as illustrated in Fig. 2.3(a) (see Appendix A). This indicates that the lower part of the energy spectrum is composed of domain-wall bound states, while above some energy threshold, we have a continuum of states [Fig. 2.3(b)]. For $\alpha \leq 2$, however, all excitations within the two-kink model are bound quasiparticles, as the confining potential $V(n)$ become unbounded when $n \to \infty$. This is in contrast with finite-range interacting models, where the potential becomes *flat* for n greater than the interaction range. In other words, for finite-range interacting systems two domain walls will behave like freely propagating particles if the domain size of the initial state exceeds the interaction range.

Fig. 2.3(b) shows the energy spectrum calculated by the two-kink model (blue dots) and exact diagonalization (ED) of the full Hamiltonian (red dots). The energy spectrum agrees well for the two methods, demonstrating that low-energy excitations are dominated by two-domain-wall states. The bound states' masses [2] and dispersion relations can be simply read out from the energy spectrum. Moreover, the Fourier frequencies of $\langle \sigma^z(t) \rangle$ [Figs. 2.2(c) and 2.2(d)] coincide, to high accuracy, with the masses of the bound states (and their differences) calculated using the two-kink model [86, 87]. This demonstrates that the quench dynamics of the long-range interacting model is indeed dominated by confined quasiparticles.

We compare the smallest quasiparticle mass, m_1, as a function of α calculated

[2] The energy difference between (bounded) excited states at $k = 0$ and the ground state.

using the two-kink model and ED [Fig. 2.3(c)]. For a large range of α, we see excellent agreement between the two methods, and the numerical difference does not increase for larger L [inset of Fig. 2.3(c)]. The masses increase with L as longer chains have more interaction terms (see Appendix A). However, $V(n)$ is finite (for finite n) in the thermodynamic limit, since the Riemann zeta function converges for $\alpha > 1$ [111]. This leads to finite masses, even for an infinite system for $\alpha > 1$. As shown in Fig. 2.3(d) , the mass calculated from the two-kink model indeed exhibits convergence in the thermodynamic limit. For the two-kink model, the difference between m_1 and its thermodynamic value, $m_{1,\infty}$, scales as $(1/L)^\beta$, with $\beta \approx \alpha - 1$ (see Appendix A for detailed derivation) , as shown in the inset. While we cannot verify convergence using ED, we do observe similar scaling of m_1 [inset of Fig. 2.3(d)]. For $0 \leq \alpha \leq 1$, $V(n)$ becomes infinite, even for finite n, and thus the quasiparticles have infinite energy (as the Riemann zeta function diverges for $0 \leq \alpha \leq 1$ [111]), consistent with the results of Ref. [112].

2.5 Strong and weak thermalization

For the quenches we have considered, both the order parameter decay and entanglement growth are slow (Fig. 2.1). This movitates us to study thermalization in our long-range model. Previous studies of the short-range Ising model have observed rapid (strong) or slow (weak) thermalization of one-point functions for different initial states [86,87,93,94,113–116]. As first shown in Ref. [86], undamped oscillations (weak thermalization) of one-point observable occurs within an intermediate time

window when the matrix element between the initial state and the quasiparticle state of the quench operator and of the observable are both non-zero [86,87]. Rapid decay occurs when this condition is not satisfied. Numerical results consistent with this finding have been observed [79,87,93,94,115]. Here, we illustrate that these two distinct behaviors also occur in the long-range Ising model and that slow thermalization can arise when the quasiparticles are the result of confinement [79,87,115].

In order to see this, we consider the time evolution of two different initial states (with the same quenched Hamiltonian): $|Z_+\rangle = \prod_j |\uparrow_j\rangle$ (the same state considered before) and $|Y_+\rangle = \prod_j \frac{1}{\sqrt{2}}(|\uparrow_j\rangle + i\,|\downarrow_j\rangle)$ [93]. For $|Z_+\rangle$, the energy expectation value is near the bottom of the spectrum. We thus expect the dynamics to be dominated by the bound states discussed above. On the other hand, the energy expectation value of $|Y_+\rangle$ is exactly zero, which is far above the energies of the bound states. We, therefore, expect the bound states to have little effect on dynamics in this case, leading to faster thermalization.

We calculate the difference between the time-dependent expectation value of single-body observables, $\langle\sigma^\mu(t)\rangle$, and their thermal expectation value, $\langle\sigma^\mu\rangle_{\text{th}} = \text{tr}(e^{-\beta_\Psi H}\sigma^\mu)/\text{tr}(e^{-\beta_\Psi H})$, where the temperature, $\frac{1}{\beta_\Psi}$, is determined by [117]:

$$\frac{\langle\Psi|\,H\,|\Psi\rangle}{\langle\Psi|\Psi\rangle} = \frac{\text{tr}(He^{-\beta_\Psi H})}{\text{tr}(e^{-\beta_\Psi H})}. \tag{2.5}$$

Here, $|\Psi\rangle$ denotes the initial state. As illustrated in Fig. 2.4(a), for $|Y_+\rangle$, all single-body observables converge to $\langle\sigma^\mu\rangle_{\text{th}}$ rapidly, indicating strong thermalization, as expected. For $|Z_+\rangle$, we instead observe strong oscillatory behavior [86, 87], with

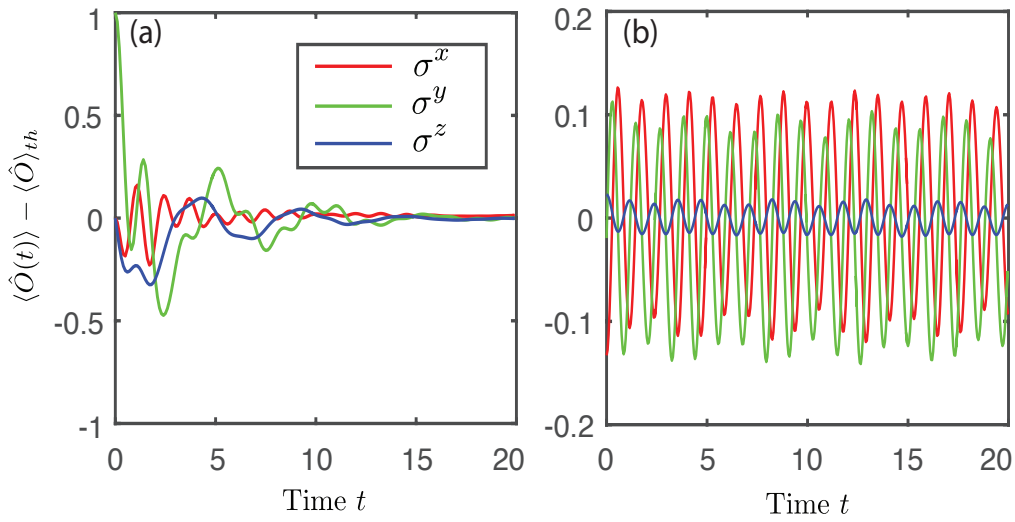

Figure 2.4: Strong (a) and weak (b) thermalization for different initial states. (a) $\langle \sigma^{\mu}(t) \rangle - \langle \sigma^{\mu} \rangle_{\text{th}}$ for initial state $|Y_+\rangle$. (b) Same as (a), but for initial state $|Z_+\rangle$. Parameters: $\alpha = 2.3$, $B = 0.37, L = 20$.

Fourier frequencies consistent with the masses of the bound quasiparticles, around $\langle \sigma^{\mu} \rangle_{\text{th}}$ [Fig. 2.4(b)]. Within the time window shown, we observe almost no decay of these observables, indicating much slower thermalization compared to $|Y_+\rangle$ [93, 94]. Therefore, we have observed the thermalization has a strong dependence on the initial state we choose. However, different types of single-body observables for the same initial state show similar thermalization behavior.

2.6 Conclusions and outlook

We have found that the low-energy excitations of the long-range transverse-field Ising model are confined domain-walls. These bound quasiparticles, which arise due to long-range interactions, have clear signatures in the quench dynamics of the system [79, 86, 87]. Furthermore, our work shows that general quantum mechanisms of quench dynamics developed for short-range interacting systems [86, 87, 89] hold for

long-range interacting systems. These results can be readily investigated in trapped ion experiments [18] and other AMO system with long-range interaction [12, 13, 55]. The slow thermalization of one-point functions induced by long-range interactions has potential applications for stabilizing non-equilibrium phases of matter, such as time crystals [95–97] and Floquet symmetry-protected topological phases of matter [118–122]. Finally, it would be interesting to study the effects of long-range interactions on quench dynamics of q-state Potts models, which admit mesonic, as well as baryonic excitations [123–126].

Chapter 3: Domain Wall Confinement and Dynamics in a Quantum Simulator

3.1 Introduction

Fundamental constituents of matter, quarks and gluons, cannot be observed in isolation, because they are confined into bound states of mesons or baryons. Although the existence of confinement in nature is well established, quantitative understanding of this phenomenon from QCD dynamics remains an active area of research [127]. Similar phenomena can occur in low-energy quantum many-body systems, which can provide insight for understanding confinement from a microscopic perspective. The static and equilibrium properties of such confined systems have been well characterized in previous theoretical [90, 128, 129] as well as experimental works [82, 130]. However, recent theoretical studies have demonstrated that confinement can also have dramatic consequences for the out-of-equilibrium dynamics of quantum many-body systems, such as suppression of information spreading and slow thermalization [79, 112–114, 131–134].

Quantum simulators allow the study of out-of-equilibrium physics of quantum many-body systems in a well-controlled environment [9, 135]. An emerging

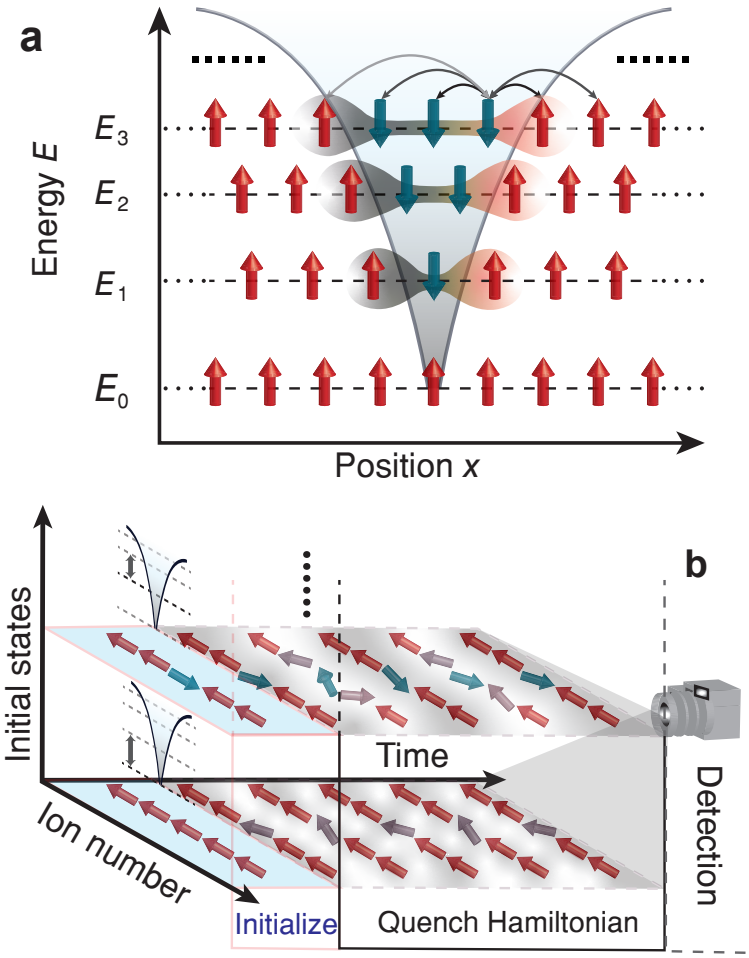

Figure 3.1: Effective confining potential and experiment sequence. (a), Magnetic domain walls in Ising spin chains can experience an effective confining potential that increases with distance analogously to the strong nuclear force. This potential results in meson-like domain wall bound states (labeled E_1 to E_3) that can dramatically influence the dynamics of the system [114, 132]. (b), This experiment begins by initializing a chain of trapped-ion spins in a product state. We introduce pairs of domain walls by flipping the initial states of chosen spins. The spins evolve according to the quenched Hamiltonian for some time, after which we measure various observables, such as magnetizations of each individual spin along a desired axis.

application of these simulators is the study of problems motivated by high-energy physics and gauge theories [136–148]. As studied in the last chapter, trapped-ion quantum simulators [18, 103, 149, 150] can be used to directly observe real-time domain wall confinement dynamics following a quantum quench, or sudden change in the Hamiltonian (Fig. 3.1). Here we carry out the experimental study and show that confinement can suppress the spreading of correlations even in the absence of disorder, and that quench dynamics can be used to characterize the excitation energies of confined bound states. Additionally, we measure the number of domain walls generated by a global quench, in and out of the confinement regime. Finally, we demonstrate that the number of domain walls can be an effective probe of the transition between two distinct dynamical regimes [18, 151].

Confinement in many-body systems occurs in one of the classic models of statistical mechanics: the Ising spin chain with both transverse and longitudinal magnetic fields. A non-zero longitudinal field confines pairs of originally freely-propagating domain wall quasiparticles into meson-like bound states in a short-range interacting system [79, 113, 114]. However, recent theoretical efforts (see Chapter 2) have demonstrated that *long-range* Ising interactions, instead of an additional longitudinal field, can naturally induce a confining potential between pairs of domain walls (Fig. 3.1(a)). As a consequence of confinement, the low-energy spectrum of such an Ising system can feature meson-like bound domain wall quasiparticles (Fig. 3.1(a)) [79, 132], similar to confinement in quantum chromodynamics (QCD) in which quarks and antiquarks are confined into hadrons due to strong interactions. In both cases confining potentials increase asymptotically with particle sep-

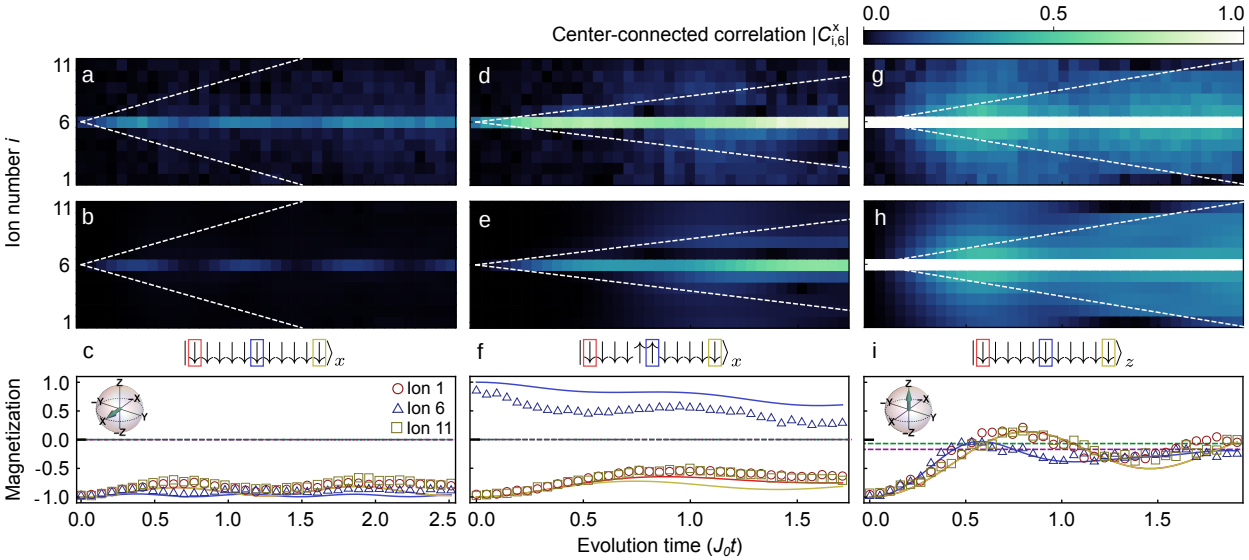

Figure 3.2: Confinement dynamics at $B/J_0 \approx 0.75, L = 11$. The top row shows the absolute value of experimental center-connected correlations $|C^x_{i,6}(t)|$ averaged over 2000 experiments. The middle row shows $|C^x_{i,6}(t)|$ calculated by solving the Schrödinger equation. Dashed white lines show correlation propagation bounds (light cones) in the limit $\alpha \to \infty$ (nearest-neighbor interactions). The bottom row shows measured individual-spin magnetizations along their initialization axes, $\langle \sigma^{x,z}_i(t) \rangle$, averaged over 2000 experiments (400 experiments for (i)). Symbols represent magnetization data and solid colored curves represent theoretical magnetizations calculated by solving the Schrödinger equation. All magnetization error bars, $\pm$1s.d., are smaller than their plot symbols and are not shown. Purple (green) dashed lines represent thermal expectation values calculated from a canonical (microcanonical) ensemble averaged over the three displayed spins (see Appendix B). (a)-(c), show a low-energy initial state containing zero domain walls. Individual magnetizations are $\langle \sigma^x_i(t) \rangle$. (d)-(f), show a low-energy initial state containing two domain walls, with a center domain of two spins. Individual magnetizations are $\langle \sigma^x_i(t) \rangle$. We attribute the discrepancy between the experimental magnetization data and numerics to imperfect state initialization. (g)-(i), show a high-energy initial state containing many domain walls. Individual magnetizations are $\langle \sigma^z_i(t) \rangle$.

aration, although with differing power-law forms. Similarly to QCD, domain wall confinement in the long-range Ising model studied here includes a discrete spectrum of bound states (Fig. 3.3), string breaking [134] (or particle/antiparticle creation), and a confinement-deconfinement crossover as a function of energy density [127,152] (Fig. 3.4). While this model does not include other aspects of QCD, such as gauge fields or chiral symmetry breaking, the similarity of the confinement mechanisms allows us to draw broadly applicable conclusions about this effect.

3.2 Domain wall confinement

As studied theoretically in the last chapter, we use a trapped-ion quantum simulator to investigate confinement in a many-body spin system governed by the Hamiltonian ($\hbar = 1$)

$$H = -\sum_{i<j}^{L} J_{i,j}\sigma_i^x\sigma_j^x - B\sum_{i}^{L}\sigma_i^z. \tag{3.1}$$

Here, σ_i^γ ($\gamma = x, y, z$) is the Pauli operator acting on the ith spin, $J_{i,j} \approx J_0/|i-j|^\alpha$ is the power-law decaying Ising coupling between spins i and j with tunable exponent α, $J_0 > 0$, B is the effective transverse field, and L is the number of spins [153,154]. We encode each spin in the ground-state hyperfine levels, $|\uparrow\rangle_z \equiv |F = 1, m_F = 0\rangle$ and $|\downarrow\rangle_z \equiv |F = 0, m_F = 0\rangle$, of the $^2S_{1/2}$ manifold of a $^{171}\mathrm{Yb}^+$ ion. The Ising couplings are produced via spin-dependent optical dipole forces, with power-law exponents α ranging from 0.8 to 1.1 and $J_0/2\pi$ ranging from 0.23 kHz to 0.66 kHz (see Appendix B).

To study the real-time dynamics of the spin chain, we use a quantum quench

to bring the system out of equilibrium (Fig. 3.1(b)). We first initialize the spins in a product state, polarized either along the x or z-directions of the Bloch sphere. Using a tightly focused individual addressing laser [34], we prepare domain walls in various initial state configurations (Fig. 3.2(c), (f), (i)). After preparing the desired initial state, we perform a sudden quench of the Hamiltonian (3.1). For $B/J_0 \approx 0.75$, the quench optimally drives the system out of equilibrium while remaining in the confinement regime. Following the time evolution of the system, we use spin-dependent fluorescence to measure the state of each spin. From this data, we calculate the time-evolution of magnetizations, $\langle \sigma_i^x(t) \rangle$ or $\langle \sigma_i^z(t) \rangle$, and connected correlations

$$C_{i,j}^x(t) = \langle \sigma_i^x(t) \sigma_j^x(t) \rangle - \langle \sigma_i^x(t) \rangle \langle \sigma_j^x(t) \rangle . \tag{3.2}$$

No post-processing or state preparation and measurement correction has been applied to any of the data reported below.

To understand the effect of confinement on information spreading, we measure the absolute value of connected correlations along x, the Ising direction (Fig. 3.2). When the initial state contains a small number of domain walls, correlations spread with a considerably smaller velocity than the velocity in a corresponding nearest-neighbor interacting system [79] ($v_0 = 4B$, Fig. 3.2). While correlation functions typically exhibit a light cone behavior following a quantum quench [104, 155, 156], we observe strongly suppressed spreading and localized correlations throughout the evolution [112, 113]. This indicates that confinement, induced by long-range inter-

actions, localizes pairs of domain walls at their initial conditions (see Appendix B).

In stark contrast, we find that correlations exhibit faster-than-linear spreading, despite quenching under the same Hamiltonian, in the case of the initial state polarized in the transverse direction z (Fig. 3.2(g), (h), (i)). In this case, the initial state is a linear superposition of all possible spin configurations in the x-direction, and thus contains a large number of domain walls. Unlike the previous initial states, this initial state has an energy density relatively far from the bottom of the many-body spectrum. The long-range interactions among these domain walls lead to fast relaxation and quantum information spreading. These results imply that this confinement effect has a significant impact only on the low-energy excitations of the system, which is consistent with recent theoretical studies [79, 113, 114, 131, 132].

To observe the effect of confinement on the thermalization of local observables, we measure the relaxation of magnetizations for the above initial states [93] (third row of Fig. 3.2). We see that, for the low-energy states, local magnetizations retain long memories of their initial configuration and exhibit slow relaxation (Fig. 3.2(c), (f)). Conversely, for the high-energy initial state, local magnetizations quickly relax to their thermal expectation values (Fig. 3.2(i), also see Appendix B). This is consistent with the observation that correlations quickly distribute across the entire system (Fig. 3.2(h)). We emphasize that the observed slow thermalization is a consequence of confinement, distinct from many-body localization with quenched disorder [96, 157, 158].

In order to quantitatively probe excitation energies of bound domain wall

states, we prepare initial states polarized along the x-direction and vary the number of spins separating the two initial domain walls (insets of Fig. 3.3(a)-(c)). Then, we quench the system under the Hamiltonian (3.1) and measure the time-evolution of local magnetizations along the transverse direction, $\langle \sigma_i^z(t) \rangle$. In the confinement regime, the prepared initial states predominantly overlaps with low-energy eigenstates of the confinement Hamiltonian [132]. All local observables should exhibit oscillations with frequencies proportional to the energy gap between these bound states before thermalizing [79, 132]. Here, we choose a single-body spin observable, $\langle \sigma_i^z(t) \rangle$, at the center of the chain (for 0 initial domain walls) or at the outer boundaries of the initial domain (for 2 initial domain walls). We make this particular choice in order to minimize edge effects from the finite spin chain and maximize the matrix elements of this observable between the prepared state i and the adjacent higher-energy bound state $i+1$ (Fig. 3.1(a)), allowing us to extract the energy gap between these two states (Appendix B).

Following this prescription, we extract oscillation frequencies using single-frequency sinusoidal fits of $\langle \sigma_i^z(t) \rangle$ to obtain the energy gap between each initialized state and the neighboring excited state (Fig. 3.3(a)-(c)). We compare these extracted energies to values predicted by numerical simulation (Appendix B). We find excellent agreement between the measured energies and the energies predicted numerically (Fig. 3.3(d)). Using these experimentally measured energy gaps, we can systematically construct the low-energy excitation spectrum of the many-body system for quasimomentum $k \approx 0$ (Fig. 3.3(e)). In general, quasiparticles with arbitrary quasimomenta can be excited by a quantum quench. However, since the

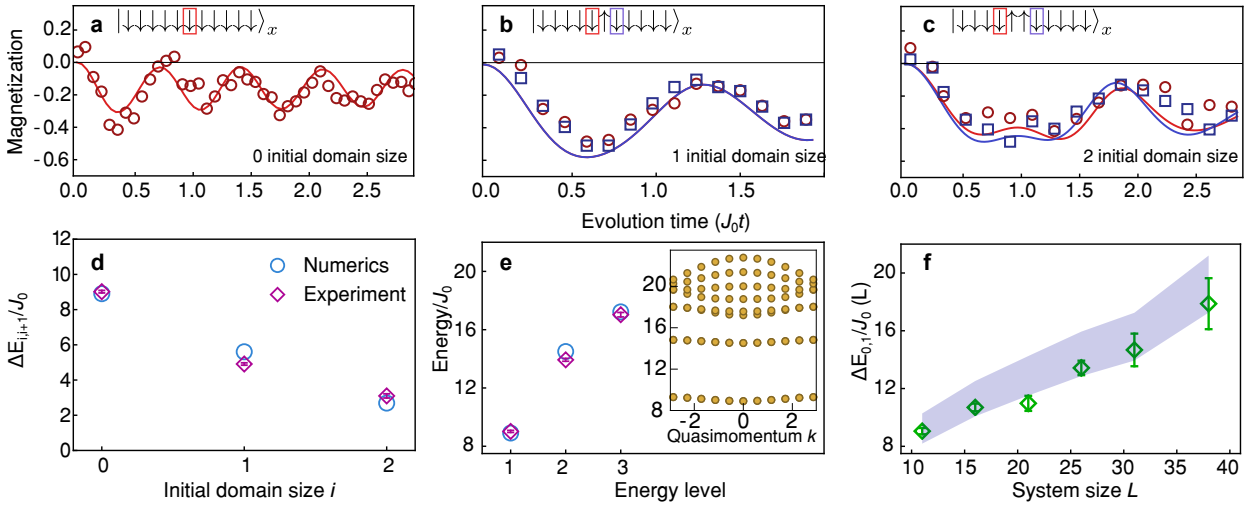

Figure 3.3: Low-energy excited states. (a)-(c), show the magnetizations of the boxed spins on the edges of the center domain at $B/J_0 \approx 0.75$. These magnetization oscillation frequencies correspond to the normalized energy gap, $\Delta E_{i,i+1}/J_0$. Solid colored lines represent theoretical calculations of dynamics by solving the Schrödinger equation. The error bars, $\pm$1s.d., are smaller than their plot markers and are not shown in (a)-(c). (a), Zero initial domain size: $\Delta E_{0,1}/J_0$ is given by the frequency of the 6th spin. (b), Initial domain size of one: $\Delta E_{1,2}/J_0$ is given by the frequency of the 5th and 7th spins. (c), Initial domain size of two: $\Delta E_{2,3}/J_0$ is given by the frequency of the 4th and 7th spins. (d), $\Delta E_{i,i+1}/J_0$ for $i \leq 2$ are measured with three different initial domain size spin configurations at $B/J_0 \approx 0.75$. The first three energy gaps ($i \leq 2$) are extracted from the magnetization oscillation frequencies shown in the top row. (e), We construct the bound state energy levels at quasimomentum $k \approx 0$ using experimental data in (d), where E_0/J_0 is set to zero. Inset: Theoretical bound state energy bands with different quasimomentum, k, within the two-domain-wall model [132]. (f), Scaling of $\Delta E_{0,1}/J_0$ with system size at $B/J_0 \approx 1$. The blue shaded region shows the two-domain-wall model [132] numerical prediction of $\Delta E_{0,1}/J_0$, with a confidence band considering $\pm$10 % fluctuations in the Ising interaction strength J_0.

confining potential is steep, excited quasiparticles remain localized and their quasi-momenta are close to zero. Furthermore, leveraging the scalability of trapped-ion systems, we perform this experiment with up to 38 spins. In order to numerically investigate these large system sizes, we use a phenomenological two-domain-wall model [132]. With this model, by restricting the full Hilbert space to a subspace of states containing only zero or two domain walls, we calculate the bound quasiparticle spectrum of Hamiltonian (3.1) for system sizes that would be challenging to exactly simulate with classical resources (Fig. 3.3(f)). We find reasonable agreement in the first excitation energy gap, $\Delta E_{0,1}$, between the experimental data and numerical predictions for all system sizes (Fig. 3.3(f)). We attribute the systematic discrepancy in larger systems to variations in J_0 during the time evolution (Appendix B). These results, taken together, suggest that quench dynamics are dominated by the confinement effect between two domain wall quasiparticles.

3.3 Beyond confinement regime

We now go beyond the confinement regime to study the number of domain walls generated by the quantum quench for a wide range of transverse B-field strengths. Although we still prepare an initial state polarized along $|\downarrow\rangle_x$, for large B the strong quench can excite a large number of domain walls which are no longer bounded. We thus expect that the out-of-equilibrium dynamics are no longer captured by the confinement picture for these parameters. To explore this regime, we

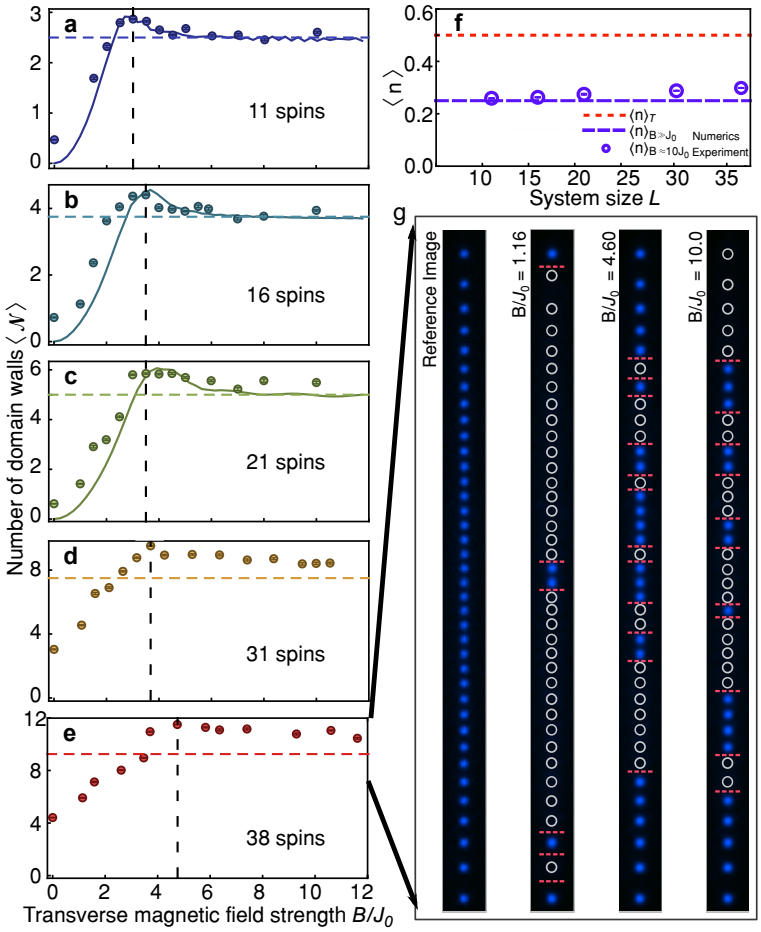

Figure 3.4: Number of domain walls in two dynamical regimes. (a)-(e), Exploring the two dynamical regimes with increasing transverse B-field strength in different system sizes. Circular dots indicate experimental data. Horizontal lines show theoretical predictions of $\langle \mathcal{N} \rangle = 0.25(L-1)$ at $B \gg J_0$. Colored continuous lines represent numerical results predicted by solving the Schrödinger equation. Vertical dashed lines indicate the experimental maxima of $\langle \mathcal{N} \rangle$. Theoretical lines for system sizes $L = 31$ and $L = 38$ are absent because we cannot compute the predicted evolution numerically for the experimental parameters. (f), Dashed purple horizontal line shows the theoretical prediction of domain wall density at $B \gg J_0$, $\langle n \rangle_{B \gg J_0}$. The purple circular dots indicate experimental data of domain wall density at $B \approx 10J_0$, $\langle n \rangle_{B \approx 10J_0}$. The dashed red line at $\langle n \rangle_T = 0.5$ shows the density of domain walls using the canonical ensemble at infinite temperature. All the experimental data is integrated within the time interval $J_0 t_1 \approx 0.34$ and $J_0 t_2 \approx 0.73$. (g), Reconstructed images based on binary detection of spin states. The leftmost image is a reference image of a 38 ion chain in a 'bright' state ($|\uparrow\rangle_x$). At the beginning of the experiment, the spins are initialized in the 'dark' state ($|\downarrow\rangle_x$). The three right images show experimental data of a combination of 'bright' and 'dark' states, marked in blue and white circles respectively, for three different B/J_0 values within the integrated time frame. The occurrences of domain walls are highlighted with orange horizontal dashed lines. The error bars are ± 1 s.d. with >150 experiments.

measure the cumulative time average of the total number of domain walls,

$$\langle \mathcal{N} \rangle = \frac{1}{t_2 - t_1} \int_{t_1}^{t_2} \sum_{i=1}^{L-1} \frac{\langle 1 - \sigma_i^x(t)\sigma_{i+1}^x(t) \rangle}{2}, \tag{3.3}$$

where t_1 and t_2 enclose a window where $\langle \mathcal{N} \rangle$ converges to a stable value (Appendix B). The expectation value is normalized by 1/2 to correctly count the number of domain walls between neighboring spins [159]. We measure $\langle \mathcal{N} \rangle$ as a function of B for different system sizes (Fig. 3.4(a)-(e)). We observe that, for small B fields, Ising interactions dominate the dynamics and the global quench can only excite a small number of domain walls. However, for a large enough transverse field, the number of generated domain walls saturates to a value that scales nearly linearly with system size (Fig. 3.4(f)). Here, we observe a transition between these two dynamical regimes at intermediate values of B for different system sizes. This behavior is analogous to the confinement-deconfinement crossover conjectured in QCD, in which increasing energy density (controlled by B in this experiment) causes hadronic matter to form a quark-gluon plasma or other exotic phase [127]. In both models, beyond a critical energy density, weaker interactions allow particles to freely move with negligible energy penalty.

To illustrate the population of domain walls in different regimes, we show typical single-shot images of the quenched state of 38 ions for different transverse B-fields in Fig. 3.4(g). We indeed see that a small (large) number of domain walls is generated by the quench with small (large) B field. Although we are unable to compute the dynamics for system size $L = 31$ and beyond with general-purpose

computers, we can intuitively understand the distinguishing behaviors. When we increase B to values significantly larger than J_0, all spins undergo Larmor precession around the z-axis of the Bloch sphere, which allows us to predict that $\langle \mathcal{N} \rangle$ saturates to $0.25(L-1)$ when $B \to \infty$ (see Appendix B for detailed derivation). We note that, for $B \gg J_0$, the experiment operates in the prethermal region in which a transient Hamiltonian is approximately conserved for an exponentially long time [108, 160–162]. Therefore, we expect the number of domain walls to approach the thermal value, $\langle n \rangle_T = 0.5$, only after an exponentially long time, beyond the reach of this experiment. The experimental results agree with the numerical prediction for system sizes within the reach of numerical simulations. We attribute the discrepancies at large system sizes to bit-flip events due to detection errors and off-resonant coupling to motional degrees of freedom (Appendix B), and to finite effective magnetic fields B compared to the total interaction energy [163], that is increasing with system size due to its long-range character.

3.4 Conclusion

In summary, we have presented a real-time observation of domain wall confinement caused by long-range interactions in trapped-ion spin systems. By measuring oscillating magnetizations, we were able to construct the spectrum of low-energy domain wall bound states. Furthermore, we observed a transition between distinct dynamical behaviors using the number of domain walls generated by the global quench. This work demonstrates that confinement, naturally induced by long-range

interactions, may provide a novel mechanism for protecting quantum information without engineering disorder. Such a feature may be applied in future studies to use long-range interactions to stabilize non-equilibrium phases of matter. All together, this work establishes the utility of trapped-ion quantum simulators for precisely studying real-time dynamics of many-body systems, potentially extending to exotic phenomena such as particle collision and string breaking [134].

Chapter 4: Realizing and Probing Baryonic Excitations in Rydberg Atom Arrays

4.1 Introduction

The development of controllable and coherent quantum simulators has the potential to provide new insights into a variety of many-body systems [164]. Such simulators are ideal for studying phenomena such as non-equilibrium physics or scattering in quantum field theories which are difficult to simulate classically [156, 165–168]. One class of quantum many-body systems that has been of interest recently is those exhibiting confinement. Confinement is the phenomenon whereby the fundamental excitations of a system experience a potential which increases indefinitely with their separation, resulting in the formation of bound states in the low-energy spectrum [79, 169, 170]. This mechanism plays an important role in quantum chromodynamics (QCD), where confinement due to gauge fluctuations explains the formation of mesons and baryons from quarks. Although confinement between quarks is well-established, there are a number of difficulties in obtaining quantitative estimates for physical observables [127].

Recently, there have been theoretical [132, 141, 152, 171–173] and experimen-

tal [174] works on quantum simulators realizing confinement. Such quantum simulators realize experimental control over isolated quantum systems at the single-atom level, which allows a great deal of sensitivity in both manipulation and detection [13, 41, 175]. To date, these systems only exhibit pairwise confinement of particle-antiparticle pairs into mesonic two-particle bound states [1]. To make closer contact with the phenomenology of QCD, it would be advantageous to realize a model Hamiltonian whose spectrum contains more complex bound states.

In this Chapter, we propose a quantum simulator scheme to implement confined baryonic and mesonic excitations in Rydberg atom arrays. The basis for our proposal involves the recent realization of crystalline states which exhibit spontaneously broken $\mathbb{Z}_q$ symmetry, where the chain is populated by a Rydberg excitation every q sites [13, 47]. The low-energy excitations above these ground states are defects which lie between the degenerate ordered ground states, and these defects may be separated from each other to arbitrary distances. We show that by adding a non-uniform on-site detuning which breaks the $\mathbb{Z}_q$ symmetry, the different types of domain-wall defects observed in Ref. [47] are bound together so that the low-energy excitations are instead composite objects such as mesons or baryons. We demonstrate that the masses of these confined quasiparticles have a clear signature in the out-of-equilibrium dynamics of the Hamiltonian, and that the correlation spreading of the system is dramatically reduced in the confined phase. We also discuss in detail the initial state preparation and measurement scheme for observing these confined

[1] Baryonic bound states have been proposed in Ref. [176], but this model does not exhibit confinement.

quasiparticles.

4.2 The model

We study a one-dimensional array of Rydberg atoms described by the following Hamiltonian [13]:

$$H_{\text{Ryd}} = \sum_i \frac{\Omega_i}{2} X_i - \sum_i \Delta_i n_i + \sum_{i<j} V_{|i-j|} n_i n_j. \tag{4.1}$$

Here, $|r_i\rangle$ ($|g_i\rangle$) denotes the Rydberg (ground) state for atom at site i (Fig. 4.1), $X_i = |g_i\rangle\langle r_i| + |r_i\rangle\langle g_i|$, $n_i = |r_i\rangle\langle r_i|$, Ω_i and Δ_i are the Rabi frequencies and detunings respectively, and $V_{|i-j|}$ describes the interaction between atoms in the Rydberg state at sites i and j. The interactions decay strongly with distance, with the scaling $V_r \propto 1/r^6$. When both the Rabi frequencies and detunings are homogeneous in space, this Hamiltonian features ordered ground states where every qth site of the lattice is in the Rydberg state ($q \geq 2$) [44, 46, 177, 178]. Recent experiments have studied the quantum many-body dynamics governed by this Hamiltonian with homogeneous parameters [13], giving insight into phenomena such as quantum many-body scars [42, 43], exotic quantum criticality [44–46], and the quantum Kibble-Zurek mechanism [47].

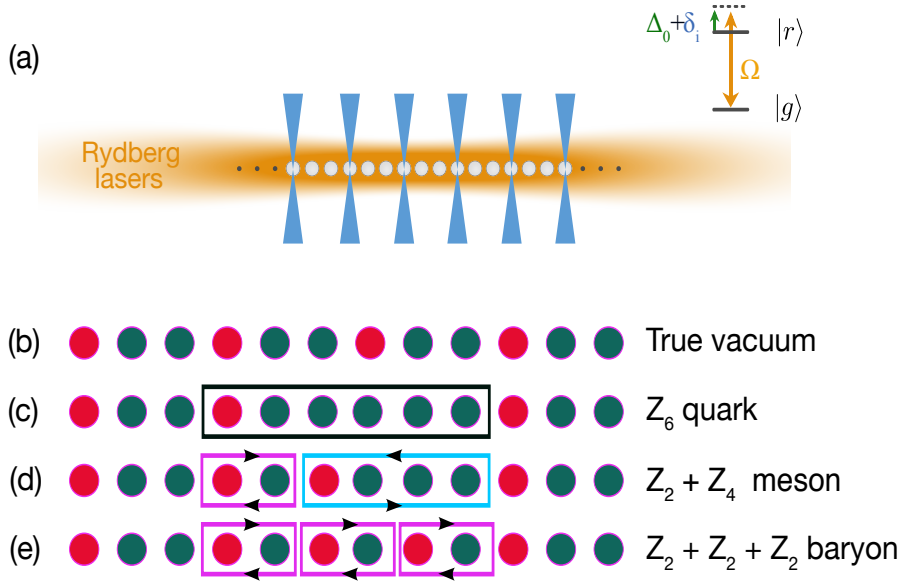

Figure 4.1: (a) Implementation of symmetry breaking fields in the Rydberg array. The beams applied on every third atom create an additional detuning δ_i that is a nonzero constant only on these atoms. (b)-(e) Schematics of mesonic and baryonic excitations formed in the Rydberg array. The red and green dots denote Rydberg and ground states, respectively. With the symmetry breaking fields, different types of low-energy excitations can exist on top of (b) the true vacuum state, including (c) a $\mathbb{Z}_6$ quark excitation, (d) a mesonic excitation formed by $\mathbb{Z}_2 + \mathbb{Z}_4$ defects, and (e) a baryonic excitation formed by $\mathbb{Z}_2 + \mathbb{Z}_2 + \mathbb{Z}_2$ defects.

4.3 Relation to the $\mathbb{Z}_3$ chiral clock model

We focus on the $\mathbb{Z}_3$ phase of the Rydberg Hamiltonian by specializing to the case where both Ω_i and Δ_i are much smaller than V_1. The low-energy quasiparticles above the ordered ground state [which is shown in Fig. 4.1(b)] are $\mathbb{Z}_2$ and $\mathbb{Z}_4$ domain walls between regions with $\mathbb{Z}_3$ order [see Fig. 4.1(d-e)] [47]. We mention that these different types of domain walls (for the homogeneous case) have been directly observed in recent experiments [47]. At higher energies, one expects to furthermore get $\mathbb{Z}_q$ domain walls for $q > 4$ [see, for example, Fig. 4.1(c)].

The system which displays similar physics with the ordered Rydberg system

is the three-state quantum chiral clock model [179, 180]

$$H_{\mathrm{CCM0}} = -f \sum_j \tau_j^\dagger - J \sum_j \sigma_j^\dagger \, \sigma_{j+1} \, \mathrm{e}^{-\mathrm{i}\,\theta} + \mathrm{h.c.}, \tag{4.2}$$

where θ is a phase factor, and the operators τ and σ commute on different sites, with the matrix representation

$$\sigma = \begin{pmatrix} 1 & 0 & 0 \\ 0 & \omega & 0 \\ 0 & 0 & \omega^2 \end{pmatrix}, \qquad \tau = \begin{pmatrix} 0 & 0 & 1 \\ 1 & 0 & 0 \\ 0 & 1 & 0 \end{pmatrix}, \tag{4.3}$$

where $\omega = e^{2\pi i/3}$. The clock model obeys a $\mathbb{Z}_3$ symmetry generated by the operator $\mathcal{G} = \prod_i \tau_i$, and the ground states ('vacua') are three-fold degenerate in the ordered phase. Consequently, the elementary excitations are the clockwise or anti-clockwise domain walls between any two different types of the three vacua [see Fig. 4.2]. Because of the degeneracy, the domain walls may be separated to infinity, since moving a domain wall costs no energy. For $\theta = 0$, the two lowest defects have the same excitation energy, and Eq. (4.2) is the ordinary three-state quantum Potts model, while when $\theta \neq 0$, the two domain walls will have differing energies. Because the lowest-energy excitations have the same structure, the phase transitions in the clock and Rydberg models lie in the same universality class [44, 45, 177]. Such clock models have been used to study low-energy confinement in a number of previous works [123–126, 170, 181], so we shall use intuition obtained from these works to understand how confinement can be engineered in the Rydberg arrays.

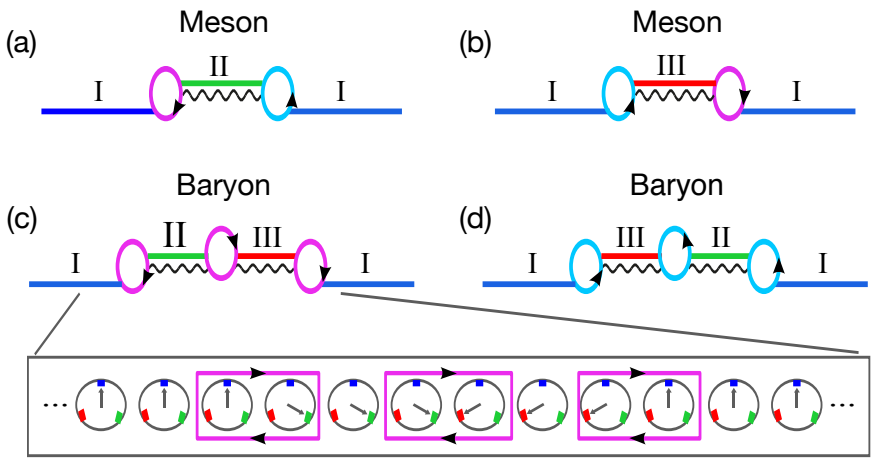

Figure 4.2: Schematics of mesonic and baryonic excitations formed by the three different vacua in the confined chiral clock model, Eq. (4.4). The different vacua are labelled by straight lines with different colors, and the clockwise (anti-clockwise) domain walls between two vacua are labelled by magenta (cyan) circles. The energy cost for creating domain walls scales linearly with their distances, as illustrated by the wavy line. For (c), we additionally give a schematic of the baryonic excitation in the clock basis.

4.4 Confinement via spatially periodic detunings

We now consider an additional spatially periodic detuning δ_i on top of the homogeneous Δ_0 in the Rydberg Hamiltonian. Specifically, we analyze the case where there is an energy decrease of the Rydberg state for every third atom [see Fig. 4.1(a)]. The periodic field can be realized in experiments by using locally addressed lasers [182]. With this field, the three-fold degeneracy of the vacua and the $\mathbb{Z}_3$ symmetry of Eq. (4.2) [and Eq. (4.1)] are explicitly broken [see Fig. 4.2]. We use I to label the 'true vacuum' which has lower energy than the other two degenerate 'false vacua' II and III . The corresponding quantum clock Hamiltonian

now includes an additional longitudinal field

$$H_{\mathrm{CCM1}} = -f \sum_j \tau_j^\dagger - J \sum_j \sigma_j^\dagger \, \sigma_{j+1} \, \mathrm{e}^{-\mathrm{i}\,\theta} - h \sum_j \sigma_j + \mathrm{h.c.} \tag{4.4}$$

In contrast to the homogeneous case, with the longitudinal field, the domain-walls between true and false vacua cannot be separated to long distances due to a confining potential (an energy penalty) which scales linearly with the separation between defects. Consequently, the low-energy excitations of the Hamiltonian for large system sizes must be entirely made up of bound states of domain walls. This is in close analogy to confinement in particle physics, where quarks cannot be directly observed in nature as two (three) of them are bound into mesons (baryons), due to similar confining potential scaling [79, 169, 170].

Fig. 4.2 schematically shows the low-energy bound quasiparticle excitations formed by different vacua, which include both mesonic and baryonic bound states. The mesonic states are formed by two domain walls, including one clockwise (connecting I→ II, II→III, or III→I) and one counterclockwise (connecting III→ II, II→I, or I→III) defect [Fig. 4.2(a-b)]. On the other hand, the baryonic excitations are composed of either three clockwise domain walls or three anti-clockwise domain walls [see Fig. 4.2(c-d)].

A schematic plot of the low energy excitations on top of the true ground state for the Rydberg array is shown in Fig. 4.1, where the picture is exact when $\Omega = 0$. The ordered ground state is mapped to the $\mathbb{Z}_3$-ordered crystalline state for the Rydberg chain [Fig. 4.1(b)]. Further, the clockwise and anti-clockwise defects map

to the $\mathbb{Z}_2$ and $\mathbb{Z}_4$ defects, respectively [Fig. 4.1(d)]. Due to the same mechanism, the additional real-space periodic potential leads to a confining potential between the domain walls, which thus leads to bound states of the $\mathbb{Z}_2$ and $\mathbb{Z}_4$ defects. It is clear that both the mesonic and baryonic excitations shown in Fig. 4.2 can be mapped to corresponding Rydberg configurations. We note that the Rydberg model of Eq. (4.1) will additionally allow higher-energy defect states such as "$\mathbb{Z}_6$ quarks" [Fig. 4.1(c)], which have no analogue in the chiral clock model.

Although we have focused on the $\mathbb{Z}_3$ case, the above can be formulated for any of the $\mathbb{Z}_q$ ordered states. For $q = 2$, this corresponds to the well-studied confinement in the Ising model with a longitudinal field [79,132]. For $q > 3$, one can additionally obtain more complicated 'tetraquark' or 'pentaquark' states, in which 4 or 5 domain walls, respectively, bind together. We note that the spectrum of confined excitations for the Potts [$\theta = 0$ in Eq. (4.4)] model has been explored in a number of theoretical works [123–126], but the general $\theta \neq 0$ case has not been explored yet. While our proposal to realize confinement does not come from a lattice gauge theory, the relation between confinement in spin models and gauge theories has a long history in the nonperturbative study of lattice gauge theories [169, 170, 183, 184]. This is particularly clear in one dimension, where the mechanism of confinement in gauge theories can be similarly described as binding together defects between degenerate vacua, although resulting from matter coupling to gauge field [185, 186]. In fact, the $\mathbb{Z}_2$ case for our present system is dual to the bosonized massive Schwinger model [187, 188].

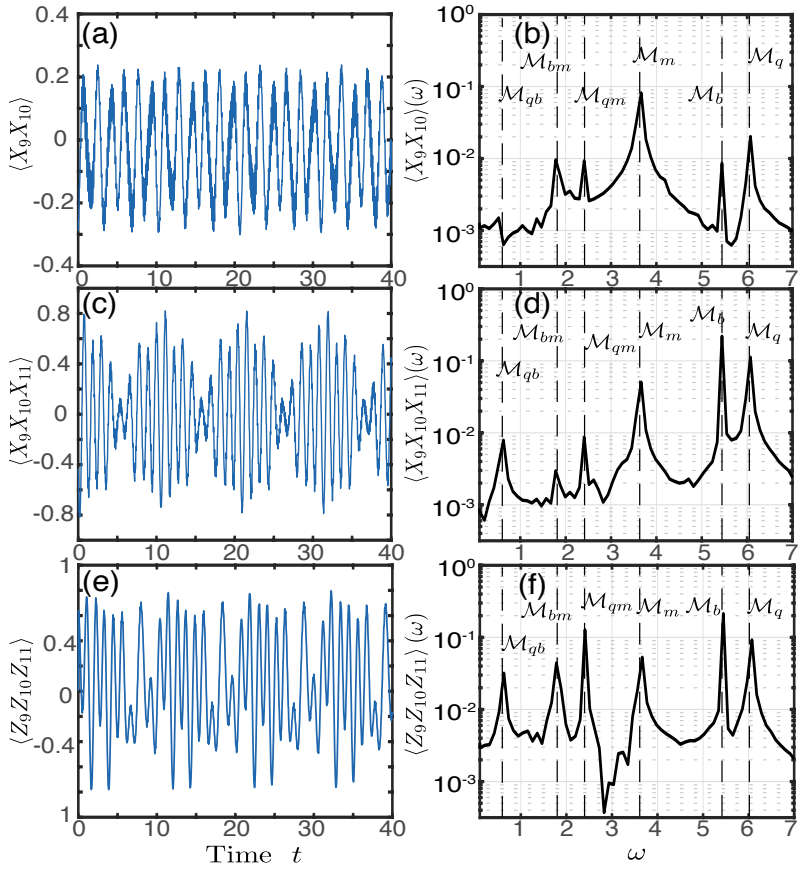

Figure 4.3: (a-b) The initial state is chosen to maximize the total probability of $|\Psi_v\rangle$ and $|\Psi_m\rangle$ under the preparation protocol discussed in the text. (c-f) The initial state is chosen to maximize total probability $|\Psi_v\rangle$ and $|\Psi_b\rangle$. Shown are the time-dependent expectation values and the associated Fourier spectra of (a-b) $\langle\Psi(t)|\, X_9X_{10}\,|\Psi(t)\rangle$, (c-d) $\langle\Psi(t)|\, X_9X_{10}X_{11}\,|\Psi(t)\rangle$, and (e-f) $\langle\Psi(t)|\, U^\dagger Z_9Z_{10}Z_{11}U\,|\Psi(t)\rangle$, where U is a $\pi/2$-pulse applied to the middle three atoms. The dotted lines denote the energy of the meson ($\mathcal{M}_m$), baryon ($\mathcal{M}_b$), quark ($\mathcal{M}_q$) and their energy differences ($\mathcal{M}_{bm}$, $\mathcal{M}_{qb}$, $\mathcal{M}_{qm}$) obtained from exact diagonalization. Parameters: $L = 18$, Ω_i is chosen to be homogeneous $\Omega = 1$; $\Delta_i = \Delta_0 + \delta_i$, where $\Delta_0 = 4$ and $\delta_i = 2$ for $(i \mod 3) = 1$ and 0 otherwise; $V_1 = 164.17$, corresponding to Rydberg radius being 2.34 [47].

4.5 Detecting quasiparticle masses

We consider using quench dynamics to probe 'mesonic' and 'baryonic' masses in Rydberg experiments. One can in principle prepare the product state of Fig. 4.1(b), and the subsequent quench dynamics under Eq. (4.1) would be set by the excitation energies of the bound quasiparticles [79]. However, since we work in the regime where Ω is much smaller than Δ and V_2, the excitation probability of bound quasiparticles can be low as it intrinsically involves high-order processes [2].

We instead choose the initial states to have sizable overlap with both the ground state and localized excited states. Since the lowest-order mesonic and baryonic excitations involve flipping the states of only three atoms (in the $\Omega_i = 0$ limit), we consider the set of initial states involving a large superposition of the true vacuum state $|\Psi_v\rangle = |...rggrggrggrgg...\rangle$ and the target mesonic $|\Psi_m\rangle = |...rggrgrgggrgg...\rangle$, or involving the true vacuum state and baryonic state $|\Psi_b\rangle = |...rggrgrgrgrgg...\rangle$ (see Fig. 4.1)[3]. The intuition for choosing such initial states comes from the $\Omega_i = 0$ limit, where the dynamics with such initial states involves oscillations between the 'true vacuum' state and the localized mesonic and/or baryonic states displayed in Fig. 4.1. We will show that the real-time dynamics involving these states can indeed resolve the many-body bound excitations for general $\Omega_i \neq 0$ [Fig. 4.3].

We first choose the time-dependent observables to be $X_9X_{10}X_{11}$ and X_9X_{10} (chain length $L = 18$), as they have non-vanishing matrix elements between the

[2]The transition from the vacuum state to the mesonic (baryonic) excitation involves a second (third) order process.

[3]The '...' denotes repeated structure of the ordered phase with rgg

vacuum state and the baryonic and mesonic state, respectively. Fig. 4.3 shows the numerical results for the time-dependent expectation value of observables and their Fourier transform. Note that the initial state is chosen to maximize the total probability of $|\Psi_v\rangle$ and $|\Psi_m\rangle$ [for Fig. 4.3(a-b)], or the total probability of $|\Psi_v\rangle$ and $|\Psi_b\rangle$ [for Fig. 4.3(c-d)], under a specific preparation protocol (discussed later). These states are evolved under the fully long-range Hamiltonian Eq. (4.1) with non-zero δ_i, and other parameters are chosen such that the ground state is in the $\mathbb{Z}_3$-ordered phase for $\delta_i = 0$. As Figs. 4.3(a) and (c) show, the observables exhibit clear periodic oscillations. Their Fourier spectra [Fig. 4.3(b) and (d)] agree perfectly with the masses of the '$\mathbb{Z}_2 + \mathbb{Z}_4$ meson' ($\mathcal{M}_m$), the '$\mathbb{Z}_2 + \mathbb{Z}_2 + \mathbb{Z}_2$ baryon' ($\mathcal{M}_b$), the '$\mathbb{Z}_6$ quark' ($\mathcal{M}_q$), and their energy differences ($\mathcal{M}_{bm}$, $\mathcal{M}_{qb}$ and $\mathcal{M}_{qm}$). We mention that the highest Fourier peaks of Fig. 4.3(b) and (d) agree with the mesonic and baryonic masses respectively, as the particular initial states have large components of the target excited states.

We note that in the current experiments only measurement in the Z-basis is possible. In order to access the masses given by X-observables, one can use a $\pi/2$ pulse (which we denote as U) rotating the states of the middle three atoms before the measurement (subject to Rydberg constraint as discussed in detail later). The observable $\langle\Psi(t)|\, U^\dagger Z_9 Z_{10} Z_{11} U\, |\Psi(t)\rangle$ after the rotation also oscillates with a large contrast [see Figs. 4.3(e)], and its Fourier spectrum accurately determines the masses of the baryonic, mesonic and the higher-energy quark excitations [Figs. 4.3(f)]

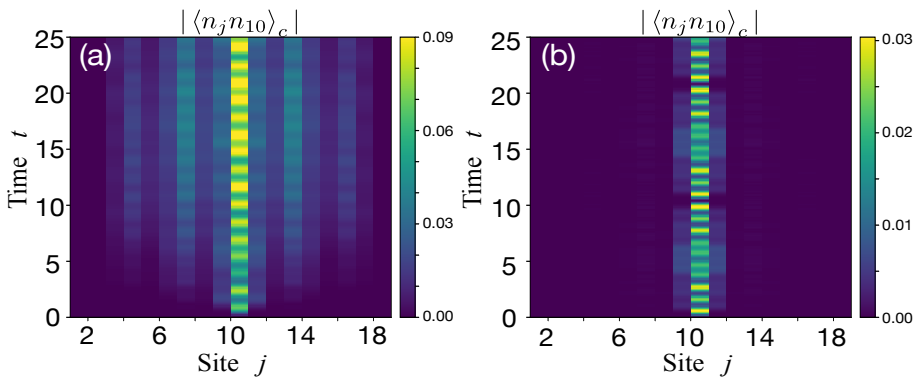

Figure 4.4: Correlation spreading after a quantum quench from the $\mathbb{Z}_3$-ordered state $|\Psi_v\rangle$. (a) shows the time-dependent $|\langle n_j n_{10}\rangle_c|$ without the additional periodic spatially detuning, i.e. $\delta_i = 0$. (b) shows the same quantity with $\delta_i = 2$ for $(i \mod 3) = 1$ and 0 otherwise. All other parameters are the same for (a) and (b): $\Omega = 1, \Delta_0 = 4, V_1 = 164.17, L = 19$.

4.6 Quantum information spreading

The confined quasiparticles at low energy can have a dramatic effect on the correlation spreading in the system. For instance, confinement can strongly suppress the spreading of correlations and lead to slow thermalization [79, 189]. Here we focus on the time-dependent connected correlation function $|\langle n_j n_k\rangle_c| = |\langle n_j n_k\rangle - \langle n_j\rangle\langle n_k\rangle|$ to study the quantum information spreading after a quantum quench from an initial $\mathbb{Z}_3$-ordered product state. Fig. 4.4(a) shows the case of a homogeneous post-quench Hamiltonian with $\delta_i = 0$. As one can clearly see, correlations spread out fast across the 1D chain, leading to a light-cone structure [4]. In contrast, with a periodic detuning field added to the Hamiltonian, the low-energy excitations are bound quasiparticles (mesons and baryons). In this case, the correlation spreads much slower than in the deconfined case [see Fig. 4.4(b)]. We emphasize that such observables can also be directly measured in experiments [13, 47].

[4] The light-cone shows a $\mathbb{Z}_3$-periodic sub-structure due to the blockade physics.

4.7 Experimental preparation and detection

To experimentally prepare the above sets of initial states, one can first prepare the ordered product state $|\Psi_v\rangle = |rggrggrggrggrggrgg\rangle$ [13,47], and rotate the 10th atom from the Rydberg to the ground state (via single-atom addressability), which yields $|\Psi_q\rangle = |rggrggrgggggrggrgg\rangle$ [5]. After this, a Rabi laser is shined only on the middle three atoms, with a Rabi frequency Ω_0 satisfying $V_2 \ll \Omega_0 \ll V_1$. To prepare the initial state for Fig. 4.3(a-b), we apply the Rabi pulse for time $1.4\pi/\Omega_0$. On the other hand, for the initial states in Fig. 4.3 (c)-(f), we choose time $3.6\pi/\Omega_0$. During the preparation, the parameters Δ and interactions V_r are the same as in the post-quenched Hamiltonian [see Fig. 4.3], while $\Omega_0 = 25$ for the three atoms, and all other atoms seeing vanishing Rabi frequencies. We have checked that the probabilities for the blockaded states (grr, rrg, rrr) for the three middle atoms are on the order of 10^{-3}.

To measure the dynamics shown in Fig. 4.3(e-f), after state preparation, we evolve the system under Hamiltonian (4.1), rotate the middle three atoms back using a $\pi/2$ pulse [i.e. apply Ω_0 for time $\pi/(2\Omega_0)$], and finally measure $Z_9Z_{10}Z_{11}$. During the $\pi/2$ pulse, all the parameters (except for the pulse time) are the same as for the preparation step.

[5] The local rotation fields can be also engineered by applying a strong light shift to the selected target atoms, and shining an additional resonant Rydberg laser beam across the whole chain.

4.8 Conclusions and outlook

Our proposal shows that Rydberg arrays are a natural platform to study exotic confined excitations not only for the mesonic case, but also for baryonic quasiparticles. These confined excitations are analogous to the more complicated bound states seen in high energy physics. Although we focus on the regime where the Rydberg system is described by an effective clock model, we expect Eq. (4.1) to exhibit confinement wherever the homogeneous Rydberg model is in the $\mathbb{Z}_3$ ordered phase. Away from the clock limit, one needs to consider more general $\mathbb{Z}_q$ defect states where $q > 4$, and this will lead to more complicated 'hadronic' excitations. Correspondingly, this analysis can be generalised to the other $\mathbb{Z}_q$-ordered phases of the Rydberg system, which will generally lead to a host of more complicated confined quasiparticles (e.g. 'tetraquarks' and 'pentaquarks'). These more complex states would require much larger system sizes which would no longer be amenable to the numerical methods used here, but can be achieved in quantum simulators. Quantum simulators can additionally access dynamical phenomena such as string breaking and inelastic scattering which are intractable using classical methods [166]. It would also be interesting to consider confinement scenarios in higher dimensions, where Rydberg systems feature more complicated phases of crystalline order [190]. In particular, the symmetry-breaking patterns in two dimensions allow for both one-dimensional domain wall excitations as well as point-like "monopole" excitations, which is similar to the distinct excitations in higher-dimensional gauge theories [184].

Chapter 5: Hilbert-Space Fragmentation from Strict Confinement

5.1 Introduction

Generic nonintegrable quantum many-body systems eventually reach thermal equilibrium under unitary time evolution from initial states having a finite energy density with respect to the Hamiltonian [191]. Such behavior arises in models satisfying the eigenstate thermalization hypothesis (ETH) [192, 193], which posits that highly excited eigenstates of generic Hamiltonians at the same energy density are indistinguishable in the thermodynamic limit as far as local observables are concerned.

Recent experimental and theoretical investigations indicate that ETH in its strongest form can be violated even in nonintegrable systems with translation symmetry. Experiments on Rydberg-atom chains, where persistent revivals in quench dynamics starting from certain initial states are observed [13], lead to the identification of certain atypical eigenstates that are embedded in an otherwise thermalizing spectrum [42, 194]. Another mechanism leading to ETH violations is dynamical constraints. Fractonic systems, where such constraints manifest themselves in the restricted mobility of excitations, turn out to be natural candidates along this direction [195–198]. Mobility restrictions in fractonic systems can be implemented by

imposing both charge (Q) and dipole moment (P) conservation [199,200], providing a simple guiding principle for systematic studies of constrained models. It is shown in Refs. [201–204] that these two conservation laws cause the Hilbert space to fracture into disconnected subspaces that are invariant under the action of the Hamiltonian; moreover, these invariant subspaces cannot be distinguished by their (Q, P) quantum numbers alone [205]. This "fragmentation" of Hilbert space [202,203,206–211] leads to a broad distribution of the eigenstate entanglement entropies within an energy window, violating the strong ETH.

Fractonic systems bear a phenomenological resemblance to lattice models exhibiting quasiparticle confinement [212]. One simple example is the one-dimensional (1D) Ising model in transverse and longitudinal magnetic fields, where the latter induces a confining potential for pairs of Ising domain-wall excitations that grows linearly with their separation [83, 90]. Recent studies of confining systems have mainly focused on physics near the ground state, where domain walls and their bound states are well-defined quasiparticles [79,94,114,132–134,142,212–214]. This leaves open the question of the effects of confinement at finite energy density, where there are generically no well-defined quasiparticles.

In this Chapter, we show that Hilbert-space fragmentation (HSF) can arise in models conserving both domain-wall number (n_{DW}) and total magnetization (S^z). These two commuting U(1) conserved quantities naturally arise from *strict confinement*, where isolated domain walls cannot move without changing the S^z quantum number, naturally leading to HSF. We exemplify this phenomenon with a 1D spin-1/2 model that features exponentially many invariant subspaces. These include

exponentially many frozen configurations (i.e., subspaces of dimension one), as well as exponentially large subspaces generated by certain "root configurations" that we enumerate. The pattern of HSF that we find is extremely rich, featuring large subspaces within which the dynamics is thermalizing, as well as others spanning entire (n_{DW}, S^z) sectors that are integrable by Bethe ansatz. We further demonstrate how the same HSF pattern arises perturbatively in the extreme confining limit of a 1D n_{DW}-conserving spin model that maps exactly onto $\mathbb{Z}_2$ gauge theory coupled to fermionic matter [142, 215], which can be realized experimentally using state-of-the-art techniques [136, 137]. We show that HSF gives rise to a complex hierarchy of timescales for quench dynamics that depends crucially on the initial state. Our results thus establish HSF as a mechanism for slow dynamics in gauge theories at finite energy density [133].

5.2 Model

Consider a 1D spin-1/2 model with n_{DW} conservation and a uniform confining longitudinal field h coupled to S^z. In the limit of strict confinement ($h \to \infty$) S^z becomes a conserved quantity. Isolated domain walls ("quarks") cannot move as this necessarily changes S^z, costing infinite energy. However, tightly bound pairs of domain walls (magnons, or "mesons") can move without violating S^z conservation. In this limit, one can write down the following Hamiltonian describing a chain of

(even) length L:

$$H = \sum_{i=2}^{L-1} [JP_{i-1,i+2}(\sigma_i^+ \sigma_{i+1}^- \ + \ \sigma_i^- \sigma_{i+1}^+) + \Delta_2 \, \sigma_i^z \sigma_{i+2}^z], \tag{5.1}$$

where $P_{i-1,i+2} = 1 + \sigma_{i-1}^z \sigma_{i+2}^z$ projects out configurations with opposite spins on sites $i-1$ and $i+2$. Note that $[H, \sigma_{1,L}^z] = 0$, so that we can fix the two edge spins to point down. Adopting the notation $1 \equiv \uparrow, 0 \equiv \downarrow$ for the local spin states, we see that the kinetic term in Eq. (5.1) hops a magnon while preserving n_{DW}: $0100 \leftrightarrow 0010$, and $1011 \leftrightarrow 1101$. Since the nearest-neighbor Ising interaction couples to the conserved quantity n_{DW}, we add a next-nearest-neighbor Ising interaction Δ_2 to make the model more generic (see below). Eq. (5.1) has two U(1) conserved quantities (n_{DW}, S^z); for our choice of boundary conditions, we have $n_{\mathrm{DW}} = 0, 2, \cdots, L-2$, and $S^z = -L + n_{\mathrm{DW}}, -L + n_{\mathrm{DW}} + 2, \cdots, L - n_{\mathrm{DW}} - 2$ for $n_{\mathrm{DW}} \neq 0$. This gives rise to $\sum_{n_{\mathrm{DW}}=2}^{L-2} (L - n_{\mathrm{DW}}) + 1 = \frac{L}{2}(\frac{L}{2} - 1) + 1$ sectors labeled by these two quantum numbers.

5.3 Strong HSF

Naively, one would expect that the Hilbert space of Hamiltonian (5.1) organizes into $\mathcal{O}(L^2)$ symmetry sectors. In Fig. 5.1(a), we visualize the symmetry sector $(n_{\mathrm{DW}} = 8, S^z = -2)$ as a graph whose nodes are z-basis configurations and whose edges correspond to nonzero matrix elements of H. We find that the Hilbert space *within* this symmetry sector further fractures into many disconnected emergent subsectors (invariant subspaces) of various sizes. In particular, there are isolated

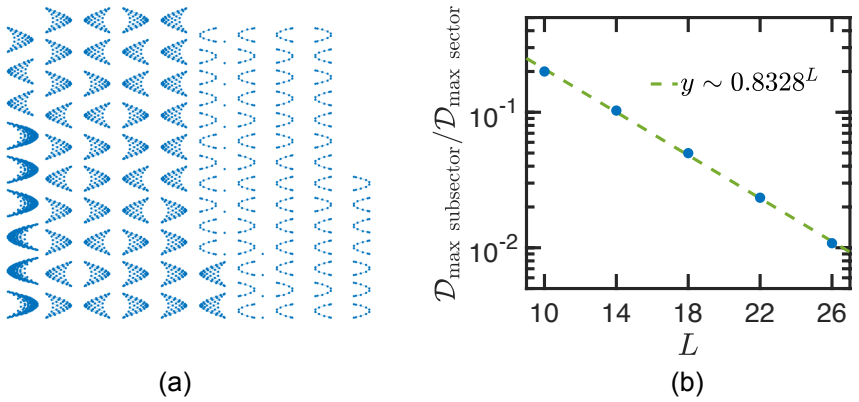

Figure 5.1: (a) Connectivity within the sector ($n_{\text{DW}} = 8, S^z = -2$) for $L = 18$. This sector has a total Hilbert space dimension of 4410. In this plot, each dot represents one state in the computational basis, and each line between two dots represents that there is a non-vanishing Hamiltonian matrix element between the two states. (b) Ratio of the size of the largest emergent subsector *within* the largest (n_{DW}, S^z) sector to that of the entire sector, for different system sizes.

nodes in Fig. 5.1(a), indicating the existence of frozen configurations constituting subsectors of dimension one. In Fig. 5.1(b) we show that Hamiltonian (5.1) exhibits *strong* HSF as defined in Ref. [203]: the ratio of the dimension of the largest emergent subsector *within* the largest (n_{DW}, S^z) sector to that of the whole sector decreases exponentially with L. This implies that in the thermodynamic limit, even the largest emergent subsector constitutes a vanishing fraction of the full (n_{DW}, S^z) sector.

We now develop an understanding of the pattern of HSF evident in Fig. 5.1, starting with the origin of the frozen states in Fig. 5.1(a). As discussed below Eq. (5.1), the only nonzero off-diagonal matrix elements of H are between configurations differing by the nearest-neighbor exchange of a single magnon. This immediately implies that the kinetic term in Eq. (5.1) annihilates any configuration containing no isolated magnons, and that such configurations are disconnected from

all others. Since an isolated magnon is equivalent to a pair of domain walls occupying neighboring bonds, it follows that any configuration in which no two neighboring bonds host a domain wall is frozen (see Appendix C). This nearest-neighbor exclusion is sometimes called the "Fibonacci constraint," which also arises in systems of Rydberg atoms with strong interactions [13]. The number of states satisfying this constraint grows as φ^L, where φ is the golden ratio. Configurations in which *every* bond is occupied by a domain wall (e.g. $0101\ldots$) are also frozen because domain walls are hardcore objects; however, the number of such configurations is independent of system size (Appendix C).

Next, we identify a class of root configurations from which each connected subsector can be built. Consider configurations of the following form:

$$0\ \underbrace{\boxed{\text{frozen state}}}_{L-2-2k}\ \underbrace{\boxed{0101\cdots01}}_{2k}\ 0, \tag{5.2}$$

which are constructed by appending a Néel state of length $2k$ to the right of any magnon-free frozen state. The two outermost 0's denote the edge spins that remain fixed. Since the Néel region contains k magnons, we shall call (5.2) a "k-magnon state." One can explicitly check that, although the two constituent subsystems are both frozen, the boundary between them becomes active once they are joined together (Appendix C). To show that any connected subsector can be built from a k-magnon state, we first point out an important property in our system which is in stark contrast to spin-1 systems with (Q, P) conservation [202, 203]. Whereas in the latter class of models mobile excitations can be contained within a finite do-

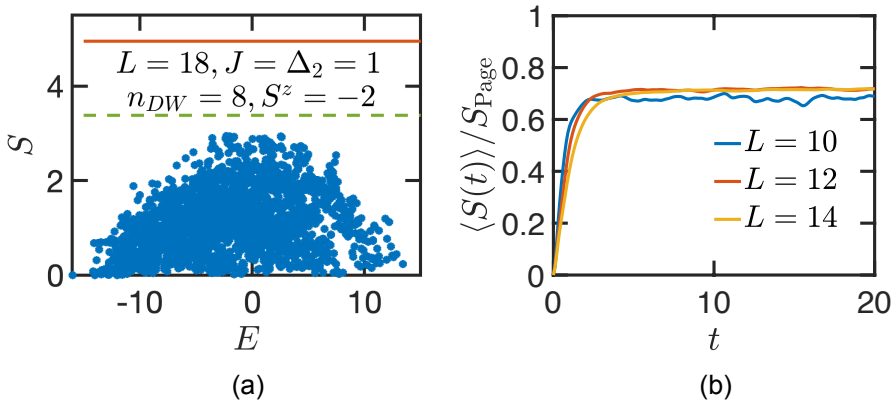

Figure 5.2: (a) Entanglement entropy of the eigenstates within the sector ($n_{\text{DW}} = 8, S^z = -2$) under an equi-bipartitioning of the system. Orange line: Page value of the (n_{DW}, S^z) sector; green line: Page value of the largest connected subsector. (b) Entanglement entropy growth (normalized by the Page value) after a quantum quench starting from random product states, averaged over 200 initial states.

main by constructing appropriate "shielding regions," there are no such regions in the model (5.1): an isolated mobile magnon sprinkled into a frozen configuration can propagate all the way to the boundary of the system. Using this fact, one can then prove (Appendix C) that any configuration that is not frozen can be brought into the form (5.2) by propagating all mobile magnons to the right boundary using Eq. (5.1). Therefore, any connected subsector can be built from an appropriate k-magnon state.

5.4 Subsector thermalization and integrability

The fracturing of the Hilbert space into exponentially many disconnected subsectors indicates that the eigenstates of Hamiltonian (5.1) strongly violate ETH, as can be diagnosed from the entanglement entropy. In Fig. 5.2(a), we plot the entanglement entropy of the eigenstates within an (n_{DW}, S^z) symmetry sector. There

is clearly a broad distribution in the entanglement entropy, even for eigenstates that are close in energy. In particular, the frozen states have exactly zero entanglement entropy although they reside in the middle of the energy spectrum. Moreover, the maximal value of the entanglement entropy stays far below the "Page value," i.e., that of a random state in the corresponding (n_{DW}, S^z) sector [216]. The non-thermalizing behavior of the full Hamiltonian also manifests itself in quantum quenches starting from random initial product states that do not belong to any particular symmetry sector. In Fig. 5.2(b), we find that the final entanglement entropy under time evolution only saturates to 70% of the Page value, confirming that the system does not thermalize under time evolution.

The fragmentation of Hilbert space seems to suggest that a more appropriate comparison of the entanglement entropy might be the Page value *restricted* to a connected subsector. To this end, we extract the effective Hilbert space dimensions of the left and right halves of the chain $\mathcal{D}_L$ and $\mathcal{D}_R$ within the largest emergent subsector, and then compute the corresponding Page value using the exact formula: $\sum_{k=n+1}^{mn} \frac{1}{k} - \frac{m-1}{2n}$, where $m = \min[\mathcal{D}_L, \mathcal{D}_R]$, and $n = \max[\mathcal{D}_L, \mathcal{D}_R]$ [216]. As shown in Fig. 5.2(a) (green dashed line), the maximal eigenstate entanglement entropy is close to the Page value restricted to the largest subsector. This strongly indicates that the system thermalizes *within* each invariant subspace [204]. Testing this scenario numerically requires larger system sizes with bigger subsector dimensions. Fortunately, armed with the knowledge of the root configurations (5.2), one can directly construct the projection of Hamiltonian (5.1) into an arbitrary emergent subsector. In Fig. 5.3(a), we show the entanglement entropy for eigenstates within a connected

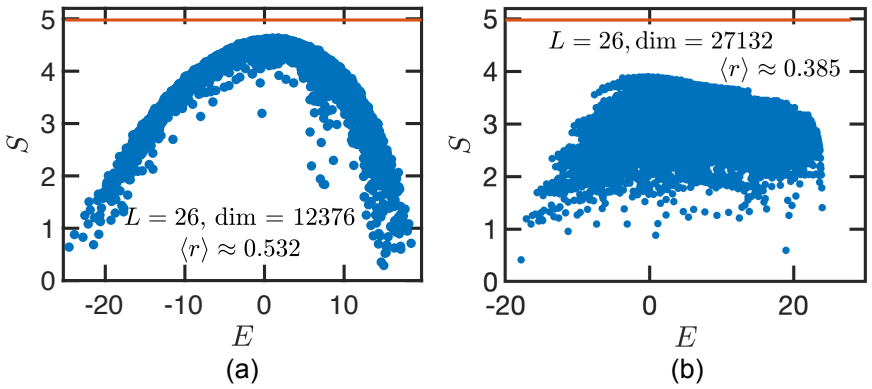

Figure 5.3: (a) Entanglement entropy of eigenstates within an emergent subsector built from the root configuration $0\boxed{111111000000}\boxed{010101010101}0$ for system size $L = 26$. This subsector has dimension 12376 and is nonintegrable. (b) Entanglement entropy of eigenstates within an emergent subsector built from the root configuration $0\boxed{000000000000}\boxed{010101010101}0$ for system size $L = 26$. This subsector has dimension 27132 and is integrable. Orange lines mark the Page value of the corresponding subsector.

subsector built from the root configuration $0\boxed{111111000000}\boxed{010101010101}0$. It is clear that the eigenstate entanglement entropy within this subsector forms a narrow ETH-like band, with maximal value close to the subspace-restricted Page value. Moreover, we compute the average energy level spacing ratio for the eigenenergies of the projected Hamiltonian: $r_i = \min\{\delta_i, \delta_{i+1}\}/\max\{\delta_i, \delta_{i+1}\}$, where $\delta_i = E_i - E_{i+1}$ is the gap between adjacent energy levels [217]. We find $\langle r \rangle \approx 0.532$, consistent with the Gaussian orthogonal ensemble in random matrix theory. Taken together, these facts suggest that there is indeed a notion of *subsector thermalization* in the present model. In the absence of Δ_2, we numerically find that the spectral properties strongly deviate from nonintegrability, which confirms the necessity of including a nonzero Δ_2.

At this point, it may seem that *all* sufficiently large connected subsectors at finite energy density thermalize when considered separately. However, as we now

show, this is not the case. Consider the sequence of symmetry sectors ($n_{\mathrm{DW}} = 2k, S^z = -L + 2k$), which have the smallest possible S^z for a given n_{DW}. These sectors can be generated from root configurations $0\boxed{00\cdots0}\boxed{0101\cdots01}0$ and are in fact fully connected, i.e, they do not fracture into subsectors. The projection of Hamiltonian (5.1) into these symmetry sectors yields a constrained XXZ model in which neighboring up spins are separated by at least two sites [142, 218]. For Hamiltonian (5.1) this constraint is automatically satisfied within these symmetry sectors, since bringing two up spins next to one another annihilates a pair of domain walls, which is forbidden by n_{DW} conservation. Remarkably, the constrained XXZ model, although interacting, is exactly solvable via Bethe ansatz, and hence integrable [218]. This is also seen numerically in Fig. 5.3(b), where the entanglement entropy does not form an ETH-like band, and where $\langle r \rangle \approx 0.385$ indicates Poissonian energy-level statistics characteristic of integrability. Notice from Fig. 5.3(b) that, although these sectors are integrable, they reside within the same energy window as the nonintegrable subsectors.

5.5 HSF in gauge theory

We now show that the pattern of HSF observed in Hamiltonian (5.1) naturally arises in the n_{DW}-conserving model [142, 215]

$$H_{\mathbb{Z}_2} = \sum_i [\lambda(\sigma_i^x - \sigma_{i-1}^z \sigma_i^x \sigma_{i+1}^z) + h\sigma_i^z]. \tag{5.3}$$

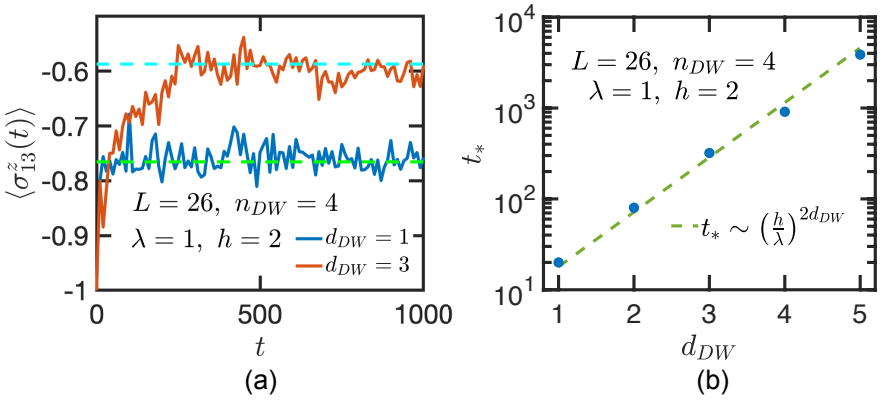

Figure 5.4: (a) Expectation value of the spin in the middle of the chain under time evolution with Hamiltonian (5.3), starting from initial configurations with two pairs of domain walls: $00\cdots011\cdots100\cdots011\cdots100\cdots0$. The dashed lines mark the diagonal ensemble average values: $\langle\sigma^z_{13}\rangle_{\text{diag}} = \sum_n \langle n|\sigma^z_{13}|n\rangle |c_n|^2$, where $|n\rangle$ denotes the eigenstate of the Hamiltonian and $c_n = \langle n|\psi_0\rangle$ is the overlap between the initial state and each eigenstate. (b) Scaling of the saturation timescale t_* as a function of d_{DW}.

As shown in Ref. [142], this model maps exactly onto $\mathbb{Z}_2$ gauge theory coupled to spinless fermions in 1D, where Ising domain walls in the spin model are reinterpreted as fermions in the gauge theory. With this in mind, we will henceforth use the terms "domain wall" and "fermion" interchangeably. The kinetic term in Eq. (5.3) induces nearest-neighbor hopping of domain walls, while the longitudinal field introduces a linearly confining potential. This model can be realized experimentally in two complementary settings. The spin model (5.3) can be realized by Floquet engineering in periodically-driven transverse-field Ising chains [118, 219], while the gauge theory itself can be realized in ultracold atomic gases [220]. Experimental steps toward the latter have already been reported in Refs. [136, 137].

To understand the effect of confinement in Eq. (5.3), we work in the limit $h \gg \lambda$. At $h = \infty$, the energy spectrum of Hamiltonian (5.3) becomes highly

degenerate, with each S^z sector forming a degenerate manifold. The dynamics at $h = \infty$ is trivial; the leading nontrivial behavior is determined by performing degenerate perturbation theory in λ/h. Formally, this is carried out by a Schrieffer-Wolff transformation (Appendix C), which yields an effective Hamiltonian $H_{\text{eff}} = \sum_n H_{\text{eff}}^{(n)}$, where $H_{\text{eff}}^{(n)}$ is of order $(\lambda/h)^n$ and conserves n_{DW} and S^z by construction. Strictly speaking this analysis is valid up to an order $n_* \sim h/\lambda$ (up to logarithmic corrections), which sets an exponentially long prethermal time scale $\sim e^{cn_*}$ for some constant c [160].

The leading contribution in perturbation theory appears at second order (Appendix C):

$$H_{\text{eff}}^{(2)} = \frac{\lambda^2}{h} \sum_i [\sigma_{i-1}^z P_{i-1,i+2} (\sigma_i^+ \sigma_{i+1}^- + \text{H.c.}) - \sigma_{i-1}^z \sigma_i^z \sigma_{i+1}^z]. \tag{5.4}$$

The kinetic term in Eq. (5.4) coincides with that of Eq. (5.1) up to a configuration-dependent local sign due to the extra factor of σ_{i-1}^z; this only affects the signs of certain matrix elements, so that Eqs. (5.4) and (5.1) exhibit the same pattern of HSF. Moreover, although Eq. (5.4) sports a three- rather than a two-body interaction, this has no effect on the (non)integrability of the various (sub)sectors. In the integrable sectors, the spin between any two up spins must point down by (n_{DW}, S^z) conservation. The three-body interaction in $H_{\text{eff}}^{(2)}$ thus reduces (up to a constant shift) to Δ_2 upon setting $\sigma_i^z = -1$ in $\sigma_{i-1}^z \sigma_i^z \sigma_{i+1}^z$. Moreover, the nonintegrable subsectors remain nonintegrable regardless of whether Δ_2 or the three-body term is used. In Appendix C, we numerically verify the above claims by reproducing

Figs. 5.2 and 5.3 using $H_{\text{eff}}^{(2)}$.

Corrections to the pattern of HSF discussed so far arise for $n > 2$, where further-neighbor domain-wall hopping processes appear (Appendix C). Such processes reduce the strong HSF of Eq. (5.4) to *weak* HSF, defined in Ref. [203]; in particular, each (n_{DW}, S^z) sector collapses into an exponentially large connected cluster that remains disconnected from a set of exponentially many frozen configurations. The base of the exponential number of such frozen configurations depends on the order in perturbation theory being considered; for example, at $n = 4$ the number of frozen states grows as 1.466^L (Appendix C). One can show that a pair of domain walls separated by a distance d_{DW} becomes mobile at order $(\lambda/h)^{2d_{\text{DW}}}$ in perturbation theory [212]. Thus, a configuration containing two domain walls with $d_{\text{DW}} > 1$, which is frozen at second order, remains frozen for any $n < 2d_{\text{DW}}$. Frozen configurations with $n_{\text{DW}} > 2$ unfreeze at order $n = \min(d_{\text{DW}})$, where the minimum is taken over all pairs of domain walls.

The preceding considerations indicate that the thermalization time when evolving with Eq. (5.3) from a configuration with minimum domain-wall separation d_{DW} will be lower-bounded by a timescale $t_* \sim (h/\lambda)^{2d_{\text{DW}}}$. In Fig. 5.4(a), we show the evolution under Eq. (5.3) of $\langle \sigma^z_{L/2}(t) \rangle$, starting from initial configurations with two well-separated pairs of domain walls: $00\cdots0\underbrace{11\cdots1}_{d_{\text{DW}}}00\cdots0\underbrace{11\cdots1}_{d_{\text{DW}}}00\cdots0$. Indeed, we find that, even for reasonably small $h/\lambda = 2$, the timescale for the local observable to saturate to the diagonal-ensemble value [221] expected at late times is longer for initial states with a larger d_{DW}. Scaling analysis of this timescale is also in agreement with the prediction $t_* \sim (h/\lambda)^{2d_{\text{DW}}}$, as shown in Fig. 5.4(b). We thus

find that the above reasoning based on HSF provides a basis to estimate relaxation timescales in the confining limit of the gauge-theory model (5.3) and the correlations between these timescales and the initial state. Deeper investigations of these timescales could be carried out in experimental realizations of the model (5.3).

5.6 Conclusion

In this work, we demonstrate that HSF naturally arises in lattice models exhibiting strict confinement. We uncover a highly unusual feature in the models we study, namely the coexistence of nonintegrable emergent subsectors with Bethe-ansatz integrable fully connected symmetry sectors. This work also elucidates the role of HSF in determining the hierarchy of relaxation timescales in the confining phases of lattice gauge theories and related spin models in 1D, paving the way for experimental tests of these ideas in emerging quantum simulation platforms. Generalization of these ideas to higher dimensions [222] is also possible, and is left for future work.

Chapter 6: Observation of Stark Many-Body Localization without Disorder

6.1 Introduction

Many-body localization was first formulated as a generalization of the non-interacting Anderson transition [223–226]. With disorder, quantum particles can experience destructive interference through multiple scattering, causing a transition to exponentially localized wavepackets. Over time, a cohesive picture of MBL in interacting systems has also developed [227, 228]. In this description, the MBL regime has extensive local conserved quantities that generalize the particle occupancies in Anderson localization. However, interactions result in additional slow spreading of correlations via entanglement. Strikingly, MBL creates a phase of matter that is non-ergodic: for a range of parameters, local features of the initial state are preserved for all times, preventing thermalization [229].

In considering MBL, it is natural to ask whether random disorder is a requirement. A partial answer has long been known: MBL is possible with incommensurate periodic potentials [230]. However, the question of whether an MBL phase might exist which preserves translational symmetry, for instance in a system with

gauge invariance [140] or multiple particle species [231, 232], has continued to generate extensive discussion [233]. Recently, this problem has been approached from a different starting point: the Bloch oscillations and Wannier-Stark localization of non-interacting particles in a uniformly tilted lattice [234]. From this, it has been predicted that interacting systems with a strong linear tilt can also display MBL-like behavior [235, 236]. This effect, sometimes called Stark MBL, has attracted considerable theoretical and experimental interest [222, 237–245]. However, clear experimental realization of Stark MBL has been complicated by exact degeneracies between states with the same center of mass that occur in the limit of short-range interactions [235, 236, 244]. The setting of a trapped-ion quantum simulator with long-range interactions naturally overcomes this complication.

6.2 Experimental setup

Investigation of many-body localization has been driven in part by the development of isolated quantum simulator platforms with site-resolved control and detection [60, 246–248]. Our experimental apparatus (Fig. 6.1(a)) exemplifies these capabilities. It consists of a chain ($N = 15$–25) of $^{171}\mathrm{Yb}^{+}$ ions, with pseudospin states $|\uparrow_z\rangle$ and $|\downarrow_z\rangle$ encoded in hyperfine ground-state levels. The Hamiltonian has two ingredients. The first is an overall spin-spin interaction, mediated by global laser beams coupling spin and motion using the Mølmer-Sørensen scheme [33]. The second, a tightly-focused beam creating a programmable effective B^z magnetic field at each ion using the AC Stark effect [34]. A key feature of this platform is its high

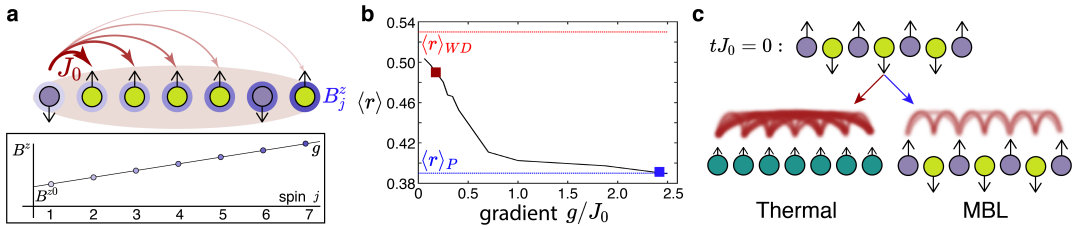

Figure 6.1: Experimental setup. (a), Each trapped ion in a chain of length N encodes a pseudospin. Global lasers controllably mediate a long-range spin-spin interaction (red), which is parameterized by the nearest-neighbor rate J_0. A tightly-focused beam provides a site-resolved effective B^z magnetic field (blue) that is used to engineer a field gradient with slope g. For clarity, we show $N = 7$. (b), The parameter $\langle r \rangle$, a measure of the level statistics of the experimental Hamiltonian ($N = 15$), shows a progression from statistics near the Wigner-Dyson limit ($\langle r \rangle_{WD}$, red dotted line) at low g/J_0, characteristic of a generic ergodic system, to Poisson statistics ($\langle r \rangle_P$, blue dotted line) at high g/J_0, characteristic of a localized system. (c), We probe the system using a quench from a non-equilibrium initial state, such as the Néel state shown here. At low g/J_0, an initial spin pattern will quickly relax to a uniform average magnetization, while at high g/J_0 the initial pattern persists. The former is consistent with a thermal state, in which uniformity is combined with entanglement reaching across the entire chain, while the latter is consistent with many-body localization, in which the magnetization remains non-uniform and entanglement spreads slowly.

degree of controllability. In addition to turning on or off either Hamiltonian term, we use the tightly-focused beam to initialize spins in any desired product state, and we measure arbitrary local observables with state-dependent fluorescence collected onto a CCD camera.

Combining the global spin-spin interactions with a programmable local field set to a linear gradient results in the tilted long-range Ising Hamiltonian ($\hbar = 1$):

$$H = \sum_{j<j'} J_{jj'} \sigma_j^x \sigma_{j'}^x + \sum_{j=1}^{N} (B^{z0} + (j-1)g) \sigma_j^z. \tag{6.1}$$

Here we have the long-range spin-spin interactions $J_{jj'}$, approximately following a power-law: $J_{jj'} \approx J_0/|j-j'|^\alpha$, with J_0 the nearest-neighbor coupling and $\alpha = 1.3$.

B^{z0} is an overall bias field, and g the gradient strength, with $\{J_0,\ B^{z0},\ g\} > 0$. In practice, we apply the terms in this Hamiltonian sequentially in time, using a Trotterization scheme that reduces decoherence while still resulting in evolution closely following the Hamiltonian in Eq. (6.1) (see Appendix D). The bias field B^{z0} is set to be large ($B^{z0}/J_0 > 5$), so that the total magnetization $\sum_j \langle \sigma_j^z \rangle$ is approximately conserved. With this constraint, and neglecting edge effects, $J_{jj'} = J_{|j-j'|}$ and this Hamiltonian is translationally invariant: the operation $j \to j + n$ for integer n is equivalent to a shift in B^{z0}, which has no effect in the bulk. For an initial state of definite total magnetization, this model can then be mapped to a chain of hard-core bosons with long-range hopping in a tilted lattice (Appendix D), indicating that it has similar ingredients to models previously shown to realize Stark MBL [235, 236]. This system has also been used previously to study MBL in a disordered field [60].

A useful numeric diagnostic of whether a model exhibits an MBL regime can be found in the level statistics, which feature similar behavior in regular MBL [249] and Stark MBL [235, 236]. A generic thermalizing ergodic system has energy levels following the Wigner-Dyson distribution that characterizes random matrices, while a generic many-body localized system has a Poissonian level distribution [249]. This difference can be quantified by the average ratio of adjacent energy level gaps, defined as

$$\langle r \rangle = \frac{1}{n} \sum_n \frac{\min(E_{n+1} - E_n, E_n - E_{n-1})}{\max(E_{n+1} - E_n, E_n - E_{n-1})}. \tag{6.2}$$

The quantity $\langle r \rangle$ varies from 0.53 for the Wigner-Dyson case to 0.39 for the Poisso-

nian case [235, 236, 249]. Diagonalizing the Hamiltonian (Eq. (6.1)) for $N = 15$, we find that $\langle r \rangle$ moves from 0.50 to 0.39 as the gradient g/J_0 is increased, suggesting localization (Fig. 6.1(b)). While Fig. 6.1(b) shows the exact experimental Hamiltonian, including deviations from uniform interactions near the edges of the chain, this behavior persists for the ideal power-law Hamiltonian (see Appendix D). Unlike the first studies of Stark MBL, where a small amount of disorder or curvature was required to create a state with generic Poissonian level statistics [235,236], Eq. (6.1) exhibits these properties without any terms perturbing the translational symmetry.

We probe the degree of localization using a quench procedure, shown schematically in Fig. 6.1(c). The initial state, such as a Néel state of staggered up and down spins, is highly excited and far-from-equilibrium. If it thermalizes, it will result in a high-temperature equilibrium in which each spin has nearly equal probabilities of being up or down. Many-body localization will instead result in persisting memory of the initial configuration, breaking ergodicity.

6.3 Ergodicity breaking in Stark MBL

Performing the quench experiment, we see the expected signature of localization: a low gradient results in quick equilibration of the spins (Fig. 6.2(a)), while in a strong gradient they are nearly unchanged from their initial values (Fig. 6.2(b)). The experimental data correspond closely to exact numerics for the system evolution.

To quantify the amount of initial state memory as the gradient is increased,

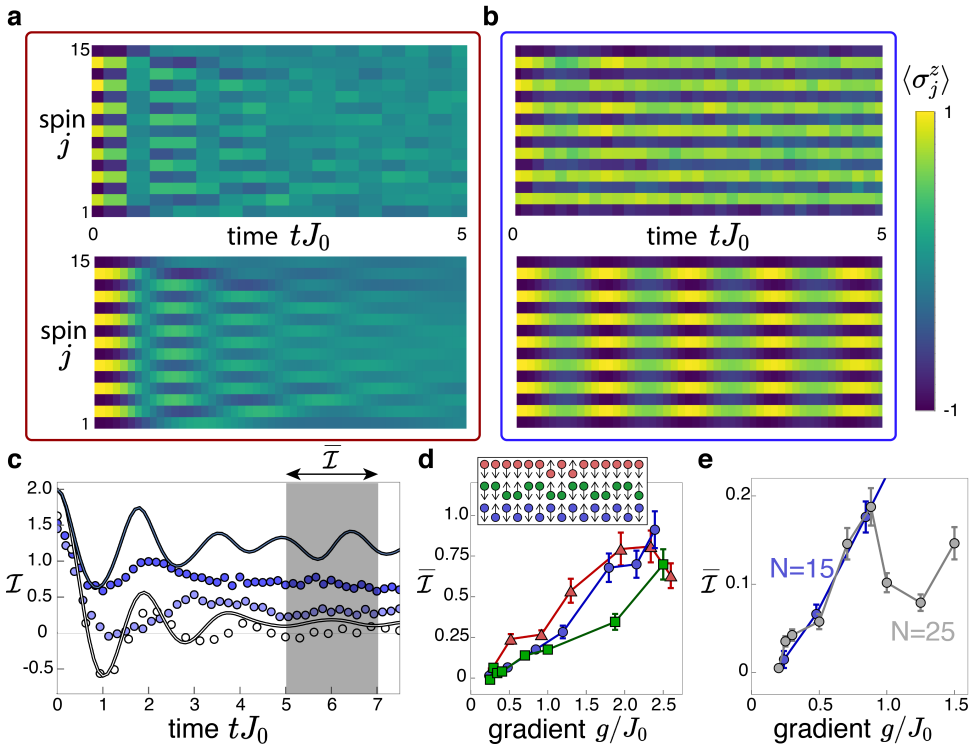

Figure 6.2: Ergodicity breaking in Stark MBL. (a), Ion-resolved dynamics for an initial Néel state ($N = 15$) at $g/J_0 = 0.24$, and (b), at $g/J_0 = 2.4$, corresponding to the red and blue points on Fig. 6.1(b). While the state quickly relaxes to a uniform magnetization in the low gradient, the large gradient results in a persisting memory of the initial state. The top row are experimental data, and the bottom row are exact numerics. (c), Memory of the initial state, here a Néel state ($N = 15$), can be quantified by the generalized imbalance $\mathcal{I}$. For a state of frozen up and down spins, $\mathcal{I} = 2$, and for complete relaxation to a uniform state, $\mathcal{I} = 0$. As the gradient is increased (light to dark), the imbalance crosses from quick relaxation towards zero to a persistent finite value. Points are experimental data at $g/J_0 = \{0.24, 1.2, 1.8\}$, with statistical error bars smaller than the symbol size, and lines are exact numerics for the lowest and highest gradient. (d), For various initial states, shown at top, we see a similar value of the late-time imbalance at large gradient, suggesting complete localization. From top to bottom, the three initial states correspond to the {triangle, square, round} points. (e), Dependence of the late-time imbalance on system size is shown, using an initial Néel state with $N = 15$ (a subset of the data in panel (b)) and $N = 25$. The overall increase of late-time imbalance with gradient is robust to the system size increase. The pronounced dip in $\overline{\mathcal{I}}$ near $g/J_0 = 1.0$ may be partly due to a resonant feature that appears near this value (see Appendix D Fig. D.5). Error bars throughout represent statistical uncertainty of the mean value (s.e.m.).

it is useful to define a measure that can serve as an effective order parameter. We choose a generalized imbalance, $\mathcal{I}(t)$, which reflects the preservation of the local magnetizations of the initial state. This observable is similar to other previously used measures of initial state memory, such as the imbalance [157] or the Hamming distance [60], but is advantageous for comparing different initial states (see Methods). For an initial state with M spins that are up, and $N-M$ down, $\mathcal{I}$ is equal to the subsequent difference between the average magnetizations of the two groups:

$$\mathcal{I}(t) = \frac{\sum_j^M \langle \sigma_j^z(t) \rangle}{M} - \frac{\sum_{j'}^{N-M} \langle \sigma_{j'}^z(t) \rangle}{N-M} \tag{6.3}$$

where the sums are respectively over the spins initially up and initially down. In general, $|\mathcal{I}(t)|$ reaches a maximum value of 2 for perfect memory of an initial state with up and down spins, and is zero for a uniform state as at thermal equilibrium.

The imbalance shows a clear trend as we increase the gradient (Fig. 6.2(c)). At lower gradients, it quickly relaxes to a decaying oscillation about zero, indicating quick thermalization. However, as the gradient is increased, the imbalance instead settles to a progressively higher value. Compared to exact numerics, we observe a damping of the imbalance oscillations, resulting in a lower steady-state imbalance. Furthermore, at the highest gradient values, decoherence causes a slow decay of $\mathcal{I}$ over time. These are both attributed primarily to intensity fluctuations in the tightly-focused beam, as well as to residual coupling to ion-chain motion from the Mølmer-Sørensen beams. However, the separation between this decoherence time and the fast relaxation dynamics allows us to characterize the late-time imbalance.

To study initial-state memory for different gradients, we average $\mathcal{I}(t)$ over a time window tJ_0 from 5 to 7. This window is chosen to be late enough that transient oscillations have largely decayed, while early enough that decoherence is limited. This late-time imbalance, $\bar{\mathcal{I}}$, captures the amount of initial-state memory after fast relaxation has subsided, and thus the approximate degree of localization (Fig. 6.2(d)). $\bar{\mathcal{I}}$ is consistent with zero at the lowest gradient: averaging over the initial states shown in Fig. 6.2(d) we have $\bar{\mathcal{I}} = 0.017 \pm 0.027$, with the standard deviation as the uncertainty. With a larger gradient, $\bar{\mathcal{I}}$ becomes clearly distinct from zero and progressively increases, reflecting an increasing memory of the initial state. Crucially, this memory does not show strong dependence on the specific initial state chosen: for states with different numbers of initial spin flips and different symmetry properties, similar behavior is observed. The initial state insensitivity observed here is consistent with many-body localization, which can have some energy dependence [239] but is a robust mechanism for breaking ergodicity that can span the entire spectrum. This insensitivity distinguishes our observations from other effects that cause thermalization to have a strong dependence on the initial state, such as quantum many-body scars [13] and domain wall confinement [174].

A key further test of the stability of Stark MBL is to characterize the dependence of the observed behavior on increasing system size. This is especially relevant to localization in systems with long-range interactions, where finite-size effects may be particularly important [60, 250]. Increasing the spin chain length to $N = 25$, we see a rise in the imbalance at low g/J_0 that is similar to the $N = 15$ case (Fig. 6.2(e)). This length reaches a regime that is challenging for numerical simu-

lation, and beyond our ability to compute exact dynamics. While we are unable to reach the deeply localized regime for $N = 25$, due to the scaling of the experimentally achievable maximum gradient with N (see Appendix D), the small nonzero value of $\overline{\mathcal{I}}$ that we observe indicates the persistence of a Stark MBL regime.

6.4 Revealing the correlated Stark MBL state

Probes of the local magnetization, as in Fig. 6.2, can establish non-ergodicity, but they do not reveal the correlations that characterize a localized phase. The structure of the regular MBL phase is understood as being defined by emergent local conserved quantities [227, 228]. These conservation laws result in localization, but the localized regions still have interactions with one another, resulting in slow spreading of correlations via entanglement after a quench from a product state (typically logarithmic spreading in time, but potentially faster for long-range interactions [251]). While the existence of similar conserved quantities in Stark MBL is debated [222, 242], there are indications that it can display similar entanglement dynamics [236, 237].

Some observables have been established to directly probe this correlation spreading, such as quantum Fisher information [60, 245] (see Appendix D and Fig. D.6) or techniques to measure subsystem entanglement entropy [247, 248]. Here we instead adopt a local interferometric scheme, the double electron-electron resonance (DEER) protocol, to reveal the spread of correlations controlled by the structure of the localized state [237, 246, 252]. This protocol, shown in Fig. 6.3(a),

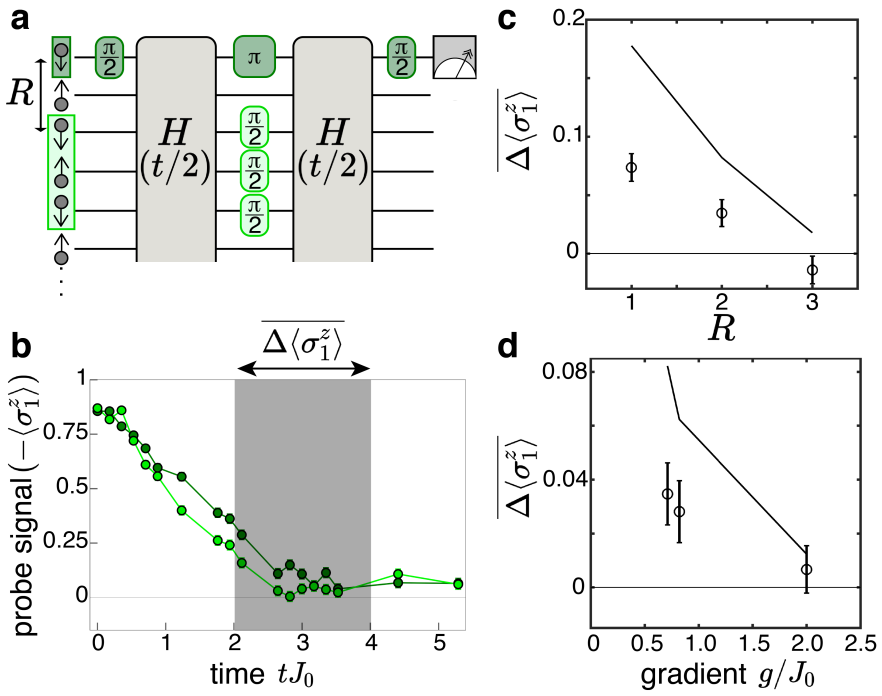

Figure 6.3: DEER Protocol. (a), In the spin-echo procedure (dark green), a single probe spin undergoes a spin-echo sequence, while the rest of the spins experience normal evolution under H for total time t. In the DEER procedure (dark and light green), there are additional perturbing $\pi/2$ pulses on a region, here fixed at a size of three spins, that is R spins away. The difference in the probe magnetization following these procedures reflects the ability of the DEER region to influence the dynamics at the probe spin. We study this protocol using an initial Néel state ($N = 15$). (b), At intermediate times, before the spin-echo signal approaches zero due to decoherence, a difference develops between the spin-echo (dark green) and DEER (light green) signals. We quantify this by taking the average difference (DEER-spin echo) between $tJ_0 = 2$ and 4 (shaded region) after imbalance dynamics have stabilized. These data are for $R = 1$ and $g/J_0 = 0.71$. (c), As R is increased (at $g/J_0 = 0.71$), the difference signal drops to zero, reflecting the incomplete spread of correlations through the system at finite time. (d), As g is increased (at $R = 2$), the difference signal also decreases with increasing gradient, consistent with the expectation that within the Stark MBL phase, increasing localization leads to progressively slower development of correlations. Points in (c). and (d). are the experimental data, and solid lines are exact numerics.

compares two experimental sequences: one that is a standard spin-echo sequence on a probe spin within a system of interest, and one that combines this with a set of $\pi/2$-pulse perturbations on a separate subregion, the 'DEER region'. The spin-echo

sequence cancels out static influences on the probe spin, either from global external fields or from fixed configurations of the surrounding spins. If this cancellation is perfect, the probe spin will return to its initial magnetization. The DEER sequence, by contrast, removes this cancellation for the DEER spins acting on the probe spin. As a result, a difference in the return to the initial probe magnetization between the two sequences reflects correlations between the probe and DEER region generated by the dynamics. At sufficiently long times, a difference between these signals will develop in an MBL phase, but not in a non-interacting localized phase. In addition, this differential measurement setup naturally makes the signal robust against common-mode non-idealities, including experimental noise.

In Fig. 6.3(b-d), we demonstrate the DEER protocol and show its use in characterizing the Stark MBL regime. As time evolves, a difference accumulates between the probe magnetization in the two procedures, reflecting the spread of correlations (Fig. 6.3(b)). These correlations continue to move through the system after imbalance dynamics have stabilized (see Appendix D and Fig. D.7), indicating that they are not solely due to the transient imbalance evolution. Picking a time range after these transient dynamics, tJ_0 =2–4, we characterize the structure of these spreading correlations by taking the average difference between the signals over this time, $\overline{\Delta\langle\sigma_1^z\rangle}$. This time window is slightly earlier than the window used for the steady-state imbalance, as the DEER signal is more sensitive to experimental decoherence. Varying the DEER spin distance, R, we see that this difference signal drops as the DEER spins move progressively farther from the probe, reflecting the local nature of correlation propagation (Fig. 6.3(c)). Similarly, by sitting at a fixed

separation and increasing the gradient, we observe the reduction of the difference signal at a given time, confirming that the correlation spread is controlled by the degree of localization (Fig. 6.3(d)). The dependences of the difference signal on both R and g/J_0 track exact numerics, with an overall scaling difference due to decoherence reducing the experimental signal. Taken together, these probes identify the Stark MBL regime as one in which correlations spread slowly through the system despite persisting memory of the initial state. These correlations capture the role that interactions play in Stark many-body localization, distinguishing it from non-interacting localization.

6.5 Disorder-free MBL beyond a linear field

If many-body localized effects are possible in the simple setting of a linearly increasing field, might they also appear in a more general class of smoothly varying fields? Utilizing the high degree of tunability of this simulator, we investigate a natural generalization: a quadratic, rather than linear, potential. We parameterize the Hamiltonian as:

$$H = \sum_{j<j'} J_{jj'} \sigma_j^x \sigma_{j'}^x + \sum_{j=1}^{N} \left(B^{z0} + \frac{\gamma J_0 (j - \frac{N+1}{2})^2}{N-1} \right) \sigma_j^z. \tag{6.4}$$

Eq. (6.4) describes a quadratic effective B^z field with a minimum in the center of the system and a maximum slope of $\pm\gamma$ at the ends of the chain. Similar models have been predicted to feature a persistent spatial separation into an ergodic core near the center and many-body localized edges [240].

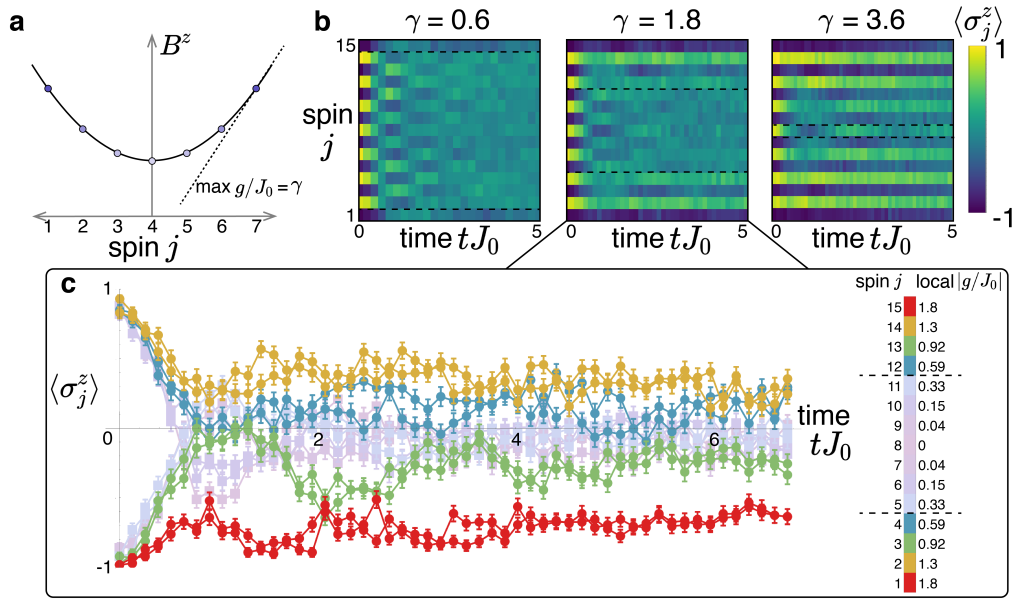

Figure 6.4: Relaxation in a quadratic field. (a), We reconfigure the site-resolved field from a linear gradient to a quadratic, characterized by the maximum slope γ. For clarity, we show $N = 7$. (b), Dynamics are split into a thermalizing region near the center of the system and localized regions near the edges, with the approximate boundaries indicated by the dashed lines. As the maximum gradient is increased, the fraction of the system in the thermalizing regime shrinks. (c), Ion-resolved traces of the dynamics for max $g/J_0 = 1.8$, showing separation of the spins into localizing regions (bright hues with round points) and thermalizing regions (faded hues with square points). Colors reflect the local field strength at each ion.

We summarize the results in Fig. 6.4. Taking an initial Néel state ($N = 15$), we observe a separation of the spins into thermalizing and localized regions, which appear to evolve largely independently. We determine an approximate dividing line between these regions by the innermost spins that are clearly distinct from the thermalizing region. For a range of slowly-varying gradients $\gamma < 3.6$, this occurs at a local slope of approximately $g/J_0 \sim 0.5$ (see Appendix D and Fig. D.8), comparable to observations in Fig. 6.2. The strongest curvature of $\gamma = 3.6$ deviates from this trend, possibly indicating a breakdown of the local-gradient approximation.

The quadratic field is an intriguing venue to explore the stability of disorder-

free many-body localization in proximity to an ergodic region. In regular MBL, it is believed that such a coupling can induce many-body avalanches that destabilize the MBL region over long times [253, 254]. The extension of this effect to disorder-free MBL, which does not feature any resonances between sites, is unclear, although there are some indications that it may be more resilient than regular MBL in general [241]. The observation of a localized region in a quadratic field is also directly relevant to longstanding questions about the state of correlated ultracold atoms in an optical lattice with harmonic confinement [255].

6.6 Discussion

We have seen the signatures of many-body localization in a system without disorder, suggesting that the concept of MBL may be relevant in settings well beyond the original considerations [225, 226]. Further work could analyze these observations in terms of Hilbert space fragmentation (or shattering) [203, 222, 242, 244], clarifying the connection between Stark and disordered MBL. Our realization of Stark MBL would not appear to naturally extend to the thermodynamic limit, as this results in infinite energy differences between different parts of the system. However, the Stark MBL Hamiltonian (Eq. (6.1)) is equivalent via a gauge transformation to a Hamiltonian without a linear potential that is time-dependent, which has a well-defined thermodynamic limit [235].

Beyond these conceptual questions, from the perspective of near-term quantum devices, our results suggest that Stark MBL retains key aspects of the disordered

MBL phase while offering certain advantages, such as not requiring a fine-grained field and being free of rare-region effects or the need for disorder averaging of observables. We summarize some aspects of the comparison in Table 6.1. Stark MBL may be a useful resource for such devices, serving as a tool to stabilize driven non-equilibrium phases [238, 256], or as a means of making a quantum memory [158] with each site spectroscopically resolved.

	Disordered MBL	Stark MBL
Ergodicity breaking	Yes [229]	Yes [235, 236]
Slow entanglement growth	Yes [229]	Yes [236]
Max. potential	$\mathcal{O}(J_0)$	$\mathcal{O}(NJ_0)$
Requires site-resolved field	Yes	No
Rare-region effects	Yes [253, 257]	No [235]

Table 6.1: Comparison of disordered MBL and Stark MBL requirements, focusing on applications with near-term quantum devices. Quasi-periodic MBL occupies an intermediate position from this perspective, with some of the advantages of both disordered and disorder-free localization. For all types of MBL, questions about the conditions for asymptotic stability of localization remain, particularly in long-range interactions or more than one dimension [235, 253, 257].

Chapter 7: Localization and Criticality in Antiblockaded 2D Rydberg Atom Arrays

7.1 Introduction

Recently, programmable Rydberg quantum simulators have attracted significant interest because they can provide insights into quantum matter's fundamental properties. With the rapid development of quantum technologies, synthetic arrays of Rydberg atoms with individual control are already available in one [39], two [40, 258], and three dimensions [41]. Recent experiments on 1D Rydberg atom arrays have shed light on various phenomena, including nonequilibrium quantum many-body dynamics [13], the Kibble-Zurek mechanism [47], and quantum many-body scars [13, 42]. The strong Rydberg-Rydberg interactions can also be used to realize quantum gates [36], making such systems promising platforms for quantum information processing [182].

Meanwhile, flat band systems are conceptually important in condensed matter physics and can harbor both nontrivial topological properties [259–262] and strongly correlated phases arising from the enhanced interaction effects [263–269]. Recent work on twisted graphene heterostructures and circuit quantum electrody-

namics (QED) opens up new venues for flat bands, enabling, respectively, the study of correlated insulators and superconductivity [270–273] and of quantum systems in hyperbolic space [274, 275]. One particular direction of interest concerns the effect of disorder on flat-band eigenstates. It has been shown that such flat bands, when coupled to disorder, can lead to critical and multifractal phenomena absent in conventional Anderson localization [276–281].

In this Chapter, we demonstrate that the physics of flat bands coupled to disorder can be naturally realized and probed using Rydberg atoms trapped in a 2D square lattice. We consider the so-called facilitation (anti-blockade) mechanism, where the excitation of a Rydberg atom is strongly enhanced in the vicinity of an already excited atom [282–284]. Under such conditions, the full Hilbert space can effectively split into subspaces separated from one another by large energy scales. We focus on the manifold of states that can be created near-resonantly starting from a single Rydberg excitation. Within this subspace, the system can effectively be described by a single particle hopping on a 2D Lieb lattice [284], which features a singular flat band in the clean limit. Although the Lieb lattice has been experimentally realized for photons [285–289], atoms [290, 291], and electrons [292], the effect of disorder on flat-band states has not yet been systematically studied. We find that the interplay between positional disorder of Rydberg atom arrays and the synthetic flat-band states gives rise to a rich phase diagram, including a critical phase, a nonergodic extended phase, and a phase with a disorder-induced flat band. We show that these intriguing properties are essentially related to the singular flat band on the Lieb lattice and are absent in 1D and quasi-1D arrays.

7.2 Antiblockaded Rydberg atom array and mapping to Lieb lattice

We consider the following Hamiltonian describing interacting Rydberg atoms trapped in a 2D $L \times L$ square lattice with spacing R_0:

$$H_{\text{Ryd}} = \frac{\Omega}{2} \sum_i^N \sigma_i^x - \Delta \sum_i^N n_i + \frac{1}{2} \sum_{i \neq j}^N V(d_{ij}) n_i n_j, \tag{7.1}$$

where i and j run over sites of the square lattice [see Fig. 7.1(a)], $\sigma_i^x = |g_i\rangle\langle r_i| + |r_i\rangle\langle g_i|$, $|g_i\rangle$ ($|r_i\rangle$) denotes the ground (Rydberg) state of the i-th atom, and $n_i = |r_i\rangle \langle r_i|$. The parameters Ω (Rabi frequency) and Δ (detuning) characterize coherent driving fields, while $V(d_{ij}) \propto 1/d_{ij}^6$ quantifies the van-der-Waals interactions between atoms in Rydberg states at sites i and j (separated by distance d_{ij}). The anti-blockade (facilitation) condition is obtained by setting $\Delta = V(R_0)$, so that an isolated excitation makes the excitation of its nearest neighbour resonant [282–284]. We work in the limit $|\Delta| \gg \Omega$ where the un-facilitated excitations are sufficiently off-resonant. We additionally require $V(\sqrt{2}R_0), V(2R_0) \gg \Omega$, so that a pair of neighbouring Rydberg excitations is unable to further facilitate the excitation of any neighbouring site. Hereafter we take $V(R_0) = 300\Omega$.

Under these conditions, the Hilbert space effectively splits into subspaces that are separated by energy scales much larger than Ω [283]. Here we focus on the simplest nontrivial subspace, which contains either a single Rydberg excitation or a pair of neighbouring Rydberg excitations. One can readily see that the connectivity graph of states in this subspace forms a 2D Lieb lattice [see Figs. 7.1(a)-(b)]. The

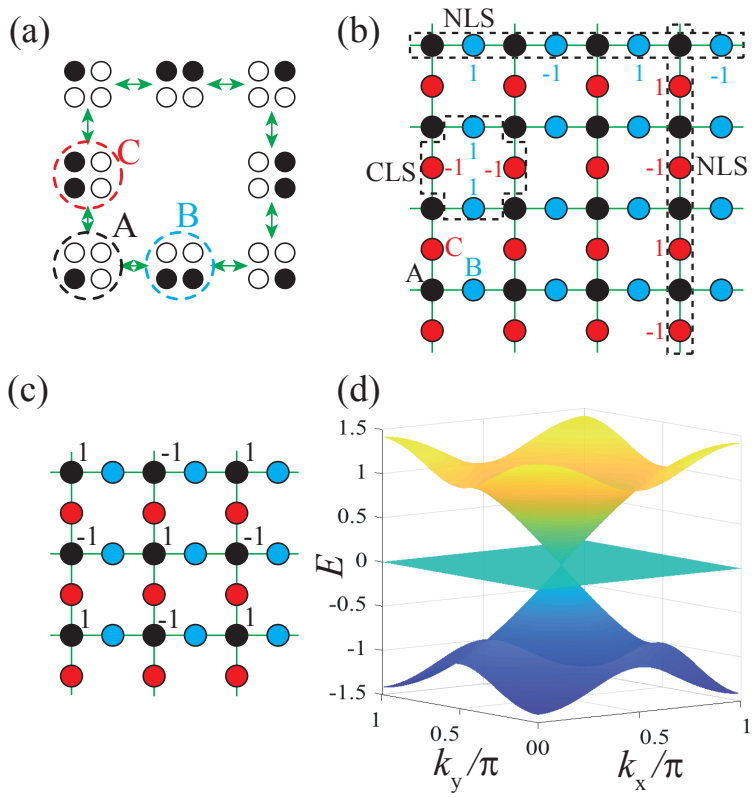

Figure 7.1: (a) Under the anti-blockade conditions, the connectivity graph of the subspace containing single isolated Rydberg excitations and single nearest-neighbor pairs thereof maps to a 2D Lieb lattice shown in (b). The black and white dots indicate atoms in Rydberg and ground states, respectively. Each unit cell of the Lieb lattice contains three sites: A, B, and C. (b) The flat-band eigenstates include compact localized states (CLSs), two non-contractible loop states (NLSs), and one non-compact state (NCS) shown in (c). The '± 1' indicate the relative wavefunction amplitudes for these states. (d) The band structure of the clean Lieb lattice, which contains two dispersive bands and one singular flat band.

Hamiltonian (7.1) thus reduces to a single particle hopping on this lattice. The Lieb lattice contains three sites per unit cell, where the A site corresponds to a single Rydberg excitation in the original model, while the B and C sites correspond, respectively, to horizontal and vertical pairs of neighbouring Rydberg excitations.

7.3 Flat band on the Lieb lattice

The single-particle hopping Hamiltonian on the Lieb lattice takes the form

$$H_{\text{Lieb}} = \sum_{\boldsymbol{k}} (\Omega \cos k_x \; A^\dagger_{\boldsymbol{k}} B_{\boldsymbol{k}} + \Omega \cos k_y \; A^\dagger_{\boldsymbol{k}} C_{\boldsymbol{k}} + \text{H.c.}), \tag{7.2}$$

where $A^\dagger_{\boldsymbol{k}}$, $B^\dagger_{\boldsymbol{k}}$, and $C^\dagger_{\boldsymbol{k}}$ are, respectively, the creation operators on A, B, and C sublattices with quasimomentum $\boldsymbol{k}$. The energy spectrum of Hamiltonian (7.2) contains two dispersive bands $E_\pm(\boldsymbol{k}) = \pm\Omega\sqrt{\cos^2(k_x) + \cos^2(k_y)}$ and one flat band $E = 0$ [see Fig. 7.1(d)]. The zero-energy flat band touches the two dispersive bands at $k_x = k_y = \pi/2$, leading to a three-fold degeneracy at this point. As shown in Refs. [293,294], the band-touching in this model is in fact irremovable, which signals a singularity in the Bloch wavefunction. The $E = 0$ band of Hamiltonian (7.2) in this case is known as a *singular* flat band. The singularity of the flat band has important consequences on the eigenstates within the band. Generically, the eigenstates of a flat band are localized in real space, hence the name compact localized states (CLSs) [see Fig. 7.1(b) for the Lieb lattice]. When the flat band is non-singular, such CLSs form a complete basis of the flat band. By contrast, when the flat band is singular, the set of all CLSs is not linearly independent. For the Lieb lattice, there exist three additional extended eigenstates of the flat band: two non-contractible loop states (NLSs) [Fig. 7.1(b)] and one non-compact state (NCS) [Fig. 7.1(c)].

	Wavefunction	Support	Feature
Regime I	critical, multifractal	B, C	original flat band
Regime II	multifractal	A, B, C	hybridization with dispersive bands
Regime III	localized ($\|E\| \gtrsim 0$), multifractal ($E \approx 0$)	A	disorder-induced flat band

Table 7.1: Main features of three distinct localization regimes.

7.4 Positional disorder

Small deviations of atomic positions from the centers of the corresponding traps can significantly affect the atom-atom interaction. Thermal distribution of atomic positions can be described as a Gaussian with width σ (in units of R_0) [182, 283]. Ignoring atomic motion during the experiment (frozen-gas approximation) [283], such randomness enters Eq. (7.1) via the interaction term: $V(R) = V(R_0 + \delta R) \approx V(R_0) + \delta V$, where δV is a random time-independent shift potential caused by the displacement. This position-disordered interaction manifests itself on the effective Lieb lattice as random, but correlated, on-site potentials for the B and C sublattices. Since the position disorder only affects Rydberg-Rydberg interactions, the A sublattice sites, which represent single Rydberg excitations, do not couple to disorder. Therefore, while the CLSs and NLSs are supported on B and C sublattices and hence are no longer exact eigenstates of the disordered Hamiltonian, the non-compact state in Fig. 7.1(c) remains unaffected by disorder.

To study the effect of disorder on the singular flat band, we numerically diagonalize Hamiltonian (7.2) in the presence of disorder on an $L \times L$ square lattice. We focus on the middle one third of eigenstates in the spectrum, which corresponds

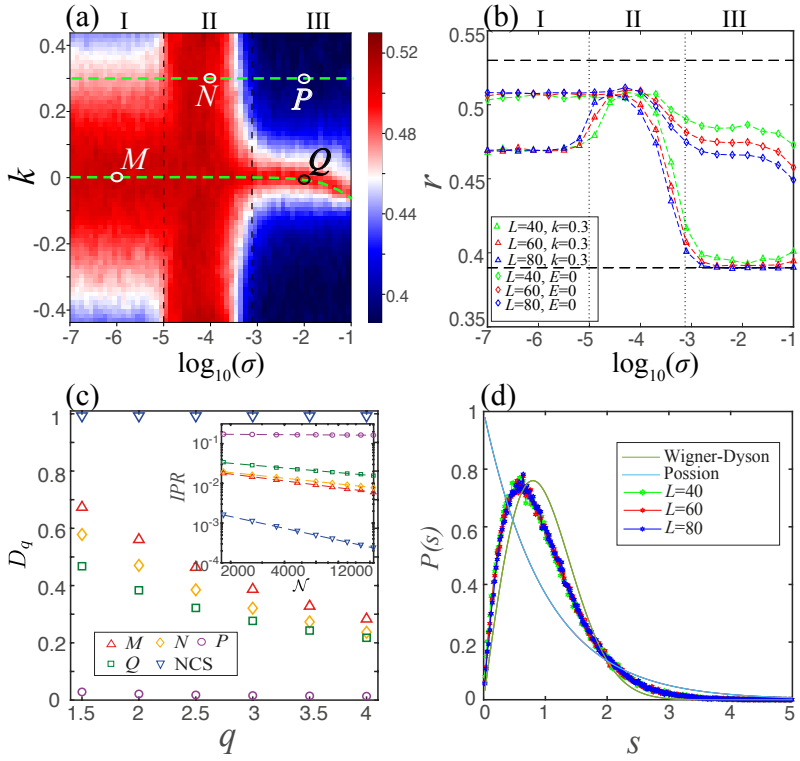

Figure 7.2: (a) Level-spacing ratio r versus the rescaled eigenstate label k and disorder strength σ. (b) r as a function of disorder strength for two cuts, shown by dashed lines in (a), along $E = 0$ and $k = 0.3$ for different system sizes. The error bars (not shown) are smaller than the plot markers. (c) Fractal dimension D_q versus q, for states at representative points in (a): M $(k = 0, \log_{10}\sigma = -6)$, N $(k = 0.3, \log_{10}\sigma = -4)$, P $(k = 0, \log_{10}\sigma = -2)$, Q $(k = 0.3, \log_{10}\sigma = -2)$, as well as the non-compact zero-energy eigenstate (NCS) for arbitrary disorder strength. Inset: scaling of IPR as a function of the Hilbert space dimension. (d) Probability distribution of the unfolded level spacings $P(s)$ for states in regime I for different system sizes [295].

to the flat-band states in the clean limit. We rank-order the eigenstates according to their energies $E_i > E_{i-1}$ and introduce a rescaled label $k = \frac{i-\mathcal{N}/2}{\mathcal{N}/3} \in (-0.5, 0.5)$, where $\mathcal{N}$ is the Hilbert-space dimension and $i \in (\mathcal{N}/3, 2\mathcal{N}/3)$. We probe ergodicity versus localization using the level-spacing ratio $r_i = \min(\delta_i, \delta_{i+1})/\max(\delta_i, \delta_{i+1})$, where $\delta_i = E_{i+1} - E_i$. Ergodic and localized phases are characterized by a Wigner-Dyson (WD) distributed spectrum with mean $\overline{r} \approx 0.53$ and a Poisson distributed spectrum with $\overline{r} \approx 0.39$, respectively. Fig. 7.2(a) shows the eigenstate-resolved r as the disorder strength σ varies. We find a rich phase diagram featuring three distinct regimes: a critical Regime I; a nonergodic extended Regime II; and a Regime III, in which a disorder-induced flat band emerges [see Table. 7.1 for the main features]. Below we shall discuss each regime in detail.

7.5 Regime I: Criticality

Let us first focus on the weak-disorder regime, where the level-spacing statistics are intermediate between WD and Poisson, with the band-edge states [near the top and bottom of Fig. 7.2(a)] being more localized. As one can see from Fig. 7.3(a), while the wavefunction is extended in real-space, it appears less ergodic than a perfectly delocalized state. Moreover, the wavefunction is mainly supported on the B and C sublattices [inset of Fig. 7.3(a)] (Appendix E), indicating that the flat-band states do not couple strongly to the original dispersing bands at weak disorder. To characterize the wavefunctions more quantitatively, we study the inverse participation ratio (IPR) $I_q(k) = \langle \sum_i |\psi_i^\alpha|^{2q} \rangle$, where ψ_i^α is the amplitude of the

α-th wavefunction on site i and the average is taken over disorder realizations and over a fixed number of states α around k [296]. It is in general expected to scale as $I_q \sim \mathcal{N}^{-D_q(q-1)}$, where D_q is known as the fractal dimension, with $D_q = 1$ for ergodic states and $D_q = 0$ for localized states. If D_q depends on q, as occurs for example at the critical point of the Anderson transition [296–300], the eigenstates are called multifractal. Fig. 7.2(c) shows the exponent D_q extracted from the IPR for point M in Fig. 7.2(a), which indeed exhibits a q dependence, signaling multifractality and nonergodicity of the wavefunctions in this regime [301, 302].

Besides delocalization and nonergodicity of the wavefunctions, another interesting feature in Regime I is that the level-spacing statistics is intermediate between WD and Poisson and shows almost no dependence on system size [Fig. 7.2(b)]. This is also clear from Fig. 7.2(d), where we plot the distribution $P(s)$ of the level-spacing s, after spectral unfolding [276, 303], for the states shown in Fig. 7.2(a), i.e. the middle one third of the states. This suggests that the level statistics remain intermediate between WD and Poisson in the thermodynamic limit; such statistics are called critical [276, 302, 304–307]. The statistics also show little dependence on disorder strength, suggesting that entire Regime I is critical even for extremely weak disorder [276, 307]. This is in contrast to the standard Anderson [296] and many-body [298] localization transitions, which involve a single critical point. The origin of the criticality in Regime I lies in the singular nature of the flat band in Hamiltonian (7.2). As shown in Ref. [276], for a flat band with a singular band-touching, the real-space matrix elements of the projection operator onto the flat band $\langle \mathbf{R}|\mathcal{P}|\mathbf{R}+\mathbf{r}\rangle$ decay as $|\mathbf{r}|^{-d}$ in d dimensions. States originating from such flat bands are generi-

cally critical in the presence of weak disorder. On the other hand, for nonsingular flat bands (e.g. in 1D ladder systems), $\langle \mathbf{R}|\mathcal{P}|\mathbf{R}+\mathbf{r}\rangle$ decays exponentially with $\mathbf{r}$ and one can use the detangling method [283, 284, 291] to observe conventional Anderson localization.

7.6 Regime II: Hybridization with dispersive bands

Similarly to Regime I, the level-spacing statistics in Regime II are also intermediate between WD and Poisson, as shown in Fig. 7.2(a). However, the physics in these two Regimes is drastically different. To see this, let us first look at a representative real-space eigenstate in Regime II, shown in Fig. 7.3(b) (Appendix E). Although the wavefunction is again extended but nonergodic, it now has support on all three sublattices [inset of Fig. 7.3(b)], indicating that the original flat band strongly hybridizes with the dispersive bands as the disorder strength increases. Moreover, the fractal dimension D_q again exhibits a q dependence, indicating multifractality in this regime. Nonetheless, Regime II no longer appears critical, as can be seen from the noticeable but subtle system size dependence of the level statistics in Fig. 7.2(b) (Appendix E).

7.7 Regime III: Disorder-induced flat band

In the strongly disordered regime, one expects that most of the eigenstates become localized, as is indeed confirmed by the level spacing statistics in Fig. 7.2(a). The real-space wavefunction shown in Fig. 7.3(d) and the fractal dimension $D_q \approx$

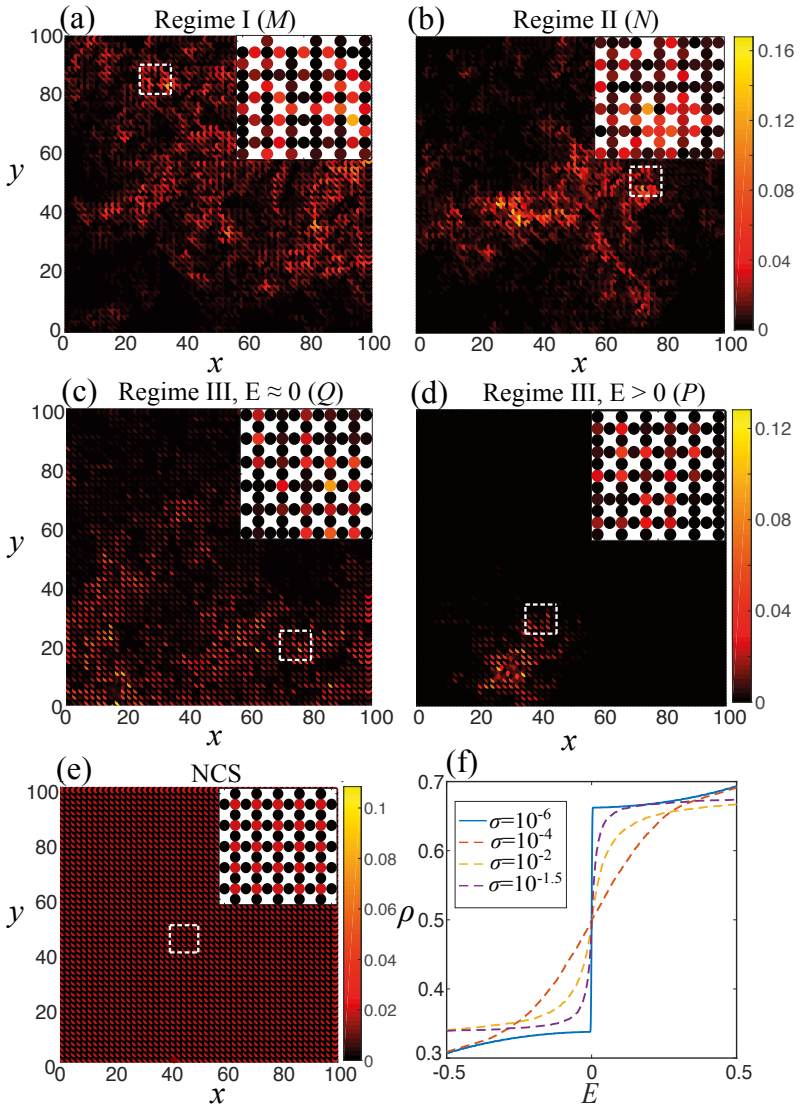

Figure 7.3: (a)-(d) Amplitudes of the real-space wavefunctions for representative points M(a), N(b), Q(c), and P(d) in Fig. 7.2(a). (e) The amplitudes of the wavefunction for the non-compact eigenstate (NCS). Each inset shows a zoomed-in view locally. (f) The integrated density of states as a function of energy, for different disorder strengths.

0 in Fig. 7.2(c) are also consistent with the states being localized. However, we find that in the middle of the spectrum where the energies are very close to $E = 0$, the eigenstates are *delocalized* [see Fig. 7.3(c)]. The fractal dimension of these delocalized states exhibits a q-dependence [see Fig. 7.2(c)], indicating multifractality. Moreover, the integrated density of states in Fig. 7.3(f) shows a sharper jump near $E = 0$ compared to the more weakly disordered Regime II, and, counterintuitively, becomes sharper with increasing disorder. This indicates the presence of a flat band in the strong-disorder regime. This disorder-induced flat band is physically distinct from the original flat band of Hamiltonian (7.2) in the clean limit [solid curve in Fig. 7.3(f)]. As can be seen from Figs. 7.3(c)-(d), the flat-band states in the strong-disorder regime have dominant support on sublattice A (Appendix E), whereas the original flat-band states are supported on sublattices B and C instead [see Fig. 7.3(a)].

To understand this disorder-induced flat band, we can write down the eigenvalue equation for the single-particle hopping Hamiltonian in real space (see Appendix E for the details of the analysis in this paragraph). By eliminating sublattice A [308], one arrives at a single-particle hopping model on the B and C sublattices only, which form a *planar pyrochlore lattice*. As shown in Refs. [276, 294], the planar pyrochlore lattice also hosts a singular flat band at $E = 0$ in the clean limit, and the flat band eigenstates become multifractal states with $E \approx 0$ in the presence of weak disorder [see also Fig. 7.2(a)]. That the wavefunctions have dominant support on sublattice A in Regime III (and dominate support on B and C sublattices in Regime I) can also be understood using the elimination procedure.

We stress that the disorder-induced flat band in Regime III only arises in the Rydberg atom setup, where disorder naturally couples to sublattices B and C only. In contrast, when disorder is present on all sublattices, as is usually the case, the density of states will instead have a broad distribution and no flat band is formed (Appendix E).

7.8 Quench dynamics

The three regimes discussed above have distinct dynamical features in quantum quench experiments (see Appendix E for numerical results). The initial state is chosen as a CLS in the clean limit, which can be prepared in experiments [284]. The Rydberg excitation probabilities have distinct features under time evolution by the 2D disordered Lieb-lattice Hamiltonian in the three respective regimes. In Regime I, the initial state hybridizes weakly with other flat-band states, and hence the distribution of Rydberg excitations spreads slowly in time. In Regime II, the initial state couples to both the flat-band states and dispersive bands, leading to much faster spreading of the Rydberg excitations. Finally, in the strong-disorder Regime III, the Rydberg excitations are strongly localized around their initial positions.

7.9 Conclusions and outlook

We have studied the effect of disorder on 2D Rydberg atom arrays in the anti-blockade regime and uncover rich localization phenomena. Besides the Rydberg system, our results are also relevant to other Lieb-lattice implementations,

e.g., with optical photons [285–289], microwave photons [274], cold atoms [290,291], and electrons [292,309]. By changing the anti-blockade conditions, our study can be extended to a wide variety of synthetic graphs. Moreover, our construction generically leads to single-particle hopping models on effective graphs that are subdivisions of the graph corresponding to the physical lattice. We expect the nonergodic extended states uncovered in this work and disorder-induced flat bands to be generic for graphs with singular flat bands under this construction. Another interesting direction is to consider 3D generalizations of our study involving the interplay of conventional Anderson localization with a mobility edge and the degenerate singular bands. Finally, it would be interesting to consider subspaces with multiple excitations, where there can be nontrivial interplay of anti-blockade conditions and many-body interactions [310–312] (or blockade constraints) in the synthetic lattice.

Chapter 8: Asymmetric Particle Transport and Light-Cone Dynamics Induced by Anyonic Statistics

8.1 Introduction

Fundamental particles in nature can be classified as either bosons or fermions, depending on their exchange statistics. However, other types of quantum statistics are possible in certain circumstances. For instance, Abelian anyons are characterized by fractional statistics interpolating between bosons and fermions [313–317]. When two anyons are exchanged, their joint wavefunction picks up a generic phase factor, $e^{i\theta}$. Anyons play important roles in several areas of modern physics research, such as fractional quantum Hall systems [317–319] and spin liquids [320–322], not only because of their fundamental physical interest, but also due to their potential applications in topological quantum computation and information processing [323–329]. In the beginning, the exploration of anyons was restricted to two-dimensional systems. Later, Haldane generalized the concept of fractional statistics and anyons to arbitrary dimensions [330, 331].

The physics of Abelian anyons in one dimension (1D) has attracted a great deal of recent interest [332–345]. Anyons in 1D exhibit a number of intriguing prop-

erties, including statistics-induced quantum phase transitions [346,347], asymmetric momentum distribution in ground states [341–346, 348], continuous fermionization of bosonic atoms [349], and anyonic symmetry protected topological phases [348]. Several schemes have been proposed for implementing anyonic statistics in ultracold atoms [346–350] and photonic systems [351] by engineering occupation-number dependent hopping using Raman-assisted tunneling [346,347] or periodic driving [349, 351]. Cold atom quantum systems [352–354] are powerful platforms not only for probing equilibrium properties of many-body systems, but also for studying uncharted non-equilibrium physics [18, 103, 156, 165, 355–360]. Yet, most of the non-equilibrium studies to date have focused on fermionic or bosonic systems, where anyonic statistics do not come into play.

In this Chapter, we study the interplay between anyonic statistics and non-equilibrium dynamics. In particular, we study the particle transport and information dynamics of Abelian anyons in 1D, motivated by recent proposals [346–349] and the experimental realization of density-dependent tunneling [350, 361], as well as by technological advances in probing non-equilibrium dynamics in ultracold atomic systems [355, 356]. As we shall see, statistics plays an important role in the non-equilibrium dynamics of anyons. First, distinct from the bosonic and fermionic cases, anyons in 1D exhibit *asymmetric* density expansion under time evolution of a homogeneous anyon-Hubbard model (AHM). The asymmetric transport is controlled by the anyonic statistical angle θ and interaction strength U. When the sign of θ or U is reversed, the expansion changes its preferred direction, thus revealing a novel dynamical symmetry of the underlying AHM. We identify this symmetry

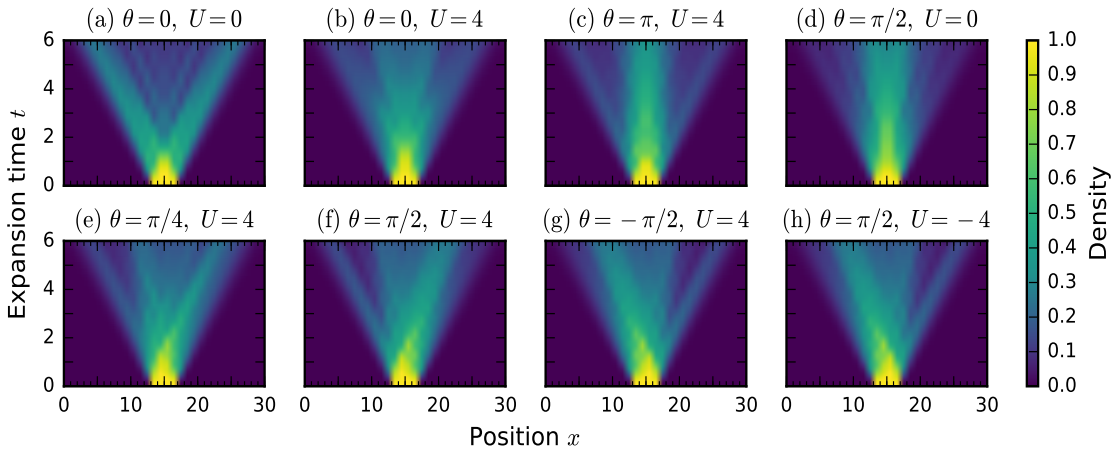

Figure 8.1: Density expansion dynamics for particles initially localized one-per-site in the central N sites, with different statistical angles θ and interaction strengths U. In all plots, the particle number is $N = 4$ and the lattice size is $L = 30$. (a)–(b) Bosonic cases with zero and non-zero interactions, respectively. (c) "Pseudofermionic" case ($\theta = \pi$) with non-zero interactions. (d)–(h) Anyonic cases with various values for θ and U.

operator and analyze the asymmetric expansion dynamics using perturbation theory, confirming the important role played by statistics and interactions. In addition, we use the so-called out-of-time-ordered correlator (OTOC) [362] to characterize the spreading of information in such systems. We find that information spreads with different velocities in the left and right directions, forming an asymmetric light cone.

In contrast to previous studies on ground-state properties [340, 342–344, 346–349] or hard-core cases [339, 345, 363] of 1D anyons, here we focus on the out-of-equilibrium physics of anyonic systems which can be implemented in experiment [346–350]. Moreover, we focus mainly on observables that both reveal anyonic properties directly and can be probed in cold atom systems, where the anyonic statistics can be realized via correlated-tunneling terms [349]. Crucially, our work provides a new method for detecting anyonic statistics even in systems where the ground state is difficult to prepare.

8.2 Model

We consider 1D lattice anyons with on-site interactions—the anyon-Hubbard model [346–351]:

$$\hat{H}_A = -J\sum_{j=1}^{L-1}\left(\hat{a}_j^\dagger\hat{a}_{j+1} + \text{H.c.}\right) + \frac{U}{2}\sum_{j=1}^{L}\hat{n}_j(\hat{n}_j - 1), \tag{8.1}$$

where $\hat{n}_j = \hat{a}_j^\dagger\hat{a}_j$, and J and U describe nearest-neighbor tunneling and on-site interaction, respectively. Throughout the paper, we set $J = 1$ as the energy unit. The anyon creation ($\hat{a}_j^\dagger$) and annihilation ($\hat{a}_j$) operators obey the generalized commutation relations

$$\left[\hat{a}_j, \hat{a}_k\right]_\theta \equiv \hat{a}_j\hat{a}_k - e^{-i\theta\,\mathrm{sgn}(j-k)}\hat{a}_k\hat{a}_j = 0, \tag{8.2}$$

$$\left[\hat{a}_j, \hat{a}_k^\dagger\right]_{-\theta} \equiv \hat{a}_j\hat{a}_k^\dagger - e^{i\theta\,\mathrm{sgn}(j-k)}\hat{a}_k^\dagger\hat{a}_j = \delta_{jk}, \tag{8.3}$$

where θ is the anyonic statistical angle. Here, $\mathrm{sgn}(k) = -1, 0, 1$ for $k < 0, = 0, > 0$, respectively. Equations (8.2) and (8.3) imply that particles on the same site behave as bosons. When $\theta = \pi$, these lattice anyons are "pseudofermions," as they behave like fermions off-site, while being bosons on-site [346].

By a generalized, fractional Jordan-Wigner transformation, $\hat{a}_j = \hat{b}_j e^{-i\theta\sum_{k=1}^{j-1}\hat{n}_k}$, the above AHM can be mapped to an extended Bose-Hubbard model (EBHM),

$$\hat{H}_B = -J\sum_{j=1}^{L-1}\left(\hat{b}_j^\dagger\hat{b}_{j+1}e^{-i\theta\hat{n}_j} + \text{H.c.}\right) + \frac{U}{2}\sum_{j=1}^{L}\hat{n}_j(\hat{n}_j - 1), \tag{8.4}$$

where $\hat{b}_j$ is the bosonic annihilation operator for site j, and $\hat{n}_j = \hat{a}_j^\dagger \hat{a}_j = \hat{b}_j^\dagger \hat{b}_j$ [336–338, 346, 347, 349]. Under this transformation, anyonic statistics have been translated to density-dependent hopping terms, which are the key ingredient to implementing anyonic statistics in 1D. As mentioned, one can realize such terms in cold atomic systems using either Raman-assisted tunneling [346, 347] or time-periodic driving [349–351].

8.3 Asymmetric particle transport

We consider the expansion dynamics of anyons initially localized at the central region of a 1D lattice, one per occupied site. The initial state can be written as a product state in Fock space, $|\Psi_0\rangle_A = \prod_i \hat{a}_i^\dagger |0\rangle$, with occupied sites distributed symmetrically around the lattice center. At times $t > 0$, the system evolves under $\hat{H}_A$ [Eq. (8.1)]. This procedure is equivalent to a quantum quench from $U/J = \infty$ to finite U/J. To characterize particle transport, we study the dynamics of the *real* space anyon density, $n_j^A(t) = {}_A\langle\Psi_0| e^{i\hat{H}_A t} \hat{n}_j e^{-i\hat{H}_A t} |\Psi_0\rangle_A$, where we have set $\hbar = 1$. Under the fractional Jordan-Wigner transformation, the particle number operator $\hat{n}_j$ remains invariant (i.e. $\hat{a}_j^\dagger \hat{a}_j = \hat{b}_j^\dagger \hat{b}_j$), $\hat{H}_A$ maps to $\hat{H}_B$, and the initial state picks up an unimportant phase ϕ, i.e. $|\Psi_0\rangle_A = e^{i\phi} \prod_i \hat{b}_i^\dagger |0\rangle = e^{i\phi} |\Psi_0\rangle_B$. These relations directly lead to the following equality:

$$n_j^A(t) = {}_B\langle\Psi_0| e^{i\hat{H}_B t} \hat{n}_j e^{-i\hat{H}_B t} |\Psi_0\rangle_B = n_j^B(t), \tag{8.5}$$

which indicates that anyonic and bosonic particle densities are equivalent under time evolution governed by their respective initial states and Hamiltonians. Equation (8.5) maps anyonic density to bosonic density, which can be directly measured in cold atom experiments [346–349,355,356]. Likewise, the state $|\Psi_0\rangle_B$ can be easily prepared in such experiments [355,356].

Exact diagonalization results on the expansion dynamics for a variety of statistical angles and interaction strengths are shown in Fig. 8.1. Figures 8.1(a) and (b) show transport dynamics for the bosonic case ($\theta = 0$). Consistent with experimental observations in Ref. [356], bosons exhibit ballistic expansion when $U = 0$ [Fig. 8.1(a)]. However, any finite interaction strength ($U \neq 0$) breaks the integrability of the Bose-Hubbard model and dramatically suppresses the density expansion [Fig. 8.1(b)], leading to diffusive (i.e., non-ballistic) dynamics [356]. In contrast to bosonic cases, for anyons with non-zero θ and even *vanishing* interaction strength, the transport shows strong signatures of being diffusive rather than ballistic [see Fig. 8.1(d)]. This implies that anyonic statistics itself can break integrability and act as a form of effective interaction [364], as is immediately clear from the correlated-tunneling terms in the EBHM in Eq. (8.4). From Figs. 8.1(a) and (d), we also note that for bosons or anyons with zero interaction strength, the density expansion is symmetric.

Different from the above symmetric transport, for anyons with $0 < \theta < \pi$ and finite interaction strength U, the dynamical density distribution is asymmetric, with one preferred propagation direction [Figs. 8.1(e)–(h)]. This is the most striking feature of anyonic statistics' effects on transport behavior. Such asymmetric expansion

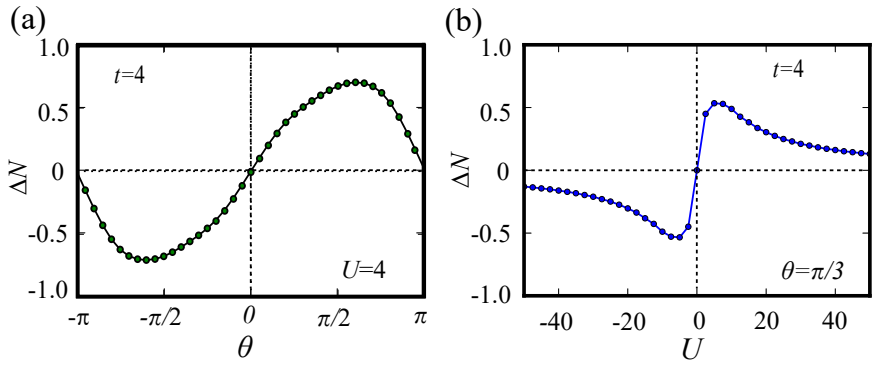

Figure 8.2: (a) Particle number difference ΔN between the right and left halves versus anyon angle θ at time $t = 4$, which is beyond the perturbative regime yet occurs before the quench hits the boundary. The interaction strength is $U = 4$. (b) ΔN versus interaction strength U at time $t = 4$, with $\theta = \pi/3$. The particle number is $N = 4$, and the lattice size is $L = 30$ for both plots, just as in Fig. 8.1.

is due to inversion symmetry breaking of the AHM [346, 365], a direct consequence of the underlying 1D anyonic statistics [Eqs. (8.2) and (8.3)]. A perturbation analysis reveals the important role played by statistics and interactions (see Appendix F for details). Our results illustrate that anyonic statistics has clear signatures in non-equilibrium transport, which may aid in their detection. Previous works have suggested detecting anyonic statistics via asymmetric momentum distributions in equilibrium ground states [342–347, 349], but ground states are often difficult to prepare experimentally.

Figure 8.2(a) plots one measure of the above-mentioned asymmetry, the particle number difference $\Delta N = \sum_{i=1}^{L/2}(n_{i+L/2} - n_i)$ between two halves versus statistical angle θ. The results indeed show clear dependence on the statistical parameter θ, thus demonstrating that one can detect the underlying anyonic statistics using expansion dynamics. Figure 8.2(b) shows the dependence of ΔN on interaction strength for fixed statistical angle. We note that the largest asymmetric measure

ΔN occurs for intermediate values of U, as the expansion dynamics are symmetric at both $U = 0$ (analyzed below) as well as in the limit of large U (the hard-core case) [339, 345, 363].

8.4 Symmetry analysis

Comparing Figs. 8.1(g) and (h) to Fig. 8.1(f), we can clearly see that by reversing the sign of the statistical angle θ or interaction strength U, anyons also reverse their preferred propagation direction. This dynamical symmetry is further illustrated in Figs. 8.2(a) and (b), which provide evidence that ΔN is indeed an odd function of θ and an odd function of U. The results differ from experimental findings for fermionic/bosonic gases [355, 356], where density expansion dynamics are identical for $\pm U$ (further analyzed in a recent theoretical work, Ref. [366]).

To understand the dynamical symmetry, we focus on the symmetry properties of the mapped EBHM for convenience. $\hat{H}_B$ explicitly breaks inversion symmetry $\mathcal{I}$, as the phase of the correlated-tunneling term depends only on the occupation number of the left site (which becomes the right site under inversion). It also breaks time-reversal symmetry, as $\mathcal{T} e^{-i\theta\hat{n}_j}\mathcal{T}^{-1} = e^{i\theta\hat{n}_j}$. However, if we consider the number-dependent gauge transformation $\mathcal{R} = e^{-i\theta\sum_j \hat{n}_j(\hat{n}_j-1)/2}$ and define a new symmetry operator $\mathcal{K} = \mathcal{R}\mathcal{I}\mathcal{T}$, $\hat{H}_B$ is invariant under $\mathcal{K}$ [348]:

$$\mathcal{K}\hat{H}_B\mathcal{K}^\dagger = \hat{H}_B. \tag{8.6}$$

The transformed EBHMs with the opposite sign of interaction or statistical angle are

related by the number parity operator $\mathcal{P} = e^{i\pi \sum_r \hat{n}_{2r+1}}$ or the time-reversal operator $\mathcal{T}$, respectively:

$$\mathcal{P}\hat{H}_{B,+U}\mathcal{P}^{\dagger} = -\hat{H}_{B,-U}, \tag{8.7}$$

$$\mathcal{T}\hat{H}_{B,+\theta}\mathcal{T}^{-1} = \hat{H}_{B,-\theta}. \tag{8.8}$$

Using Eqs. (8.6)–(8.8), one can derive the following relations (Appendix F):

$$\langle \hat{n}_j(t) \rangle_{+U} = \langle \hat{n}_{j'}(t) \rangle_{-U}, \tag{8.9}$$

$$\langle \hat{n}_j(t) \rangle_{+\theta} = \langle \hat{n}_{j'}(t) \rangle_{-\theta}, \tag{8.10}$$

where $\langle \cdot \rangle$ denotes the expectation value of a Heisenberg operator taken with respect to the initial state given above, and sites $j, j^{'}$ are related by the inversion operator $\mathcal{I}$. In fact, the above equations hold for a more general class of initial states (see Appendix F). Therefore, in contrast to fermionic/bosonic gases [366] (symmetric expansion), the above relations indicate that anyons flip their preferred expansion direction when one changes the sign of U or θ in Eq. (8.1). The above equalities also immediately imply when $\theta = 0$ or π (bosons or "pseudofermions," respectively) or when $U = 0$, the transport is symmetric [shown in Figs. 8.1(a)–(d)], consistent with previous results for integrable systems [339, 345, 363].

8.5 Information dynamics

The spreading of information in an interacting quantum many-body system has received tremendous interest [69, 105, 155, 156, 367–369]. For conventional fermionic or bosonic systems with translation invariance, information spreading occurs in a spatially symmetric way [155, 367, 368]. However, as we demonstrate below, this is not generally the case for anyonic systems, where statistics can manifest itself in the information dynamics.

We diagnose information spreading by examining the OTOC, a quantity that has received a great deal of recent interest in studies of quantum scrambling [105, 369–379]. We define the anyonic OTOC as $C_{jk}(t) = \left\langle |[\hat{a}_j(t), \hat{a}_k(0)]_\theta|^2 \right\rangle_\beta$. Here, $\langle\cdot\rangle_\beta$ is taken with respect to the thermal ensemble $e^{-\beta \hat{H}_A}/\operatorname{Tr}(e^{-\beta \hat{H}_A})$ with inverse temperature β. The use of the generalized commutator defined by Eqs. (8.2) and (8.3) ensures that $C_{jk}(t)$ vanishes at $t = 0$. It then starts to grow when quantum information propagates from site k to site j [105, 368, 369, 371]. We focus on the out-of-time-ordered part of the above commutator,

$$F_{jk}(t) = \left\langle \hat{a}_j^\dagger(t)\hat{a}_k^\dagger(0)\hat{a}_j(t)\hat{a}_k(0) \right\rangle_\beta e^{i\theta\,\mathrm{sgn}(j-k)}. \tag{8.11}$$

Figures 8.3(a)–(d) show numerical results for various interaction strengths U and statistical angles θ. In contrast to the density transport shown in Fig. 8.1(b), quantum information spreads in a ballistic way for bosons even when $U \neq 0$ [155, 367]. Indeed, for bosons ($\theta = 0$), the OTOCs map out a symmetric light cone, as

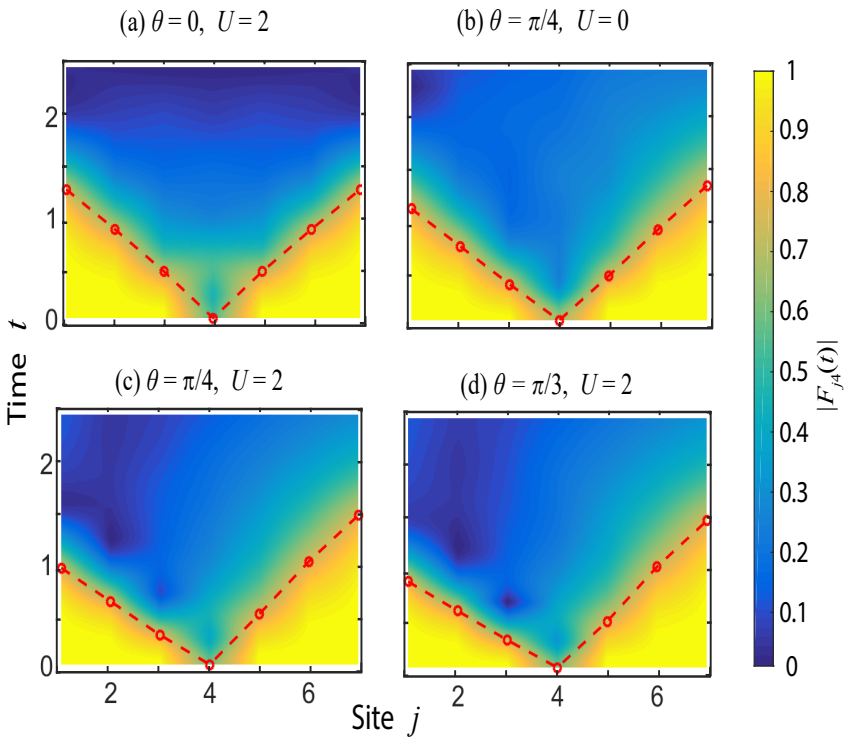

Figure 8.3: OTOC growth $|F_{jk}(t)|$ for different statistical angles θ and interaction strengths U. Here, $L = 7$, $\beta^{-1} = 6$, $k = 4$, and the local Hilbert space of each site is truncated to three states. Plotted is (a) a bosonic case ($\theta = 0$) with non-zero interaction, as well as anyonic cases with (b) vanishing and (c),(d) non-vanishing interaction strengths. The red dots denote where the OTOCs fall to 75% of their initial values. The colormaps are interpolated to non-integer j to better illustrate the light cone behavior.

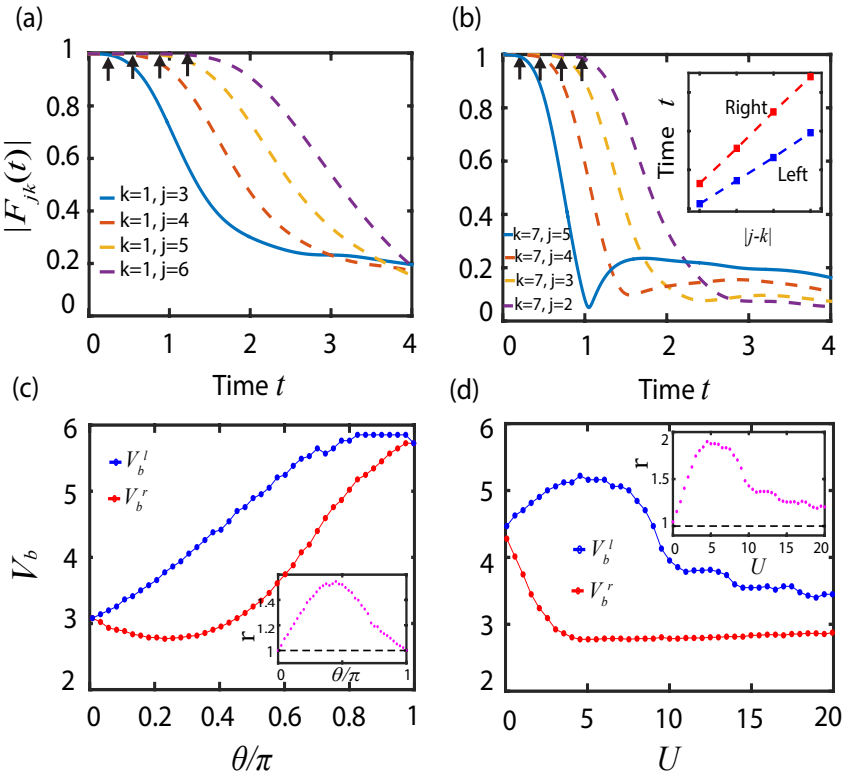

Figure 8.4: (a) OTOC growth characterizing quantum information spreading from the left-most site, $k = 1$, rightward. The OTOC starts to fall when information reaches the jth site, and the black arrows denote the OTOCs' fall to 99% of their initial values. Parameters: $\theta = \pi/3$, $U = 2$, $L = 7$. (b) Same as (a) but shows information spreading from the right-most site $k = 7$ toward the left. Inset: linear fit to extract the butterfly velocities for left (blue) and right (red) directions, respectively. (c) Left (V_b^l) and right (V_b^r) butterfly velocities' dependence on statistical angle θ when $U = 2$. Inset: velocity ratio $r = V_b^l/V_b^r$ versus angle θ. (d) Dependence of V_b^l and V_b^r on interaction strength U when $\theta = \pi/2$. Inset: velocity ratio $r = V_b^l/V_b^r$ versus interaction strength U.

shown in Fig. 8.3(a). However, for the anyonic case ($\theta \neq 0, \pi$), information propagation is asymmetric for the left and right directions [Figs. 8.3(b)–(d)], resulting in an asymmetric light cone. We emphasize that this occurs even when $U = 0$, as the aforementioned dynamical symmetry [Eqs. (8.9) and (8.10)] does not hold for the OTOC.

Figures 8.4(a) and (b) further illustrate the OTOC's growth for right and

left propagation directions, respectively, with $\theta = \pi/3$ and $U = 2$. Indeed, information clearly propagates faster from right to left [Fig. 8.4(b)] than from left to right [Fig. 8.4(a)]. In order to extract the butterfly velocities most accurately in a finite-size system, we choose the left-most site as the reference point for probing information spreading rightward (and vice-versa for information spreading leftward). We define a butterfly velocity V_b by the boundary of the space-time region where $|F_{jk}(t)|$ is suppressed by at least 1% of its initial value. The linear fits of butterfly velocities $V_b^{l,r}$ for two directions are shown in the inset of Fig. 8.4(b). The extracted velocities' dependence on θ and U are further illustrated in Figs. 8.4(c) and (d), respectively. As the results show, when $U > 0$ and $0 < \theta < \pi$, the left information propagation velocity is always larger than the right one, with the greatest disparity at intermediate values of U and θ.

8.6 Experimental detection

To study the transport and information dynamics of the AHM, one can experimentally realize the transformed EBHM. As mentioned, the correlated-tunneling terms in $\hat{H}_B$ can be engineered using laser-assisted tunneling [346, 347] or lattice shaking [349–351]. Particle transport can be studied using similar protocols as in previous experiments [355, 356], where bosonic atoms are first loaded in the center of a 1D optical lattice before being allowed to move under a homogeneous bosonic Hamiltonian. The time-dependent densities, as measured by absorption imaging, directly reflect the anyons' expansion dynamics. On the other hand, measurement of

the OTOC defined by Eq. (8.11) is more challenging than mapping out the atomic density. However, instead of measuring Eq. (8.11), one can focus on a bosonic OTOC, $\widetilde{F}_{jk}(t) = \langle \hat{b}_j^\dagger(t)\hat{b}_k^\dagger(0)\hat{b}_j(t)\hat{b}_k(0)\rangle$, which, by recent proposals, is experimentally accessible by inverting the sign of $\hat{H}_B$ [380–382] or by preparing two identical copies of the system [368,369]. Numerics show that $\widetilde{F}_{jk}(t)$ can also capture the asymmetric features of OTOC growth (Appendix F), thus reflecting anyonic statistics' effect on information dynamics, albeit in an indirect way.

8.7 Conclusion and outlook

We have studied non-equilibrium dynamics of Abelian anyons in a 1D system and found that statistics plays a crucial role in both particle transport and information dynamics. Our work provides a novel method for detecting anyonic statistics using non-equilibrium dynamics in ultracold atom systems [350].

We note the intriguing possibility that a similar dynamical symmetry may exist in other models, such as the $\mathbb{Z}_n$ chiral clock model [44, 45], which has symmetry properties similar to the AHM. Finally, we point out that the inversion symmetry breaking associated with anyonic statistics is also present for non-Abelian anyons in quasi-1D systems [383–385]—for example, Majorana fermions (or, more generally, parafermions) at the edge of (fractional) quantum Hall systems, in deep connection with the underlying chirality. We hope this study could motivate future investigation of out-of-equilibrium dynamics and chiral information propagation in these topological systems.

Chapter 9: Circuit Complexity across a Topological Phase Transition

9.1 Introduction

In computer science, the notion of computational complexity refers to the minimum number of elementary operations for implementing a given task. This concept readily extends to quantum information science, where quantum circuit complexity denotes the minimum number of gates to implement a desired unitary transformation. The corresponding circuit complexity of a quantum state characterizes how difficult it is to construct a unitary transformation U which evolves a reference state to the desired target state [386, 387]. Nielsen and collaborators used a geometric approach to tackle the problem of quantum complexity [388–390]. Suppose that the unitary transformation $U(t)$ is generated by some time-dependent Hamiltonian $H(t)$, with the requirement that $U(t_f) = U$ (where t_f denotes the final time). Then, the quantum state complexity is quantified by imposing a cost functional $F[H(t)]$ on the control Hamiltonian $H(t)$. By choosing a cost functional that defines a Riemannian geometry in the space of circuits, the problem of finding the optimal control Hamiltonian synthesizing U then corresponds to finding minimal geodesic paths in

a Riemannian geometry [388–390].

Recently, Nielsen's approach has been adopted in high-energy physics to quantify the complexity of quantum field theory states [391–403]. This is motivated, in part, by previous conjectures that relate the complexity of the boundary field theory to the bulk space-time geometry, i.e. the so-called "complexity equals volume" [404, 405] and "complexity equals action" [406, 407] proposals. Jefferson *et al.* used Nielsen's approach to calculate the complexity of a free scalar field [391], and found surprising similarities to the results of holographic complexity. A complementary study by Chapman et al., using the Fubini-Study metric to quantify complexity [408], gave similar results. Several recent works have generalized these studies to other states, including coherent states [393,409], thermofield double states [392,396], and free fermion fields [397–399]. However, the connection between the geometric definition of circuit complexity and quantum phase transitions has so far remained unexplored. This connection is important both fundamentally, and is also intimately related to the long-standing problem of quantum state preparations across critical points [410–412].

In this Chapter, we consider the circuit complexity of a topological quantum system. In particular, we use Nielsen's approach to study the circuit complexity of the Kitaev chain, a prototypical model exhibiting topological phase transitions and hosting Majorana zero modes [328,413–417]. Strikingly, we find that the circuit complexity derived using this approach exhibits non-analytical behaviors at the critical points, for both *equilibrium* and *dynamical* topological phase transitions. Moreover, the optimal Hamiltonian connecting the initial and final states must be

non-local in *real-space* when evolving across a critical point. We further generalize our results to a Kitaev chain with long-range pairing, and discuss universal features of non-analyticities at the critical points in higher dimensions. Our work establishes a connection between geometrical circuit complexity and quantum phase transitions, and paves the way towards using complexity as a novel tool to study quantum many-body systems.

9.2 The model

The 1D Kitaev model is described by the following Hamiltonian [413, 414]:

$$\begin{aligned}\hat{H} = &-\frac{J}{2}\sum_{j=1}^{L}\left(\hat{a}_j^\dagger \hat{a}_{j+1} + \text{H.c.}\right) - \mu\sum_{j=1}^{L}\left(\hat{a}_j^\dagger \hat{a}_j - \frac{1}{2}\right) \\ &+ \frac{\Delta}{2}\sum_{j=1}^{L}\left(\hat{a}_j^\dagger \hat{a}_{j+1}^\dagger + \text{H.c.}\right),\end{aligned} \tag{9.1}$$

where J is the hopping amplitude, Δ is the superconducting pairing strength, μ is the chemical potential, L is the total number of sites (assumed to be even), and $\hat{a}_j^\dagger$ ($\hat{a}_j$) creates (annihilates) a fermion at site j. We set $J = 1$ and assume antiperiodic boundary conditions ($\hat{a}_{L+1} = -\hat{a}_1$). Upon Fourier transforming Eq. (9.1) can be written in the momentum basis

$$\begin{aligned}\hat{H} = &-\sum_{k_n}[\mu + \cos k_n]\left(\hat{a}_{k_n}^\dagger \hat{a}_{k_n} - \hat{a}_{-k_n}\hat{a}_{-k_n}^\dagger\right) \\ &+ i\Delta \sin k_n \left(\hat{a}_{k_n}^\dagger \hat{a}_{-k_n}^\dagger - \hat{a}_{-k_n}\hat{a}_{k_n}\right),\end{aligned} \tag{9.2}$$

where $k_n = \frac{2\pi}{L}(n+1/2)$ with $n = 0, 1, \ldots, L/2-1$. The above Hamiltonian can be diagonalized via a Bogoliubov transformation, which yields the excitation spectrum: $\varepsilon_{k_n} = \sqrt{(\mu + \cos k_n)^2 + \Delta^2 \sin^2 k_n}$. The ground state of Eq. (9.1) can be written as

$$|\Psi_{\rm gs}\rangle = \prod_{n=0}^{L/2-1} (\cos\theta_{k_n} - i \sin\theta_{k_n} \hat{a}^\dagger_{k_n} \hat{a}^\dagger_{-k_n}) |0\rangle \,, \tag{9.3}$$

where $\tan(2\theta_{k_n}) = \Delta \sin k_n/(\mu + \cos k_n)$. A topological phase transition occurs when the quasiparticle spectrum is gapless [413], as illustrated in Fig. 9.1(a). The nontrivial topological phase is characterized by a nonzero winding number and the presence of Majorana edge modes [328, 413–417].

9.3 Complexity for a pair of fermions

Since Hamiltonian (9.1) is non-interacting, the ground state wavefunction (9.3) couples only pairs of fermionic modes with momenta $\pm k_n$, and different momentum pairs are decoupled. Hence, we first compute the circuit complexity of one such fermionic pair [397–399], and then obtain the complexity of the full system by summing over all momentum contributions [391, 408].

Let us consider the reference ("R") and target ("T") states with the same momentum but different Bogoliubov angles: $|\psi_{R,T}\rangle = (\cos\theta_k^{R,T} - i \sin\theta_k^{R,T} \hat{a}^\dagger_k \hat{a}^\dagger_{-k}) |0\rangle$. Expanding the target state in the basis of $|\psi_R\rangle$ and $|\psi_R\rangle_\perp$ (i.e., the state orthogonal to $|\psi_R\rangle$), we have $|\psi_T\rangle = \cos(\Delta\theta_k) |\psi_R\rangle - i \sin(\Delta\theta_k) |\psi_R\rangle_\perp$, where $\Delta\theta_k = \theta_k^R - \theta_k^T$. Now the goal is to find the optimal circuit to achieve the unitary transformation

connecting $|\psi_R\rangle$ and $|\psi_T\rangle$:

$$U_k = \begin{bmatrix} \cos(\Delta\theta_k) & -ie^{-i\phi}\sin(\Delta\theta_k) \\ -i\sin(\Delta\theta_k) & e^{-i\phi}\cos(\Delta\theta_k) \end{bmatrix}, \tag{9.4}$$

where ϕ is an arbitrary phase. Nielsen approached this as a Hamiltonian control problem, i.e. finding a time-dependent Hamiltonian $\mathcal{H}_k(s)$ that synthesizes the trajectory in the space of unitaries [388, 389]:

$$U_k(s) = \overleftarrow{\mathcal{P}} \exp\left[\int_0^s dt\, \mathcal{H}(t)\right], \ \mathcal{H}_k(t) = \sum_I Y_k^I(t) O_I \tag{9.5}$$

with boundary conditions $U_k(s=0) = \mathbb{1}$, and $U_k(s=1) = U_k$. Here, $\overleftarrow{\mathcal{P}}$ is the path-ordering operator and O_I are the generators of $U(2)$. The idea is then to define a *cost* (i.e. 'length') functional for the various possible paths to achieve U_k [388,389,391,397]: $\mathcal{D}[U_k] = \int_0^1 ds \sum_I |Y_k^I(s)|^2$, and to identify the optimal circuit or path by minimizing this functional. The cost of the *optimal* path is called the circuit complexity $\mathcal{C}$ of the target state, i.e.

$$\mathcal{C}[U_k] = \min_{\{Y_k^I(s)\}} \mathcal{D}[U_k]\,. \tag{9.6}$$

To illustrate the procedure, let us explicitly derive the circuit complexity for the case of a pair of fermions. By taking the derivative with respect to s in Eq. (9.5),

we get the following expression:

$$\sum_I Y^I(s) O_I = (\partial_s U(s)) U^{-1}(s), \tag{9.7}$$

where $U(s)$ is a unitary transformation which depends on s, and we have omitted the label k for notational clarity.

The unitary $U(s)$ can be parametrized in matrix form:

$$U(s) = e^{i\beta} \begin{bmatrix} e^{-i\phi_1} \cos\omega & e^{-i\phi_2} \sin\omega \\ -e^{i\phi_2} \sin\omega & e^{i\phi_1} \cos\omega \end{bmatrix}, \tag{9.8}$$

where $\beta, \phi_1, \phi_2, \omega$ explicitly depend on the parameter s. The above matrix can be expressed in terms of the generators of $U(2)$, which we choose as follows:

$$O_0 = \begin{bmatrix} i & 0 \\ 0 & i \end{bmatrix}, O_1 = \begin{bmatrix} 0 & i \\ i & 0 \end{bmatrix}, O_2 = \begin{bmatrix} 0 & 1 \\ -1 & 0 \end{bmatrix}, O_3 = \begin{bmatrix} i & 0 \\ 0 & -i \end{bmatrix}. \tag{9.9}$$

Using the relation

$$\mathrm{Tr}(O_a O_b) = -2\delta_{ab}, \tag{9.10}$$

one can extract the strength, $Y^I(s)$, of generator O_I [cf. Eq. (9.5)] as follows:

$$Y^I(s) = -\frac{1}{2} \mathrm{Tr}\left[(\partial_s U(s)) U^{-1}(s) O_I\right]. \tag{9.11}$$

Our cost functional can then be expressed as

$$\begin{aligned}\mathcal{D} &= \int_0^1 ds \sum_I |Y^I(s)|^2 \\ &= \int_0^1 ds \Bigg[\left(\frac{d\beta}{ds}\right)^2 + \left(\frac{d\omega}{ds}\right)^2 + \cos^2\omega \left(\frac{d\phi_1}{ds}\right)^2 \\ &\qquad + \sin^2\omega \left(\frac{d\phi_2}{ds}\right)^2 \Bigg]. \end{aligned} \tag{9.12}$$

Now, by exploiting the boundary condition at $s = 0$, i.e. $U(s = 0) = I$, we get

$$\begin{pmatrix} \beta(s=0) \\ \phi_1(s=0) \\ \phi_2(s=0) \\ \omega(s=0) \end{pmatrix} = \begin{pmatrix} 0 \\ 0 \\ \phi_2(0) \\ 0 \end{pmatrix}, \tag{9.13}$$

where $\phi_2(0)$ is an arbitrary phase. Furthermore, we have the boundary condition at $s = 1$,

$$U(s=1) = \begin{bmatrix} \cos(\Delta\theta) & -ie^{-i\phi}\sin(\Delta\theta) \\ -i\sin(\Delta\theta) & e^{-i\phi}\cos(\Delta\theta) \end{bmatrix}, \tag{9.14}$$

which results in

$$\begin{pmatrix} \beta(s=1) \\ \phi_1(s=1) \\ \phi_2(s=1) \\ \omega(s=1) \end{pmatrix} = \begin{pmatrix} 0 \\ 0 \\ \pi/2 \\ \Delta\theta \end{pmatrix}. \tag{9.15}$$

The integrand in Eq. (9.12) is a sum of four non-negative terms. Setting $\beta(s) = \phi_1(s) = 0$ and $\phi_2(s) = \pi/2$ minimizes (i.e. sets to zero) three of the four terms

without imposing any additional constraints on the minimization of the remaining $(d\omega/ds)^2$ term. One can then easily check that the linear function $w(s) = s\Delta\theta$ minimizes the remaining term and yields

$$\mathcal{C} = \int_0^1 ds\, |\Delta\theta|^2 = |\Delta\theta|^2. \tag{9.16}$$

For the whole quadratic Hamiltonians, it is a simple expression that sums up all the momentum contributions,

$$\mathcal{C}\left(|\psi_R\rangle \to |\psi_T\rangle\right) = |\Delta\theta_k|^2. \tag{9.17}$$

Note that the complexity $\mathcal{C}$ for two fermions is at most $\pi^2/4$, since $|\Delta\theta_k| \in [0, \pi/2]$. The maximum value is achieved when the target state has vanishing overlap with the reference state.

9.4 Complexity for the full wavefunction

Given the circuit complexity for a pair of fermionic modes, one can readily obtain the complexity of the full many-body wavefunction. The total unitary transformation that connects the two different ground states [Eq. (9.3)] is:

$$|\Psi^T_{\rm gs}\rangle = \left(\prod_{n=0}^{L/2-1} U_{k_n}\right) |\Psi^R_{\rm gs}\rangle\,, \tag{9.18}$$

where U_{k_n}, given by Eq. (9.4), connects two fermionic states with momenta $\pm k_n$. By choosing the cost function to be a summation of all momentum contributions [391, 397–399], it is straightforward to obtain the total circuit complexity

$$\mathcal{C}\left(|\Psi_{\rm gs}^R\rangle \to |\Psi_{\rm gs}^T\rangle\right) = \sum_{k_n} |\Delta\theta_{k_n}|^2, \tag{9.19}$$

where $\Delta\theta_{k_n}$ is the difference of the Bogoliubov angles for momentum k_n. In the infinite-system-size limit, the summation can be replaced by an integral, and one can derive that $\mathcal{C} \propto L$. This "volume law" dependence is reminiscent of the "complexity equals volume" conjecture in holography [404, 405], albeit in a different setting.

The circuit complexity given by Eq. (9.19) has a geometric interpretation, as it is the squared Euclidean distance in a high dimensional space [1]. The geodesic path (or optimal circuit) in unitary space turns out to be a straight line connecting the two points [i.e. $H_k(s)$ indepedent of s). In the remainder of this Chapter, we demonstrate that the circuit complexity between two states is able to reveal both *equilibrium* and *dynamical* topological phase transitions.

We first choose a fixed ground state as the reference state and calculate the circuit complexities for target ground states with various chemical potentials μ_T, crossing the phase transition point. The circuit complexity increases as the difference between the parameters of reference and target states is increased [Fig. 9.1(b)]. More importantly, the complexity grows rapidly around the critical points ($\mu_T = \pm 1$), changing from a convex function to a concave function at the critical points. This

[1] In such a space, each state is represented by one point, with its coordinates labeled by the Bogoliubov angles, i.e. $(\theta_{k_0}, \theta_{k_1}, \ldots, \theta_{k_{L/2-1}})$

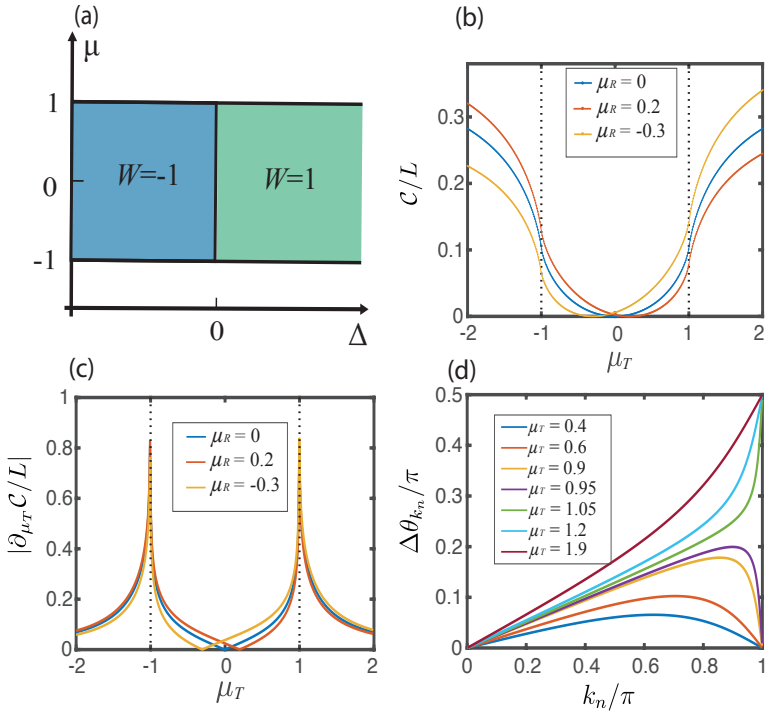

Figure 9.1: (a) Phase diagram of the Kitaev chain, with W denoting the winding number. (b) Ground state circuit complexity and (c) its derivative versus target state chemical potential (μ_T) for several reference states, each with a different chemical potential μ_R. (d) Bogoliubov angle difference, $\Delta\theta_{k_n}$, for different target ground states, with $\mu_R = 0$. $\Delta_R = \Delta_T = 1$ for (b)–(d), and $L = 1000$ for (b) and (c).

is further illustrated in Fig. 9.1(c), where we plot the derivative (susceptibility) of circuit complexity with respect to μ_T . The clear divergence at the critical points indicates that circuit complexity is nonanalytical at the critical points (see Appendix G.1 for derivation), and thus can signal the presence of a quantum phase transition. We emphasize that these features are robust signatures of phase transitions, which do not change if one chooses a different reference state in the same phase [see Figs. 9.1(b) and (c)].

We further plot $\Delta\theta_{k_n}$ versus the momentum k_n, for various target states (with a fixed reference state) in Fig. 9.1(d). When both states are in the same phase, $\Delta\theta_{k_n}$ first increases with momentum, and finally decreases to 0 when k_n approaches π. In contrast, when μ_T is beyond its critical value, $\Delta\theta_{k_n}$ increases monotonically with momentum, and takes the maximal value of $\pi/2$ at $k_n = \pi$. This is closely related to the topological phase transition characterized by winding numbers, where the Bogoliubov angles of two different states end up at the same pole (on the Bloch sphere) upon winding half of the Brillouin zone if the states belong to the same phase [414]. Hence, the non-analytical nature of the circuit complexity is closely related to change of topological number (and topological phase transition).

Analytically, the derivatives of the circuit complexity (9.17) can be explicitly recast into a closed contour integral over the complex variable $z = e^{ik}$ (see Appendix G.1 for detailed derivations). Depending on the parameters of the target states, the poles associated with the integrand are located inside or outside the contour. When the target state goes across a phase transition, the poles sit exactly on the contour, resulting in the divergence of the derivatives of the circuit complexity at critical

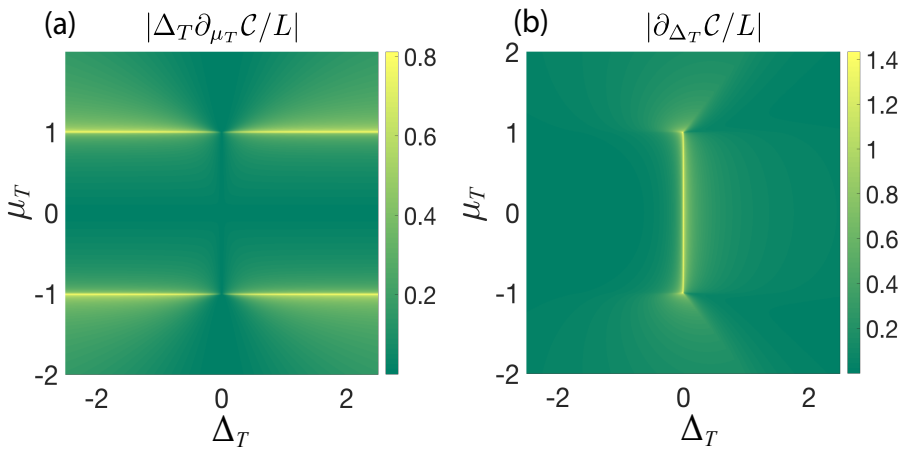

Figure 9.2: Derivative of circuit complexity as a function of μ_T and Δ_T. Panel (a) plots the derivative with respect to μ_T (in units of $1/\Delta_T$), and panel (b) plots the derivative with respect to Δ_T. The reference state is chosen as the ground state of Eq. (9.1) with $\mu_R = 0$ and $\Delta_R = -1$, and $L = 1000$.

points [Appendix G.1]. Interestingly, the whole parameter space can be classified into four different phase regimes depending on which poles lie inside the contour [see Fig. G.1 in Appendix G.1] , which agrees exactly with the phase diagram shown in Fig. 9.1(a).

Figures 9.2(a) and (b) show the derivative of circuit complexity with respect to μ_T and Δ_T for the whole parameter regime. The derivatives show clear singular behavior at both the horizontal [Fig. 9.2(a)] and vertical [Fig. 9.2(b)] phase boundaries. Therefore, by using the first-order derivative of complexity with respect to μ_T and Δ_T, one can map out the entire equilibrium phase boundaries of the Kitaev chain.

9.5 Real-space locality of the optimal Hamiltonian

Since the ground state [Eq. (9.3)] is a product of all momentum pairs, the optimal circuit connecting two different ground states corresponds to the following

Hamiltonian:

$$\hat{H}_c = \sum_{k>0} \hat{H}_k = \sum_{k>0} -i\Delta\theta(k)\hat{\psi}_k^\dagger \tau_1 \hat{\psi}_k, \tag{9.20}$$

where τ_i are the Pauli matrices, and $\hat{\psi}_k$ denotes the Nambu spinor $\hat{\psi}_k = \begin{pmatrix} \hat{a}_k \\ \hat{a}_{-k}^\dagger \end{pmatrix}$. By taking a Fourier series of the above optimal Hamiltonian, one can show that the Hamiltonian can be written in real space (see Appdendix for details G.2):

$$\hat{H}_c = \sum_j \sum_{n=1}^{\infty} \omega_n \left(\hat{a}_j \hat{a}_{j+n} - \text{H.c.} \right), \tag{9.21}$$

where $\Delta\theta(k) = 2\sum_{n=1}^{\infty} \omega_n \sin(nk)$.

One crucial observation is that when the two ground states are in the same phase, $\Delta\theta(0) = \Delta\theta(\pi) = 0$ [see Fig. 9.1(d)]; hence the Fourier series of $\Delta\theta(k)$ converges *uniformly*. Therefore, the full series can be approximated by a *finite* order N^* with arbitrarily small error. This immediately implies that the real-space optimal Hamiltonian (9.21) is local, with a *finite range* N^*. In sharp contrast, if the two states belong to different phases, $\Delta\theta(\pi) = \pi/2 \neq \Delta\theta(0) = 0$; the Fourier series of $\Delta\theta(k)$ converges at most pointwise. Thus the optimal Hamiltonian must be truly *long-range* (non-local) in real-space [Appendix G.2], given that the total evolution time is chosen to be a constant [Eq. (9.5)]. Comparing to previous works on classifying gapped phases of matter using local unitary circuits [418–420], our results provide an alternative approach that has a natural geometric interpretation.

9.6 Complexity for dynamical topological phase transition

Dynamical phase transitions have received tremendous interest recently [18, 103, 360, 421–430]. Studies on quench dynamics of circuit complexity have mostly focused on growth rates in the short-time regime [395, 400]. Here, we show that the long-time steady-state value of the circuit complexity following a quantum quench can be used to detect *dynamical* topological phase transitions.

We take the initial state to be the ground state of a Hamiltonian $\hat{H}_i$, and consider circuit complexity growth under a sudden quench to a different Hamiltonian, $\hat{H}_f$. The reference and target states are chosen as the initial state $|\Psi_i\rangle$ and time-evolved state $|\Psi(t)\rangle$ respectively. The time-dependent $|\Psi(t)\rangle$ can be written as [431, 432]

$$|\Psi(t)\rangle = \prod_{n=0}^{\frac{L}{2}-1} \left[\cos(\Delta\theta_{k_n}) - ie^{2i\varepsilon_{k_n}t} \sin(\Delta\theta_{k_n}) \hat{A}^\dagger_{k_n} \hat{A}^\dagger_{-k_n} \right] |0\rangle \,, \tag{9.22}$$

where $\Delta\theta_{k_n}$ is the Bogoliubov angle difference between eigenstates of $\hat{H}_i$ and $\hat{H}_f$, and ε_{k_n} and $\hat{A}_{k_n}$ are the energy levels and normal mode operators, respectively, for the post-quench Hamiltonian. Similar to the previous derivations, one can obtain the time-dependent circuit complexity,

$$\mathcal{C}(|\Psi_i\rangle \to |\Psi(t)\rangle) = \sum_{k_n} \phi^2_{k_n}(t) \tag{9.23}$$

where $\phi_{k_n}(t) = \arccos\sqrt{1 - \sin^2(2\Delta\theta_{k_n}) \sin^2(\varepsilon_{k_n} t)}$.

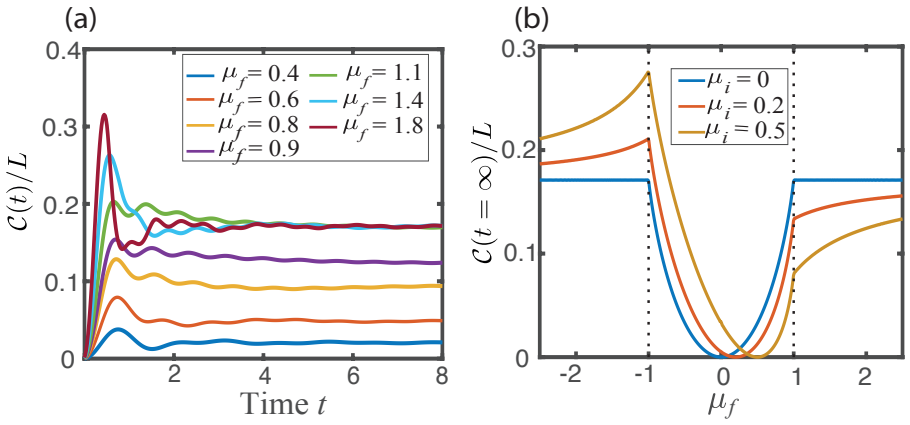

Figure 9.3: (a) Circuit complexity growth for various post-quench chemical potentials, μ_f. The initial state (serves as the reference state) is the ground state of Eq. (9.1) with $\mu_i = 0$. (b) Steady-state values of complexity versus μ_f. The different lines denote different initial/reference states. $\Delta_i = \Delta_f = 1$ and $L = 1000$ in both plots.

As shown in Fig. 9.3(a), the circuit complexity first increases linearly and then oscillates [394, 395, 400] before quickly approaching a time-independent value. The steady-state value of circuit complexity increases with μ_f of the post-quench Hamiltonian, until the phase transition occurs [Fig. 9.3(a)]. Fig. 9.3(b) further illustrates the long-time steady-state values of circuit complexity versus μ_f for different initial states. The steady-state complexity clearly exhibits *nonanalytical* behavior at the critical point. This behavior arises because the time-averaged value of $\phi_{k_n}(t)$ exhibits an upper bound after the phase transition (see Appendix G.3), and it is a robust feature of the dynamical phase transition regardless of the initial state.

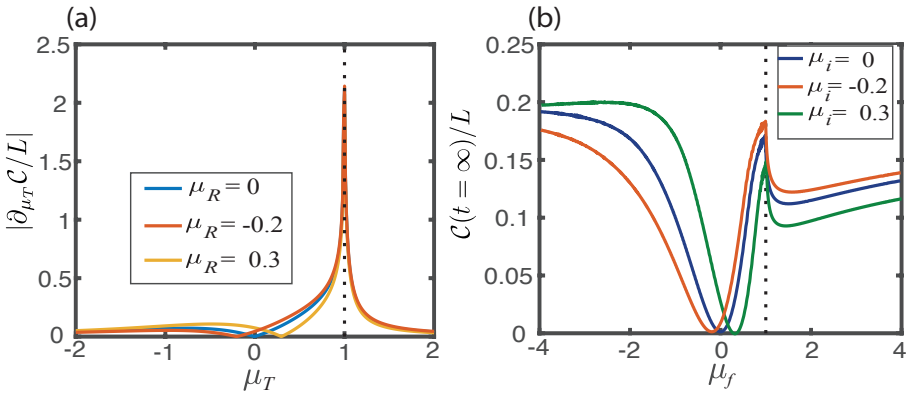

Figure 9.4: (a) Derivative of circuit complexity with respect to μ_T for three different reference ground states of the long-range Kitaev chain, with $\Delta_R = \Delta_T = 1.3$. (b) Steady-state value of circuit complexity versus μ_f for three different initial ground states, with $\Delta_i = \Delta_f = 1$. $L = 1000$ and $\alpha = 0$ in both plots.

9.7 Generalization to long-range Kitaev chain and higher dimensions

We further give an example of a Kitaev chain with long-range pairing [433–436]:

$$\begin{aligned}\hat{H}_{\mathrm{LR}} = &-\frac{J}{2}\sum_{j=1}^{L}(\hat{a}_j^\dagger \hat{a}_{j+1} + \mathrm{H.c.}) - \mu\sum_{j=1}^{L}(\hat{a}_j^\dagger \hat{a}_j - \frac{1}{2}) \\ &+ \frac{\Delta}{2}\sum_{j=1}^{L}\sum_{\ell=1}^{L-1}\frac{1}{d_\ell^\alpha}(\hat{a}_j^\dagger \hat{a}_{j+\ell}^\dagger + \mathrm{H.c.}),\end{aligned} \tag{9.24}$$

where $d_\ell = \min(\ell, L-\ell)$. In contrast to the short-range model, the long-range model with $\alpha < 1$ hosts topological phases with semi-integer winding numbers [433, 436]. As one can see, the derivative of ground state circuit complexity only diverges at $\mu_T = 1$ [Fig. 9.4(a)], in contrast with Fig. 9.1(c). This agrees perfectly with the phase diagram for the long-range interacting model, where a topological phase transition occurs only at $\mu = 1$ for $\alpha = 0$ [436]. Figure 9.4(b) shows the long-time steady-state values of the circuit complexity after a sudden quench. Again, one observes

nonanalytical behavior only at $\mu_T = 1$.

While we have so far restricted ourselves to 1D, the results we found can be readily generalized to higher dimensions [437], for example, to $p + ip$ topological superconductors in 2D. The ground state wavefunction of a $p + ip$ superconductor essentially takes the same form as Eq. (9.3), with the momenta now being restricted to the 2D Brillouin zone, and $\tan(2\theta_{\boldsymbol{k}}) = |\Delta_{\boldsymbol{k}}|/\varepsilon_{\boldsymbol{k}}$, where Δ_k and $\varepsilon_{\boldsymbol{k}}$ denote pairing and kinetic terms in 2D. The circuit complexity can still be written as $\mathcal{C} = \sum_{\boldsymbol{k}} |\Delta\theta_{\boldsymbol{k}}|^2 = \frac{L^2}{(2\pi)^2} \int \mathrm{d}^2\boldsymbol{k} |\Delta\theta(\boldsymbol{k})|^2$. One can show again that the derivative of the circuit complexity is given by (see Appendix G.4)

$$\partial_{\mu_T} \mathcal{C} = \frac{L^2}{(2\pi)^2} \int \mathrm{d}^2\boldsymbol{k} \frac{\theta^T(\boldsymbol{k}) |\Delta(\boldsymbol{k})|}{E(\boldsymbol{k})^2}, \tag{9.25}$$

where $E(\boldsymbol{k})^2 = \epsilon(\boldsymbol{k})^2 + |\Delta(\boldsymbol{k})|^2$ and $\theta^T(\boldsymbol{k})$ denotes the Bogoliubov angle for the target state. It is thus obvious that non-analyticity happens at the critical point where $E(\boldsymbol{k}) = 0$ [Appendix G.4].

9.8 Conclusions and outlook

We use Nielsen's approach to quantify the circuit complexity of ground states and nonequilibrium steady states of the Kitaev chain with short- and long-range pairing. We find that, in both situations, circuit complexity can be used to detect topological phase transitions. The non-analytic behaviors can be generalized to higher-dimensional systems, such as $p + ip$ topological superconductors [438, 439].

One interesting future direction is to use the geometric approach to quantify

circuit complexity when the control Hamiltonians are constrained to be local in real-space [420, 440, 441], and study its connection to quantum phase transitions [410, 442–444]. It would also be of interest to investigate the circuit complexity of *interacting* many-body systems. One particular example is the XXZ spin-half chain, whose low-energy physics can be modeled by the Luttinger liquid [445–447]. By restricting to certain classes of gates (i.e., by imposing penalties on the cost function) [388, 391], it might be possible to find improved methods to efficiently prepare the ground state of the XXZ model by calculating the geodesic path in gate space.

Chapter 10: Summary and Outlook

Programmable quantum simulators allow the study of quantum systems that are difficult to model with a supercomputer. In this dissertation, we have used various quantum simulation platforms to study physical phenomena including confined quasiparticles, Stark many-body localization, Hilbert space fragmentation, localization in topological lattices, and anyonic statistics. We focused on non-equilibrium quantum dynamics due to these phenomena. Quantum information quantities, such as correlation functions and circuit complexity, were used to characterize quantum information dynamics and topological phase transitions. Below, we give summaries of each chapter and point out several potential research directions based on our studies.

In Chapters 2 and 3, we studied the existence of mesonic confined quasiparticles generated by long-range interactions both theoretically and experimentally. We showed that these quasiparticles have signatures in the quench dynamics of different observables following a global quench. Going beyond the confinement regime, we studied the number of domain wall excitations created for large quench parameters, where the dynamics is difficult to model with classical computers. This work can motivate future studies on using quantum simulators to model more exotic high-

energy physics phenomena, such as particle collision, string breaking dynamics, and dynamics described by non-Abelian gauge fields [141]. It would be interesting to investigate how to use the slow thermalization effect (induced by long-range interactions) to stabilize non-equilibrium phases of matter, such as time crystals [95–97] and Floquet symmetry-protected topological phases of matter [118–122]. Future research can also explore how to use hybrid quantum-classical algorithms[1] to model quantum many-body physics that could not be *directly* realized using synthetic quantum systems.

Chapter 4 showed that we can use Rydberg atom arrays to realize baryonic quasiparticle excitations, going beyond the mesonic case studied in previous chapters. Recent experiments showed that Rydberg atom systems possess a $\mathbb{Z}_3$-ordered crystalline phase whose low-energy quasiparticles are defects in the crystalline order. By engineering a $\mathbb{Z}_3$-translational-symmetry breaking field, we showed that different types of defects experience confinement, and as a consequence form mesonic or baryonic quasiparticle excitations. This proposal is readily applicable to current Rydberg experiments, and the method can be easily generalized to more complex confined excitations (e.g. 'tetraquarks', 'pentaquarks') in phases with $\mathbb{Z}_q$ order for $q > 3$. These more complex states would require much larger system sizes which would no longer be amenable to the numerical methods but can be achieved in quantum simulators. In future studies, it would also be interesting to consider confinement scenarios in higher dimensions, where Rydberg systems feature more complicated

[1]These algorithms aim to variationally solve optimization problems using a feedback loop between a classical computer and a quantum co-processor while benefiting from quantum resources

phases of crystalline order [190]. In particular, the symmetry-breaking patterns in two dimensions allow for both one-dimensional domain wall excitations as well as point-like "monopole" excitations, which is similar to the distinct excitations in higher-dimensional gauge theories [184].

In Chapter 5, we went beyond the approximate domain-wall confinement situations studied in the previous three chapters. We showed that a one-dimensional spin-1/2 model with strict confinement of Ising domain walls exhibits a fragmented Hilbert space. Whereas most of the previous works emphasize dipole moment conservation as an essential ingredient for such fragmentation, we instead require two commuting $U(1)$ conserved quantities associated with the total domain-wall number and the total magnetization. We further demonstrate how this Hilbert-space fragmentation pattern arises perturbatively from $\mathbb{Z}_2$ gauge theory coupled to fermionic matter, leading to a hierarchy of time scales for the motion of the fermions. In future studies, it would be interesting to use experimental platforms to observe the fragmented Hilbert space. It would also be interesting to investigate if Hilbert space fragmentation is a general mechanism for slow dynamics in different gauge theories. The generalization of our study to higher dimensions would also be an interesting direction to pursue.

Chapter 6 realized Stark many-body localization in a trapped-ion quantum simulator and demonstrated its key properties: halting of thermalization and slow propagation of correlations without the disorder. Our study suggests that the concept of many-body localization may be relevant in settings well beyond the original considerations [225, 226]. For all types of MBL, questions about the conditions for

asymptotic stability of localization remain, particularly in systems with long-range terms or more than one dimension [235, 253, 257]. To this end, future work could study the dependence of Stark MBL on the power-law exponent α. This plays a key role in the stability of disordered MBL, by determining whether rare resonant regions can cause delocalization, while a disorder-free system is expected to avoid this source of relaxation [241]. Further work could also explore connections between our observations and the approximate Hilbert space fragmentation (or shattering) that arises in certain short-range tilted models [242, 244, 448, 449]. A natural step in this direction would be to characterize the low-gradient regime of incomplete localization in more detail. The hydrodynamic behavior in this regime could be examined in a larger system.

In Chapter 7, we studied the effect of experimentally relevant positional disorder on Rydberg atoms trapped in a 2D square lattice under anti-blockade (facilitation) conditions. We found three distinct regimes as the disorder strength is varied: a critical regime, a delocalized but nonergodic regime, and a regime with a disorder-induced flat band. The critical regime's existence depends crucially upon the singular flat band in our model and is absent in any 1D array or ladder system. Besides the Rydberg system, our results can be generalized to other Lieb-lattice implementations, e.g., with optical photons [285–289], microwave photons [274], cold atoms [290, 291], and electrons [292, 309]. By changing the anti-blockade conditions, our study can be extended to a wide variety of synthetic graphs. Moreover, our construction generically leads to single-particle hopping models on effective graphs that are subdivisions of the graph corresponding to the physical lattice. We expect the

nonergodic extended states uncovered in this work and disorder-induced flat bands to be generic for graphs with singular flat bands under this construction. Another interesting direction is to consider the 3D generalizations of our study involving the interplay of conventional Anderson localization with a mobility edge and the degenerate singular bands. Finally, it would be interesting to consider subspaces with multiple excitations, where there can be the nontrivial interplay of anti-blockade conditions and many-body interactions [310–312] (or blockade constraints) in the synthetic lattice.

Chapter 8 studied the non-equilibrium dynamics of Abelian anyons in a one-dimensional system. We found that the interplay of anyonic statistics and interactions gives rise to spatially asymmetric particle transport together with a novel dynamical symmetry that depends on the anyonic statistical angle and the sign of interactions. Moreover, we show that anyonic statistics induces asymmetric spreading of quantum information, characterized by asymmetric light cones of out-of-time-ordered correlators. Such asymmetric dynamics is in sharp contrast with the dynamics of conventional fermions or bosons, where both the transport and information dynamics are spatially symmetric. In the future, it would be interesting to use cold-atom experiments to observe the predicted phenomena. It would also be interesting to identify similar dynamical symmetry in other models, such as the $\mathbb{Z}_n$ chiral clock model [450, 451]. We pointed out that the inversion symmetry breaking associated with anyonic statistics is also present for non-Abelian anyons in quasi-1D systems [383–385]—for example, Majorana fermions (or, more generally, parafermions) at the edge of (fractional) quantum Hall systems, in deep connection

with the underlying chirality. We hope this study could motivate the future investigation of out-of-equilibrium dynamics and chiral information propagation in these topological systems. The generalization of our study to higher dimensions (such as 2D) would also be an interesting direction to pursue.

In Chapter 9, we used Nielsen's geometric approach to quantify the circuit complexity in a one-dimensional Kitaev chain across a topological phase transition. We find that the circuit complexities of both the ground states and non-equilibrium steady states of the Kitaev model exhibit non-analytical behaviors at the critical points, and thus can be used to detect both *equilibrium* and *dynamical* topological phase transitions. We further generalize our results to a Kitaev chain with long-range pairing and discuss generalizations to higher dimensions. One interesting future direction is to use the geometric approach to quantify circuit complexity when the control Hamiltonians are constrained to be local in real-space [420,440,441], and study its connection to quantum phase transitions [410,442–444]. It would also be interesting to use circuit complexity as a novel tool to understand quantum many-body systems. One particular example is the XXZ spin-half chain, whose low-energy physics can be modeled by the Luttinger liquid [445–447]. By restricting to certain classes of gates (i.e., by imposing penalties on the cost function) [388,391], it might be possible to find improved methods to efficiently prepare the ground state of the XXZ model by calculating the geodesic path in gate space.

Appendix A: Appendices to Chapter 2

A.1 Light-cone spreading of correlation functions

In the main text, we have shown that the magnitude of $\langle \sigma_j^z(t)\sigma_k^z(t)\rangle_c$ is suppressed by long-range interactions. As stressed in the main text, this does not indicate the disappearance of the light-cone spreading of correlations (quantum information). In this section, we provide detailed numerics showing that the light-cone behaviour is still present by zooming in on the weak-signal regions of Figs. 2.1(b) and (c) of the main text.

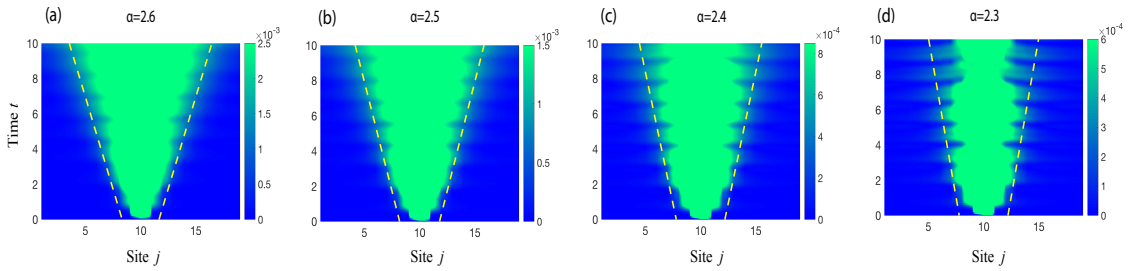

Figure A.1: (color online) $\langle \sigma_j^z \sigma_k^z \rangle_c$ after a quantum quench with initial state $|\Psi_0\rangle$. Parameters: $L = 19$, $k = 10$, and $B = 0.27$. (a) $\alpha = 2.6$, (b) $\alpha = 2.5$, (c) $\alpha = 2.4$, (d) $\alpha = 2.3$. The green regions represent out-of-range values of the correlation functions. The yellow dashed lines illustrate twice the maximal velocity of quasiparticles (within the three lowest energy bands). The maximal velocity for each α is calculated using the two-kink model, and takes the value of $v_{max} = 0.24J,\ 0.20J,\ 0.17J,\ 0.14J$ for (a), (b), (c), and (d), respectively. The speed at which the front of the time-dependent correlation function propagates is consistent with twice the maximal velocity of the quasiparticles.

Figs. A.1(a)-(d) show correlation spreading after a sudden quench (for the

same initial state, $|\Psi_0\rangle$, as in the main text) for several different α. Figs. A.1 (a) and (d) take the same parameters of the post-quench Hamiltonians as Figs. 2.1 (b) and (c) in the main text, but use an intensity scale up to two orders magnitude smaller. By zooming in on the weak-signal regions, we observe that correlations do indeed exhibit light-cone spreading, though they may spread at different maximal velocities compared to the short-range case. These results are consistent with the general theory of quench dynamics in one-dimensional systems first formulated in Refs. [86, 87] for short-range interacting systems, where the light-cone spreading of correlations is always present with a slope equal to twice the maximal velocity of the quasiparticles.

A.2 Scaling and convergence analysis of confining potential

In this section, we provide a detailed analysis on the scaling and convergence of the potential that appears in the two-kink model. We use integrals to approximate sums. While this does not give an exact value for the potential, we will see that scaling exponents given by this approximation agree well with numerics presented in the main text.

We use $V(n, L, \alpha)$ to denote the potential energy of a two-domain-wall state with length n on a finite chain of length L. The potential can be rewritten in the following form:

$$V(n, L, \alpha) = 4\left[\sum_{r=1}^{L} \frac{1}{r^\alpha} + \sum_{r=2}^{L} \frac{1}{r^\alpha} + ... + \sum_{r=n}^{L} \frac{1}{r^\alpha} - 1\right]. \tag{A.1}$$

Note that Eq. (2.4) in the main text can be obtained by taking the above equation to the thermodynamic limit.

We now approximate the above sums with integrals, which gives

$$\widetilde{V}(n,L,\alpha) = 4\left[\int_1^L \frac{1}{r^\alpha}dr + \int_2^L \frac{1}{r^\alpha}dr + ... + \int_n^L \frac{1}{r^\alpha}dr - 1\right] \tag{A.2}$$

$$= 4\left[\frac{1}{\alpha-1}\left(\sum_{r=1}^{n}\frac{1}{r^{\alpha-1}} - \frac{n}{L^{\alpha-1}}\right) - 1\right]. \tag{A.3}$$

After approximating the remaining sum, we obtain

$$\widetilde{\widetilde{V}}(n,L,\alpha) = 4\left[\frac{1}{\alpha-1}\left(\int_1^n \frac{1}{r^{\alpha-1}}dr - \frac{n}{L^{\alpha-1}}\right) - 1\right] \tag{A.4}$$

$$= 4\left[\frac{1-1/n^{\alpha-2}}{(\alpha-1)(\alpha-2)} - \frac{n}{(\alpha-1)L^{\alpha-1}} - 1\right]. \tag{A.5}$$

Three comments are in order: (i) The second term in the above expression tells us that, for finite n, the potential is finite in the thermodynamic limit ($L \to \infty$) only when $\alpha > 1$. Therefore, the masses of these bound states are finite when $\alpha > 1$. This agrees with the convergence properties of the Riemann zeta function. (ii) For a finite system, the potential $\widetilde{\widetilde{V}}(n,L,\alpha)$ scales as $c_0 - c_1/L^{\alpha-1}$. Since all the potential energies of the two-domain-wall states have such scaling, the masses given by eigenenergies of Eq. (2.3) in the main text should also have the same scaling. This implies that β (defined in the caption to Fig. 2.3 of the main text) is equal to $\alpha - 1$, which is in agreement with the numerical results presented in the inset of Fig. 2.3(d). (iii) Because of the first term of the above equation, $V(n)$ goes to infinity when n goes to infinity for $1 < \alpha \leq 2$, while it is upper-bounded when

$\alpha > 2$. This is also reflected in Fig. 2.3(a) of the main text. Therefore, when $\alpha > 2$, the two-kink model predicts that only the lower part of the energy spectrum is composed of bound states. In other words, for a high enough energy, we have a continuum of states. However, for $\alpha \leq 2$, all eigenstates of the two-kink model are bound quasiparticles.

Appendix B: Appendices to Chapter 3

B.1 Methods

B.1.1 Trapped-ion quantum simulators

In this work, we use two quantum simulators, which we refer to as System 1 [153] and System 2 [154]. System 1 is a room temperature trapped-ion apparatus. It employs a 3-layer linear Paul trap with transverse center-of-mass (COM) motional mode frequency $\nu_{COM} = 4.7$ MHz and axial COM frequency $\nu_z \approx 0.5$ MHz [153]. The main limitation of this apparatus is the rate of collisions with the residual background gas in ultra-high vacuum (UHV), limiting the practical size of the chain. During such collision events, the ion crystal melts and ions are ejected from the trap due to RF heating. However, this apparatus has individual addressing capabilities, allowing for initialization of arbitrary spin flips, which is crucial in this work. Therefore, we use it to investigate low-energy domain wall bound states in smaller system sizes.

System 2 is a linear blade Paul trap in a cryogenic environment with only global qubit control [154]. The trap is held at ≈ 8 K in a closed cycle cryostat, where the background pressure is below 1.33×10^{-10} Pa due to differential cryop-

umping. This allows for longer storage lifetimes of large ion chains as compared to System 1. For this reason, System 2 can support larger chains to measure the lowest bound state energy and investigate the two distinct dynamical regimes by increasing the transverse B-field. To take the anharmonicity of the trap into account, we measure all the transverse motional modes of the ion chain. The transverse motional frequencies are set to $\nu^x_{COM} = 4.4$ MHz and $\nu^y_{COM} = 4.3$ MHz, the x-tilt frequency ν^x_{tilt} ranges from 4.37 MHz to 4.38 MHz and the y-tilt frequency ν^y_{tilt} ranges from 4.24 MHz to 4.25 MHz, depending on the number of trapped ions.

B.1.2 Initial state preparation

In both systems, every experiment begins by Doppler cooling a chain of trapped $^{171}\mathrm{Yb}^+$ ions using 369.5 nm light red-detuned from the $^2S_{1/2}$ to $^2P_{1/2}$ transition. The ions are initialized to the $|\downarrow\rangle_z$ qubit state, defined as the $^2S_{1/2}\,|F = 0, m_F = 0\rangle$ hyperfine level, by an incoherent optical pumping process. Optical pumping lasts approximately 20 μs and initializes all ions to $|\downarrow\rangle_z$ with at least 99 % fidelity. Next, the ions are cooled to their motional ground state (≤ 0.1 average motional quanta for the COM mode) with Raman sideband cooling.

Once the spins are cooled and initialized, we can prepare them in product states along any axis of the Bloch sphere by applying global rotation pulses. System 1 has the ability to manipulate spins with an individual addressing beam focused to a waist of 500 nm, 3 to 4 times smaller than the typical inter-ion spacing in System 1. This beam applies a fourth-order AC Stark shift to the qubit splitting [34], causing

an effective σ_i^z rotation on a single spin i. This rotation can be mapped to a rotation about any axis with global $\pi/2$-pulses, which allows preparation of product states with arbitrary spin flips.

B.1.3 State detection

Following an experiment, we measure each spin's magnetization using spin-dependent fluorescence imaged onto an Andor iXon Ultra 897 EMCCD camera. A 369.5 nm laser resonant with the $^2S_{1/2}\,|F=1\rangle$ to $^2P_{1/2}\,|F=0\rangle$ transition (linewidth $\gamma/2\pi \approx 19.6$ MHz) causes photons to scatter off each ion if the qubit is projected to the $|\uparrow\rangle_z$ state. Conversely, ions projected to the $|\downarrow\rangle_z$ qubit state scatter a negligible number of photons because the laser is detuned from resonance by the $^2S_{1/2}$ hyperfine splitting. By applying global $\pi/2$-pulses, we rotate the x and y bases into the z basis. This allows us to measure all individual magnetizations and many-body correlators along any single axis.

Both systems collect scattered 369.5 nm photons using a finite conjugate 0.4 NA objective lens system with total magnification of 70x for System 1 and 90x for System 2. Before taking data, high-contrast calibration images of the ion chain, illuminated by Doppler cooling light, are used to identify a region of interest (ROI) on the camera sensor for each ion. System 2 may take multiple calibration images in between experiments to account for slow drifts of the ions' positions. During data collection, System 1 (2) integrates collected fluorescence for 0.65 (1.0) ms, after which a pre-calibrated binary threshold is applied to discriminate the qubit state

of each ion with approximately 97 % accuracy per ion. The dominant detection error sources are: off-resonant mixing of qubit states during the detection period, cross-talk between ion ROIs due to small inter-ion spacings near the center of the chain, electronic camera noise, and laser power fluctuations. We do not perform any post-processing, including state preparation and measurement correction, on the data presented in this work. Specific product citations are for the purpose of clarification only, and are not an endorsement by the authors or NIST.

B.1.4 Generating the Ising Hamiltonian

We generate spin-spin interactions by applying spin-dependent dipole forces with a pair of non-copropagating 355 nm Raman beams for which the beatnote wavevector, Δk, is aligned along the transverse motional modes of the ion chain. These two beams are controlled with acousto-optic modulators that generate a pair of beat note frequencies $\nu_0 \pm \mu$ for the Mølmer Sørensen (MS) scheme [33], where μ is the frequency detuning from the COM motional mode. In the Lamb-Dicke regime [452], the laser-ion interaction gives rise to an effective spin-spin Hamiltonian where the coupling between spins i and j is:

$$J_{i,j} = \Omega^2 \nu_R \sum_m \frac{b_{i,m} b_{j,m}}{\mu^2 - \nu_m^2} \approx \frac{J_0}{|i-j|^\alpha} \tag{B.1}$$

where Ω is the resonant Rabi frequency coupling the two qubit states, $\nu_R = \hbar \Delta k^2/(2M)$ is the recoil frequency, ν_m is the frequency of the m-th motional mode, b_{im} is the eigenvector matrix element of the i-th ion's participation in the m-th motional mode

$(\sum_i |b_{im}|^2 = \sum_m |b_{im}|^2 = 1)$, and M is the mass of a single ion.

Unlike System 1, where Δk is aligned along one set of transverse motional modes, System 2 couples to both sets of transverse motional modes as the Raman beams project onto the two radial principal axes of the trap. While coupling to these additional modes creates the same Hamiltonian, Eq. (3.1) as System 1, the coupling strengths between ions differ. To account for this, Eq. (B.1) can be generalized to:

$$J_{i,j} = J^x_{i,j} + J^y_{i,j} \tag{B.2}$$

$$J^\beta_{i,j} = \Omega^2_\beta \nu^\beta_R \sum_m \frac{b^\beta_{i,m} b^\beta_{j,m}}{\mu^2 - (\nu^\beta)^2}, \quad \beta = x, y \tag{B.3}$$

where ν^β_R is the recoil frequency given by the β projection of Δk (Δk^x and Δk^y). Both experiments work in the MS regime where the beatnote frequencies are detuned by μ far from all the motional sidebands, $|\mu - \nu_m| \gg \eta\Omega$, where η is the Lamb-Dicke parameter, to suppress phonon production via virtually coupling spins to motion.

The approximate power law exponent, α, in Eq. (B.1) theoretically can be tuned within the range $0 < \alpha < 3$. However, in practice, we are restricted to $0.5 < \alpha < 1.8$ to avoid motional decoherence and to maintain sufficiently large interaction strengths. Therefore, in this work, we are in the regime where all excitations within the two-domain-wall model are bounded, where $\alpha < 2$ (see Methods 1.5 for details). In the reported experiments, the power-law exponent is $\alpha = 1.1$ with $J_0/2\pi$ ranging from 0.45 kHz to 0.66 kHz for System 1. System 2 operates in the regime with α between 0.8 and 1 with $J_0/2\pi$ ranging from 0.23 kHz to 0.42 kHz.

We apply a global offset to the two Raman lasers by $2B_z$, creating a rotating frame shift between the qubit and the Raman beatnote to generate an effective transverse magnetic field B_z. We limit the effective transverse B-field to $B \ll \eta\Omega_{COM} \ll \delta_{COM}$, where $\eta\Omega_{COM}$ is the COM sideband Rabi frequency and δ_{COM} is the beatnote's detuning from the transverse COM mode.

These trapped-ion quantum simulators natively realize an antiferromagnetic Ising model. All measured observables $O(t)$ of the evolution are real and symmetric under time-reversal. This implies the measured observables of Hamiltonians H and -H are the same. Therefore, the expectation values we obtain from $J_{i,j} > 0$ and $B > 0$ are identical to $J_{i,j} < 0$ and $B < 0$. For this reason, we can simulate the dynamics of a ferromagnetic system [73].

B.1.5 Two-domain-wall model

Previous experimental and theoretical studies [82,132] have found that the low-energy excitations of confinement Hamiltonians, such as Eq. (3.1), largely consist of states containing zero or two domain walls. By restricting the Hilbert space to include only these states, we can build a relatively simple phenomenological model that mimics the low-energy behavior of the system. Liu et al. describe such a 'two-kink model' for a ferromagnetic long-range transverse field Ising chain with closed boundary conditions and $B < J_0$ in Reference 11, which we will summarize here.

The Hilbert space of this model contains states with two down-aligned domains surrounding an up-aligned domain of length l. These domains are separated by two

domain walls: one between spin positions $j-1$ and j and another between positions $j+l-1$ and $j+l$. Such a state $|j,l\rangle$ has the form

$$|j,l\rangle = |\downarrow_1 \ldots \downarrow\downarrow_{j-1}\uparrow_j\uparrow \ldots \uparrow\uparrow_{j+l-1}\downarrow_{j+l}\downarrow \ldots \downarrow\rangle\,. \tag{B.4}$$

The Hamiltonian for this set of basis states is given by Eq. (2) in Reference 11. For a translational invariant system, it is useful to transform to a set of quasi-momentum basis states $|k,l\rangle = (1/L)\sum_{j=1}^{L}\exp(-ikj - ikl/2)\,|j,l\rangle$. We now write the Hamiltonian as

$$\begin{aligned} H = \sum_{k,l} V(l)\,|k,l\rangle\langle k,l| - 2B\cos\left(\frac{k}{2}\right)|k,l\rangle\langle k,l+1| \\ - 2B\cos\left(\frac{k}{2}\right)|k,l\rangle\langle k,l-1|\,. \end{aligned} \tag{B.5}$$

Both terms involving the transverse field B describe the effective kinetic energy of the domain walls with quasimomentum k. The potential $V(l)$ depends on the interaction strengths $J_{i,j}$ in the system

$$V(l) = -\sum_{i<j}^{L} J_{i,j}\,s_i(\mathcal{S})s_j(\mathcal{S}) \tag{B.6}$$

where $s_i(\mathcal{S}) = \pm 1$ is the value of the spin at site i corresponding to the configuration $\mathcal{S}$ with domain of length l. This Hamiltonian can be diagonalized to reveal the presence of energy bands in the low-energy spectrum (inset of Fig. 3.3(e)). These bands represent domain wall states bounded by the potential $V(l)$. For $\alpha < 2$ this potential is unbounded and all domain wall pairs will be confined into quasiparticles.

The trapped-ion spin system is finite with open boundary conditions. Boundary effects [453] are minimized in this experiment because the center-to-center spin interaction strength is much stronger than the center-to-edge interaction strength. To minimize deviations from this model due to finite-size effects, we consider only those states with short, up-aligned domains ($l \ll L$) centered in the spin chain. With this constraint, we find good agreement between exact diagonalization ($L \leq 21$), the two-domain-wall model, and experimental results. The two-domain-wall model numerics for this experiment are implemented by taking the experimental $J_{i,j}$ matrix to calculate the energy gaps for each experiment. We first extract a vector of interaction parameters from the experimental interaction matrix, $J_{k,j}$, by fixing the site k to be the center ion for each ion chain length. Then, we virtually place the ions on a ring and impose a periodic boundary condition by requiring the Ising interaction to be translationally invariant, i.e. $J_{l,m} = J_{k,k+m-l}$. Using this method, we obtain the spectrum of energy bands and energy gaps for the trapped-ion system by diagonalizing Eq. (B.5) (Fig. 3.3(e)).

The two-domain-wall model focuses on the potential due to the separation between domain walls, which is largely independent of the center position of the bound domain wall pair. We expect some dispersion in the domain wall pair position due to hopping throughout the spin chain. However, the strength of this hopping is much smaller than the strength of the confining potential. For example, the hopping strength for the initial state with 1 domain size is on the order of $B^2/\Delta E_{1,2} = 0.11 J_0$, which corresponds to ≈ 65 Hz in the lab. We expect that this effect can be observed at a timescale (> 15 ms) which is beyond the coherence time of these

experiments. Therefore, the domain wall pairs are expected to be effectively pinned at their original positions over the experimental time, and we do not observe any effects of moving domain walls pairs in the data. Instead, we observe local coherent oscillations between different bands of bound states.

B.1.6 Energy levels of bound states

The initial state $|n\rangle$ can be written as a superposition of post-quench eigenstates $|s\rangle$

$$|n\rangle = \sum_s c_{ns} |s\rangle \tag{B.7}$$

where c_{ns} is the overlap of $|s\rangle$ with the initial state $|n\rangle$. Thus, any observable M as a function of time is

$$\langle M(t)\rangle = \sum_{ss'} c_{ns} c^*_{ns'} e^{-i(E_s - E'_s)} \langle s'| M |s\rangle \tag{B.8}$$

where E_s is the energy of state $|s\rangle$. Therefore, $\langle M(t)\rangle$ exhibits oscillation frequencies corresponding to multiple bound-state energy differences, $\Delta E_{s,s'} = E_s - E_{s'}$ with different amplitudes, depending on the initial state. In the experiment, we prepare initial states that overlap closely with low-energy eigenstates of the confinement Hamiltonian in Eq. (3.1) and choose to observe spins on the outer boundaries of the domain walls. This allows us to maximize the matrix elements ($\langle s'| M |s\rangle$) which couple the lower-energy bound state i to the adjacent higher-energy bound state $i+1$. Therefore, the oscillation frequencies that we observe in Fig. 3.3 represent

$\Delta E_{i,i+1}$. Due to the limited coherence time of the system, we cannot resolve the Fourier spectrum of the dynamics, especially for $\Delta E_{2,3}$, to extract the bound-state energy differences. Instead, we fit these frequencies to an exponentially-decaying sine function. The error bars are the standard errors of these fits (Fig. 3.3(d)-(f)). This fitting choice works well because we maximize the signal for $\Delta E_{i,i+1}$. $\Delta E_{i,i+1}$ also decreases as the energy level i increases (inset of Fig. 3.3(e)). Using this knowledge, we can measure $\Delta E_{i,i+1}$ starting from the lowest energy initial state (all x-polarized) to the higher energy initial state (two domain walls with domain size of two). Then, we take a suitable single frequency as a guess value in fitting the quench dynamics. The guess value is chosen such that it is the next lowest frequency from the oscillation frequency measured in the lower energy initial state. In the end, this method yields results that match closely with the two-domain-wall model and numerics calculated by solving the Schrödinger equation. For a complete picture, the Fourier-transformed experimental data is also shown in this Appendix.

B.1.7 Domain wall convergence at high transverse B-field

In this domain wall investigation, we use the following Bloch sphere mapping: $z \leftrightarrow x$. The orientation of the ith spin in the Bloch sphere is defined as $|\psi_i(t)\rangle = \cos\theta(t)/2\,|0\rangle + e^{i\phi}\sin\theta(t)/2\,|1\rangle$. Let $|\psi\rangle = |\psi_i(t)\rangle \otimes |\psi_{i+1}(t)\rangle$ since we are interested in a two-body correlator for $\langle\mathcal{N}\rangle$. At high transverse B-field, global Larmor precession about the transverse direction dominates over the Ising interaction term in (3.1). The expectation value of the two-body correlator along z is $\langle\sigma_i^z(t)\sigma_{i+1}^z(t)\rangle = 1 -$

$\sin^2(\theta(t))$. Inserting $\langle \sigma_i^z(t)\sigma_{i+1}^z(t)\rangle$ into Eq. (3.3) gives

$$\langle \mathcal{N} \rangle = \frac{1}{t_2 - t_1} \int_{t_1}^{t_2} \sum_{i}^{L-1} \frac{\sin^2(\theta(t))}{2} dt. \tag{B.9}$$

Therefore, $\langle \mathcal{N} \rangle = 0.25(L-1)$ when $B \gg J_0$. Values of t_1 and t_2 are chosen to include the plateaus of $\langle \mathcal{N} \rangle$ while excluding dephasing of the spins. We fix the scaled integration time $J_0(t_2 - t_1)$, as J_0 differs with system size (Fig. B.1).

We note that the last experiment, data from which is presented in Fig. 3.4, bears resemblance with a previous experiment published by Zhang et al. [18]. Both experiments involve measuring an observable related to a two-spin magnetization correlator and its dependence on the transverse field strength of a quenched Ising Hamiltonian. The two-spin correlator defined in Ref. [18] is expected to be qualitatively similar to the average number of domain walls (Eq. (3.3)).

Several notable aspects distinguish the experiment shown in Fig. 4 from the Ref. [18] project. Each experiment was performed with different scopes and goals. The goal of Ref. [18], performed in System 1, was to identify the precise critical point of a dynamical phase transition. Meanwhile this experiment, performed in System 2, was designed to contrast the behavior of a spin system deep in the confinement regime ($B \ll J_0$) with behavior deep in the deconfinement regime ($B \ll J_0$), using an observable derived from the confined-quasiparticle picture. The confinement picture provides valuable context for understanding the dynamics observed in each regime.

B.1.8 Error sources

Experimental noise decreases the fidelity of any quantum simulation. All the possible sources of error described here are consistently present in the experiment. However, the effects of certain noise sources are different depending on the observable.

One significant error is 'bit-flip error', which we attribute to two main sources. One source is spin-motion entanglement due to off-resonant excitation of the ion chain's motional modes [454] in the MS regime, where both quantum simulators operate. Unwanted bit-flip errors occur when spin-entangled motional degrees of freedom are traced out at the end of an experiment. The probability of this error to occur on the ith ion is proportional to $\sum_{m=1}^{N}(\eta_{im}\Omega/\delta_m)^2$, where $\eta_{im} = b_{im}\sqrt{\nu_R/\nu_m}$ and $\delta_m = \mu - \nu_m$ is the beatnote detuning from the mth motional mode [455]. To minimize this error, we choose δ_{COM} such that $(\eta_{COM}\Omega/\delta_{COM})^2 \lesssim 1/9$. Another source of bit-flip error is imperfect state detection. These two sources of bit-flip error are independent, and therefore add in quadrature. This error affects the observable $\langle\mathcal{N}\rangle$ significantly because it induces error in counting the number of domain walls. We find that, by including the bit-flip error in the $L = 11$ spins numerical calculation for $\langle\mathcal{N}\rangle$, the experimental data agrees well with the error-included numerical calculation at $B/J_0 = 0$, as shown in Fig. B.2. Presently, we are limited to computing this error for $L < 15$ spins. Regarding individual spin magnetization and connected-correlation observables, this 'bit-flip error' will decrease the contrast of the spin magnetization. The qualitative features, as well as oscillation frequencies,

will remain unchanged.

Besides that, slow experimental drifts, involving laser intensity noise at the ions and drifts of the trap frequency (which determines transverse motional modes for generating the Ising interaction), influence the experiment over the course of a few hours during data taking. These fluctuations will cause the system to average over different effective Hamiltonians which can be approximated as ± 10 % fluctuations in the Ising interaction strength, J_0 for numerical predictions. For longer spin chains, this effect is more prominent as $1/J_0$ is on order of experiment sequence duration (see Supplementary Information).

Furthermore, this system has a residual effective linear magnetic field gradient across the ion chains due to the fourth-order AC Stark shift gradient from imperfect overlap of the two Raman laser beams at the ions. This effective magnetic gradient noise is more prominent for small B-fields and is typically < 15 Hz/μm across the ion chain. As a result, there is an effective depolarization of the initial states, which is depicted clearly in the data in Fig. 3.4. However, we find that errors caused by this effective magnetic field gradient are much smaller than those caused by bit-flip errors.

Another source of noise is off-resonant Raman scattering during the quantum quench. This error rate is estimated to be 7×10^{-5} Hz per ion, given typical experimental parameters. Small errors due to RF heating of the transverse COM motional mode are present in System 1. Although System 2 is in a cryogenic setup that is less susceptible to RF heating, it has mechanical vibrations at 41 Hz and 39 Hz due to residual mechanical coupling to the cryostat [154]. This mechanical

vibration noise is equivalent to phase-noise on the Raman beams, which leads to qubit dephasing. Therefore, we integrate the number of domain walls before the dephasing occurs (Fig. 3.4).

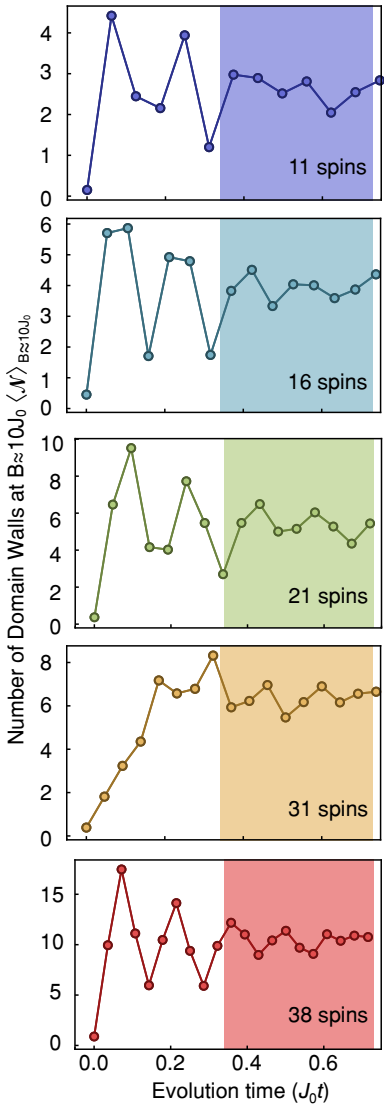

Figure B.1: Evolution of domain wall population. Experimental data of evolution of the number of domain walls $\langle \mathcal{N} \rangle$ during a quench of Hamiltonian (3.1) with $B/J_0 \approx 10$ for multiple system sizes. The shaded area indicates when $\langle \mathcal{N} \rangle$ converges to a steady state and before qubit dephasing occurs.

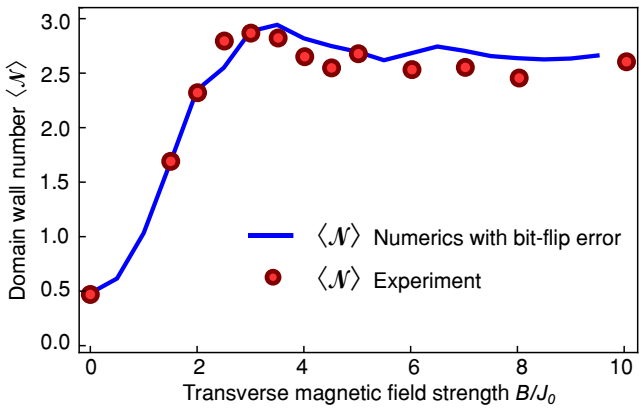

Figure B.2: Bit-flip error numerical study in $L = 11$ chain for dynamical regimes investigation. Red dots show the $L = 11$ data displayed in Fig. 4a. The blue line illustrates the numerical value of $\langle \mathcal{N} \rangle$ with increasing B-field, taking bit-flip error into account. We found that a bit-flip error per ion of 2.47 % in the numerical calculation matches the experimental data well. The most notable effect of bit-flip errors is an increase in the number of domain walls at $B/J_0 = 0$ (see Fig. 3.4(a) for comparison with zero bit-flip error numerics).

B.2 Supplementary Information

B.2.1 Domain wall localization in the confinement regime

In the main text, we claim that slow or negligible spreading of correlations following a quench of the confinement Hamiltonian (3.1) indicates that domain walls are localized at their initial positions. In this section, we extend that argument by measuring the average number of domain walls at each available position of an $L = 11$ spins chain after a quench. The average number of domain walls $\langle N_j(t) \rangle$ at site $j \in \{1, L-1\}$ at time t is given by

$$\langle N_j(t) \rangle = \frac{\langle 1 - \sigma_j^x(t)\sigma_{j+1}^x(t) \rangle}{2}. \tag{B.10}$$

Fig. B.3 shows both experimental measurements and numerics of the evolution of $\langle N_j(t)\rangle$ for six initial states. The first three rows correspond to data shown in Figs. 3.2 and 3.3(a)-(e) and represent states within the two-domain-wall model. In these cases, pairs of domain walls are strongly localized near their initial positions, showing excellent agreement with numerics. The bottom two rows show higher-energy initial states outside of the two-domain-wall regime. The Néel (staggered) state along x is initialized with domain walls at every position, while each site in the z-polarized state is initialized with, on average, one half of a domain wall. These high-energy density states are not expected to show domain wall confinement.

B.2.2 Thermalization

The initial energy of a system in state $|\psi_0\rangle$ immediately following a quench under Hamiltonian H is $E_0 \equiv \langle\psi_0|H|\psi_0\rangle$. In general, such a system will *thermalize* under the evolution of a non-integrable Hamiltonian according to the Eigenstate Thermalization Hypothesis (ETH) [156]. We define a system as thermalized once it has relaxed to a state indistinguishable from a thermal ensemble of eigenstates. To determine whether a system is distinguishable from the thermal ensemble, we compare measured local observables (e.g. individual magnetizations) to their thermal expectation values. Here we consider two appropriate thermal ensembles: the microcanonical ensemble and the canonical (Gibbs) ensemble. We also note that the canonical ensemble is more sensitive to finite size effects than microcanonical and thus we consider both calculations.

We first consider the microcanonical ensemble. The microcanonical thermal expectation value of an observable $\hat{\mathcal{O}}$ is

$$\langle \hat{\mathcal{O}} \rangle_{MC} = \frac{1}{N_s} \sum_{|E_s - E_0| < \Delta} \langle s | \hat{\mathcal{O}} | s \rangle \tag{B.11}$$

where $|s\rangle$ is an eigenstate of Hamiltonian (3.1) with energy E_s, which is found in a window of width 2Δ, containing N_s states, centered around E_0. We choose Δ such that this window contains about $N_s = 50$ eigenstates with energies close to E_0. Given these parameters, we calculate microcanonical thermal expectation values of individual magnetizations for the initial states $|\downarrow\downarrow\downarrow\downarrow\downarrow\downarrow\downarrow\downarrow\downarrow\downarrow\downarrow\rangle_x$, $|\downarrow\downarrow\downarrow\downarrow\uparrow\uparrow\downarrow\downarrow\downarrow\downarrow\downarrow\rangle_x$, and $|\downarrow\downarrow\downarrow\downarrow\downarrow\downarrow\downarrow\downarrow\downarrow\downarrow\downarrow\rangle_z$ shown in Fig. 3.2(c), (f), and (i) respectively. Fig. B.4(a) shows the experimental evolution of some individual magnetizations overlayed with their microcanonical thermal expectation values. The microcanonical thermal values of individual x-magnetizations $\langle \sigma_i^x \rangle_{MC}$ of the confined states $|\downarrow\downarrow\downarrow\downarrow\downarrow\downarrow\downarrow\downarrow\downarrow\downarrow\downarrow\rangle_x$ and $|\downarrow\downarrow\downarrow\downarrow\uparrow\uparrow\downarrow\downarrow\downarrow\downarrow\downarrow\rangle_x$ are zero for all spins. The microcanonical thermal values of individual z-magnetizations $\langle \sigma_i^z \rangle_{MC}$ for spins 1, 6, and 11 evolving from state $|\downarrow\downarrow\downarrow\downarrow\downarrow\downarrow\downarrow\downarrow\downarrow\downarrow\downarrow\rangle_z$ are $\{-0.049, -0.057, -0.049\}$.

Next, we consider thermalization to a canonical (Gibbs) thermal ensemble, represented by a density matrix

$$\rho_T \propto e^{-\beta H} \tag{B.12}$$

where β is the effective inverse temperature of the system. Assuming the Hamilto-

nian is conserved, the system's energy must remain constant throughout the evolution. It follows that the initial energy E_0 equals the thermal value predicted by the canonical ensemble

$$E_0 = \frac{\mathrm{Tr}(H\rho_T)}{\mathrm{Tr}(\rho_T)} = \frac{\mathrm{Tr}(He^{-\beta H})}{\mathrm{Tr}(e^{-\beta H})}. \tag{B.13}$$

This relationship fixes the value of β based on the initial state of the system.

For small system sizes (e.g. $L = 11$), we can exactly diagonalize Hamiltonian (3.1) and calculate the canonical thermal density matrix ρ_T corresponding to the initial states prepared in Fig. 3.2. With this, we may calculate the canonical thermal expectation values of various local observables

$$\langle \hat{\mathcal{O}} \rangle_T = \mathrm{Tr}(\hat{\mathcal{O}}\rho_T) \tag{B.14}$$

By numerically solving Eq. (B.13), we find effective inverse temperatures of $J_0\beta = \{0.666, 0.214, 0.233\}$ for initial states $|\downarrow\downarrow\downarrow\downarrow\downarrow\downarrow\downarrow\downarrow\downarrow\downarrow\downarrow\rangle_x$, $|\downarrow\downarrow\downarrow\downarrow\uparrow\uparrow\downarrow\downarrow\downarrow\downarrow\downarrow\rangle_x$, and $|\downarrow\downarrow\downarrow\downarrow\downarrow\downarrow\downarrow\downarrow\downarrow\downarrow\downarrow\rangle_z$ shown in Fig. 3.2(c), (f), and (i) respectively. Fig. B.4(b) shows the experimental evolution of some individual magnetizations overlayed with their canonical thermal expectation values. The canonical thermal values of individual x-magnetizations $\langle \sigma_i^x \rangle_T$ of the confined states $|\downarrow\downarrow\downarrow\downarrow\downarrow\downarrow\downarrow\downarrow\downarrow\downarrow\downarrow\rangle_x$ and $|\downarrow\downarrow\downarrow\downarrow\uparrow\uparrow\downarrow\downarrow\downarrow\downarrow\downarrow\rangle_x$ are zero for all spins. The canonical thermal values of individual z-magnetizations $\langle \sigma_i^z \rangle_T$ for spins 1, 6, and 11 evolving from state $|\downarrow\downarrow\downarrow\downarrow\downarrow\downarrow\downarrow\downarrow\downarrow\downarrow\downarrow\rangle_z$ are $\{-0.164, -0.154, -0.164\}$.

Both thermal ensemble calculations yield consistent results. It is clear that the experimental magnetizations of the confined initial states (Fig. 3.2(c) and (f))

remain distinct from their canonical and microcanonical thermal values throughout the evolution. On the other hand, for the unconfined initial state (Fig. 3.2(i)), each spin relaxes to or begins oscillating about its thermal expectation value by $J_0 t \sim 1$, after which the system is indistinguishable from either thermal ensemble. From these observations, we claim that the two confined states exhibit slow thermalization compared to the unconfined state's fast thermalization.

B.2.3 Data analysis of bound-state energy differences, $\Delta E_{i,i+1}$

Fourier transformation is a useful tool to determine bound-state energy differences, as shown as in Ref. [132]. The experimental Fourier-transformed data can be fitted to a Lorentzian function to extract the bound-state energy differences. Most of the measured bound-state energies match well with the numerical results (Fig. B.5 (a), (b), and Fig. B.6), except for initial states with domain size of two as the resolution of the Fourier spectrum is limited by the finite coherence time of the system (Fig. B.5(c)). Therefore, we use an exponentially-decaying sine fit in the main text for the bound-state energies for data analysis consistency. Here, we show the Fourier transform analysis of the data in Fig. 2.3. In the bound-state energies investigation of the 11 spins (Fig. B.5), the Lorentzian fits of the experimental Fourier spectrum match well (except for Fig. B.5(c)) with the numerics by solving the Schrödinger equation and the two-domain-wall model. The bound-state energy differences can be extracted by choosing the frequency which is the closest, but lower, to the previous bound-state energy difference as shown in the set of Fig. 2.3(e), with the energy

spectrum of low energy excitations. However, for Fig. B.5(c), the Lorentzian fit (the green band) does not provide a good prediction due to the low resolution of the Fourier spectrum. Furthermore, based on the results of the Fourier transform of the dynamics of the zero domain size state with varying system size (Fig. 2.3(f)), $\Delta E_{0,1}$ lies within the confidence band predicted by the two-domain-wall model (Fig. B.7).

B.2.4 Scaling of the experiment

We perform quantum simulations with up to 38 spins, as shown in Fig. 2.3(f) and Fig. 2.4. We are currently limited to this system size due to non-fundamental technical constraints in the imaging setup, which can be overcome by redesigning the ion imaging optical path or by using a camera with more pixels.

The effective spin-spin Hamiltonian that gives rise to the interactions (Eq. (B.1)) in a trapped-ions quantum simulator depends on experimentally tunable parameters. These parameters include: laser power, laser detuning from motional mode frequencies (δ), and inter-ion spacing, which is set by the axial trap frequency. As we scale up the system size, we adjust these parameters to keep $\alpha \approx 1$ while maintaining a linear ion chain, which decreases the average interaction strength J_0. We can continue scaling up until $1/J_0$ approaches the coherence time of the system. A lower J_0 also leaves the system more vulnerable to various system drifts (see Methods). In principle, this can be solved by increasing the laser power. In the experiment however, we are limited by commercially available laser power. To establish a maximum system size under this limitation, we numerically calculate the

interaction matrix, $J_{i,j}$ with Eq (B.1) and (B.2) with the assumption that the ions are trapped in a harmonic potential (Fig. B.5). With constant laser power, constant δ, and while relaxing the axial trap frequency as necessary, we could maintain $\alpha \approx 1$ by allowing J_0 to decrease as we scale up. Based on the numerics of the interaction matrix, we still have $\alpha \approx 1$ and a reasonable J_0 strength with 250 ions.

For such large system sizes, we must consider how the system energy scales with system size. Specifically, the long-range interaction energy in Hamiltonian (3.1) diverges with system size L when the power-law exponent α is less than the system dimensionality. To counter this unphysical behaviour and to establish a scalable thermodynamic limit for this long-range interacting system such as this, one could renormalize the coupling matrix $J_{i,j}$ according to the Kac prescription [18,456]. This definition would allow the interaction energy to scale extensively with system size.

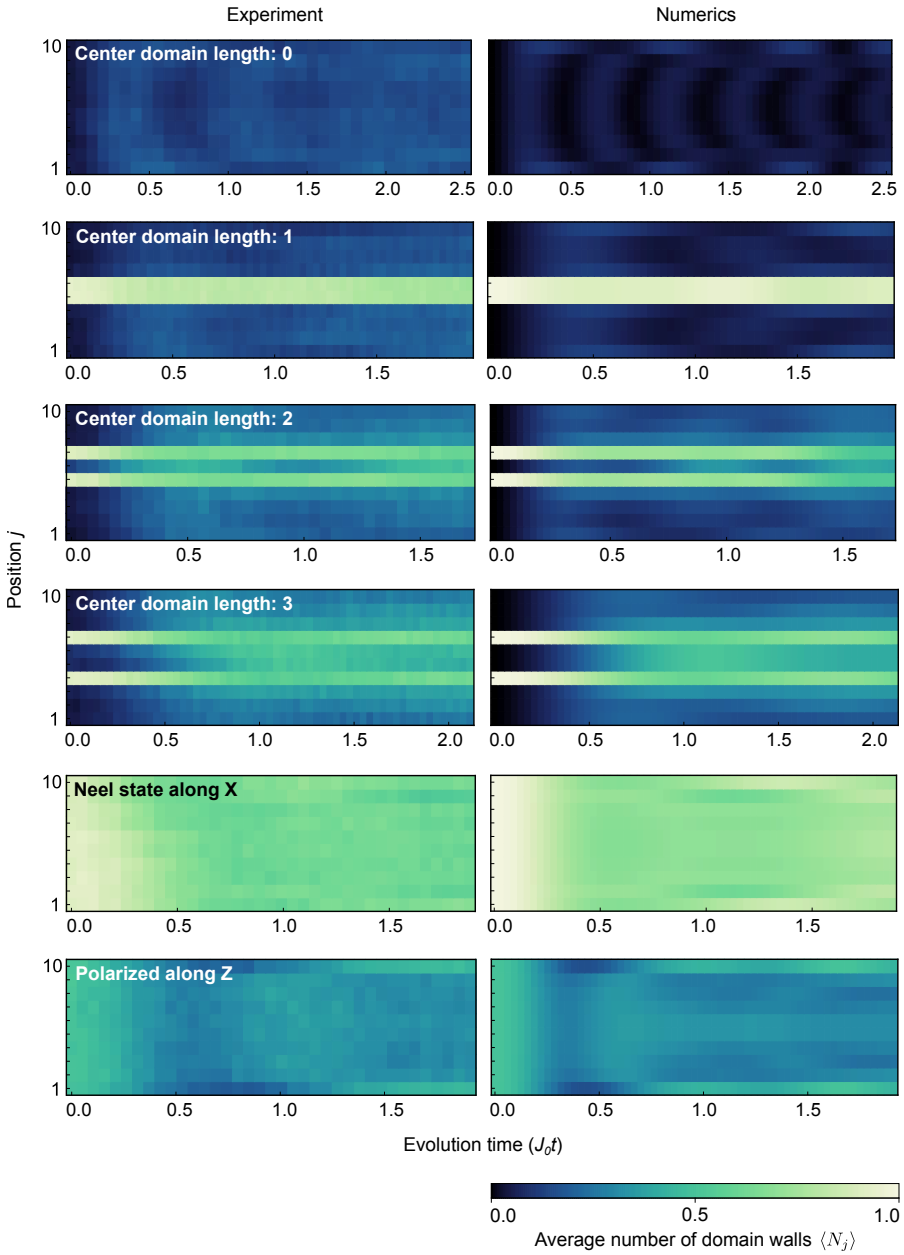

Figure B.3: Domain wall localization under a confinement Hamiltonian quench. Evolution of the average number of domain walls $\langle N_j(t) \rangle$ (Eq. (B.10)) for six $L = 11$ initial states, each following a quench of the confinement Hamiltonian (Eq. 3.1) with $B/J_0 \approx 0.75$. The left column shows experimental data averaged over 2000 experiments and the right column shows numerics calculated by solving the Schrödinger equation. Domain wall pairs are prepared by flipping the initial polarization of a central domain of spins. The Néel state is prepared by flipping the initial magnetization of spins at even-numbered positions.

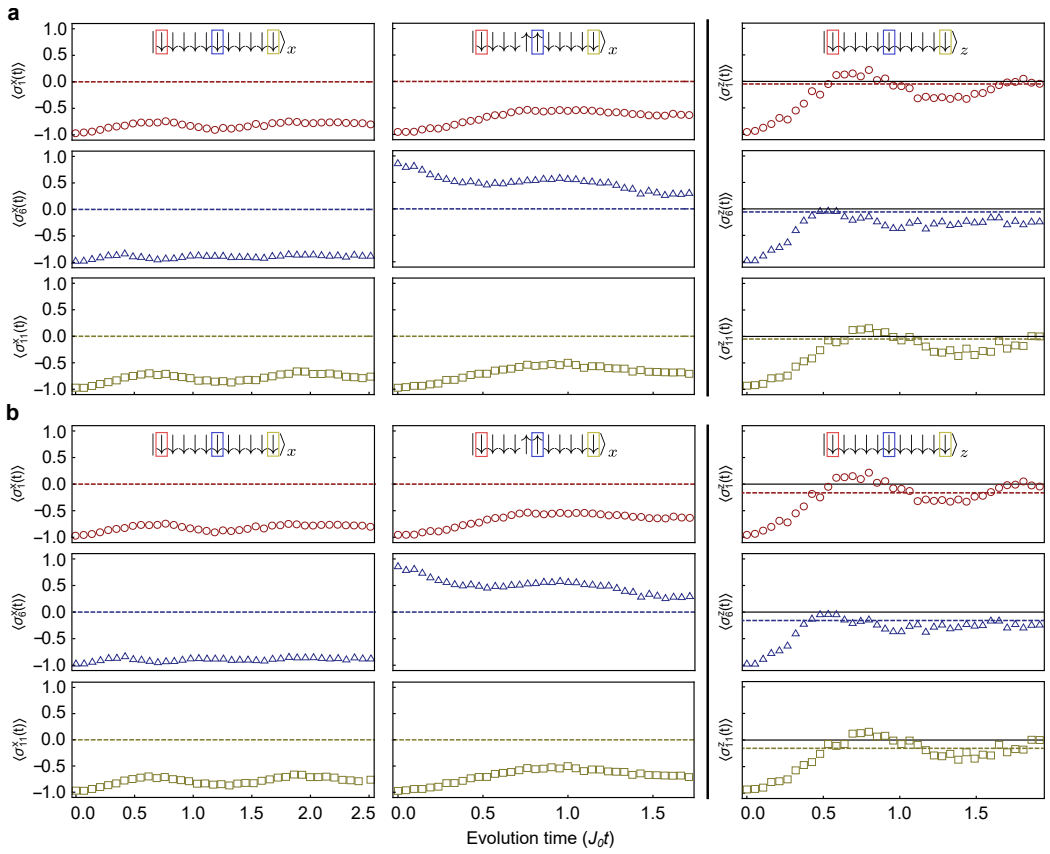

Figure B.4: Magnetization relaxation compared with thermal values. Evolution of individual magnetizations of spins 1, 6, and 11 overlayed with corresponding thermal expectation values calculated from (a) a microcanonical ensemble and (b) a canonical ensemble. Dashed lines indicate the thermal expectation value of each spin, calculated from a thermal ensemble. Left: Initial state is polarized along the x-axis of the Bloch sphere. Thermal expectation values are zero for all spins. Center: Initial state is polarized along the x-axis of the Bloch sphere with center domain of two spins. Thermal expectation values are zero for all spins. Right: Initial state is polarized along the z-axis of the Bloch sphere. Microcanonical thermal expectation values for spins 1, 6, and 11 are $\{-0.049, -0.057, -0.049\}$. Canonical thermal expectation values for spins 1, 6, and 11 are $\{-0.164, -0.154, -0.164\}$. All data points are averaged over 400 experiments. Statistical error bars, $\pm$1s.d., are smaller than their plot markers and are not shown.

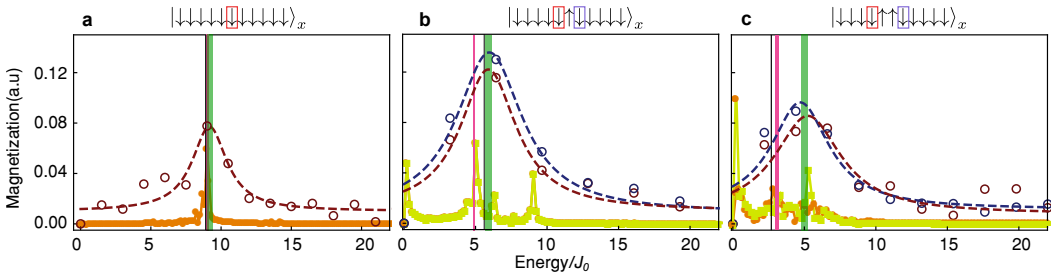

Figure B.5: Fourier-transformed spectrum of the bound-state energies with three different initial center-domain-size states in the $L = 11$ spin chain. The top row represents the initial state before the quantum quench. The dashed colored lines show the Fourier transform of the experimental data corresponding to the boxed spin shown in the top row. The black line describes the value predicted by the two-domain-wall model (see Methods). The magenta band shows the bound-state energies from the sine fit of the data along with the errors of the fit. The green band represents the bound-state energies from Lorentzian fits of the Fourier-transformed experimental data along with the errors of the fits. The orange and yellow lines are the Fourier transform of theoretical calculations of dynamics by solving the Schrödinger equation for the corresponding labelled spins of each initial state.

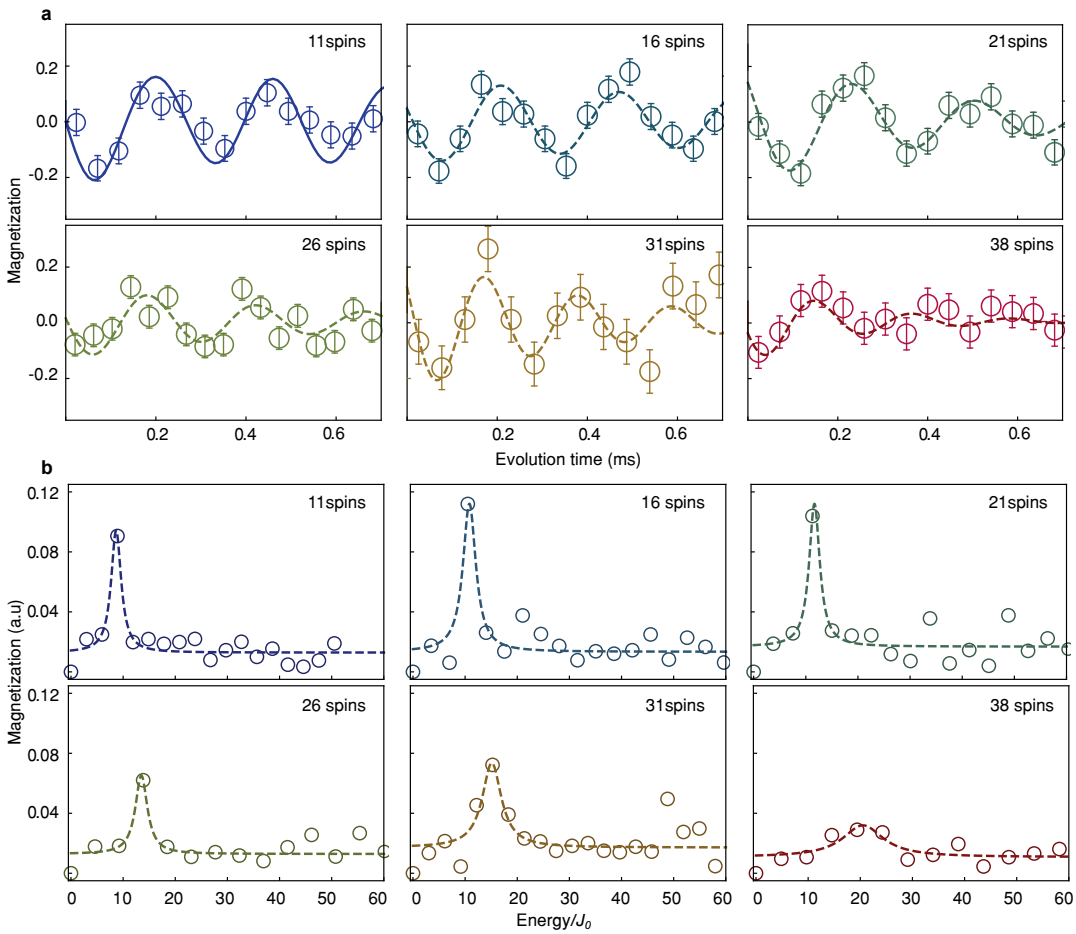

Figure B.6: $\Delta E_{0,1}/J_0$ of all system sizes L at $B/J_0 \approx 1$. Circular dots indicate experimental data. a, shows the magnetization evolution of the center spin in a zero domain size initial state of various size L, measured in the y-basis. Solid blue line represents theoretical calculations of dynamics by solving the Schrödinger equation for the center spin of the $L = 11$ spin chain. Dashed colored lines show best fit curves of an exponentially-decaying sine function for $L = 16$ through $L = 38$. The oscillation frequencies are extracted from the fit and are normalized to each respective J_0 to obtain $\Delta E_{0,1}/J_0$. The error bars, $\pm$1s.d., are calculated from the standard deviation of the mean with > 150 experiments per point. b, Fourier-transformed experimental results from a. Each $\Delta E_{0,1}/J_0$ of the different system size is extracted using a Lorentzian fit.

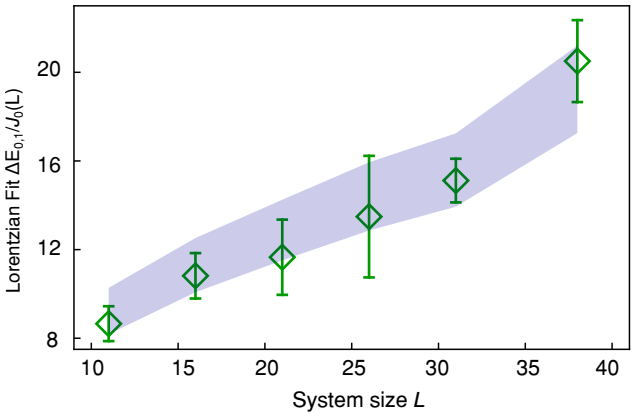

Figure B.7: $\Delta E_{0,1}/J_0$ extracted from Lorentzian fit in different system sizes L. Diamond markers show $\Delta E_{0,1}/J_0$ for each system size with errors bars from the fit (See Fig. S4). The blue band shows the two-domain-wall model (Methods) numerical prediction of $\Delta E_{0,1}/J_0$, with a confidence band considering ± 10 % fluctuations in the Ising interaction strength J_0.

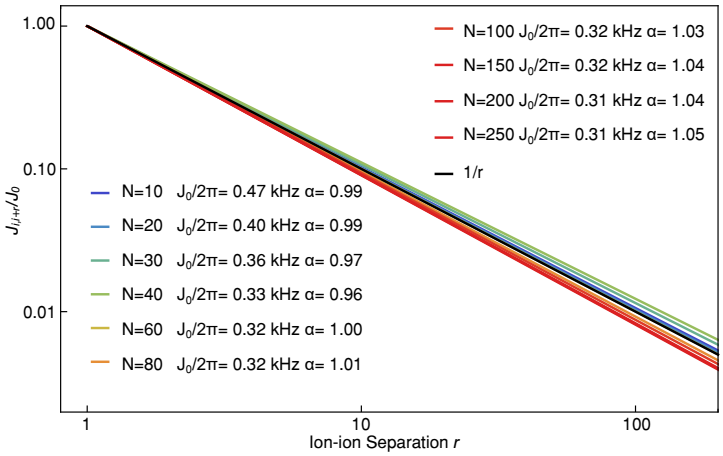

Figure B.8: Log-log plot of spin-spin interactions with system size L. Colored lines represent the normalized average interaction couplings between spin i and j, $r = |i-j|$, $J_{i,i+r}/J_0$. Interactions are numerically calculated using fixed laser power, $\delta/2\pi = 45$ kHz, and with the assumption that ions are trapped in a harmonic potential. J_0 and α for different system sizes N are labelled with their corresponding colors. The black line shows $1/r$ scaling.

Appendix C: Appendices to Chapter 5

C.1 Counting of frozen states

In this section, we prove that Hamiltonian (5.1) harbors exponentially many exactly frozen eigenstates in its spectrum. The proof follows from an inductive method analogous to ref. [202]. Starting from $L = 4$, it is easy to enumerate explicitly that there are 12 frozen states. Suppose we have a frozen state of size L and we would like to increase its size by one, going from L to $L + 1$, such that the longer chain remains frozen. Since the kinetic term in Hamiltonian (5.1) involves at most four spins, the new dynamics introduced by the added spin only depends on the last three spins close to the edge of the original chain. For example, if the last three spins of the original chain are 000, then the added spin can be either 0 or 1, and the new state of size $L + 1$ remains frozen. However, if the last three spins are 001 instead, the added spin must be 1 otherwise the new state becomes active. It is straightforward to enumerate all $2^3 = 8$ possibilities of the last three spins' configurations and the allowed state(s) of the added spin, which we list below:

spin configuration of the last three sites of system size L	added spin state can be
000	0 or 1
001	1
010	1
011	0 or 1
100	0 or 1
101	0
110	0
111	0 or 1

Let $N_{abc}(L)$ be the number of frozen states in a system of size L with spin configurations of the last three sites being abc. Then $N_{abc}(L+1)$ can be obtained from $N_{abc}(L)$ using Table C.1 as following:

$$\begin{pmatrix} N_{000} \\ N_{001} \\ N_{010} \\ N_{011} \\ N_{100} \\ N_{101} \\ N_{110} \\ N_{111} \end{pmatrix}_{L+1} = \begin{pmatrix} 1 & 0 & 0 & 0 & 1 & 0 & 0 & 0 \\ 1 & 0 & 0 & 0 & 1 & 0 & 0 & 0 \\ 0 & 0 & 0 & 0 & 0 & 1 & 0 & 0 \\ 0 & 1 & 0 & 0 & 0 & 0 & 0 & 0 \\ 0 & 0 & 0 & 0 & 0 & 0 & 1 & 0 \\ 0 & 0 & 1 & 0 & 0 & 0 & 0 & 0 \\ 0 & 0 & 0 & 1 & 0 & 0 & 0 & 1 \\ 0 & 0 & 0 & 1 & 0 & 0 & 0 & 1 \end{pmatrix} \begin{pmatrix} N_{000} \\ N_{001} \\ N_{010} \\ N_{011} \\ N_{100} \\ N_{101} \\ N_{110} \\ N_{111} \end{pmatrix}_{L} . \tag{C.1}$$

This matrix can be diagonalized to obtain all of its eigenvalues and eigenvectors, which, combined with the initial value $N_{abc}(4)$, can be used to calculate exactly the number of frozen states at arbitrary L. However, the asymptotic behavior in the

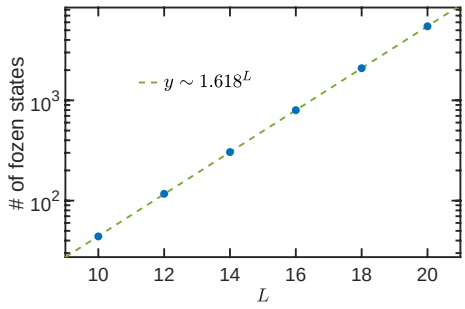

Figure C.1: Scaling of the total number of frozen states as a function of the system size. The result agrees with the scaling form $y \sim 1.618^L$.

large L limit is controlled by the largest eigenvalue of this matrix α, and the number of frozen states goes as $\sim |\alpha|^L$. In this case, we find $\alpha = \frac{1+\sqrt{5}}{2} = \varphi \approx 1.618^L$, which coincides with the asymptotic behavior of the Fibonacci sequence. In Fig. C.1, we check this scaling form numerically and find good agreement.

As explained in the main text, there is indeed an emergent "Fibonacci constraint" in the frozen subspaces, namely, there cannot be two adjacent domain walls. In the present case, there is one exception to this constraint, which is the Néel state $\cdots 010101 \cdots$. Nevertheless, one can see from Eq. (C.1) that N_{010} and N_{101} form an independent block, and hence are not important in the asymptotics. Indeed, we find that the corresponding eigenvector of α has zero amplitude on these two components. Therefore, one can ignore the Néel configurations as far as only the asymptotics are concerned.

C.2 Proof of the existence of "k-magnon state" in each emergent subsector

We point out in the main text that each emergent subsector can be constructed from the k-magnon root state of the following form:

$$0\ \underbrace{\boxed{\text{frozen state}}}_{L-2-2k}\ \underbrace{\boxed{0101\cdots01}}_{2k}\ 0, \tag{C.2}$$

where we append a Néel state of length $2k$ to the right of any magnon-free frozen state. By construction, the two subsystems are both inert by themselves. However, the boundary between the two regions will become active. At the boundary of the two regions, the only possible configurations are $00|0101, 11|0101$, or $10|0101$ (by definition $01|01$ cannot be the boundary), and one can see the in any case the boundary contains mobile magnons.

We now prove that each connected subsector contains a k-magnon root state of this form. In other words, any configuration that is not frozen can be brought to a k-magnon state under Hamiltonian (5.1). We start by showing the following fact in our model: an isolated mobile magnon inserted in the system can tunnel through the entire system. That is to say, there is no "shielding region" that can localize a mobile magnon within a certain spatial region, which is in stark contrast to previously studied spin-1 models with (Q, P) conservation.

Consider a single mobile magnon of the form 0100 or 1011 embedded in the system. Consider the configuration of its two neighboring spins to the right (the left

can be analyzed in a symmetric way). The two neighboring spins can be 01, 10, 00, or 11. Let us inspect what happens after the mobile magnon moves 1 step:

$$
\begin{aligned}
0100 \mid 01 \quad &\rightarrow \quad 0\,\underbrace{010 \mid 0}\,1 \\
01\,\underbrace{00 \mid 10} \quad &\rightarrow \quad 0010 \mid 10 \\
0100 \mid 00 \quad &\rightarrow \quad 0\,\underbrace{010 \mid 0}\,0 \\
0100 \mid 11 \quad &\rightarrow \quad 00\,\underbrace{10 \mid 11},
\end{aligned}
$$

and

$$
\begin{aligned}
10\,\underbrace{11 \mid 01} \quad &\rightarrow \quad 1101 \mid 01 \\
1011 \mid 10 \quad &\rightarrow \quad 1\,\underbrace{101 \mid 1}\,0 \\
1011 \mid 00 \quad &\rightarrow \quad 11\,\underbrace{01 \mid 00} \\
1011 \mid 11 \quad &\rightarrow \quad 1\,\underbrace{101 \mid 1}\,1.
\end{aligned}
\tag{C.3}
$$

In each case above, we denote in brackets the new mobile region that emerges at the boundary of the original mobile region and its neighboring sites. It is thus obvious that, in any case, there will always be new active regions induced by embedding a single mobile magnon into the system. By carrying out the above analysis iteratively, one can demonstrate that this single active magnon can propagate all the way to the right boundary. When the magnon reaches the boundary, since the boundary

spin at the right edge is fixed to be zero, the only possible scenarios are the 2nd and 3rd lines in the above processes. For each of these cases, we can check that it can be brought into the form of a k-magnon state:

$$
\begin{array}{lllllllll}
01001|0 & \to & 00101|0 & & & & & & \\
01000|0 & \to & 00100|0 & \to & 00010|0 & \to & 00001|0 \\
10111|0 & \to & 11011|0 & \to & 11101|0 & & & & \\
10110|0 & \to & 11010|0 & \to & 11001|0 & & & &
\end{array}
$$

Thus, we have shown that the k-magnon state exists in each connected subsector, and each subsector can also be constructed using the k-magnon state as the root configuration.

C.3 Effective Hamiltonian from Schrieffer-Wolff transformation

We analyze the effects of confinement in $H_{\mathbb{Z}_2}$ [Eq. (**??**)] at large h using degenerate perturbation theory in the small parameter λ/h based on the Schrieffer-Wolff (SW) transformation [457, 458]. This is formulated in terms of a unitary transformation

$$H_{\text{eff}} = e^{S}\, H\, e^{-S} = H + [S,H] + \frac{1}{2!}[S,[S,H]] + \frac{1}{3!}[S,[S,[S,H]]] + \cdots = \sum_{n=0}^{\infty} H_{\text{eff}}^{(n)}, \tag{C.4}$$

where the SW generator S is antiunitary and where $H_{\text{eff}}^{(n)}$ is of order $(\lambda/h)^n$. The choice of S is based on the decomposition

$$H = H_0 + V \tag{C.5a}$$

$$H_0 = h \sum_i \sigma_i^z \tag{C.5b}$$

$$V = \lambda \sum_i (\sigma_i^x - \sigma_{i-1}^z \sigma_i^x \sigma_{i+1}^z). \tag{C.5c}$$

In the local z-basis, H_0 is diagonal while V is strictly off-diagonal. In particular, V connects blocks of configurations that differ by a single spin flip, whose energies with respect to H_0 differ by $\sim h$ and whose magnetizations S^z differ by 2. The goal is to choose S such that block-off-diagonal contributions to H_{eff} can be consistently eliminated order by order in λ/h, so that $[H_{\text{eff}}^{(n)}, S^z] = 0$ for each n.

Formally, this can be accomplished by writing

$$S = \sum_{n=1}^{\infty} S^{(n)}, \tag{C.6}$$

where $S^{(n)}$ is of order $(\lambda/h)^n$. Inserting this expression into Eq. (C.4) and grouping terms according to their order in λ/h yields

$$\begin{aligned} H_{\text{eff}} = H_0 + \big([S^{(1)}, H_0] + V\big) + \Big([S^{(2)}, H_0] + [S^{(1)}, V] + \frac{1}{2!}[S^{(1)}, [S^{(1)}, H_0]]\Big) \\ + [S^{(3)}, H_0] + [S^{(2)}, V] + \frac{1}{2!}\left([S^{(1)}, [S^{(1)}, V]] + [S^{(1)}, [S^{(2)}, H_0]] + [S^{(2)}, [S^{(1)}, H_0]]\right) \\ + \frac{1}{3!}[S^{(1)}, [S^{(1)}, [S^{(1)}, H_0]]] + \dots . \end{aligned} \tag{C.7}$$

$S^{(n)}$ is then chosen such that $[S^{(n)}, H_0]$ cancels all block-off-diagonal (i.e., non-S^z-conserving) terms at order n. This strategy is well-defined and straightforward to automate on a computer (see, e.g., Ref. [459]), however it is cumbersome to write out explicitly.

Another (completely equivalent) strategy is to set $S^{(n)} = 0$ for $n \geq 2$ and manually project out non-S^z-conserving terms at each order. $S^{(1)}$ is still chosen to satisfy $[S^{(1)}, H_0] + V = 0$, which is accomplished with the choice

$$\langle\sigma|S^{(1)}|\sigma'\rangle = \frac{\langle\sigma|V|\sigma'\rangle}{\langle\sigma|H_0|\sigma\rangle - \langle\sigma'|H_0|\sigma'\rangle}. \tag{C.8}$$

This gives rise to the leading-order effective Hamiltonian

$$H^{(2)}_{\text{eff}} = \mathcal{P}\left([S^{(1)}, V] + \frac{1}{2!}[S^{(1)}, [S^{(1)}, H_0]]\right)\mathcal{P} \tag{C.9a}$$

$$= \frac{\lambda^2}{h}\sum_i [\sigma^z_{i-1} P_{i-1,i+2}(\sigma^+_i \sigma^-_{i+1} + \text{H.c.}) - \sigma^z_{i-1}\sigma^z_i\sigma^z_{i+1}], \tag{C.9b}$$

where the first line contains the projection operator $\mathcal{P}$ that eliminates non-S^z-conserving processes and the second line is the result quoted in the main text.

This procedure can be straightforwardly extended to higher orders. It is readily seen from substituting Eq. (C.8) into Eq. (C.7) and setting $H^{(n)} = 0$ for $n \geq 2$ that $H^{(3)}_{\text{eff}} = 0$ due to the strictly block-off-diagonal nature of V and hence $S^{(1)}$. (This pattern extends to arbitrary odd orders.) The leading correction to $H^{(2)}_{\text{eff}}$ thus arises

at fourth order and is given by

$$H_{\text{eff}}^{(4)} = \mathcal{P}\left(\frac{1}{3!}[S^{(1)},[S^{(1)},[S^{(1)},V]]] + \frac{1}{4!}[S^{(1)},[S^{(1)},[S^{(1)},[S^{(1)},H_0]]]]\right)\mathcal{P} \tag{C.10a}$$

$$= \frac{\lambda^4}{2h^3}\sum_i \Big\{ \left(\sigma_{i-1}^z + \sigma_{i+3}^z\right)\left[\frac{3}{2} - \frac{5}{4}\left(\sigma_{i-1}^z\sigma_{i+1}^z + \sigma_{i+1}^z\sigma_{i+3}^z\right)\right]\left(\sigma_i^+\sigma_{i+2}^- + \text{H.c.}\right)$$

$$+ \left(\sigma_{i-1}^z + \sigma_{i+4}^z\right)\left(\sigma_i^+\sigma_{i+2}^- + \text{H.c.}\right)\left(\sigma_{i+1}^+\sigma_{i+3}^- + \text{H.c.}\right) \tag{C.10b}$$

$$- \left(\sigma_{i-1}^z + \sigma_{i+4}^z\right)\left(1 - \sigma_{i+1}^z\sigma_{i+2}^z\right)\left(\sigma_i^+\sigma_{i+1}^- + \text{H.c.}\right)\left(\sigma_{i+2}^+\sigma_{i+3}^- + \text{H.c.}\right)\Big\} + \ldots,$$

where ... denotes the omission of subleading corrections to matrix elements induced at second order and diagonal terms (i.e., additional interactions) that do not affect Hilbert space connectivity. The first line of Eq. (C.10b) induces matrix elements for processes like $01100 \leftrightarrow 00110$, while the second line leads to processes like $011000 \leftrightarrow 000110$. The third line allows for correlated hopping of nearby single magnons, i.e. $01010 \leftrightarrow 00101$. We thus see that domain walls separated by two sites become mobile at order $(\lambda/h)^4$, as discussed in the main text and in Appendix C.5 below.

C.4 Numerical results on the effective Hamiltonian $H_{\text{eff}}^{(2)}$

In this section, we present numerical results demonstrating that the key features of Hamiltonian (5.1) discussed in the main text can be reproduced by the effective Hamiltonian $H_{\text{eff}}^{(2)}$.

In Fig. C.2, we reproduce Figs. 5.2 & 5.3 shown in the main text, using $H_{\text{eff}}^{(2)}$ instead. We have set the overal energy scale in front of $H_{\text{eff}}^{(2)}$ to unity. Indeed,

we find good qualitative agreement between Fig. C.2 and those in the main text. In Fig. C.2(a), we again find a broad distribution in the entanglement entropy for eigenstates that are close in energy. The maximal value stays far below the Page value for the given symmetry sector. The entanglement entropy evolution after quantum quenches starting from random product states also saturates only to 70% of the Page value, indicating non-thermal behavior in the long time dynamics under $H^{(2)}_{\text{eff}}$ [Fig. C.2(b)].

We further check that the nonintegrable and integrable (sub)sectors remain the same as Hamiltonian (5.1), despite the slight differences in the sign structure of the kinetic term and the interactions. In Fig. C.2(c), we plot the entanglement entropy of the eigenstates within an emergent subsector. We again find an ETH-like band in the entanglement entropy, with the maximal value close to the subsector-restricted Page value. Moreover, the average energy level spacing ratio gives $\langle r \rangle \approx 0.5272$, which agrees with that of the Gaussian orthogonal ensemble in random matrix theory. This indicates that the same nonintegrable subsector of Hamiltonian (5.1) in the main text remains nonintegrable under $H^{(2)}_{\text{eff}}$. As we have also explained in the main text, when projected to the integrable sectors, $H^{(2)}_{\text{eff}}$ once again reduces to a constrained XXZ model which is integrable. In Fig. C.2(d), we plot the entanglement entropy of eigenstates within an integrable sector of Hamiltonian (5.1). We see that the behavior strongly deviates from that of ETH, and the average energy level spacing ratio yields $\langle r \rangle \approx 0.385$, indicating a Poisson distributed energy spectrum. Therefore, we conclude that the key features of Hamiltonian (5.1) are indeed captured by Hamiltonian (5.3) in the confining limit.

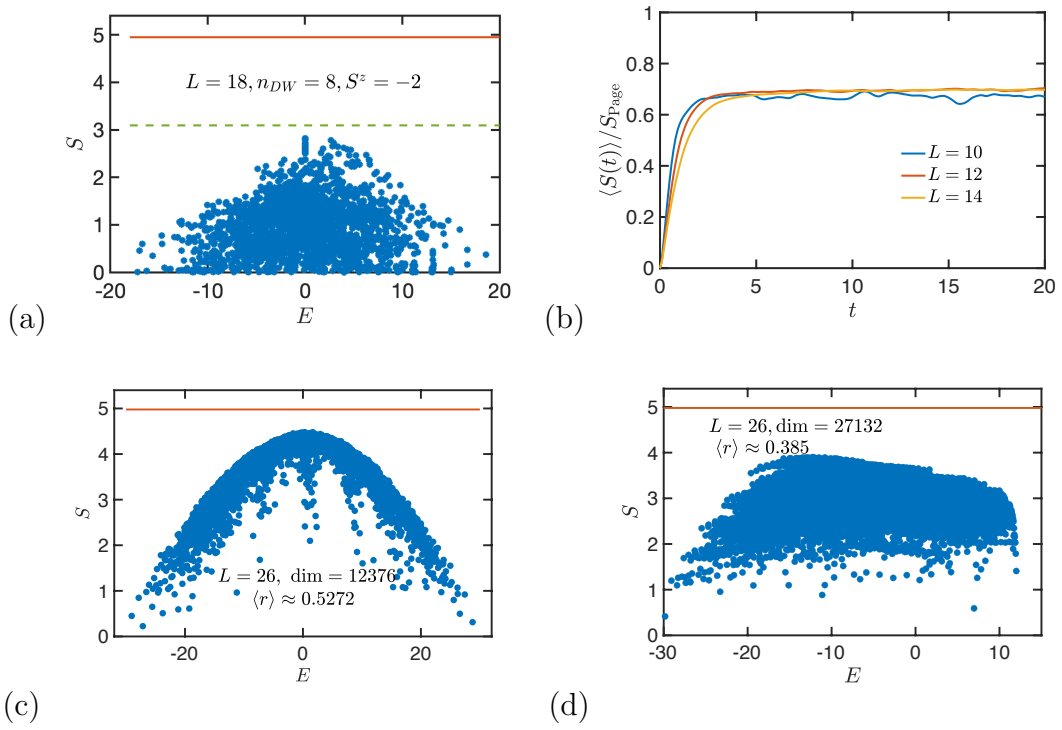

Figure C.2: (a) Entanglement entropy of the eigenstates of $H^{(2)}_{\text{eff}}$ within the sector $(n_{\text{DW}} = 8, S^z = -2)$ under an equi-bipartitioning of the system in the middle. Orange line: Page value of the (n_{DW}, S^z) sector; green line: Page value of the largest connected subsector. (b) Entanglement entropy growth (normalized by the Page value) after a quantum quench starting from random product states, averaged over 200 initial states. (c) Entanglement entropy of eigenstates within an emergent subsector built from the root configuration $0\boxed{111111000000}\boxed{010101010101}0$ for system size $L = 26$. This subsector has dimension 12376 and is nonintegrable. (d) Entanglement entropy of eigenstates within an emergent subsector built from the root configuration $0\boxed{000000000000}\boxed{010101010101}0$ for system size $L = 26$. This subsector has dimension 27132 and is integrable. Orange lines mark the Page value of the corresponding subsector.

C.5 $H^{(4)}_{\text{eff}}$ and "Narayana constraint"

We now briefly examine the Hilbert space structure of the effective Hamiltonian at fourth-order $H^{(4)}_{\text{eff}}$. Under $H^{(4)}_{\text{eff}}$, pairs of domain walls separated by distance two become mobile. We find that there are still exponentially many frozen states in the spectrum. However, other than these frozen states, each (n_{DW}, S^z) sector

becomes fully connected. Therefore, in this case, we no longer have Hilbert space fragmentation. Instead, we now have exponentially many "scar" states with exactly zero entanglement entropy embedded in the spectrum.

One can carry out a similar inductive counting procedure as outlined in the previous section of this Appendix. However, if one is only interested in the asymptotic behavior in the limit of large system size L, one can show that the frozen space subspace satisfies a generalized Fibonacci constraint which we call the "Narayana constraint". Since under $H^{(4)}_{\text{eff}}$, domain walls separated by distance two are no longer frozen, the new constraint now becomes: there cannot be two next-nearest-neighbor domain walls in the frozen subspace. Let us denote a domain wall by $|\bullet\rangle$, and the absence of a domain wall by $|\circ\rangle$. If a frozen configuration of size L has its boundary in state $|\cdots\circ\rangle$, it could have been obtained by appending $\circ$ to any frozen state of size $L-1$. However, if its boundary is in state $|\cdots\bullet\rangle$, it can only be obtained by appending $\circ\circ\bullet$ to a frozen state of size $L-3$. Therefore the Hilbert space dimension of the frozen subspace grows according to $d_L = d_{L-1} + d_{L-3}$, which is known as the Narayana sequence. The asymptotic behavior of this sequence can be obtained from the characteristic polynomial, from which we obtain $d_L \sim 1.466^L$. Numerical verfication of this scaling is shown in Fig. C.3, where we find good agreement.

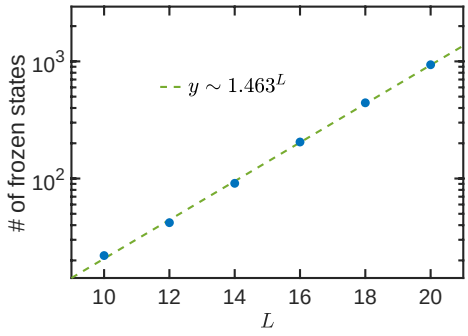

Figure C.3: Scaling of the total number of frozen states in $H_{\text{eff}}^{(4)}$ as a function of the system size. The result agrees with the scaling form $y \sim 1.466^L$.

Appendix D: Appendices to Chapter 6

D.1 Experimental Apparatus

D.1.1 State preparation and readout

Our apparatus has been previously described in [7, 18, 95, 460]. We employ a three-layer Paul trap to confine $^{171}Yb^{+}$ ions in a harmonic pseudopotential with trapping frequencies $f_{x,y} = 4.64$ MHz and either $f_z = 0.51$ MHz ($N = 15$) or 0.35 MHz ($N = 25$). There is a 1-2% day-to-day variation in these frequencies. Pseudospins are encoded in the two clock ground hyperfine states, with $|F = 0, m_F = 0\rangle = |\downarrow_z\rangle$ and $|F = 1, m_F = 0\rangle = |\uparrow_z\rangle$. We drive coherent global rotations between these spin states using stimulated Raman transitions. Long-range spin-spin interactions are generated via a bichromatic beatnote that couples these states via motional modes along the $\hat{x}$ direction. This is generated by three Raman beams from a pulsed 355 nm laser driving a symmetric pair of transitions, with average detunings of $\mu/2\pi = 200$ kHz from the red and blue sideband transitions of the highest frequency (center-of-mass) transverse motional mode along $\hat{x}$. The resulting distribution of $J_{jj'}$ couplings has a best-fit power law of $\alpha = 1.28$ for $N = 15$ and $\alpha = 1.31$ for $N = 25$, and a best-fit $J_0/2\pi$ between 0.25 and 0.33 kHz, depending on day-to-day variations in

laser power. This value of J_0, calibrated for a given day, is used to scale energies and times in the main text.

Each experimental cycle begins with state initialization via optical pumping and Doppler and resolved-sideband cooling, which prepares the spin state $|\downarrow_z\rangle$ with fidelity > 0.99 and the ground motional state with fidelity > 0.9. Arbitrary product states are initialized using the site-dependent AC Stark shift from the individual addressing beam (from the same 355 nm light generating the Ising interactions), combined with overall rotations, with typical preparation fidelities of > 0.9 per spin. Readout is performed via state-dependent fluorescence using the 369.5 nm $|\uparrow_z\rangle \rightarrow {}^2P_{1/2}$ transition collected on a CCD camera, with typical detection errors of 3%. All measurements presented in the main text, except for the DEER measurements, are repeated at each setting 200 times for statistics. For the DEER measurements, we instead average over 2000 repetitions, which are taken alternating between DEER and spin-echo sequences every 100 measurements so that to a very good approximation both sample any noise profile equally. The data presented have not been corrected for state preparation and measurement (SPAM) errors.

D.1.2 Calibration of Hamiltonian parameters

The experimental $J_{jj'}$ matrix is determined by measurements of motional sideband Rabi frequencies and trap parameters. Past work has validated this model against direct measurements of the matrix elements [60].

We directly measure and calibrate the linear field for each spin individually.

As this calibration process is imperfect, each spin has a finite amount of deviation from the ideal linear gradient and thus there is a finite amount of effective site-by-site disorder in the experimental realization, with $\delta\frac{B_j^z}{gj} \approx 0.02$. While a small amount of disorder can be crucial in simulations of Stark MBL with short-ranged interactions, because it breaks the exact degeneracies of that problem [235], in the context of long-range interactions the level statistics are already generic, and this disorder does not have a substantial effect on the system in numerics. As such, we call our system 'disorder-free' in the sense that we only have small, technical and well-understood imperfections limiting our realization of the ideal disorder-free Hamiltonian. Any real quantum simulator can only hope to asymptotically approach a perfectly uniform environment, just as any quantum simulator can only hope to approximately realize MBL because there will always be some residual coupling to the environment that restores ergodicity at sufficiently long times.

D.2 Numerics

Studies of Hamiltonian level statistics with $\langle r \rangle$ use exact diagonalization of the Hamiltonian. For simulations of dynamics we solve the Schroedinger equation using the Krylov space technique [105, 106].

For all numerics, except those shown in the subsequent Methods sections 'Numerical studies of the ideal power-law Hamiltonian' and 'Scaling of $\overline{\mathcal{I}}$ with system size,' we use the experimentally determined $J_{jj'}$ matrix. These couplings show some inhomogeneity across the chain, with the nearest-neighbor hopping varying 7% for

$N = 15$. At large ion-ion separation they also show deviations from power-law behavior, with the couplings falling off faster than the best-fit power law [7]. The comparison to power-law numerics shows that each of these effects does not strongly alter the dynamics.

D.3 Trotterized M-S Hamiltonian

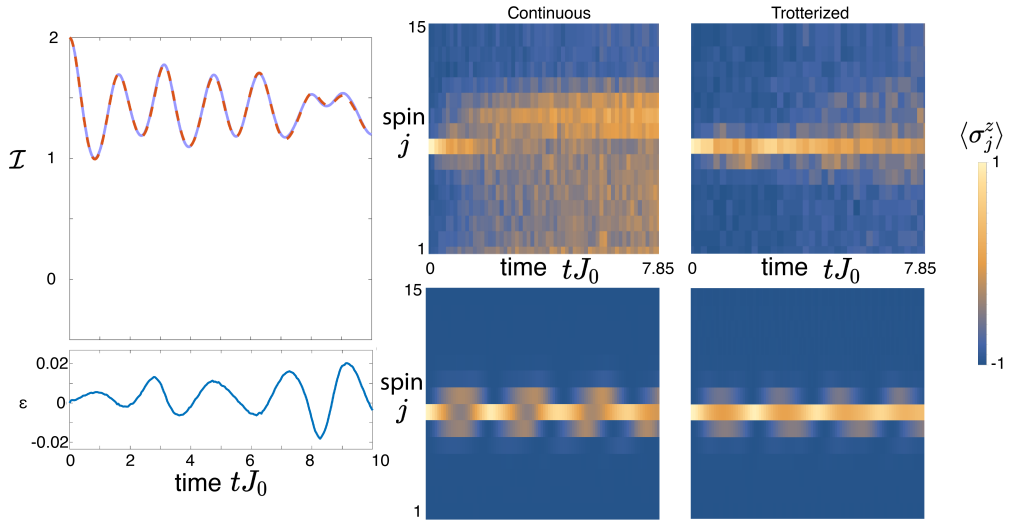

Figure D.1: Trotterization scheme. Left top: Comparison of the imbalance dynamics for the averaged Hamiltonian of Eq. (D.8) (solid blue line) with the full Trotter evolution (dashed orange), for the case of an initial Néel state ($N = 15$) and parameters corresponding to the strongest experimental field gradient. Left bottom: difference (averaged - Trotter), showing the the error over experimental timescales is on the order of one percent. Right: experimental examples (top row) of continuous and Trotterized evolution, both at $g/J_0 = 1.5$, compared to simulations (bottom row) using the (slightly different) parameters of the individual experimental realizations. Although the Trotterized evolution lasts nearly twice as much time in absolute units, since the averaged J_0 is roughly half as large, it nonetheless shows a substantial reduction in decoherence and improvement in fidelity to the desired Hamiltonian. An initial state with one spin flip is chosen for this comparison, as it makes the effect of decoherence due to phonons more pronounced compared with a state near zero net magnetization.

We generate two types of Hamiltonian terms in this work. The first is the Mølmer-Sørensen Hamiltonian in the resolved sideband and Lamb-Dicke limits [7], created with a pair of detuned bichromatic beatnotes:

$$H_1(t) = \sum_{j,\nu} \sigma_j^+ \left[\frac{-i\Omega\eta_\nu b_j^\nu}{2} (a_\nu e^{-i\omega_\nu t} + a_\nu^\dagger e^{i\omega_\nu t}) \right.$$
$$\left. (e^{-i\delta_B t} - e^{-i\delta_R t}) \right] + h.c. \tag{D.1}$$

Here j is the ion index and ν is the normal mode index, a_ν is the destruction operator of a phonon of motion for a given normal mode of the ion chain, Ω is the carrier Rabi rate, η_ν is the Lamb-Dicke parameter, b_j^ν is the mode amplitude for ion j, ω_ν is the mode frequency, and $\delta_{B(R)}$ is the red(blue) detuning. This term generates spin-motion entanglement, and in the limit $\eta_\nu\Omega \ll |\delta_{R,B} - \omega_\nu|$ the motion can be adiabatically eliminated for an effective spin-spin interaction.

The second Hamiltonian term is the local field generated by the individual addressing beam. This beam only addresses one ion at a time, and is rastered across the chain to create an overall field landscape. A single cycle of this term can be written as:

$$H_2(t) = \sum_j^N B_j^z \sigma_j^z \Theta(t - (j-1)t_{\text{pulse}}) \Theta(jt_{\text{pulse}} - t), \tag{D.2}$$

with $\Theta(t)$ as the Heaviside theta and t_{pulse} the time for a pulse of the beam on one ion, which we experimentally fix at $t_{\text{pulse}} = 0.5\ \mu$s.

When these terms are applied simultaneously, in the limit $|\delta_{R,B} - \omega_\nu| \gg \eta_\nu\Omega \gg$

B_j^z, the transverse Ising Hamiltonian is approximately realized:

$$H_{TFIM} = \sum_{j,j'} J_{jj'} \sigma_j^x \sigma_{j'}^x + \sum_j \frac{B_j^z}{N} \sigma_j^z. \tag{D.3}$$

However, the validity of this Hamiltonian is limited to small B_j^z. Therefore, when realizing a linear field gradient, $B_j^z = gj$, this results in the constraint $gN^2 \ll \eta_\nu \Omega$, which prevents the simultaneous attainment of long chains and large linear field gradients. For example, for typical experimental parameters of $N = 15$, $\eta\Omega = 2\pi \cdot 30$ kHz, and $J_0 = 2\pi \cdot$ 250 Hz, this would require that $g/J_0 \ll 0.5$. When this is not satisfied, additional phonon terms are present in the Hamiltonian that result in undesired spin-motion entanglement, or effective decoherence of the dynamics when measuring only spin.

We can reduce these constraints by applying a Trotterized Hamiltonian [461]. The evolution under this time-varying Hamiltonian can be analyzed using the Magnus expansion, to find the dominant contributions to time-averaged dynamics [7]. Within this framework, the undesired effects arise from the commutator $[H_1(t), H_2(t)]$. Intuitively, when these terms are no longer applied simultaneously the effect of this commutator is reduced.

Consider unitary evolution of a single Trotter cycle, using the lowest-order symmetrized sequence:

$$\begin{aligned} U = & e^{-i\int_0^{\Delta t_2/2} H_2(t)dt} \\ & \times e^{-i\int_{\Delta t_2/2}^{\Delta t_1+\Delta t_2/2} H_1(t)dt} e^{-i\int_{\Delta t_1+\Delta t_2/2}^{\Delta t_1+\Delta t_2} H_2(t)dt} \end{aligned} \tag{D.4}$$

The Hamiltonians governing each part of the unitary evolution may be approximately replaced by their time-averaged values, simplifying both. For H_2 we have

$$\int_0^{\Delta t_2/2} H_2(t)dt =$$
$$\int_0^{\Delta t_2/2} \sum_j B_j^z \sigma_j^z \Theta(t-(j-1)t_{\text{pulse}})\Theta(jt_{\text{pulse}}-t)dt$$
$$= \frac{\Delta t_2}{2N} \sum_j B_j^z \sigma_j^z, \tag{D.5}$$

an exact identity since each of the terms in $H_2(t)$ commute with one another. For $H_1(t)$ we have

$$\int_0^{\Delta t_1} dt \sum_{j,\nu} \sigma_j^+ \left[\frac{-i\Omega\eta_\nu b_j^\nu}{2} (a_\nu e^{-i\omega_\nu t} + a_\nu^\dagger e^{i\omega_\nu t}) \right.$$
$$\left. (e^{-i\delta_B t} - e^{-i\delta_R t}) \right] + h.c. \tag{D.6}$$

However, this is just the usual $M-S$ Hamiltonian, and in the limit that $|\delta_{R,B} - \omega_\nu|t \gg 1$ the only significant contributing terms are the stationary ones. When $\delta_R = -\delta_B$ this results in the pure $\sigma^x\sigma^x$ interaction. When instead a small rotating frame transformation is applied we generate the Ising Hamiltonian with a small overall transverse field [7]:

$$\int_0^{\Delta t_1} dt H_1(t) \approx \Delta t_1 \left(\sum_{j,j'} J_{jj'} \sigma_j^x \sigma_{j'}^x + B^{z0} \sum_j \sigma_j^z \right). \tag{D.7}$$

The combined evolution of the full Trotter cycle is then, to lowest order, de-

scribed by the Hamiltonian

$$H = \frac{\Delta t_1}{\Delta t_1 + \Delta t_2} \sum_{j,j'} J_{jj'} \sigma_j^x \sigma_{j'}^x + \sum_j \sigma_j^z \left(B^{z0} + \frac{\Delta t_2}{\Delta t_1 + \Delta t_2} \frac{B_j^z}{N} \right) + \mathcal{O}(\Delta t^3). \tag{D.8}$$

We program B_j^z to the desired functional form and absorb the factors with Δt_1 and Δt_2 into re-definitions of J_0 and B_j^z, leading to Eqs. 1 and 4 of the main text. The constant term B^{z0} does not depend on these times, because it is created by moving into a rotating frame that is applied to the entire time evolution. This approximation requires that $|\delta_{R,B} - \omega_\nu|\Delta t_1 \gg 1$ (for Eq. (D.7)), which is satisfied in the experiment: $|\delta_{R,B} - \omega_\nu|_{min} = \mu = 2\pi \cdot 200$ kHz and $\Delta t_1 \geq 18$ μs, whose product is 22.6. Additionally, Δt_1 and Δt_2 must not be so long that the Trotter approximation (Eq. (D.8)) breaks down. However, the low energy scale of J_0 and the use of the symmetrized Trotter form make this limit less constraining than the limit for continuous evolution, allowing us to reach $g/J_0 = 2.5$ (1.5) for 15 (25) spins. Because the Trotter error consists of undesired spin terms, rather than spin-phonon terms, it can also be easily simulated numerically. Fig. D.1 shows comparisons of the Trotterized and ideal evolution in the case of the strongest gradient, showing that the Trotter error is negligible over the experimental timescale and that the Trotterization results in a significant improvement in the simulation fidelity.

In addition to reducing phonon errors, this scheme has the advantage of allowing us to tune the average Hamiltonian (Eq. (D.8)) simply by varying Δt_1 and

Δt_2, because $[g/J_0]_{avg} = (\Delta t_2/\Delta t_1)g/J_0$. This capability allows us to scan over a range of gradient values with a single calibration, and it makes any errors on the gradient calibration common to all these scans. In the data presented here, we fix the instantaneous values of g and J_0 and vary Δt_1 (see Trotterized Hamiltonian parameters). In addition, we ramp the interactions up and down over 9 μs with a shaped Tukey profile to reduce adiabatic creation of phonons [95].

This implementation of Trotterized Stark MBL dynamics would be difficult to extend to more than tens of spins, as the maximum instantaneous shift required on the edge ion scales as N^2, leading to the requirement of an increasingly fast drive. However, given the unbounded nature of a linear gradient, any large- scale simulation of Stark MBL is likely to be challenged by the required field difference between the two ends.

Throughout this discussion, we have taken the perspective of a Trotterized quantum simulation of a desired Hamiltonian. We could also understand this experiment in terms of Floquet theory. From this perspective, this driven system is described stroboscopically by a Floquet Hamiltonian, which to lowest order is the Hamiltonian (D.8), and the steady-state equilibration that we see represents prethermal evolution under this effective Hamiltonian that is expected be altered at long times by Floquet heating arising from the higher-order terms. While this picture offers a complementary way to understand these results, and interesting connections to studies of driven localization [462], for simplicity we focus on the Trotterized perspective.

D.3.1 Trotterized Hamiltonian parameters

For imbalance measurements at $N = 15$, we calibrate to g/J_0 of 2.5 for $\Delta t_1 = \Delta t_2$. To scan the gradient strength, Δt_2 is fixed at 18 μs and Δt_1 is varied from 18-180 μs. In addition, there is an extra 9 μs of effective dead time per Trotter step associated with the Tukey pulse shaping. We fix B^{z0} at $2\pi\cdot$ 1.25 kHz. For data in a quadratic field, we set $\gamma = 2.0$ for $\Delta t_1 = \Delta t_2$, and vary Δt_2 from 10-180 μs, with all other settings kept the same as in the linear gradient.

For $N = 25$, we instead set g/J_0 to 1.25 for $\Delta t_1 = \Delta t_2$. Δt_1 is fixed at 30 μs, and Δt_2 is varied between 25 and 190 μs, again with an extra 9 μs of effective dead time per cycle due to pulse shaping. B^{z0} is again fixed at $2\pi\cdot$ 1.25 kHz.

For DEER measurements, we calibrate to g/J_0 of 2.0. Δt_2 is fixed at 18 μs and Δt_1 is varied from 18-180 μs, plus an extra 9 μs of dead time associated with Tukey pulse shaping. We fix B^{z0} at values varying for different datasets between $2\pi\cdot$ 0.9 and 1.25 kHz.

D.4 Mapping to boson model

Our experimental Hamiltonian, from Eq. (6.1) of the main text, is:

$$H = \sum_{j<j'} J_{jj'}\sigma_j^x\sigma_{j'}^x + \sum_{j=1}^{N}(B^{z0} + (j-1)g)\sigma_j^z. \tag{D.9}$$

In the limit of $B^{z0} \gg J_0$, and assuming that B^{z0} and g have the same sign, the total magnetization $\sum_j \langle\sigma_j^z\rangle$ is conserved. For an initial state of definite total magneti-

zation, the system then reduces to the long-range tilted XY Hamiltonian [58]:

$$H_{XY} = \sum_{j<j'} \frac{J_{jj'}}{2} \left(\sigma_j^+ \sigma_{j'}^- + \sigma_j^- \sigma_{j'}^+\right) + \sum_{j=1}^{N} (B^{z0} + (j-1)g)\sigma_j^z. \tag{D.10}$$

This can be mapped to a system of hard-core bosons taking $\sigma_j^{-(+)} \to a_j^{(\dagger)}$ and $n_j = a_j^\dagger a_j = (\sigma_j^z + 1)/2$, resulting in the Hamiltonian:

$$H_{HC} = \sum_{j<j'} \frac{J_{jj'}}{2} \left(a_j^\dagger a_{j'} + a_j a_{j'}^\dagger\right) + U \sum_{j=1}^{N} n_j(n_j - 1) + \sum_{j=1}^{N} (\mu_N + 2(j-1)g)n_j, \tag{D.11}$$

with $\mu_N = 2B^{z0}$, taking the limit $U \to \infty$, and dropping a constant energy contribution.

This model clarifies the connection between our system and work studying Stark MBL in the context of hopping particles with interactions [235, 236]. It also illustrates the translational symmetry in our system. If j is shifted by an integer, this is equivalent to changing the chemical potential term $\sum_j \mu_N n_j$, which has no effect in a closed system with particle conservation.

D.5 Full level statistics of experimental Hamiltonian

A typical ergodic system has a single-particle density matrix with support throughout the bulk, and thus has a high degree of overlap between particles. This

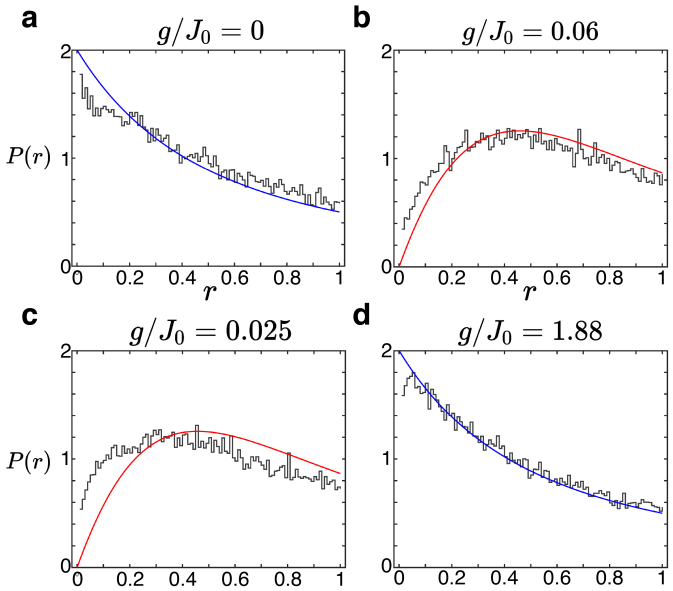

Figure D.2: Probability density distributions of r, the ratio of adjacent energy level spacings, for the experimental Hamiltonian at various values of g/J_0 and $N = 15$. Numerics are compared with the distribution expected for either a Poisson level distribution (blue lines in (a). and (d).) or a Wigner-Dyson distribution (red lines in (b). and (c).). The level statistics in the absence of a field gradient are near the Poissonian limit, which may reflect the proximity to an integrable limit for the low-energy sector [453]. A small gradient results in statistics near the Wigner-Dyson limit, followed by an approach to Poisson statistics as the gradient is increased.

results in level repulsion in the many-body spectrum, leading to a Wigner-Dyson energy level distribution characteristic of random matrices [249]. A typical localized system, on the other hand, has single particles that are spatially confined, and thus have little overlap, resulting in a Poissonian distribution of the many-body spectrum. In Fig. D.2 we show the full distribution of r, the ratio of adjacent energy level spacings, for the experimental Hamiltonian at selected values of g/J_0. We compare it to the probability density distributions resulting from Poisson and Wigner-Dyson statistics [236]:

$$P_p(r) = \frac{2}{(1+r)^2} \text{ (Poisson)}, \tag{D.12}$$

$$P_{WD}(r) = \frac{27(r+r^2)}{4(1+r+r^2)^{5/2}} \text{ (Wigner-Dyson)}, \tag{D.13}$$

where Eq. (D.13) is an analytic approximation to the Gaussian Orthogonal Ensemble based on the Wigner Surmise [463].

While a small field gradient is needed to break the approximate integrability of the Hamiltonian [453] in the limits of $g = 0$ and $B^{z0} \gg J_0$, over the range of tilts studied experimentally the level statistics cross from being close to the Wigner-Dyson limit, with an evident dip at low r due to the proliferation of avoided crossings, to very close to the Poisson limit at high gradients. This should be contrasted with the case of short-range hopping, in which the level statistics may be highly non-generic due to exact degeneracies associated with center-of-mass conservation, making concepts of Hilbert space fragmentation (or shattering) especially relevant [203, 204, 222, 235, 236, 244]. However, we cannot exclude the possibility of a 'quasi-

ergodic' regime at low gradient [242]. Although the level statistics shown here are for an experimentally measured Hamiltonian, featuring small deviations from a perfectly linear gradient, these deviations do not substantially affect the level statistics, as the long-range interactions already lift the degeneracies. In the next section we show this explicitly, using the ideal power-law Hamiltonian to study more general features of Stark MBL with long-range interactions such as the scaling behavior.

D.6 Numerical studies of the ideal power-law Hamiltonian

The experimental system is approximately described by a Hamiltonian with a power-law hopping. However, as the exact experimental couplings feature inhomogeneity across the chain and deviations from power-law scaling for large ion separations, all numerics shown in the main text (as well as the previous section) use the exact Hamiltonian as determined by experimental measurements of mode structure and detuning. Nonetheless, to study the general behavior of the system it is useful to also look at the power-law Hamiltonian, which captures the dominant behavior while being translation-invariant and therefore having a more natural scaling with size. We study this numerically to characterize the behavior of $\langle r \rangle$ with respect to α and g/J_0, and to study the finite-size dependence.

D.6.1 Dependence of $\langle r \rangle$ on α and g/J_0

Fig. D.3 shows the dependence of the level statistics $\langle r \rangle$ on the Hamiltonian parameters α and g/J_0. The primary features of the experimental Hamiltonian

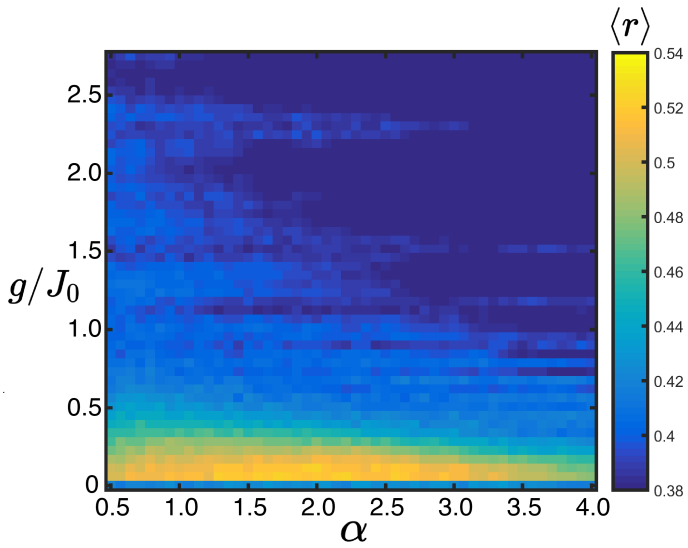

Figure D.3: Dependence of $\langle r \rangle$ on power-law range α and g/J_0 (N=13, $B^{z0}/J_0 = 5$). In the experiments presented in the main text $\alpha \approx 1.3$.

statistics are retained, such as non-generic statistics for very low gradient values and a crossover from $\langle r \rangle \approx 0.5$ to 0.39 for g/J_0 between 0.1 and 2.0. For $\alpha < 1$, the ergodic regime progressively increases, as the interaction energy is superextensive in this regime and thus delocalization is always expected for a sufficiently large system. For large α, $\langle r \rangle$ generally decreases, which may reflect an approach to the exact degeneracies that are present in the short-range limit. The general features observed are consistent with a recent study of long-range hopping in a tilt [241] that also found persistence of a crossover in $\langle r \rangle$ up to $N = 18$ and for $\alpha > 1$.

D.6.2 Dependence of $\langle r \rangle$ on system size

Using the power-law Hamiltonian, we can study the dependence of the level statistics on system size. Fig. D.4 shows this for N ranging from 9 to 15. In general, the curves do not exhibit a simple finite-size scaling. This may be due to the long-range interactions, which also cause a system size-dependent shift in the transition

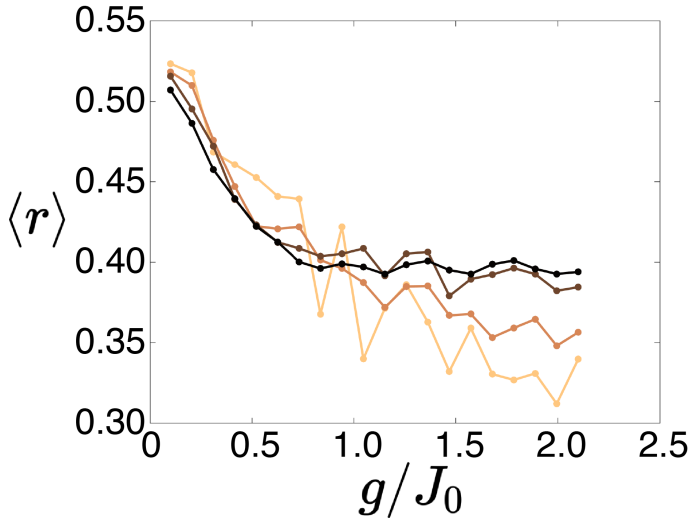

Figure D.4: Dependence of level statistics on system size. Level statistics for $N = \{9,11,13,15\}$ (light to dark), for $\alpha = 1.3$ and $B^{z0}/J_0 = 5$.

in numerics for the disordered MBL case [250]. We see that the gradient-driven localization persists up to the largest systems we can diagonalize, coinciding with the size used for most of the data presented in the main text, with a full study of the scaling left as an interesting subject for future work.

D.7 Generalized Imbalance

The generalized imbalance used in the main text is defined as:

$$\mathcal{I}(t) = \frac{\sum_j \langle \sigma_j^z(t) \rangle (1 + \langle \sigma_j^z(0) \rangle)}{\sum_j (1 + \langle \sigma_j^z(0) \rangle)} - \frac{\sum_j \langle \sigma_j^z(t) \rangle (1 - \langle \sigma_j^z(0) \rangle)}{\sum_j (1 - \langle \sigma_j^z(0) \rangle)} \tag{D.14}$$

For an initial state that is a product of up and down spins along z, this reduces to a simple form: the average magnetization of the spins initialized up minus the

average magnetization of the spins initialized down. For an initial state that is fully polarized this imbalance is undefined, which may be considered as a drawback to this measure, but such a state is already near equilibrium and thus is not useful for quantifying equilibration.

This definition is similar to many other variations of the imbalance. For an initial Néel state with an even number of spins it is identical up to scaling factors to both the imbalance and the Hamming distance, while for a general initial state of up and down spins it reduces to an alternate 'generalized imbalance' that has been used in previous studies [245, 464, 465]. However, in general this definition offers a few advantages:

- Unlike the imbalance, it is exactly zero for a thermalized system with an odd number of spins.
- It does not require any knowledge of the initial state to be added in by hand, unlike alternative observables in which the initially flipped spins are tracked.
- Unlike the Hamming distance, this generalized imbalance is zero for a thermalized system, and has units of magnetization difference (therefore ranging from -2 to 2).
- Finally, this generalized imbalance is less sensitive to noise than the Hamming distance. An example is useful: consider an initial state of one flipped spin ($\langle\sigma^z\rangle = 1$), with $N = 10$, and a background of spin-down ($\langle\sigma^z\rangle = -1$). Then, suppose that after some time this system has either evolved to a completely uniform system with an average magnetization of -1, or a state where the

initially flipped spin relaxes to a magnetization of +0.8 and the remaining spins relax to -0.8. Both of these final spins have the same Hamming distance from the initial state, because they both represent a system that is an average of one spin flip from the initial state. However, the first final state is completely equilibrated, while the second has a strong memory of the initial state. The Hamming distance, therefore, is not an optimal measure of initial state memory in a situation where a few flipped spins give you more information about the initial state than the background spins.

While the Hamming distance is always 1 at time zero, this generalized imbalance only starts at 2 for an initial state in which each spin is in a definite state of σ^z. In Fig. 6.2(c) the experimental imbalances do not start exactly at 2, reflecting SPAM errors.

D.8 Scaling of $\overline{\mathcal{I}}$ with system size

Fig. D.5 shows a comparison of our data for $\overline{\mathcal{I}}$ varying system size (Fig. 6.2(e)) with numerics. We cannot present an exact comparison, due to the computational resources needed to solve the Schroedinger equation for a 25-spin system. However, we instead present data for $N = 9$ and $N = 15$, corresponding to the same scaling factor and the lower of the two experimental system sizes. To facilitate system size comparison, we use the ideal power-law Hamiltonian for these numerics.

For the most part, $\overline{\mathcal{I}}$ only shows a slight shift with increasing N. However, there is a sharp feature near $g/J_0 = 1.0$ that grows more prominent with increasing

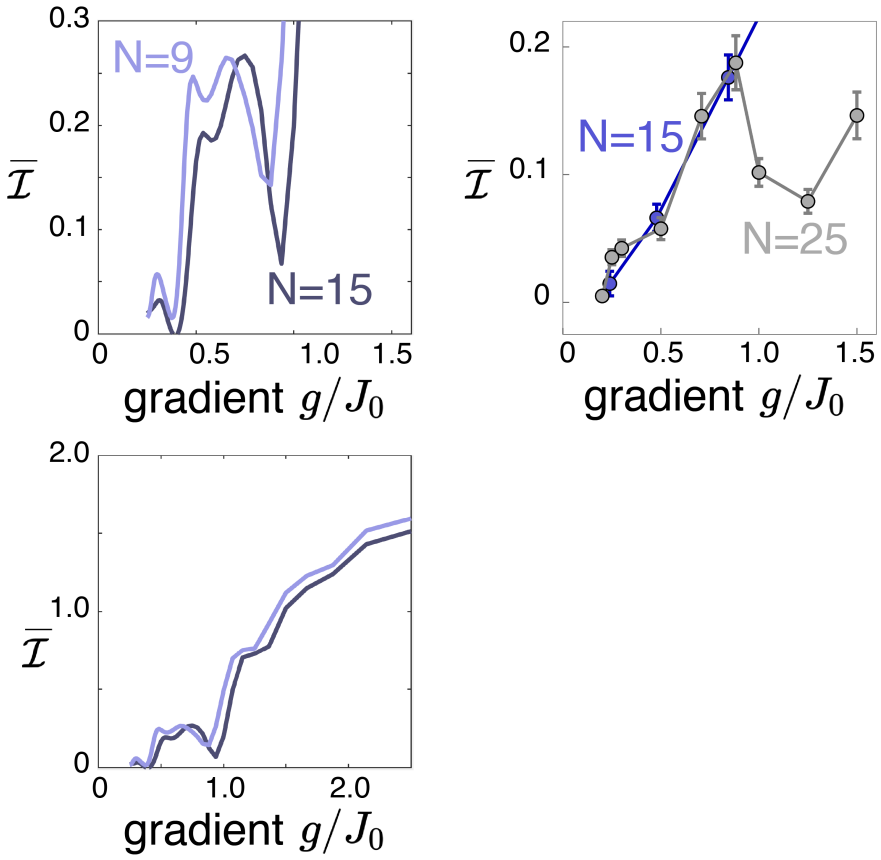

Figure D.5: Scaling of $\overline{\mathcal{I}}$ with system size. Top left: As the system increases from $N = 9$ to $N = 15$, the largest change is in a sharpening feature near $g/J_0 = 1$ that shifts downward and towards higher gradient. Top right: while we cannot solve for $\overline{\mathcal{I}}$ for $N = 25$, experimentally we see a similar dip (reproduced from Fig. 6.2(e) of the main text). Bottom left: expanded view of $\overline{\mathcal{I}}$ for $N = 9$ and $N = 15$, showing similar localization beyond $g/J_0 = 1$.

size, and appears similar to the experimental dip observed for $N = 25$. Interpretation of this feature in experimental data is complicated by decoherence that increases both with g/J_0 and with N.

The dip feature seen here is initial-state dependent, and may reflect a few-body delocalization process that is especially favorable for the Néel state. This illustrates the challenge of determining the onset of localization in finite size systems, and in quenches from a particular initial state [242]. However, any such few-body process would only occur for $g/J_0 < 1$, the regime where such resonances are possible, and we expect (consistent with the bottom panel of Fig. D.5) that for $g/J_0 > 1$ the localization that we observe is not strongly affected by this consideration.

D.9 Quantum Fisher information

Quantum Fisher information (QFI) has gained attention as a scalable entanglement witness [60, 466]. For a pure state, it is nothing more than the variance of the witness operator $\mathcal{O}$: $f_Q = 4(\langle \mathcal{O}^2 \rangle - \langle \mathcal{O} \rangle^2)/N$. For $f_Q > 1$, entanglement is guaranteed to be present within the system [466]. As a correlator that carries some information about entanglement, QFI is also similar in spirit to measures such as the Quantum Mutual Information [237] and the configurational correlator [247].

In the context of the Néel state we measure the QFI for a staggered magnetization operator, which reduces to:

$$f_Q = \frac{1}{N}\left[\sum_{jj'}(-1)^{j+j'}\langle \sigma_j^z \sigma_{j'}^z \rangle - (\sum_j (-1)^j \langle \sigma_j^z \rangle)^2\right]. \tag{D.15}$$

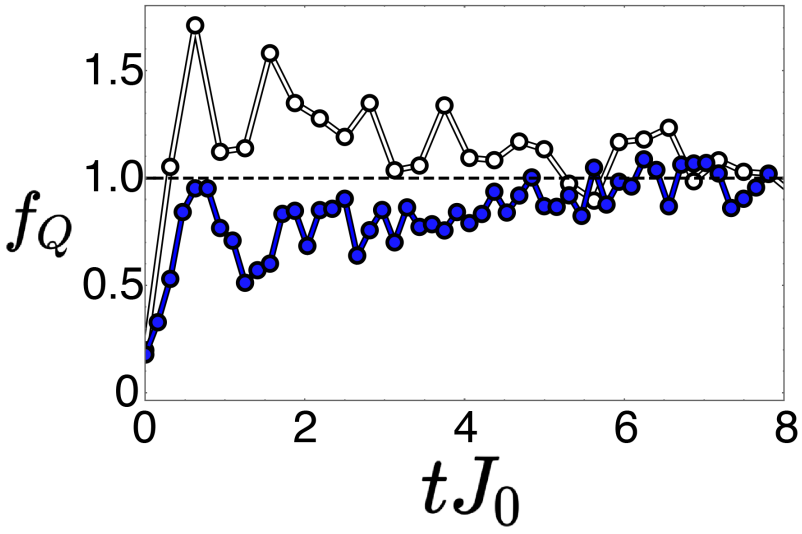

Figure D.6: Quantum Fisher information. Normalized quantum Fisher information for a Néel state ($N = 15$) with $g/J_0 = 0.24$ (white) and $g/J_0 = 2.4$ (blue), corresponding to the lowest and highest-gradient data in Fig. 6.2(d). Points are experimental observations, with lines as guides to the eye. A value greater than one (dashed line) is an entanglement witness. After the initial fast dynamics up to $tJ_0 \approx 1$, the QFI is consistent with saturation for the low gradient, and with slow entanglement growth for the high gradient, with behavior very similar to that previously observed in disordered MBL [60]

The results are shown in Fig. D.6. We see a significant difference between f_Q with weak and strong field gradients. In a weak gradient, entanglement builds up rapidly before slowly tapering off. In a strong gradient f_Q instead grows slowly, exhibiting similar behavior as expected for entanglement in an MBL phase and in Stark MBL [236].

A few shortcomings limit the value of the QFI. First, it is only easily calculated when assuming a pure state. Second, it can only be interpreted as an entanglement witness when it exceeds one, challenging in a strongly localized phase. Finally, unlike the DEER protocol it does not give spatially resolved information. Still, within its limits the QFI behavior is consistent with the expectations for an MBL phase. The QFI dynamics also closely resemble previous observations for disordered

MBL [60], consistent with expectations that disorder or strong gradients result in similar entanglement spreading.

D.10 Additional DEER Data

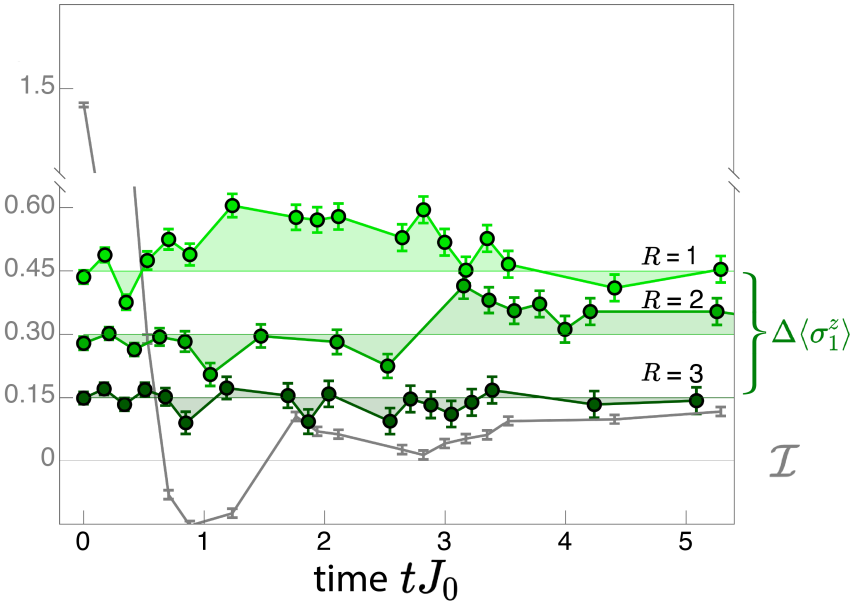

Figure D.7: DEER Difference signal for $R = \{1,2,3\}$ (light to dark), compared with the imbalance $\mathcal{I}(t)$ for the same parameters. Data are offset for clarity but otherwise share the same axes. $\mathcal{I}$ is taken from the same dataset as the $R = 1$ spin-echo data, with the probe spin excluded from the imbalance calculation. After $tJ_0 \approx 2$, the imbalance is essentially constant at the low but finite steady-state value corresponding to this gradient strength. However, correlation dynamics are still progressing- in particular, correlations as measured by the difference signal only begin to develop for $R = 2$ after this point. This is similar to the disordered MBL state, in which slow entanglement dynamics continue after the locally conserved populations have reached a steady state [227, 228, 247].

Additional data for the DEER protocol difference signal ($\Delta\langle\sigma_1^z\rangle$) is shown in Fig. D.7. Looking at the DEER difference signal, we see that correlations develop more slowly as the DEER region R is moved progressively away from the source. For $R = 2$, these correlations are only visible after the imbalance dynamics have reached a steady state. This rules out attribution of the correlations to the transient

population dynamics, and instead resembles the slow correlation dynamics that occur in a disordered MBL system after populations have reached a steady state [227, 228, 247].

D.11 Critical slope in quadratic field

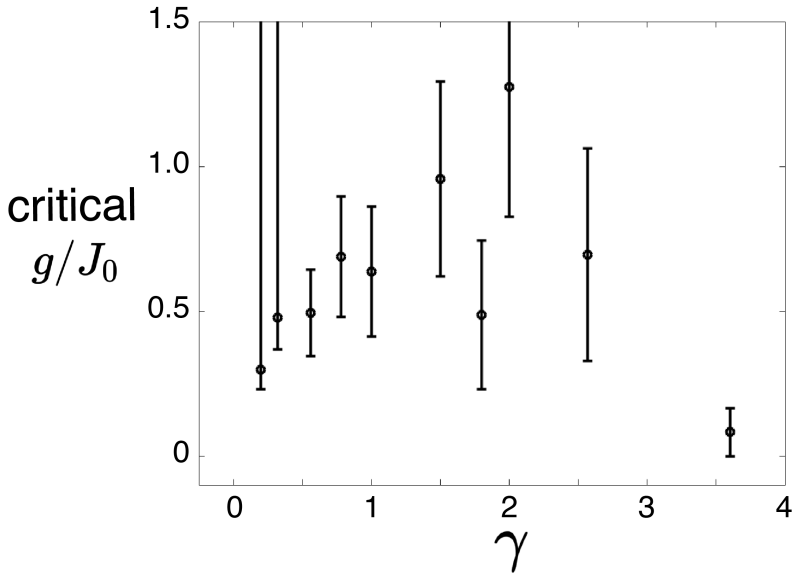

Figure D.8: Dependence of the critical slope separating thermalizing and non-thermalized regions on the curvature γ. As the quadratic curvature is varied, the division between thermalizing and nonthermal regions is largely consistent with a critical slope near $g/J_0 = 0.5$. However, the strongest curvature of $\gamma = 3.6$ deviates from this rule. For the lowest two values of γ the system was completely delocalized, and thus only the lower bound is meaningful. Error bars (aside from the first two points) denote a variation of ± 1 spin location.

Fig. D.8 presents the dependence of the critical value of g/J_0 for a quadratic field with different values of the curvature γ. The critical value is determined by the innermost pair of spins that are both separated from the center spin by more than their mutual error bars, judged by taking the mean and standard deviation of the average magnetizations for the last five time points.

The data are largely consistent in suggesting a critical gradient value on the order of $g/J_0 = 0.5$. However, the strongest curvature is notably different, possibly reflecting a breakdown of the local gradient approximation for this case. For curvatures less than this, we conclude that the system seems roughly consistent with a picture of localization that is determined by the local Stark MBL field slope at any given spin.

Appendix E: Appendices to Chapter 7

E.1 Derivation of effective planar-pyrochlore hopping model

In this section, we derive the effective planar-pyrochlore hopping model by eliminating the wavefunction amplitudes on sublattice A. For clarity, we show the Lieb lattice and the wavefunction amplitudes $\psi_1, \ldots, \psi_9$ on each lattice site in Fig. E.1.

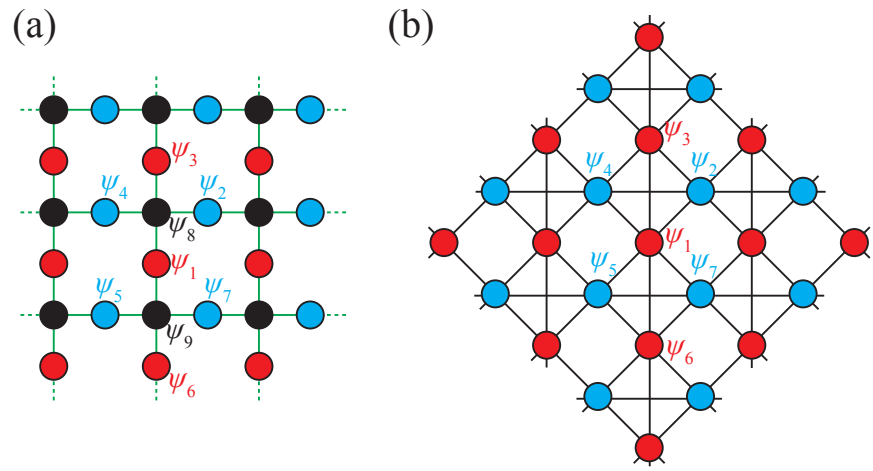

Figure E.1: (a) The Lieb lattice and the wavefunction amplitudes $\psi_1, \ldots, \psi_9$ in a local region. (b) The mapped planar-pyrochlore hopping model after eliminating the sublattice A.

Let us focus on a particular eigenstate with eigenenergy E. The eigenvalue

equation centered around the site with wavefunction amplitude ψ_1 is given by

$$\frac{\Omega}{2}(\psi_8 + \psi_9) + V_1\psi_1 = E\psi_1, \tag{E.1}$$

where V_1 is the disorder strength on site 1. Similarly, we can write down the eigenvalue equations for ψ_8 and ψ_9:

$$\frac{\Omega}{2}(\psi_1 + \psi_2 + \psi_3 + \psi_4) = E\psi_8, \tag{E.2a}$$

$$\frac{\Omega}{2}(\psi_1 + \psi_5 + \psi_6 + \psi_7) = E\psi_9. \tag{E.2b}$$

By plugging Eqs. (E.2) into Eq. (E.1) and multiplying through by $4E$, one arrives at [308]:

$$\Omega^2 \sum_{i=2}^{7} \psi_i + (4EV_1 + 2\Omega^2)\psi_1 = 4E^2\psi_1, \tag{E.3}$$

where V_1 is the on-site random potential on site 1. The above equation corresponds to a single particle hopping on the planar pyrochlore lattice, see Fig. E.1(b). Eq. (E.3) now describes a single-particle hopping model on the B and C sublattices only, which form a *planar pyrochlore lattice*. As shown in Refs. [276, 294], the planar pyrochlore lattice also hosts a singular flat band in the clean limit, and the flat band eigenstates also exhibit multifractality in the presence of weak disorder. Indeed, for $E \approx 0$, the right-hand side of Eq. (E.3) can be neglected, and when $EV_1 \ll \Omega^2$, Eq. (E.3) describes a single-particle hopping model in the presence of weak disorder. That the wavefunctions have dominant support on sublattice A can also be understood. When eliminating sublattice A from the eigenvalue equations,

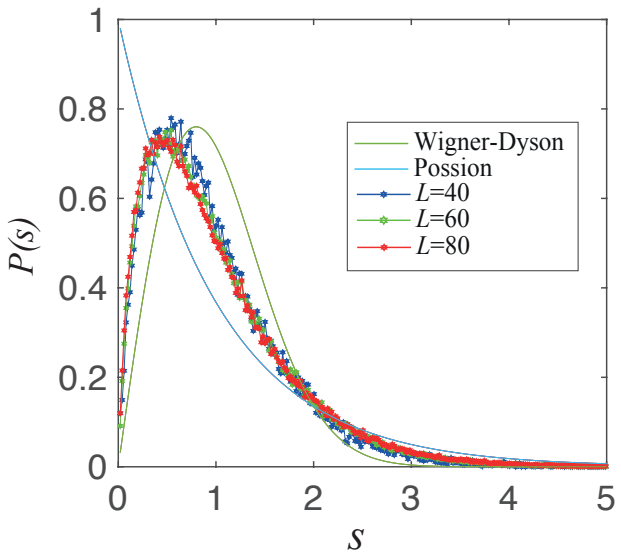

Figure E.2: Probability distribution of the unfolded level spacings $P(s)$ for states in Regime II for different system sizes. The disorder strength $\sigma = 10^{-3.6}$. The data shown in this figure are averaged over 800 realizations of disorder.

we have used $\psi_8 = \frac{\Omega}{2E}(\psi_1 + \psi_2 + \psi_3 + \psi_4)$, where site 8 belongs to sublattice A [see Fig. 7.1(b)]. When $E \approx 0$, the weight on sublattice A is enhanced. On the other hand, in Regime I near the clean limit, the original CLS has $\psi_1 + \psi_2 + \psi_3 + \psi_4 = 0$, hence the weight on sublattice A remains negligible.

E.2 Level spacing statistics in Regime II

In Fig. E.2, we show the probability distribution of the unfolded level spacings $P(s)$ for states in Regime II for different system sizes. Compared to that in Regime I [Fig. 7.2(d)], we find that the system-size dependence of the level spacing distribution in Regime II is more prominent. The level statistics appear to tend towards Poisson as the system size increases. This suggests that Regime II is not critical, but rather localized in the thermodynamic limit.

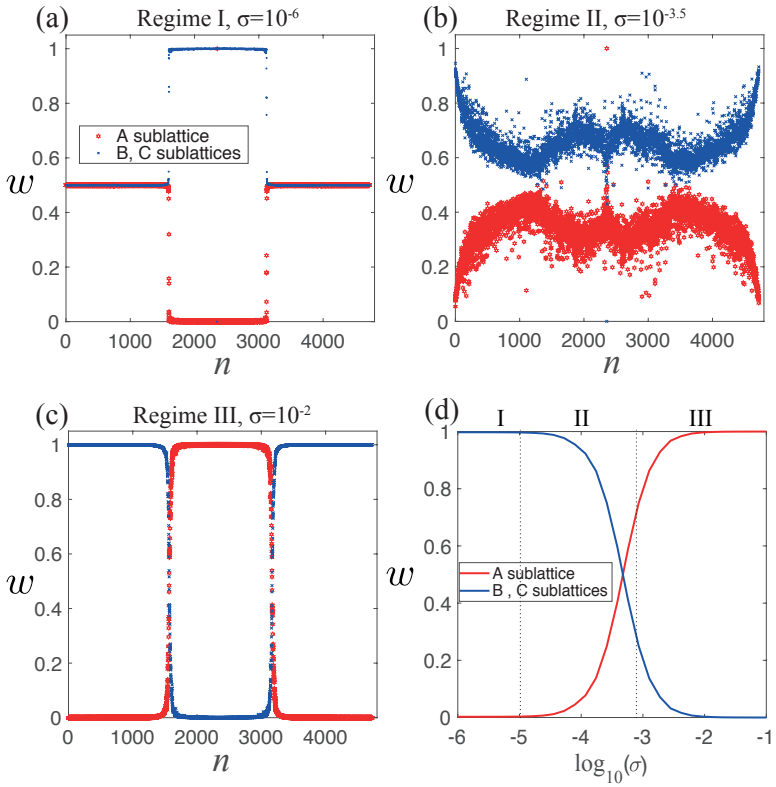

Figure E.3: (a)-(c) Sublattice dependence of the wavefunction weight w versus the eigenstate number n sorted by eigenenergy in each regime. (d) w versus the disorder strength for states near $k = 0$. The system size is $L = 40$. The dashed vertical lines separate the three Regimes, as in Fig. 2(a) of the main text.

E.3 Sublattice-resolved wavefunction weight

In this section, we plot the sublattice dependence of the wavefunction weight in each regime. From Fig. E.3(a), one can see that, in Regime I, the wavefunction weights w in the middle one-third of the spectrum have major support on the B and C sublattices, and negligible support on the A sublattice. This is consistent with our discussion in the main text that disorder in this regime only slightly modifies the flat band in the clean limit, and does not induce hybridization with other bands. In contrast, the wavefunction in Regime II has substantial support on all lattice sites [Fig. E.3(b)]. This indicates that disorder in Regime II induces strong hybridization

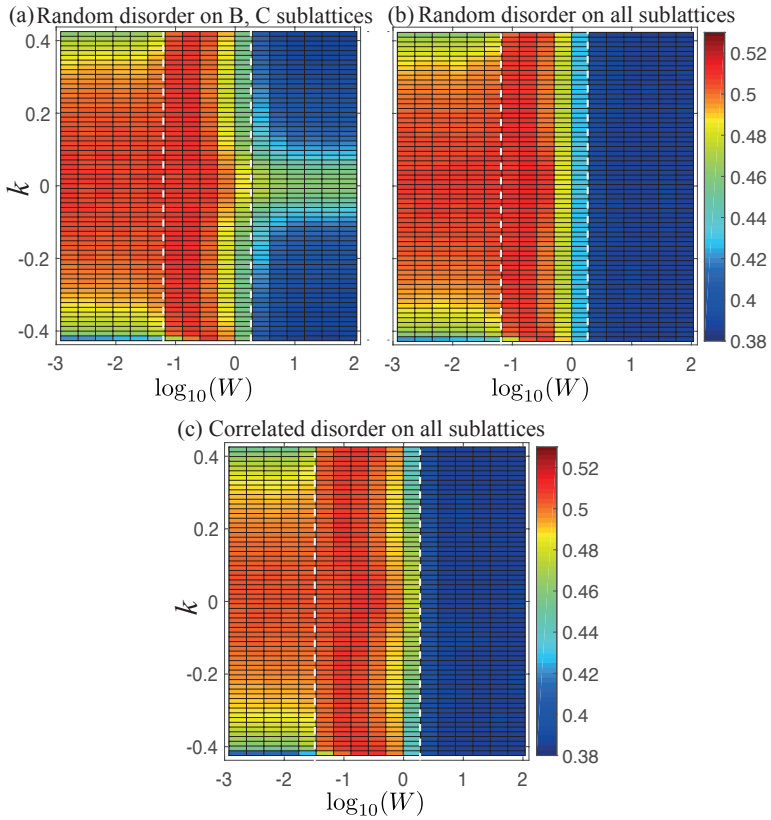

Figure E.4: (a) Level spacing ratio r for uncorrelated disorder coupled to the B and C sublattices. (b) Level spacing ratio r for random disorder coupled to all sublattices. (c) Level spacing ratio r for correlated disorder on all sublattices in which the shift on B and C sites is given by the sum of the shifts on the two neighbouring A sites. The disorders in (a) and (b) both have a uniform distribution in $[-W, W]$. The disorder in (c) uses the same uniform distribution for the A sites only. The system size is $L = 60$. The data shown in this figure are averaged over 800 realizations of disorder.

between the flat band and the dispersive bands. In Regime III, strong disorder gives rise to a new flat band in the middle of the spectrum, whose wavefunctions now have major support on sublattice A, in stark contrast to the flat band in Regime I. Another interesting observation in this Regime is that eigenstates in the rest of the spectrum show opposite support, i.e. they are mainly supported on the B and C sublattices. These eigenstates do not belong to the flat band, and the corresponding energies are far from zero.

Fig. E.3(d) shows the wavefunction weight as a function of the disorder strength for states near $k = 0$. From this figure, one can see that there is indeed a flip of the support from the B and C sublattices to the A sublattice as the disorder strength increases. This plot also corroborates the existence of three distinct localization regimes as discussed in the main text.

E.4 Numerical results on different disorder types

In this section, we provide additional numerical results on three other types of disorder as shown in Figs. E.4(a)-(c), namely, (a) uncorrelated disorder on sublattices B and C only, (b) uncorrelated disorder coupled to all three sublattices, and (c) correlated disorder on all sublattices in which the shift on B and C sites is given by the sum of the shifts on the two neighbouring A sites. Disorder of type (b) can be implemented in other experimental platforms, e.g., lattice systems of optical photons, microwave photons, cold atoms, and electrons. Disorder of type (c)

corresponds to the frequency shift due to the Rydberg setup's Doppler effect. While this effect is present in the Rydberg platform discussed in the main text, we neglect it because the positional disorder is much stronger [13].

We first consider uncorrelated disorder coupled to the B and C sublattices only with a uniform distribution in $[-W, W]$, in contrast to the correlated disorder studied in the main text. From Fig. E.4(a), we again find three regimes similar to Fig. 7.2(a) in the main text. We have also confirmed that the properties of the three regimes' wavefunctions are similar to those of the correlated-disorder case. We thus conclude that the presence or absence of correlations in the disorder on adjacent lattice sites has little effect on the main results of this work.

Fig. E.4(b) and (c) also show three regimes. However, in stark contrast to Fig. E.4(a) and Fig. 7.2(a) in the main text, all states in Regime III are strongly localized, and the flat band with extended states near the middle of the spectrum is absent. This is because the disorder is present on all sites, and all states in this regime undergo an Anderson localization transition. On the other hand, we have checked that the wavefunction properties in Regimes I and II are similar to the case where disorder couples to the B and C sublattices only.

E.5 Numerical results of the quench dynamics

In this section, we provide numerical results demonstrating that the three regimes discussed in the main text have distinct dynamical features in quantum quench experiments. The initial state is chosen as a CLS in the clean limit [see

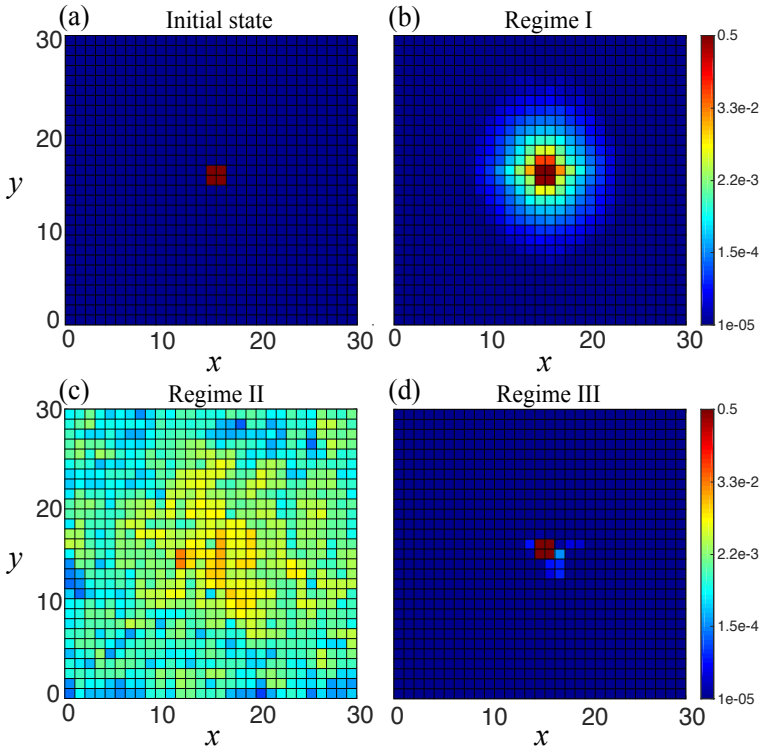

Figure E.5: (a) Rydberg excitation probability in real space for the initial state, which is chosen as a CLS at the center of the system. (b)-(d) Excitation probabilities after evolving for time $300/\Omega$, under the 2D Lieb-lattice Hamiltonian with disorder strength: $\sigma = 10^{-6}$ (b), $\sigma = 10^{-4}$ (c), and $\sigma = 10^{-2}$ (d).

Fig. E.5(a)]. For the original Rydberg lattice, such a state corresponds to $\Psi_{ij} = \frac{1}{2}\left(|11\rangle^{x}_{i,j} + |11\rangle^{x}_{i,j+1} - |11\rangle^{y}_{i,j} - |11\rangle^{y}_{i+1,j}\right)$, where $|11\rangle^{x/y}_{i,j}$ represents a pair of nearest-neighbour Rydberg excitations emanating from site (i,j) in the x/y direction. All the other atoms are in the ground state. Such a state can be experimentally prepared with single-site addressing, as proposed in Ref. [284].

Figs. E.5(b)-(d) show the Rydberg excitation probabilities in real-space after evolving for a fixed amount of time under the 2D disordered Lieb-lattice Hamiltonian in the three respective regimes. In Regime I (weak disorder), the initial state hybridizes weakly with other flat-band states, and hence the distribution of Rydberg excitations spreads slowly in time [Fig. E.5(b)]. We also verify that the time-evolved state has large weight on pair excitations, correpsonding to B and C sublattices of the Lieb lattice. In Regime II, the initial state couples to both the flat-band states and dispersive bands. The Rydberg excitations thus spread much faster in this case [Fig. E.5(c)], and the time-evolved state has nonzero weight on both single and pair Rydberg excitations. Finally, in the strong-disorder Regime III, since the delocalized states have dominant weight on single excitations instead, the initial state couples only to the localized states at much higher energies. The Rydberg excitations are thus strongly localized around their initial positions [Fig. E.5(d)].

Appendix F: Appendices to Chapter 8

F.1 Dynamical symmetry of density expansion

In this section, we give detailed derivations for the dynamical symmetry observed in the main text in Eqs. (8.9) and (8.10). The inversion symmetry operator $\mathcal{I}$ acts on a bosonic operator as $\mathcal{I}\hat{b}_j\mathcal{I}^\dagger = \hat{b}_{j'}$, where j' is the site that j is mapped to under reflection about the middle of the 1D system. The time-reversal operator $\mathcal{T}$ acts by complex-conjugating the entries of a state (or operator) written in the bosonic Fock basis; for instance, $\mathcal{T}\hat{b}_j\mathcal{T}^{-1} = \hat{b}_j$ and $\mathcal{T}i\mathcal{T}^{-1} = -i$. Although $\hat{H}_B$ respects neither time-reversal nor inversion symmetry, it does obey the following $\mathcal{K}$ symmetry [348]:

$$\mathcal{K}\hat{H}_B\mathcal{K}^\dagger = \hat{H}_B, \tag{F.1}$$

where $\mathcal{K} = \mathcal{R}\mathcal{I}\mathcal{T}$, and $\mathcal{R}$ is defined as

$$\mathcal{R} = e^{-i\theta\sum_j \hat{n}_j(\hat{n}_j-1)/2}. \tag{F.2}$$

With this, we now consider the symmetry properties of the particle dynamics. Using Eq. (F.1), one has:

$$\mathcal{K} e^{-i\hat{H}_B t} \mathcal{K}^\dagger = e^{i\hat{H}_B t}, \tag{F.3}$$

where we have used the anti-unitary property of the $\mathcal{K}$ operator. We first focus on the symmetry properties when flipping the sign of θ [Eq. (8.10) in the main text]. We label $\hat{H}_B$ with the sign of θ for convenience:

$$\hat{H}_{B,\pm\theta} = -J \sum_{j=1}^{L-1} \left(\hat{b}_j^\dagger \hat{b}_{j+1} e^{\pm i\theta \hat{n}_j} + \text{H.c.} \right) + \frac{U}{2} \sum_{j=1}^{L} \hat{n}_j (\hat{n}_j - 1). \tag{F.4}$$

The time-dependent density at site j is

$$\langle \hat{n}_j(t) \rangle_{\pm\theta} \equiv \langle \Psi_0 | \, e^{i\hat{H}_{B,\pm\theta} t} \; \hat{n}_j \; e^{-i\hat{H}_{B,\pm\theta} t} \, | \Psi_0 \rangle \, , \tag{F.5}$$

where $|\Psi_0\rangle$ is the initial Fock product state given in the main text, $|\Psi_0\rangle = \prod_i \hat{b}_i^\dagger |0\rangle$. (We have omitted the subscript "B" for simplicity.) We obtain

$$\begin{aligned}
\langle \hat{n}_j(t) \rangle_{+\theta} &\equiv \langle \Psi_0 | \, e^{i\hat{H}_{B,+\theta} t} \; \hat{n}_j \; e^{-i\hat{H}_{B,+\theta} t} \, | \Psi_0 \rangle \\
&= \langle \Psi_0 | \, \mathcal{K}^\dagger e^{-i\hat{H}_{B,+\theta} t} \mathcal{K} \; \hat{n}_j \; \mathcal{K}^\dagger e^{i\hat{H}_{B,+\theta} t} \mathcal{K} \, | \Psi_0 \rangle \\
&= \langle \Psi_0 | \, e^{-i\hat{H}_{B,+\theta} t} \mathcal{I} \; \hat{n}_j \; \mathcal{I}^\dagger e^{i\hat{H}_{B,+\theta} t} \, | \Psi_0 \rangle \\
&= \langle \Psi_0 | \, e^{-i\hat{H}_{B,+\theta} t} \; \hat{n}_{j'} \; e^{i\hat{H}_{B,+\theta} t} \, | \Psi_0 \rangle \, ,
\end{aligned} \tag{F.6}$$

where, in the second line, we have sandwiched $\mathcal{K}^\dagger \mathcal{K}$ between each two operators and used Eq. (F.3); in the third line, we have used (i) the fact that when $\mathcal{K}$ operates on

the initial state $|\Psi_0\rangle$ in the main text, it gives an unimportant phase after complex conjugation, and (ii) the relation $\mathcal{K}\hat{n}_j\mathcal{K}^\dagger = \mathcal{I}\hat{n}_j\mathcal{I}^\dagger$; in the fourth line, we have defined the density operator $\hat{n}_{j'}$ on site j', which is related to $\hat{n}_j$ by the inversion symmetry operator $\mathcal{I}$.

To proceed, we relate $\hat{H}_{B,\pm\theta}$ by the time-reversal symmetry operator $\mathcal{T}$:

$$\mathcal{T}\hat{H}_{B,+\theta}\mathcal{T}^{-1} = \hat{H}_{B,-\theta}. \tag{F.7}$$

Thus,

$$\mathcal{T}e^{-i\hat{H}_{B,+\theta}t}\mathcal{T}^{-1} = e^{i\hat{H}_{B,-\theta}t}. \tag{F.8}$$

Substituting the above equation into Eq. (F.6), we get:

$$\begin{aligned}
\langle\hat{n}_j(t)\rangle_{+\theta} &= \langle\Psi_0|\, e^{-i\hat{H}_{B,+\theta}t}\ \hat{n}_{j'}\ e^{i\hat{H}_{B,+\theta}t}\,|\Psi_0\rangle \\
&= \langle\Psi_0|\, \mathcal{T}^{-1}e^{i\hat{H}_{B,-\theta}t}\mathcal{T}\ \hat{n}_{j'}\ \mathcal{T}^{-1}e^{-i\hat{H}_{B,-\theta}t}\mathcal{T}\,|\Psi_0\rangle \\
&= \langle\Psi_0|\, e^{i\hat{H}_{B,-\theta}t}\ \hat{n}_{j'}\ e^{-i\hat{H}_{B,-\theta}t}\,|\Psi_0\rangle \\
&\equiv \langle\hat{n}_{j'}(t)\rangle_{-\theta}.
\end{aligned} \tag{F.9}$$

Finally, we arrive at a very simple equation [Eq. (8.10) in the main text]: $\langle\hat{n}_j(t)\rangle_{+\theta} = \langle\hat{n}_{j'}(t)\rangle_{-\theta}$. This relation just tells us that when flipping the statistical angle θ, the density expectation values are related by inversion, which agrees with our results in Figs. 9.1(f) and (g) in the main text. For $\theta = 0$ or π, we have $\langle\hat{n}_j(t)\rangle_{0,+\pi} = \langle\hat{n}_{j'}(t)\rangle_{0,-\pi} = \langle\hat{n}_{j'}(t)\rangle_{0,+\pi}$; that is, for the boson case ($\theta = 0$) or the pseudofermion case ($\theta = \pi$), the density expands symmetrically whether or not $U = 0$.

There remains another dynamical symmetry [Eq. (8.9) in the main text]: when changing the sign of the interaction U, one gets the same behavior as changing the sign of θ, i.e., the two density expansions are related by inversion symmetry. Let us now derive this relation.

Like in Eq. (F.4), we label $\hat{H}_B$ with the sign of U:

$$\hat{H}_{B,\pm U} = -J\sum_{j=1}^{L}\left(\hat{b}_j^\dagger \hat{b}_{j+1} e^{i\theta\hat{n}_j} + \text{H.c.}\right) \pm \frac{U}{2}\sum_{j=1}^{L}\hat{n}_j(\hat{n}_j - 1). \tag{F.10}$$

Replacing $\hat{H}_{B,+\theta}$ with $\hat{H}_{B,+U}$ in Eq. (F.6), we get

$$\langle \hat{n}_j(t)\rangle_{+U} = \langle \Psi_0 | \, e^{-i\hat{H}_{B,+U}t} \; \hat{n}_{j'} \; e^{i\hat{H}_{B,+U}t} \, |\Psi_0\rangle \, . \tag{F.11}$$

Now let us define a number parity operator, $\mathcal{P} = e^{i\pi\sum_r \hat{n}_{2r+1}}$, which measures the parity of total particle number on the odd sites. This operator anti-commutes with the first term of Eq. (F.10), but commutes with the second term. Therefore,

$$\begin{aligned}\mathcal{P}\hat{H}_{B,+U}\mathcal{P}^\dagger &= J\sum_{j=1}^{L}\left(\hat{b}_j^\dagger \hat{b}_{j+1} e^{i\theta\hat{n}_j} + \text{H.c.}\right) + \frac{U}{2}\sum_{j=1}^{L}\hat{n}_j(\hat{n}_j - 1) \\ &\equiv -\hat{H}_{B,-U}.\end{aligned} \tag{F.12}$$

Thus,

$$\mathcal{P}e^{-i\hat{H}_{B,+U}t}\mathcal{P}^\dagger = e^{i\hat{H}_{B,-U}t}. \tag{F.13}$$

Substituting the above equation into Eq. (F.11) results in

$$\begin{aligned}
\langle \hat{n}_j(t)\rangle_{+U} &= \langle \Psi_0 |\, e^{-i\hat{H}_{B,+U}t}\ \hat{n}_{j'}\ e^{i\hat{H}_{B,+U}t}\, |\Psi_0\rangle \\
&= \langle \Psi_0 |\, \mathcal{P}^\dagger e^{i\hat{H}_{B,-U}t}\mathcal{P}\ \hat{n}_{j'}\ \mathcal{P}^\dagger e^{-i\hat{H}_{B,-U}t}\mathcal{P}\, |\Psi_0\rangle \\
&= \langle \Psi_0 |\, e^{i\hat{H}_{B,-U}t}\ \hat{n}_{j'}\ e^{-i\hat{H}_{B,-U}t}\, |\Psi_0\rangle \\
&= \langle \hat{n}_{j'}(t)\rangle_{-U}.
\end{aligned} \tag{F.14}$$

Once again, we arrive at a simple expression [Eq. (8.9) in the main text], $\langle \hat{n}_j(t)\rangle_{+U} = \langle \hat{n}_{j'}(t)\rangle_{-U}$, which confirms that by changing the sign of interaction U, the density expansion of anyons undergoes an inversion operation. For zero interaction strength, we have $\langle \hat{n}_j(t)\rangle_{U=+0} = \langle \hat{n}_{j'}(t)\rangle_{U=-0} = \langle \hat{n}_{j'}(t)\rangle_{U=+0}$. Therefore, the density expansion of anyons is symmetric when $U = 0$, regardless of whether θ is a multiple of π.

More generally, it is straightforward to show that the dynamical symmetry relations shown in Eqs. (F.9) and (F.14) hold for a class of initial states satisfying $\mathcal{K}\,|\Psi\rangle = e^{i\phi}(|\Psi\rangle)^*$ for some ϕ.

F.2 Perturbation analysis of asymmetric expansion

In this section, we provide intuition while deriving the asymmetric expansion using perturbation theory. Specifically, we show that the interference between the lowest two order terms in the unitary evolution generally gives rise to asymmetric density expansion dynamics. Once again, we focus on the transformed bosonic Hamiltonian ($\hat{H}_B$) for simplicity.

Using a Taylor expansion, the unitary time evolution operator can be written as

$$\mathcal{U} = e^{-i\hat{H}_B t} = \sum_{n=0}^{\infty} \frac{(-i\hat{H}_B t)^n}{n!} = 1 - i\hat{H}_B t + \frac{(i\hat{H}_B t)^2}{2!} - \cdots . \tag{F.15}$$

We assume the initial state $|\psi_0\rangle$ to be a product state (in Fock space) that is inversion symmetric around the lattice center (i.e., $\mathcal{I}\,|\psi_0\rangle = |\psi_0\rangle$). The final state after time evolution can be expanded as a sum of product states in Fock space. We consider, as target states, a pair of such product states which are related by inversion symmetry, $|\psi_2\rangle = \mathcal{I}\,|\psi_1\rangle$, and show that their overlaps with the time-evolved state are different due to the interference of the kth and $(k+1)$th order terms in the expansion.

We denote the matrix element corresponding to the kth order term evolving $|\psi_0\rangle$ to $|\psi_1\rangle$ as

$$M_k^{(1)} = \left\langle \psi_1 \left| \frac{(-i\hat{H}_B t)^k}{k!} \right| \psi_0 \right\rangle = \frac{(-it)^k}{k!} A_k, \tag{F.16}$$

where we have defined $A_k = \langle\psi_1|\hat{H}_B^k|\psi_0\rangle$. Similarly, $M_k^{(2)}$ is the matrix element from $|\psi_0\rangle$ to $|\psi_2\rangle$ due to the kth order term:

$$M_k^{(2)} = \left\langle \psi_2 \left| \frac{(-i\hat{H}_B t)^k}{k!} \right| \psi_0 \right\rangle = \frac{(-it)^k}{k!} B_k, \tag{F.17}$$

where $B_k = \langle\psi_2|\hat{H}_B^k|\psi_0\rangle$. Using the symmetry properties of the Hamiltonian, we

can get:

$$\begin{aligned} B_k &= \langle\psi_2|\, \hat{H}_B^k \,|\psi_0\rangle = \langle\psi_1|\, \mathcal{I}^\dagger \hat{H}_B^k \mathcal{I} \,|\psi_0\rangle \\ &= e^{i(\phi_2-\phi_0)} \langle\psi_1|\, \mathcal{I}^\dagger \mathcal{R}^\dagger \hat{H}_B^k \mathcal{R}\mathcal{I} \,|\psi_0\rangle \\ &= e^{i(\phi_2-\phi_0)} \langle\psi_1|\, (\mathcal{T}\hat{H}_B^k \mathcal{T}^{-1}) \,|\psi_0\rangle \\ &= e^{i(\phi_2-\phi_0)} (\langle\psi_1|\, \hat{H}_B^k \,|\psi_0\rangle)^* \\ &= e^{i(\phi_2-\phi_0)} A_k^*, \end{aligned} \tag{F.18}$$

where in the second line, we have used the symmetry relation between $|\psi_1\rangle$ and $|\psi_2\rangle$ and the fact that $|\psi_0\rangle$ is symmetric under $\mathcal{I}$; in the third line, we extract the phase factor associated with the action of the $\mathcal{R}$ symmetry operator [defined in Eq. (F.2)] on states $|\psi_{0,2}\rangle$: $\mathcal{R}\,|\psi_{0,2}\rangle = e^{i\phi_{0,2}}\,|\psi_{0,2}\rangle$; in the fourth line, we have used the symmetry property given by Eq. (F.1); and in the fifth line, we have used the fact that the time-reversal operator acting on $\hat{H}_B$ is equivalent to changing the matrix element to its complex conjugate.

From here forward, let k be the lowest order for which $M_k^{(1)}$ [or, equivalently, $M_k^{(2)}$] is non-zero. Because the Hamiltonian $\hat{H}_B$ can have non-zero interactions U, the $(k+1)$th expansion terms could also evolve the initial state to $|\psi_{1,2}\rangle$. Therefore, we consider the leading two order terms which contribute to the matrix element for $\langle\psi_{1,2}|\mathcal{U}\,|\psi_0\rangle$: $M_k^{(1,2)}$ and $M_{k+1}^{(1,2)}$. We define $S_{1,2}$ to be amplitudes including the total

contribution of the kth and $(k+1)$th orders:

$$S_1 = \left| M_k^{(1)} + M_{k+1}^{(1)} \right| = \frac{t^k}{k!} \left| A_k + \frac{-it}{k+1} A_{k+1} \right|, \tag{F.19}$$

$$S_2 = \left| M_k^{(2)} + M_{k+1}^{(2)} \right| = \frac{t^k}{k!} \left| B_k + \frac{-it}{k+1} B_{k+1} \right|. \tag{F.20}$$

Using Eq. (F.18), Eq. (F.20) can be re-written as

$$\begin{aligned} S_2 &= \frac{t^k}{k!} \left| B_k + \frac{-it}{k+1} B_{k+1} \right| = \frac{t^k}{k!} \left| A_k^* + \frac{-it}{k+1} A_{k+1}^* \right| \\ &= \frac{t^k}{k!} \left| A_k - \frac{-it}{k+1} A_{k+1} \right|. \end{aligned} \tag{F.21}$$

Comparing Eqs. (F.19) and (F.21), we can see that because the sign before A_{k+1} is different, the two amplitudes S_1 and S_2 are in general not equal to each other. This is a simple way of understanding the observed asymmetric expansion in the left and right directions.

The following remarks regarding S_1 and S_2 are in order: (i) If we set $\theta = 0$ or $\theta = \pi$, the matrix elements A_k and A_{k+1} are both real numbers. In this case, S_1 and S_2 are exactly equal to each other. This implies that for zero statistical angle θ, the perturbation analysis predicts symmetric density expansion, consistent with our numerics. (ii) On the other hand, for non-zero θ, A_k and A_{k+1} are generally complex numbers, and S_1 and S_2 are not necessarily equal, therefore predicting asymmetric expansion in general. (iii) When θ reverses its sign, all the matrix elements change to their complex conjugates, and therefore the values of S_1 and S_2 are swapped. In this way, the anyons reverse their preferred propagation directions, in agreement

with the numerical results. (iv) When the interaction strength U is zero, the matrix element $M_{k+1}^{(1)}$ vanishes, since the Hamiltonian only has hopping terms and hopping once more could not get back to the same state configuration as $|\psi_{1,2}\rangle$. Therefore, S_1 and S_2 are the same when $U = 0$. (v) When U's sign is reversed, A_{k+1} also reverses its sign, therefore swapping the values of S_1 and S_2. Thus, the anyons once again reverse their preferred propagation directions.

The above analysis is completely consistent with the numerical results in the main text. We have once again demonstrated that the crucial ingredients for asymmetric expansion are non-zero statistics θ and interaction U. To illustrate more clearly the above derivations, we consider a very simple example for clarification. Let us choose $|\psi_0\rangle = |\cdots 0110 \cdots\rangle$, $|\psi_1\rangle = |\cdots 0011 \cdots\rangle$, $|\psi_2\rangle = |\cdots 1100 \cdots\rangle$. In this case, the second- and third-order terms in the perturbative time evolution could evolve $|\psi_0\rangle$ to $|\psi_1\rangle$ if U is non-zero. For second-order processes, there are two paths one can start from $|\psi_0\rangle$ and end up with $|\psi_1\rangle$: either $|\cdots 0110 \cdots\rangle \to |\cdots 0101 \cdots\rangle \to |\cdots 0011 \cdots\rangle$ or $|\cdots 0110 \cdots\rangle \to |\cdots 0020 \cdots\rangle \to |\cdots 0011 \cdots\rangle$. The two paths contribute to a total second-order matrix element $\langle\psi_1| \hat{H}_B^2 |\psi_0\rangle = J^2 + J^2 e^{i\theta}$. Due to the on-site interactions, there is also a third-order process which evolves $|\psi_0\rangle$ to $|\psi_1\rangle$: $|\cdots 0110 \cdots\rangle \to |\cdots 0020 \cdots\rangle \to |\cdots 0020 \cdots\rangle \to |\cdots 0011 \cdots\rangle$, whose matrix element is $\langle\psi_1| \hat{H}_B^3 |\psi_0\rangle = J^2 U e^{i\theta}$. The total amplitude for second and third order processes is $S_1 = \frac{t^2}{2}|J^2(1 + e^{i\theta}) + \frac{-it}{3} J^2 U e^{i\theta}|$. Similarly we can also obtain $S_2 = \frac{t^2}{2}|J^2(1 + e^{-i\theta}) + \frac{-it}{3} J^2 U e^{-i\theta}|$. For non-zero θ and U, $S_1 \neq S_2$, implying asymmetric expansion. The expressions also predict that the expansion changes its preferred direction when either θ or U reverses its sign.

F.3 Numerical comparison of anyonic and bosonic out-of-time-ordered correlators

In this section, we provide numerical results for the bosonic OTOC, $\widetilde{F}_{jk}(t) = \langle \hat{b}_j^\dagger(t)\hat{b}_k^\dagger(0)\hat{b}_j(t)\hat{b}_k(0)\rangle$, to illustrate that such experimentally measurable quantities can indeed capture the asymmetric information spreading.

Figure F.1 shows the bosonic OTOC growth, with parameters the same as Fig. 8.3 in the main text. As one can see, the bosonic OTOCs with non-zero statistical angle also exhibit asymmetric information propagation, similar to their anyonic counterparts.

Figure F.2 shows the butterfly velocities extracted from the bosonic OTOC. In order to make comparisons to anyonic results, we also plot data from Figs. 8.4(c) and (d) of the main text. As the figures illustrate, the bosonic butterfly velocities are highly asymmetric for the left and right propagation directions. Moreover, in the regimes of either small θ or large U, both the left and right velocities of the bosonic OTOC agree well with the anyonic OTOC. This can be understood intuitively, as the fractional Jordan-Wigner transformation has reduced effect at small θ, and large U corresponds to the hard-core limit, where anyonic statistics becomes less important. Moreover, the bosonic/anyonic plots in Fig. F.2 share qualitative features for all values of θ or U. This suggests that the bosonic OTOC also exhibits signatures of the asymmetric propagation of information due to anyonic statistics.

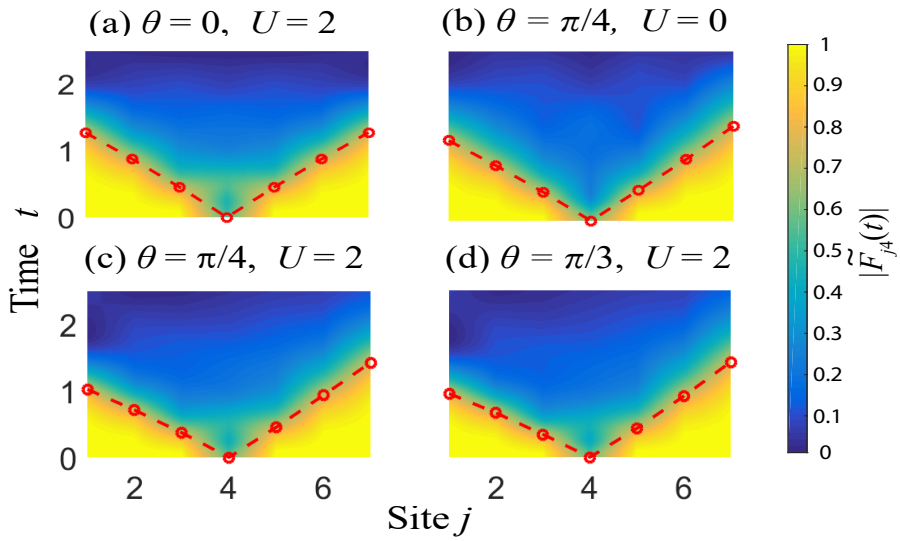

Figure F.1: Growth of the bosonic OTOC $|\widetilde{F}_{jk}(t)|$ for different statistical angles θ and interaction strengths U. (a) Bosonic case ($\theta = 0$) with interaction strength $U = 2$. Anyonic case with (b) vanishing and (c),(d) non-vanishing interaction strengths. As in Fig. 8.3, $L = 7$, $\beta^{-1} = 6$, the local Hilbert space of each site is truncated to three states, and the red dots denote the OTOC falling to 75% of its initial value.

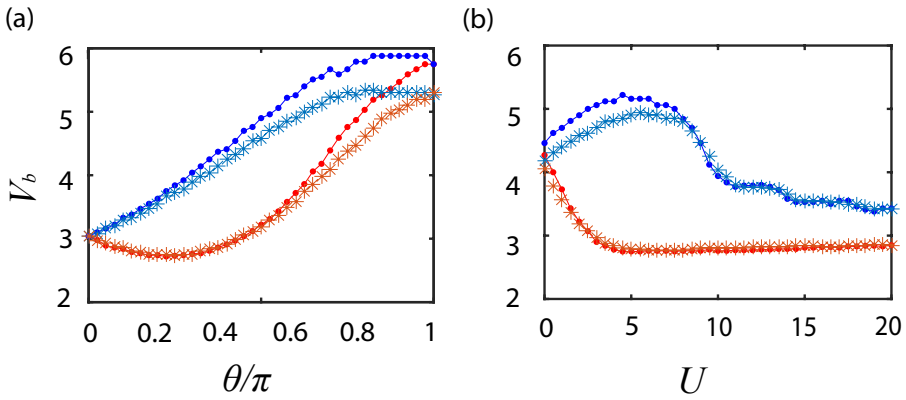

Figure F.2: Comparison of butterfly velocities extracted from the anyonic (dots) and bosonic (asterisks) OTOCs' growth. (a) The butterfly velocities' dependence on statistical angle θ for fixed $U = 2$. The blue dots/asterisks denote the butterfly velocities in the left direction, while the red dots/asterisks denote the butterfly velocities in the right direction. (b) Similar to (a), but for fixed statistical angle $\theta = \pi/2$ and varying interaction strength U.

Appendix G: Appendices to Chapter 9

G.1 Analytical Derivation of divergent derivatives in ground states

In this appendix, we provide a detailed analytical derivation to show that the first-order derivative indeed diverges at the critical points in the thermodynamic limit. We first derive how the derivative diverges when the reference state is in the trivial phase ($|\mu_R| > 1$), and then we generalize our results to show how this divergent behavior depends on the particular choice of the reference state. Throughout this section we assume the reference lies within a given phase, and allow the target state to approach an arbitrary point in the phase diagram. Our analytical derivations show that these divergences necessarily map out the phase boundary, as illustrated in Figs. 9.2(a) and (b) and Fig. G.1 below.

We begin with our general expression for the complexity as a function of our reference and target states. The Bogoliubov angle difference $\Delta\theta_k$ for each momentum sector k can be expressed as

$$\Delta\theta_k = \frac{1}{2}\arctan\frac{\sin k\left[\Delta_R\mu_T - \Delta_T\mu_R + (\Delta_R - \Delta_T)\cos k\right]}{(\mu_R + \cos k)(\mu_T + \cos k) + \Delta_R\Delta_T \sin^2 k}, \tag{G.1}$$

and the circuit complexity is written in terms of $\Delta\theta_k$:

$$\mathcal{C}/L = \frac{1}{2\pi}\int_0^\pi |\Delta\theta_k|^2\, dk. \tag{G.2}$$

Note that we have replaced the discrete sum in the main text with an integral for the thermodynamic limit, and written "$\mathcal{C}\left(|\Psi^R_{\rm gs}\rangle \to |\Psi^T_{\rm gs}\rangle\right)$" as "$\mathcal{C}$" for brevity.

Now we substitute Eq. (G.1) into Eq. (G.2), and take the derivatives with respect to μ_T and Δ_T. We obtain

$$\begin{aligned}
\partial_{\mu_T}\mathcal{C}/L &= \frac{\Delta_T}{4\pi}\int_{-\pi}^{\pi}\frac{\Delta\theta_k \sin k}{(\mu_T+\cos k)^2+\Delta_T^2\sin^2 k}\, dk,\\
\partial_{\Delta_T}\mathcal{C}/L &= -\frac{1}{4\pi}\int_{-\pi}^{\pi}\frac{\Delta\theta_k \sin k\,(\mu_T+\cos k)}{(\mu_T+\cos k)^2+\Delta_T^2\sin^2 k}\, dk.
\end{aligned} \tag{G.3}$$

Here, we have used the fact that these functions are even in k to extend the integrals to $-\pi$. In spite of the complicated nature of these integrals, much can be learned about their analytic properties by recasting them as closed contour integrals in the complex plane. Defining the variable $z = e^{ik}$, we find that the integrals take the form

$$\begin{aligned}
\partial_{\mu_T}\mathcal{C}/L &= -i\Delta_T\oint\frac{dz}{2\pi i}\frac{\Delta\theta(z)(z^2-1)}{(z^2+2\mu_T z+1)^2-\Delta_T^2(z^2-1)^2},\\
\partial_{\Delta_T}\mathcal{C}/L &= \frac{i}{2}\oint\frac{dz}{2\pi i z}\frac{\Delta\theta(z)\,(z^2-1)\,(z^2+2\mu_T z+1)}{(z^2+2\mu_T z+1)^2-\Delta_T^2(z^2-1)^2},
\end{aligned} \tag{G.4}$$

where the integration is taken counter-clockwise over the contour $|z| = 1$. In this

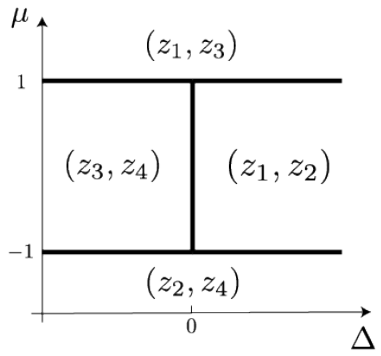

Figure G.1: The phase diagram of the Kitaev chain, where in each phase we list which of the two branch points given in Eq. (G.8) lie inside the contour integrals in Eq. (G.4). The integrals can only diverge at the phase transitions, where the branch points cross the contour,

form, we may use the fact that the value of the integrals is entirely determined by the non-analyticities of the integrand which are located inside the contour, and that the value of the integration will only diverge if there is a divergence located on the contour.

We proceed by defining the following variables,

$$z_{1,a} = \frac{-\mu_a + \sqrt{\mu_a^2 + \Delta_a^2 - 1}}{1 + \Delta_a}, \tag{G.5}$$

$$z_{2,a} = \frac{-\mu_a - \sqrt{\mu_a^2 + \Delta_a^2 - 1}}{1 + \Delta_a}, \tag{G.6}$$

$$z_{3,a} = \frac{-\mu_a + \sqrt{\mu_a^2 + \Delta_a^2 - 1}}{1 - \Delta_a}, \tag{G.7}$$

$$z_{4,a} = \frac{-\mu_a - \sqrt{\mu_a^2 + \Delta_a^2 - 1}}{1 - \Delta_a}, \tag{G.8}$$

where $a = R, T$. From Eq. (G.4), both derivatives contain simple poles at $z_{i,T}$ for $i = 1, 2, 3, 4$, while $\partial_{\Delta_T}\mathcal{C}$ additionally has a simple pole at $z = 0$. Also, using the formula $\arctan(z) = (i/2)\log\frac{1-iz}{1+iz}$, we can write the Bogoliubov angle as

$$\Delta\theta(z) = \frac{i}{4}\log\left[\frac{(\Delta_T+1)(z-z_{1,T})(z-z_{2,T})}{(\Delta_T-1)(z-z_{3,T})(z-z_{4,T})}\right. \tag{G.9}$$

$$\left.\times\,\frac{(\Delta_R-1)(z-z_{3,R})(z-z_{4,R})}{(\Delta_R+1)(z-z_{1,R})(z-z_{2,R})}\right]. \tag{G.10}$$

The important fact we will need is that the complex logarithm contains branch cuts running from the zeros to the infinities of its argument; therefore, the z_{ia} are really branch points of the integrand. We now note that the derivatives of the complexity will only diverge if the couplings are tuned to a phase transition. This is because the $z_{i,a}$ can only have unit modulus if we are at one of the phase transitions, and at the phase transitions the branch points cross the contour resulting in a divergent integral, see Fig. G.1. In particular, we may characterize the phase diagram in terms of which branch points are inside or outside the contour integral.

In addition, we may actually compute the integrals exactly in certain cases and limits, which allows us to obtain the exact analytic dependence of the divergence on the couplings. As a definite example, we consider the case $|\mu_T| > 1$. In this case, there is a branch cut inside the logarithm running from $z_{1,T}$ to $z_{3,T}$, and one outside between $z_{2,T}$ and $z_{4,T}$, and the divergences seen at $\mu_T \to 1$ will be due to these branch cuts approaching the contour. In this case we may entirely factor out the

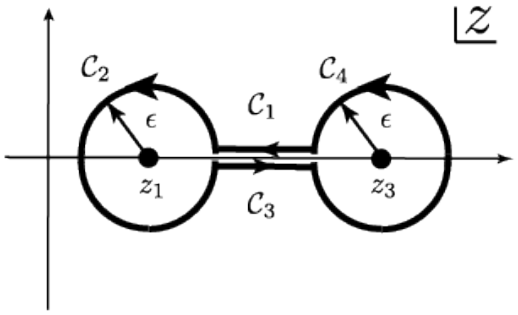

Figure G.2: The deformation of the integration contour used to compute the gradients of the circuit complexity in the case $\mu_T > 1$. There is a branch cut running between the branch points z_1 and z_3, where the imaginary part of the integrand is discontinuous and the integrand diverges near the branch points.

dependence on the reference state from the logarithm and focus on the terms which depend on the target state. We deform the contour so that it skirts the branch cut [see the parametrization into four contours in Fig. G.2]. A key point here is that the argument of the logarithm is $-\pi$ upon approaching the branch cut from the bottom-half plane, while it is $+\pi$ upon approaching it from the top half. Therefore, in the sum of the two contours running along the branch cut, the logarithm simply contributes a phase factor and we may evaluate the resulting simplified integrand by elementary methods, and for small ϵ we find

$$\int_{\mathcal{C}_1} + \int_{\mathcal{C}_3} = \frac{1}{16\sqrt{\mu_T^2+\Delta_T^2-1}} \log \left| \frac{(z_3-z_2)(z_1-z_4)\epsilon^2}{(z_1-z_2)(z_3-z_4)(z_1-z_3)^2} \right| . \tag{G.11}$$

We perform the integral around contour $\mathcal{C}_2$ by writing $z = z_1 + \epsilon e^{i\theta}$, and integrating from $-\pi < \theta < \pi$. At small ϵ, we find

$$\int_{\mathcal{C}_2} = -\frac{1}{16\sqrt{\mu_T^2+\Delta_T^2-1}} \log \left| \frac{(\Delta_T+1)\epsilon(z_1-z_2)}{(\Delta_T-1)(z_1-z_3)(z_1-z_4)} \right| . \tag{G.12}$$

The computation for contour $\mathcal{C}_4$ is similar, although the phase winds around the other way:

$$\int_{\mathcal{C}_4} = -\frac{1}{16\sqrt{\mu_T^2+\Delta_T^2-1}} \log \left| \frac{(\Delta_T-1)\epsilon(z_3-z_4)}{(\Delta_T+1)(z_3-z_1)(z_3-z_2)} \right| . \tag{G.13}$$

Finally, taking the sum of all four contours, we find that the $\log \epsilon$ divergence in each integral cancels, and we obtain the desired result:

$$\begin{aligned} \partial_{\mu_T}\mathcal{C}/L &= \frac{1}{8\sqrt{\mu_T^2+\Delta_T^2-1}} \log \left| \frac{\mu_T^2-1}{\mu_T^2+\Delta_T^2-1} \right| \\ &\quad + I_2(\mu_R, \Delta_R, \mu_T, \Delta_T), \end{aligned} \tag{G.14}$$

where the function I_2 depends on μ_R and Δ_R, but is analytic as the phase transition is approached. Therefore, when approaching from $\mu_T > 1$, the quantity $\partial_{\mu_T}\mathcal{C}/L$ diverges as $\log(\mu_T - 1)/8\Delta_T$ if $\Delta_T \neq 0$, but it is analytic if one approaches the multicritical point at $\Delta_T = 0$.

Similar manipulations may be made for $\partial_{\Delta_T}\mathcal{C}/L$ and in other phases. Sometimes the branch cuts take a complicated form in the complex plane so that we cannot reduce the expression into elementary integrals, but we can still deduce the form of the divergence by considering how the contour integrals behave as the branch points cross the contour.

Our final results are summarized as follows. The expression $\partial_{\mu_T}\mathcal{C}/L$ is always

analytic unless $\mu_T \to \pm 1$. Near these phase transitions, it diverges as

$$\partial_{\mu_T} \mathcal{C}/L \sim \frac{\text{sign}(\mu_T)}{8\sqrt{\mu_T^2 + \Delta_T^2 - 1}} \log \left| \frac{\mu_T^2 - 1}{\mu_T^2 + \Delta_T^2 - 1} \right|, \tag{G.15}$$

so the divergence is $\text{sign}(\mu_T) \log |\mu_T - 1|/8\Delta_T$ if $\Delta_T \neq 0$, but there is not a divergence at $\Delta_T = 0$.

In contrast, the expression $\partial_{\Delta_T} \mathcal{C}/L$ is analytic whenever $\Delta_T \neq 0$. In this case, the divergence depends on whether the couplings (μ_T, Δ_T) approach the phase transitions from the topological phase or the trivial phase. If we approach the multicritical points from the trivial phases, we find that $\partial_{\Delta_T} \mathcal{C}/L$ remains analytic. In contrast, if we approach $\Delta_T = 0$ from the topological phases, we find

$$\partial_{\Delta_T} \mathcal{C}/L \sim \frac{1}{4} \left(1 + \frac{|\mu_T \Delta_T|}{\sqrt{|\mu_T^2 + \Delta_T^2 - 1|}} \right) \log |\Delta_T| \,. \tag{G.16}$$

In this case, we have a $\log |\Delta_T|/4$ divergence when $|\mu_T| < 1$, but now we find that the divergence crosses over to $\log |\Delta_T|/2$ as we approach the multicritical points.

G.2 Real-space behavior of the optimal circuits

In this appendix, we show how that the real-space optimal circuit behaves differently depending on whether or not the initial and target states are in the same topological phase.

As we have derived in Appendix **??**, for a single momentum sector k, the circuit complexity is found to be the squared difference between the Bogoliubov angles

[Eq. (9.17)], and the optimal circuit is generated by the following time-independent Hamiltonian,

$$\mathcal{H}_k = -\Delta\theta_k \, O_{1,k}, \tag{G.17}$$

where $O_{1,k}$ is the same generator given by Eq. (9.9) for momentum sector k. Here, we have omitted the time label 's' for simplicity as the circuit is time independent (and the total evolution time is fixed to be constant 1). As in the main text and following the circuit complexity literature, we have defined $\mathcal{H}_k$ to be anti-Hermitian [Eq. (9.5)].

Since the ground state of the Hamiltonian is a product of all momentum sectors with $k > 0$, the optimal circuit which generates the evolution between two ground states can be written as

$$\mathcal{H} = \sum_{k>0} \mathcal{H}_k = \sum_{k>0} -\Delta\theta_k \, O_{1,k}. \tag{G.18}$$

We are interested in the real-space behavior of the above Hamiltonian. To discern this, we first write the above Hamiltonian in operator form

$$\mathcal{H} = \sum_{k>0} \mathcal{H}_k = \sum_{k>0} -i\Delta\theta(k) \hat{\psi}_k^\dagger \tau_1 \hat{\psi}_k, \tag{G.19}$$

where τ_i are the Pauli matrices, and $\hat{\psi}_k$ denotes the Nambu spinor

$$\hat{\psi}_k = \begin{pmatrix} \hat{a}_k \\ \hat{a}_{-k}^\dagger \end{pmatrix}. \tag{G.20}$$

Utilizing the particle-hole symmetry of the Nambu spinor

$$\hat{\psi}_{-k} = \tau_1(\hat{\psi}_k^\dagger)^T, \tag{G.21}$$

we can extend the sum in the evolution Hamiltonian to be over the entire Brillouin zone

$$\mathcal{H} = \sum_k -i\omega(k)\hat{\psi}_k^\dagger \tau_1 \hat{\psi}_k, \tag{G.22}$$

where $\omega(k)$ satisfies

$$\omega(k) - \omega(-k) = \Delta\theta(k) \tag{G.23}$$

for $k > 0$. In particular, only the odd part of the function contributes since the even part cancels in the τ_1 pairing channel.

We now proceed by performing a Fourier series expansion of the function $\omega(k)$ over the Brillouin zone. Without loss of generality we may consider only the odd Fourier series since the even terms will cancel. Thus, we write

$$\omega(k) = \sum_{n=1}^{\infty} \omega_n \sin(nk) = \frac{\Delta\theta(k)}{2}, \tag{G.24}$$

where the last equality is used to determine the Fourier coefficients.

Our crucial observation is that when the two states are within the same phase, the Fourier sine series for $\Delta\theta(k)$ ought to be *uniformly convergent*. This can be seen by considering the boundary conditions, which in this case read $\Delta\theta(0) = \Delta\theta(\pi) = 0$, as shown in Fig. 9.1(d) in the main text. Thus, if we allow the time-evolved state

$|\Psi_T'\rangle$ to be within an arbitrarily small error ϵ to the real target state $|\Psi_T\rangle$, this Fourier series can be accurately truncated to a finite order N^* over the entire Brillouin zone.

This is relevant because in real-space, the Fourier harmonic $\sin(lk)\,\hat{\psi}_k^\dagger \tau_1 \hat{\psi}_k$ is generated by a term involving two fermionic operators separated by l sites. More specifically, as this occurs in the τ_1 channel, $\mathcal{H}$ must involve real-space pairing terms such that

$$\mathcal{H} = \sum_j \sum_{n=1}^{N^*} \omega_n \left(\hat{a}_j \hat{a}_{j+n} - \text{H.c.}\right). \tag{G.25}$$

The above argument holds when the system size L is taken to be infinite. In such a case, the finite-range interacting evolution Hamiltonian can be regarded as a truly short-range Hamiltonian, and our results imply that the optimal circuit (with constant time or depth) which evolve states within the same phase region is *short-range*.

On the other hand, when the two states are in different phases, the boundary conditions $\Delta\theta(\pi) = \pi/2 \neq \Delta\theta(0) = 0$ obstruct uniform convergence, analogous to the Gibbs phenomenon. In this case, the Fourier sine series may still converge pointwise, but for fixed error the series *cannot* be truncated to finite order N^* over the entire Brillouin zone. In such cases, the optimal evolution Hamiltonian $\mathcal{H}$ that transforms states between different topological phases must be *long-range* when the evolution time is fixed to be a constant. Again, this is because the longest real-space distance required to generate the evolution Hamiltonian is given by the highest order of Fourier mode appearing in the momentum space series, which now cannot be accurately truncated.

G.3 Numerical evidence for nonanalyticity of quench dynamics

In this appendix, we provide detailed numerical explanations for the nonanalyticity of the long-time steady-state value of the circuit complexity at critical points, as observed in Fig. 9.3(b).

As derived in the main text, the time-dependent circuit complexity is given by

$$\mathcal{C}(|\Psi_i\rangle \to |\Psi(t)\rangle) = \sum_{k_n} \phi_{k_n}^2(t), \tag{G.26}$$

where

$$\phi_{k_n}(t) = \arccos \sqrt{1 - \sin^2(2\Delta\theta_{k_n}) \sin^2(\varepsilon_{k_n} t)}. \tag{G.27}$$

Then the long-time steady-state complexity is just given by the time-averaged value of the above expression,

$$\overline{\mathcal{C}(|\Psi_i\rangle \to |\Psi(t)\rangle)} = \sum_{k_n} \overline{\phi_{k_n}^2(t)}, \tag{G.28}$$

where the overline denotes time averaging. Because $\phi_{k_n}^2(t)$ is such a complex expression, it is unknown to us how to derive an analytical function for the time-averaged circuit complexity. Instead, we plot $\overline{\phi_{k_n}(t)}$ numerically, and show that the nonanalyticity indeed occurs at the phase transition.

From the expression of $\phi_{k_n}(t)$, it is clear that its value oscillates with time, and it reaches its maximal value (envelope) for each momentum sector k_n when $\sin(\epsilon_{k_n} t) = 1$. In Fig. G.3(a), we plot the maximum value of $\phi_{k_n}(t)$ for different post-

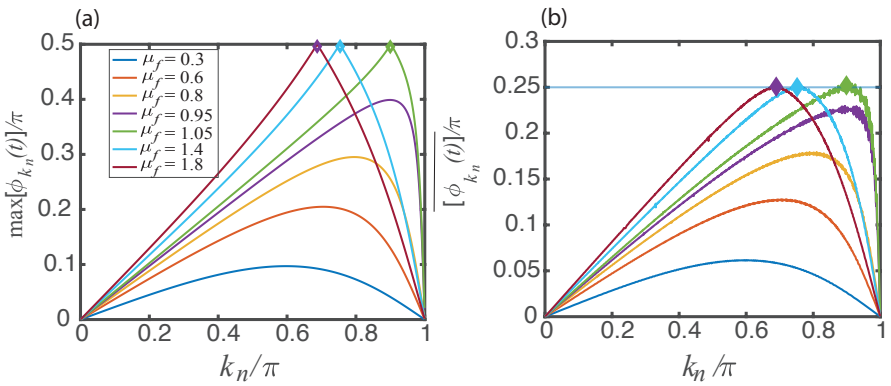

Figure G.3: (a) Maximum value of $\phi_{k_n}(t)$ versus k_n for different post-quench Hamiltonian parameters. (b) Time-averaged value of $\phi_{k_n}(t)$ versus k_n for different post-quench Hamiltonian parameters. In both panels, $\mu_i = 0$, $\Delta_i = \Delta_f = 1$, and $L = 1000$. The diamond markers denote the expected locations of the maxima across the phase transition, given by solutions to $1 + \mu_f \cos k_n = 0$ (see text).

quench Hamiltonian parameters. As the figure clearly shows, when the chemical potential μ_f of the post-quench Hamiltonian is below the critical value ($\mu_f = 1$), $\max[\phi_{k_n}(t)]$ is a smooth function of k_n. However, when μ_f is above the critical value, $\max[\phi_{k_n}(t)]$ exhibits a kink at a certain momentum k_n, with its maximal value reaching $\frac{\pi}{2}$. To understand this behavior, we can write down the expression for $\max[\phi_{k_n}(t)]$ given the choice of parameters $\mu_i = 0, \Delta_i = \Delta_f = 1$:

$$\max[\phi_{k_n}(t)] = \arccos \left| \frac{1 + \mu_f \cos k_n}{\sqrt{\mu_f^2 + 2\mu_f \cos k_n + 1}} \right|. \tag{G.29}$$

From the above expression, it is clear that when $\mu_f < 1$, $\max[\phi_{k_n}(t)]$ is always smaller than $\pi/2$; when $\mu_f > 1$, $\max[\phi_{k_n}(t)]$ can obtain the maximal value of $\pi/2$ when $1 + \mu_f \cos k_n = 0$. Because one needs to take the absolute value for the arguments of arccos, the quantity $\max[\phi_{k_n}(t)]$ exhibits a kink when reaching $\pi/2$, in agreement with Fig. G.3(a).

We plot the time-averaged value of $\phi_{k_n}(t)$ in Fig. G.3(b). Again, we see an upper bound of $\overline{\phi_{k_n}(t)}$ when quenching across the critical point. Similar to Fig. G.3(a), $\overline{\phi_{k_n}(t)}$ reaches its maximal value when $1 + \mu_f \cos k_n = 0$, i.e. when $\sin(2\Delta\theta_{k_n}) = 1$. For this special momentum sector, the expression for $\phi_{k_n}(t)$ can be written as

$$\phi_{k_n}(t) = \arcsin |\sin(\varepsilon_{k_n} t)|. \tag{G.30}$$

Clearly, the time-averaged value of the above expression is just $\pi/4$, in agreement with the numerical results shown in Fig. G.3(b). Therefore, after the phase transition takes place, the maximal value of $\overline{\phi_{k_n}(t)}$ is bounded by $\pi/4$. (This feature is independent of the parameters of the pre-quench Hamiltonian.)

Having revealed this feature of $\overline{\phi_{k_n}(t)}$, the nonanalyticity can be understood as follows: as μ_f increases but is still below the phase transition point, the integral of $\overline{\phi^2_{k_n}(t)}$ increases smoothly with μ_f. After reaching the phase transition, $\overline{\phi^2_{k_n}(t)}$ saturates the bound, and thus the integral's (circuit complexity's) dependence on μ_f takes a different form. In particular, for the parameters shown in Fig. G.3 [blue line in Fig. 9.3(b)], the integral (i.e., the circuit complexity) becomes a constant after the phase transition. This leads to a clear nonanalytical (kink) point at $\mu_f = 1$.

G.4 Circuit complexity for two-dimensional $p+ip$ topological superconductors

In this appendix, we show how our results for the 1D Kitaev chain can be generalized to 2D. In particular, we consider a $p+ip$ topological superconductor for which the Hamiltonian can be written in momentum space as:

$$\hat{H} = \sum_{\boldsymbol{k}} \hat{\psi}^{\dagger}_{\boldsymbol{k}} \mathcal{H}_{\boldsymbol{k}} \hat{\psi}_{\boldsymbol{k}}, \tag{G.31}$$

where the summation is taken over the 2D Brillouin zone, and $\hat{\psi}_k = \begin{pmatrix} \hat{a}_k \\ \hat{a}^{\dagger}_{-k} \end{pmatrix}$ is the Nambu spinor. The single-particle Hamiltonian takes the following form:

$$\mathcal{H}_{\boldsymbol{k}} = \begin{pmatrix} \varepsilon_{\boldsymbol{k}} & \Delta^{*}_{\boldsymbol{k}} \\ \Delta_{\boldsymbol{k}} & -\varepsilon_{\boldsymbol{k}} \end{pmatrix}, \tag{G.32}$$

where $\varepsilon_{\boldsymbol{k}}$ and $\Delta_{\boldsymbol{k}}$ denote the kinetic and pairing terms in 2D respectively. The ground state wavefunction can be written as

$$|\Psi_{\mathrm{gs}}\rangle = \prod_{\boldsymbol{k}} (\cos\theta_{\boldsymbol{k}} - i \sin\theta_{\boldsymbol{k}} \hat{a}^{\dagger}_{\boldsymbol{k}} \hat{a}^{\dagger}_{-\boldsymbol{k}}) |0\rangle , \tag{G.33}$$

where $\tan(2\theta_{\boldsymbol{k}}) = |\Delta_{\boldsymbol{k}}|/\varepsilon_{\boldsymbol{k}}$. Similar to 1D, the circuit complexity of the full wavefunction is given by

$$\mathcal{C} = \sum_{\boldsymbol{k}} |\Delta\theta_{\boldsymbol{k}}|^2 = \frac{L^2}{(2\pi)^2} \int \mathrm{d}^2\boldsymbol{k} |\Delta\theta(\boldsymbol{k})|^2, \tag{G.34}$$

where we have replaced the summmation by an integral in the infinite-system limit. In this continuum limit, $\varepsilon(\boldsymbol{k}) \approx \frac{k^2}{2m} - \mu$ and $\Delta(\boldsymbol{k}) \approx i\Delta(k_x + ik_y)$.

We expect that the non-analyticity should not depend on the particular choice of initial reference state, so we take $\mu_R \to -\infty$ [with $\theta^R(\boldsymbol{k}) = 0$] for simplicity. This corresponds to the trivial vacuum with no particle. Upon tuning μ, the system undergoes a quantum phase transition into the topological phase at $\mu = 0$. Taking the derivative of $\mathcal{C}$ with respect to μ_T, we obtain

$$\begin{aligned} \partial_{\mu_T}\mathcal{C} &= \frac{L^2}{(2\pi)^2} \int \mathrm{d}^2\boldsymbol{k}\ 2\theta^T(\boldsymbol{k}) \partial_{\mu_T}\theta^T(\boldsymbol{k}) \\ &= \frac{L^2}{(2\pi)^2} \int \mathrm{d}^2\boldsymbol{k} \theta^T(\boldsymbol{k}) \partial_{\mu_T} \left[\arctan \frac{|\Delta(\boldsymbol{k})|}{\varepsilon(\boldsymbol{k})}\right] \\ &= \frac{L^2}{(2\pi)^2} \int \mathrm{d}^2\boldsymbol{k} \frac{\theta^T(\boldsymbol{k})|\Delta(\boldsymbol{k})|}{E(\boldsymbol{k})^2}. \end{aligned} \tag{G.35}$$

Bibliography

[1] I. I. Rabi, J. R. Zacharias, S. Millman, and P. Kusch. A new method of measuring nuclear magnetic moment. *Phys. Rev.*, 53:318.

[2] T. D. Ladd, F. Jelezko, R. Laflamme, Y. Nakamura, C. Monroe, and J. L. O'Brien. Quantum computers. *Nature*, 464(7285):45, 2010.

[3] A. Steane. Quantum computing. *Rep. Prog. Phys.*, 61(2):117, 1998.

[4] A. Ekert and R. Jozsa. Quantum computation and shor's factoring algorithm. *Rev. Mod. Phys.*, 68(3):733, 1996.

[5] P. W. Shor. Polynomial-time algorithms for prime factorization and discrete logarithms on a quantum computer. *SIAM Rev.*, 41(2):303, 1999.

[6] L. K. Grover. Quantum mechanics helps in searching for a needle in a haystack. *Phys. Rev. Lett.*, 79:325, 1997.

[7] C. Monroe, W. C. Campbell, L.-M. Duan, Z.-X. Gong, A. V. Gorshkov, P. W. Hess, R. Islam, K. Kim, N. M. Linke, G. Pagano, P. Richerme, C. Senko, and N. Y. Yao. Programmable quantum simulations of spin systems with trapped ions. *Rev. Mod. Phys.*, 93:025001, 2021.

[8] J. Preskill. Quantum computing in the NISQ era and beyond. *Quantum*, 2:79, 2018.

[9] R. P Feynman. Simulating physics with computers. *Int. J. Theor. Phys*, 21(6), 1982.

[10] D. Leibfried, R. Blatt, C. Monroe, and D. Wineland. Quantum dynamics of single trapped ions. *Rev. Mod. Phys.*, 75:281, 2003.

[11] D. J. Wineland and D. Leibfried. Quantum information processing and metrology with trapped ions. *Laser Phys. Lett.*, 8(3):175, 2011.

[12] M. Saffman, T. G. Walker, and K. Mølmer. Quantum information with rydberg atoms. *Rev. Mod. Phys.*, 82:2313, 2010.

[13] H. Bernien, S. Schwartz, A. Keesling, H. Levine, A. Omran, H. Pichler, S. Choi, A. S. Zibrov, M. Endres, M. Greiner, V. Vuletić, and M. D. Lukin. Probing many-body dynamics on a 51-atom quantum simulator. *Nature*, 551:579, 2017.

[14] A. Aspuru-Guzik and P. Walther. Photonic quantum simulators. *Nat. Phys.*, 8(4):285, 2012.

[15] J. L. O'brien, A. Furusawa, and J. Vučković. Photonic quantum technologies. *Nat. Photonics*, 3(12):687, 2009.

[16] M. Hofheinz, H. Wang, M. Ansmann, R. C. Bialczak, E. Lucero, M. Neeley, A. D. O'connell, D. Sank, J. Wenner, J. M. Martinis, et al. Synthesizing arbitrary quantum states in a superconducting resonator. *Nature*, 459(7246):546, 2009.

[17] L. DiCarlo, J. M Chow, J. M. Gambetta, L. S. Bishop, B. R. Johnson, D. I. Schuster, J. Majer, A. Blais, L. Frunzio, S. M. Girvin, et al. Demonstration of two-qubit algorithms with a superconducting quantum processor. *Nature*, 460(7252):240, 2009.

[18] J. Zhang, G. Pagano, P. W. Hess, A. Kyprianidis, P. Becker, H. Kaplan, A. V. Gorshkov, Z.-X. Gong, and C. Monroe. Observation of a many-body dynamical phase transition with a 53-qubit quantum simulator. *Nature*, 551:601, 2017.

[19] M. Aidelsburger, M. Atala, M. Lohse, J. T. Barreiro, B. Paredes, and I. Bloch. Realization of the hofstadter hamiltonian with ultracold atoms in optical lattices. *Phys. Rev. Lett.*, 111(18):185301, 2013.

[20] N. Goldman, J. C. Budich, and P. Zoller. Topological quantum matter with ultracold gases in optical lattices. *Nat. Phys.*, 12(7):639, 2016.

[21] N. R. Cooper, J. Dalibard, and I. B. Spielman. Topological bands for ultracold atoms. *Rev. Mod. Phys.*, 91:015005, 2019.

[22] A. V. Gorshkov, M. Hermele, V. Gurarie, C. Xu, P. S. Julienne, J. Ye, P. Zoller, E. Demler, M. D. Lukin, and A. M. Rey. Two-orbital SU (N) magnetism with ultracold alkaline-earth atoms. *Nat. Phys.*, 6(4):289, 2010.

[23] X. Zhang, M. Bishof, S. L. Bromley, C. V. Kraus, M. S. Safronova, P. Zoller, A. M. Rey, and J. Ye. Spectroscopic observation of SU(N)-symmetric interactions in Sr orbital magnetism. *Science*, 345(6203):1467, 2014.

[24] L. W. Clark, L. Feng, and C. Chin. Universal space-time scaling symmetry in the dynamics of bosons across a quantum phase transition. *Science*, 354(6312):606, 2016.

[25] L. Feng, J. Hu, L. W. Clark, and C. Chin. Correlations in high-harmonic generation of matter-wave jets revealed by pattern recognition. *Science*, 363(6426):521, 2019.

[26] D. Kielpinski, C. Monroe, and D. J. Wineland. Architecture for a large-scale ion-trap quantum computer. *Nature*, 417(6890):709, 2002.

[27] C. D. Bruzewicz, R. Chiaverini, J.and McConnell, and J. M. Sage. Trapped-ion quantum computing: Progress and challenges. *Appl. Phys. Rev.*, 6(2):021314, 2019.

[28] Y. Wang, M. Um, J. Zhang, S. An, M. Lyu, J.-N. Zhang, L. M. Duan, D. Yum, and K. Kim. Single-qubit quantum memory exceeding ten-minute coherence time. *Nat. Photonics*, 11(10):646, 2017.

[29] T. P. Harty, D. T. C. Allcock, C. J. Ballance, L. Guidoni, H. A. Janacek, N. M. Linke, D. N. Stacey, and D. M. Lucas. High-fidelity preparation, gates, memory, and readout of a trapped-ion quantum bit. *Phys. Rev. Lett.*, 113:220501, 2014.

[30] Rainer Blatt and Christian F Roos. Quantum simulations with trapped ions. *Nat. Phys.*, 8(4):277, 2012.

[31] W. Paul. Electromagnetic traps for charged and neutral particles. *Rev. Mod. Phys.*, 62:531, 1990.

[32] L. S. Brown and G. Gabrielse. Geonium theory: Physics of a single electron or ion in a penning trap. *Rev. Mod. Phys.*, 58:233, 1986.

[33] K. Mølmer and A. Sørensen. Multiparticle entanglement of hot trapped ions. *Phys. Rev. Lett.*, 82:1835, 1999.

[34] A. C. Lee, J. Smith, P. Richerme, B. Neyenhuis, P. W. Hess, J. Zhang, and C. Monroe. Engineering large stark shifts for control of individual clock state qubits. *Phys. Rev. A*, 94:042308, 2016.

[35] G. Semeghini, H. Levine, A. Keesling, S. Ebadi, T. T. Wang, D. Bluvstein, R. Verresen, H. Pichler, M. Kalinowski, R. Samajdar, et al. Probing topological spin liquids on a programmable quantum simulator. *arXiv:2104.04119*, 2021.

[36] H. Levine, A. Keesling, A. Omran, H. Bernien, S. Schwartz, A. S. Zibrov, M. Endres, M. Greiner, V. Vuletić, and M. D. Lukin. High-Fidelity Control and Entanglement of Rydberg-Atom Qubits. *Phys. Rev. Lett.*, 121:123603, 2018.

[37] C. S. Adams, J. D. Pritchard, and J. P. Shaffer. Rydberg atom quantum technologies. *J. Phys. B*, 53(1):012002, 2019.

[38] Antoine Browaeys and Thierry Lahaye. Many-body physics with individually controlled rydberg atoms. *Nat. Phys.*, 16(2):132, 2020.

[39] M. Endres, H. Bernien, A. Keesling, H. Levine, E. R Anschuetz, A. Krajenbrink, C. Senko, V. Vuletic, M. Greiner, and M. D Lukin. Atom-by-atom assembly of defect-free one-dimensional cold atom arrays. *Science*, 354(6315):1024, 2016.

[40] D. Barredo, S. D. Léséleuc, V. Lienhard, T. Lahaye, and A. Browaeys. An atom-by-atom assembler of defect-free arbitrary two-dimensional atomic arrays. *Science*, 354(6315):1021, 2016.

[41] D. Barredo, V. Lienhard, S. de Léséleuc, T. Lahaye, and A. Browaeys. Synthetic three-dimensional atomic structures assembled atom by atom. *Nature*, 561(7721):79, 2018.

[42] C. J. Turner, A. A. Michailidis, D. A. Abanin, M. Serbyn, Papić, and Z. . Weak ergodicity breaking from quantum many-body scars. *Nat. Phys.*, 14(7):745, 2018.

[43] W. W. Ho, S. Choi, H. Pichler, and M. D. Lukin. Periodic orbits, entanglement, and quantum many-body scars in constrained models: Matrix product state approach. *Phys. Rev. Lett.*, 122:040603, 2019.

[44] R. Samajdar, S. Choi, H. Pichler, M. D. Lukin, and S. Sachdev. Numerical study of the chiral $\mathbb{Z}_3$ quantum phase transition in one spatial dimension. *Phys. Rev. A*, 98:023614, 2018.

[45] S. Whitsitt, R. Samajdar, and S. Sachdev. Quantum field theory for the chiral clock transition in one spatial dimension. *Phys. Rev. B*, 98:205118, 2018.

[46] M. Rader and A. M. Läuchli. Floating phases in one-dimensional rydberg ising chains. *arXiv:1908.02068*, 2019.

[47] A. Keesling, A. Omran, H. Levine, H. Bernien, H. Pichler, S. Choi, R. Samajdar, S. Schwartz, P. Silvi, S. Sachdev, P. Zoller, M. Endres, M. Greiner, Vuletić, V. , and M. D. Lukin. Quantum Kibble-Zurek mechanism and critical dynamics on a programmable Rydberg simulator. *Nature*, 568:207, 2019.

[48] P. Schauß, M. Cheneau, M. Endres, T. Fukuhara, S. Hild, A. Omran, T. Pohl, C. Gross, S. Kuhr, and I. Bloch. Observation of spatially ordered structures in a two-dimensional Rydberg gas. *Nature*, 491:87, 2012.

[49] R. Islam, C. Senko, W. C. Campbell, S. Korenblit, J. Smith, A. Lee, E. E. Edwards, C.-C. J. Wang, J. K. Freericks, and C. Monroe. Emergence and Frustration of Magnetism with Variable-Range Interactions in a Quantum Simulator. *Science*, 340:583, 2013.

[50] F. Dolde, I. Jakobi, B. Naydenov, N. Zhao, S. Pezzagna, C. Trautmann, J. Meijer, P. Neumann, F. Jelezko, and J. Wrachtrup. Room-temperature entanglement between single defect spins in diamond. *Nat. Phys.*, 9:139, 2013.

[51] M. Lu, N. Q. Burdick, and B. L. Lev. Quantum degenerate dipolar fermi gas. *Phys. Rev. Lett.*, 108:215301, 2012.

[52] L. Childress, M. V. G. Dutt, J. M. Taylor, A. S. Zibrov, F. Jelezko, J. Wrachtrup, P. R. Hemmer, and M. D. Lukin. Coherent Dynamics of Coupled Electron and Nuclear Spin Qubits in Diamond. *Science*, 314:281, 2006.

[53] J. R. Weber, W. F. Koehl, J. B. Varley, A. Janotti, B. B. Buckley, C. G. Van de Walle, and D. D. Awschalom. Quantum computing with defects. *Proc. Natl. Acad. Sci. U.S.A.*, 107:8513, 2010.

[54] S. Gopalakrishnan, B. L. Lev, and P. M. Goldbart. Frustration and glassiness in spin models with cavity-mediated interactions. *Phys. Rev. Lett.*, 107:277201, 2011.

[55] J. S. Douglas, H. Habibian, C.-L. Hung, A. V. Gorshkov, H. J. Kimble, and D. E. Chang. Quantum many-body models with cold atoms coupled to photonic crystals. *Nat. Photonics*, 9:326, 2015.

[56] C.-L. Hung, A. González-Tudela, J. I. Cirac, and H. J. Kimble. Quantum spin dynamics with pairwise-tunable, long-range interactions. *Proc. Natl. Acad. Sci. U.S.A.*, 113:E4946, 2016.

[57] J. W. Britton, B. C. Sawyer, A. C. Keith, C.-C. J. Wang, J. K. Freericks, H. Uys, M. J. Biercuk, and J. J. Bollinger. Engineered two-dimensional Ising interactions in a trapped-ion quantum simulator with hundreds of spins. *Nature*, 484:489, 2012.

[58] P. Richerme, Z.-X. Gong, A. Lee, C. Senko, J. Smith, M. Foss-Feig, S. Michalakis, A. V. Gorshkov, and C. Monroe. Non-local propagation of correlations in quantum systems with long-range interactions. *Nature*, 511:198, 2014.

[59] P. Jurcevic, B. P. Lanyon, P. Hauke, C. Hempel, P. Zoller, R. Blatt, and C. F. Roos. Quasiparticle engineering and entanglement propagation in a quantum many-body system. *Nature*, 511:202, 2014.

[60] J. Smith, A. Lee, P. Richerme, B. Neyenhuis, P. W. Hess, P. Hauke, M. Heyl, D. A. Huse, and C. Monroe. Many-body localization in a quantum simulator with programmable random disorder. *Nat. Phys.*, 12:907, 2016.

[61] K.-K. Ni, S. Ospelkaus, M. H. G. de Miranda, A. Pe'er, B. Neyenhuis, J. J. Zirbel, S. Kotochigova, P. S. Julienne, D. S. Jin, and J. Ye. A High Phase-Space-Density Gas of Polar Molecules. *Science*, 322:231, 2008.

[62] K.-K. Ni, S. Ospelkaus, D. Wang, G. Quéméner, B. Neyenhuis, M. H. G. de Miranda, J. L. Bohn, J. Ye, and D. S. Jin. Dipolar collisions of polar molecules in the quantum regime. *Nature*, 464:1324, 2010.

[63] A. Chotia, B. Neyenhuis, S. A. Moses, B. Yan, J. P. Covey, M. Foss-Feig, A. M. Rey, D. S. Jin, and J. Ye. Long-Lived Dipolar Molecules and Feshbach Molecules in a 3D Optical Lattice. *Phys. Rev. Lett.*, 108:080405, 2012.

[64] P. K. Molony, P. D. Gregory, Z. Ji, B. Lu, M. P. Köppinger, C. R. Le Sueur, C. L. Blackley, J. M. Hutson, and S. L. Cornish. Creation of ultracold $^{87}Rb^{133}Cs$ molecules in the rovibrational ground state. *Phys. Rev. Lett.*, 113:255301, 2014.

[65] K. Aikawa, A. Frisch, M. Mark, S. Baier, A. Rietzler, R. Grimm, and F. Ferlaino. Bose-einstein condensation of erbium. *Phys. Rev. Lett.*, 108:210401, 2012.

[66] G. Balasubramanian, P. Neumann, D. Twitchen, M. Markham, R. Kolesov, N. Mizuochi, J. Isoya, J. Achard, J. Beck, J. Tissler, V. Jacques, P. R. Hemmer, F. Jelezko, and J. Wrachtrup. Ultralong spin coherence time in isotopically engineered diamond. *Nat. Mater.*, 8:383, 2009.

[67] L. Béguin, A. Vernier, R. Chicireanu, T. Lahaye, and A. Browaeys. Direct Measurement of the van der Waals Interaction between Two Rydberg Atoms. *Phys. Rev. Lett.*, 110:263201, 2013.

[68] Y. O. Dudin and A. Kuzmich. Strongly Interacting Rydberg Excitations of a Cold Atomic Gas. *Science*, 336:887, 2012.

[69] E. H. Lieb and D. W. Robinson. The finite group velocity of quantum spin systems. *Commun. Math. Phys.*, 28:251–257, 1972.

[70] Z.-X. Gong, M. Foss-Feig, S. Michalakis, and Alexey V. G. Persistence of locality in systems with power-law interactions. *Phys. Rev. Lett.*, 113:030602, 2014.

[71] M. Foss-Feig, Z.-X. Gong, C. W. Clark, and A. V. Gorshkov. Nearly linear light cones in long-range interacting quantum systems. *Phys. Rev. Lett.*, 114:157201, 2015.

[72] P. Hauke and L. Tagliacozzo. Spread of correlations in long-range interacting quantum systems. *Phys. Rev. Lett.*, 111:207202, 2013.

[73] J. Schachenmayer, B. P. Lanyon, C. F. Roos, and A. J. Daley. Entanglement growth in quench dynamics with variable range interactions. *Phys. Rev. X*, 3:031015, 2013.

[74] L. Vanderstraeten, M. V. Damme, H. P. Büchler, and F. Verstraete. Quasiparticles in quantum spin chains with long-range interactions. *Phys. Rev. Lett.*, 121:090603, 2018.

[75] A. S. Buyskikh, M. Fagotti, J. Schachenmayer, F. Essler, and A. J. Daley. Entanglement growth and correlation spreading with variable-range interactions in spin and fermionic tunneling models. *Phys. Rev. A*, 93:053620, 2016.

[76] M. B. Hastings and T. Koma. Spectral Gap and Exponential Decay of Correlations. *Commun. Math. Phys.*, 265:781, 2006.

[77] M. F. Maghrebi, Z.-X. Gong, and A.V. Gorshkov. Continuous symmetry breaking in 1d long-range interacting quantum systems. *Phys. Rev. Lett.*, 119:023001, 2017.

[78] N. D. Mermin and H. Wagner. Absence of ferromagnetism or antiferromagnetism in one- or two-dimensional isotropic heisenberg models. *Phys. Rev. Lett.*, 17:1133, 1966.

[79] M. Kormos, M. Collura, G. Takács, and P. Calabrese. Real-time confinement following a quantum quench to a non-integrable model. *Nat. Phys.*, 13:246, 2017.

[80] J. Greensite. An introduction to the confinement problem. *Lect. Notes Phys.*, 821:1, 2011.

[81] N. Vandersickel and D. Zwanziger. The Gribov problem and QCD dynamics. *Phys. Rep.*, 520:175, 2012.

[82] R. Coldea, D. A. Tennant, E. M. Wheeler, E. Wawrzynska, D. Prabhakaran, M. Telling, K. Habicht, P. Smeibidl, and K. Kiefer. Quantum Criticality in an Ising Chain: Experimental Evidence for Emergent E_8 Symmetry. *Science*, 327:177, 2010.

[83] S. B. Rutkevich. Energy Spectrum of Bound-Spinons in the Quantum Ising Spin-Chain Ferromagnet. *J. Stat. Phys.*, 131:917, 2008.

[84] C. M. Morris, R. Valdés Aguilar, A. Ghosh, S. M. Koohpayeh, J. Krizan, R. J. Cava, O. Tchernyshyov, T. M. McQueen, and N. P. Armitage. Hierarchy of Bound States in the One-Dimensional Ferromagnetic Ising Chain $CoNb_2O_6$ Investigated by High-Resolution Time-Domain Terahertz Spectroscopy. *Phys. Rev. Lett.*, 112:137403, 2014.

[85] J. A. Kjäll, F. Pollmann, and J. E. Moore. Bound states and E_8 symmetry effects in perturbed quantum ising chains. *Phys. Rev. B*, 83:020407, 2011.

[86] G. Delfino. Quantum quenches with integrable pre-quench dynamics. *J. Phys. A*, 47(40):402001, 2014.

[87] G. Delfino and J. Viti. On the theory of quantum quenches in near-critical systems. *J. Phys. A*, 50(8):084004, 2017.

[88] P. Calabrese, F. H. L. Essler, and M. Fagotti. Quantum Quench in the Transverse-Field Ising Chain. *Phys. Rev. Lett.*, 106(22):227203, 2011.

[89] G. Delfino. Correlation spreading and properties of the quantum state in quench dynamics. *Phys. Rev. E*, 97:062138, 2018.

[90] B. M. McCoy and T. T. Wu. Two-dimensional ising field theory in a magnetic field: Breakup of the cut in the two-point function. *Phys. Rev. D*, 18:1259, 1978.

[91] B. M. McCoy and T. T. Wu. Theory of a two-dimensional ising model with random impurities. i. thermodynamics. *Phys. Rev.*, 176:631, 1968.

[92] B. M. McCoy and J.-M. Maillard. The importance of the ising model. *Prog. Theor. Phys.*, 127(5):791, 2012.

[93] M. C. Bañuls, J. I. Cirac, and M. B. Hastings. Strong and weak thermalization of infinite nonintegrable quantum systems. *Phys. Rev. Lett.*, 106:050405, 2011.

[94] C.-J. Lin and O. I. Motrunich. Quasiparticle explanation of the weak-thermalization regime under quench in a nonintegrable quantum spin chain. *Phys. Rev. A*, 95(2):023621, 2017.

[95] J. Zhang, P. W. Hess, A. Kyprianidis, P. Becker, A. Lee, J. Smith, G. Pagano, I.-D. Potirniche, A. C. Potter, A. Vishwanath, N. Y. Yao, and C. Monroe. Observation of a discrete time crystal. *Nature*, 543:217, 2017.

[96] P. W. Hess, P. Becker, H. B. Kaplan, A. Kyprianidis, A. C. Lee, B. Neyenhuis, G. Pagano, P. Richerme, C. Senko, J. Smith, W. L. Tan, J. Zhang, and C. Monroe. Non-thermalization in trapped atomic ion spin chains. *Philos. Trans. Royal Soc. A*, 375:20170107, 2017.

[97] F. Machado, G. D. Kahanamoku-Meyer, D. V. Else, C. Nayak, and N. Y. Yao. Exponentially slow heating in short and long-range interacting floquet systems. *Phys. Rev. Research*, 1:033202, 2019.

[98] S. Sachdev. *Quantum phase transitions*. Oxford University Press, 2011.

[99] T. Koffel, M. Lewenstein, and L. Tagliacozzo. Entanglement Entropy for the Long-Range Ising Chain in a Transverse Field. *Phys. Rev. Lett.*, 109(26):267203, 2012.

[100] M. Knap, A. Kantian, T. Giamarchi, I. Bloch, M. D. Lukin, and E. Demler. Probing real-space and time-resolved correlation functions with many-body ramsey interferometry. *Phys. Rev. Lett.*, 111:147205, 2013.

[101] S. Fey and K. P. Schmidt. Critical behavior of quantum magnets with long-range interactions in the thermodynamic limit. *Phys. Rev. B*, 94:075156, 2016.

[102] Sebastian Fey, Sebastian C. Kapfer, and Kai Phillip Schmidt. Quantum criticality of two-dimensional quantum magnets with long-range interactions. *Phys. Rev. Lett.*, 122:017203, 2019.

[103] P. Jurcevic, H. Shen, P. Hauke, C. Maier, T. Brydges, C. Hempel, B. P. Lanyon, M. Heyl, R. Blatt, and C. F. Roos. Direct observation of dynamical quantum phase transitions in an interacting many-body system. *Phys. Rev. Lett.*, 119:080501, 2017.

[104] P. Calabrese and J. Cardy. Time dependence of correlation functions following a quantum quench. *Phys. Rev. Lett.*, 96:136801, 2006.

[105] D. J. Luitz and Y. B. Lev. The ergodic side of the many-body localization transition. *Ann. Phys. (Berlin)*, 529:1600350, 2017.

[106] A. Nauts and R. E. Wyatt. New approach to many-state quantum dynamics: The recursive-residue-generation method. *Phys. Rev. Lett.*, 51:2238, 1983.

[107] V. Zauner-Stauber and J. C. Halimeh. Probing the anomalous dynamical phase in long-range quantum spin chains through fisher-zero lines. *Phys. Rev. E*, 96:062118, 2017.

[108] J. C. Halimeh, V. Zauner-Stauber, I. P. McCulloch, I. de Vega, U. Schollwöck, and M. Kastner. Prethermalization and persistent order in the absence of a thermal phase transition. *Phys. Rev. B*, 95:024302, 2017.

[109] J. C. Halimeh and V. Zauner-Stauber. Dynamical phase diagram of quantum spin chains with long-range interactions. *Phys. Rev. B*, 96:134427, 2017.

[110] S. B. Rutkevich. On the weak confinement of kinks in the one-dimensional quantum ferromagnet $CoNb_2O_6$. *J. Stat. Mech. Theory Exp.*, 7:07015, 2010.

[111] E. C. Titchmarsh and D. R. Heath-Brown. *The theory of the Riemann zeta-function*. Oxford University Press, 1986.

[112] L. F. Santos, F. Borgonovi, and G. L. Celardo. Cooperative Shielding in Many-Body Systems with Long-Range Interaction. *Phys. Rev. Lett.*, 116(25):250402, 2016.

[113] A. J. A. James, R. M. Konik, and N. J. Robinson. Nonthermal states arising from confinement in one and two dimensions. *Phys. Rev. Lett.*, 122:130603, 2019.

[114] P. P. Mazza, G. Perfetto, A. Lerose, M. Collura, and A. Gambassi. Suppression of transport in nondisordered quantum spin chains due to confined excitations. *Phys. Rev. B*, 99:180302, 2019.

[115] T. Rakovszky, M. Mestyán, M. Collura, M. Kormos, and G. Takács. Hamiltonian truncation approach to quenches in the Ising field theory. *Nucl. Phys. B*, 911:805, 2016.

[116] N. J. Robinson, A. J. A. James, and R. M. Konik. Signatures of rare states and thermalization in a theory with confinement. *Phys. Rev. B*, 99:195108, 2019.

[117] J. R. Garrison and T. Grover. Does a single eigenstate encode the full hamiltonian? *Phys. Rev. X*, 8:021026, 2018.

[118] I.-D. Potirniche, A. C. Potter, M. Schleier-Smith, A. Vishwanath, and N. Y. Yao. Floquet Symmetry-Protected Topological Phases in Cold-Atom Systems. *Phys. Rev. Lett.*, 119(12):123601, 2017.

[119] C. W. von Keyserlingk and S. L. Sondhi. Phase structure of one-dimensional interacting floquet systems. i. abelian symmetry-protected topological phases. *Phys. Rev. B*, 93:245145, 2016.

[120] C. W. von Keyserlingk and S. L. Sondhi. Phase structure of one-dimensional interacting floquet systems. ii. symmetry-broken phases. *Phys. Rev. B*, 93:245146, 2016.

[121] A. C. Potter, T. Morimoto, and A. Vishwanath. Classification of interacting topological floquet phases in one dimension. *Phys. Rev. X*, 6:041001, 2016.

[122] D. V. Else and C. Nayak. Classification of topological phases in periodically driven interacting systems. *Phys. Rev. B*, 93:201103, 2016.

[123] G. Delfino and P. Grinza. Confinement in the q-state Potts field theory. *Nucl. Phys. B*, 791:265, 2008.

[124] L. Lepori, G. Z. Tóth, and G. Delfino. The particle spectrum of the three-state Potts field theory: a numerical study. *J. Stat. Mech. Theory Exp.*, 2009:11007, 2009.

[125] S. B. Rutkevich. Baryon masses in the three-state Potts field theory in a weak magnetic field. *J. Stat. Mech. Theory Exp.*, 1:01010, 2015.

[126] M. Lencsés and G. Takács. Confinement in the q-state Potts model: an RG-TCSA study. *J. High Energy Phys.*, 9:146, 2015.

[127] N. et. al. Brambilla. Qcd and strongly coupled gauge theories: challenges and perspectives. *Eur. Phys. J. C*, 74(10):1, 2014.

[128] G. Delfino and G. Mussardo. The spin-spin correlation function in the two-diensional Ising model in a magnetic field at $T = T_c$. *Nucl. Phys. B*, 455(3):724, 1995.

[129] P. Fonseca and A. Zamolodchikov. Ising spectroscopy i: Mesons at $t < t_c$. *arXiv preprint hep-th/0612304*, 2006.

[130] B. Lake, A. M. Tsvelik, S. Notbohm, D. Alan Tennant, T. G. Perring, M. Reehuis, C. Sekar, G. Krabbes, and B. Büchner. Confinement of fractional quantum number particles in a condensed-matter system. *Nat. Phys.*, 6(1):50, 2010.

[131] A. Lerose, B. Žunkovič, A. Silva, and A. Gambassi. Quasilocalized excitations induced by long-range interactions in translationally invariant quantum spin chains. *Phys. Rev. B*, 99:121112, 2019.

[132] F. Liu, R. Lundgren, P. Titum, G. Pagano, J. Zhang, C. Monroe, and A. V. Gorshkov. Confined quasiparticle dynamics in long-range interacting quantum spin chains. *Phys. Rev. Lett.*, 122:150601, 2019.

[133] A. Lerose, F. M. Surace, P. P. Mazza, G. Perfetto, M. Collura, and A. Gambassi. Quasilocalized dynamics from confinement of quantum excitations. *Phys. Rev. B*, 102:041118, 2020.

[134] R. Verdel, F. Liu, S. Whitsitt, A. V. Gorshkov, and M. Heyl. Real-time dynamics of string breaking in quantum spin chains. *Phys. Rev. B*, 102:014308, 2020.

[135] I. M. Georgescu, S. Ashhab, and F. Nori. Quantum simulation. *Rev. Mod. Phys.*, 86:153, 2014.

[136] F. Görg, K. Sandholzer, J. Minguzzi, R. Desbuquois, M. Messer, and T. Esslinger. Realization of density-dependent Peierls phases to engineer quantized gauge fields coupled to ultracold matter. *Nat. Phys.*, 15(11):1161, 2019.

[137] C. Schweizer, F. Grusdt, M. Berngruber, L. Barbiero, E. Demler, N. Goldman, I. Bloch, and M. Aidelsburger. Floquet approach to Z_2 lattice gauge theories with ultracold atoms in optical lattices. *Nat. Phys.*, 15(11):1168, 2019.

[138] A. Mil, T. V. Zache, A. Hegde, A. Xia, R. P. Bhatt, M. K. Oberthaler, P. Hauke, J. Berges, and F. Jendrzejewski. A scalable realization of local u (1) gauge invariance in cold atomic mixtures. *Science*, 367(6482):1128, 2020.

[139] C. Muschik, M. Heyl, E. Martinez, T. Monz, P. Schindler, B. Vogell, M. Dalmonte, P. Hauke, R. Blatt, and P. Zoller. U(1) Wilson lattice gauge theories in digital quantum simulators. *New J. Phys*, 19(10):103020, 2017.

[140] M. Brenes, M. Dalmonte, M. Heyl, and A. Scardicchio. Many-body localization dynamics from gauge invariance. *Phys. Rev. Lett.*, 120:030601, 2018.

[141] M. C. Banuls, R. Blatt, J. Catani, A. Celi, J. I. Cirac, M. Dalmonte, L. Fallani, K. Jansen, M. Lewenstein, S. Montangero, et al. Simulating lattice gauge theories within quantum technologies. *Eur. Phys. J. D*, 74(8):1, 2020.

[142] U. Borla, R. Verresen, F. Grusdt, and S. Moroz. Confined phases of one-dimensional spinless fermions coupled to Z_2 gauge theory. *Phys. Rev. Lett.*, 124:120503, 2020.

[143] Z. Davoudi, N. M. Linke, and G. Pagano. Toward simulating quantum field theories with controlled phonon-ion dynamics: A hybrid analog-digital approach. *arXiv:2104.09346*, 2021.

[144] Z. Davoudi, M. Hafezi, C. Monroe, G. Pagano, A. Seif, and A. Shaw. Towards analog quantum simulations of lattice gauge theories with trapped ions. *Phys. Rev. Research*, 2:023015, Apr 2020.

[145] L. Tagliacozzo, A. Celi, P. Orland, M. W. Mitchell, and M. Lewenstein. Simulation of non-abelian gauge theories with optical lattices. *Nat. Commun.*, 4(1):1, 2013.

[146] E. Zohar, J. I. Cirac, and B. Reznik. Cold-atom quantum simulator for su(2) yang-mills lattice gauge theory. *Phys. Rev. Lett.*, 110:125304, 2013.

[147] D. Banerjee, M. Dalmonte, M. Müller, E. Rico, P. Stebler, U.-J. Wiese, and P. Zoller. Atomic quantum simulation of dynamical gauge fields coupled to fermionic matter: From string breaking to evolution after a quench. *Phys. Rev. Lett.*, 109:175302, 2012.

[148] E. Zohar, J. I. Cirac, and Be. Reznik. Simulating compact quantum electrodynamics with ultracold atoms: Probing confinement and nonperturbative effects. *Phys. Rev. Lett.*, 109:125302, 2012.

[149] D. Porras and J. I. Cirac. Effective quantum spin systems with trapped ions. *Phys. Rev. Lett.*, 92:207901, 2004.

[150] J. G. Bohnet, B. C. Sawyer, J. W. Britton, M. L. Wall, A. M. Rey, M. Foss-Feig, and J. J. Bollinger. Quantum spin dynamics and entanglement generation with hundreds of trapped ions. *Science*, 352(6291):1297, 2016.

[151] B. Žunkovič, M. Heyl, M. Knap, and A. Silva. Dynamical quantum phase transitions in spin chains with long-range interactions: Merging different concepts of nonequilibrium criticality. *Phys. Rev. Lett.*, 120:130601, 2018.

[152] G. Magnifico, Ma. Dalmonte, P. Facchi, S. Pascazio, F. V. Pepe, and E. Ercolessi. Real Time Dynamics and Confinement in the $\mathbb{Z}_n$ Schwinger-Weyl lattice model for 1+1 QED. *Quantum*, 4:281, 2020.

[153] K. Kim, M.-S. Chang, R. Islam, S. Korenblit, L.-M. Duan, and C. Monroe. Entanglement and tunable spin-spin couplings between trapped ions using multiple transverse modes. *Phys. Rev. Lett.*, 103:120502, 2009.

[154] G. Pagano, P. W. Hess, H. B. Kaplan, W. L. Tan, P. Richerme, P. Becker, A. Kyprianidis, J. Zhang, E. Birckelbaw, M. R. Hernandez, Y. Wu, and C. Monroe. Cryogenic trapped-ion system for large scale quantum simulation. *Quantum Sci. Technol.*, 4(1):014004, 2019.

[155] M. Cheneau, P. Barmettler, D. Poletti, M. Endres, P. Schauß, T. Fukuhara, C. Gross, I. Bloch, C. Kollath, and S. Kuhr. Light-cone-like spreading of correlations in a quantum many-body system. *Nature*, 481(7382):484, 2012.

[156] J. Eisert, M. Friesdorf, and C. Gogolin. Quantum many-body systems out of equilibrium. *Nat. Phys.*, 11(2):124, 2015.

[157] M. Schreiber, S. S. Hodgman, P. Bordia, H. P. Lüschen, M. H. Fischer, R. Vosk, E. Altman, U. Schneider, and I. Bloch. Observation of many-body localization of interacting fermions in a quasirandom optical lattice. *Science*, 349(6250):842, 2015.

[158] R. Nandkishore and D. A. Huse. Many-Body Localization and Thermalization in Quantum Statistical Mechanics. *Annu. Rev. Condens. Matter Phys.*, 6:15, 2015.

[159] A. D. Campo and W. H. Zurek. Universality of phase transition dynamics: Topological defects from symmetry breaking. *Int. J. Mod. Phys. A*, 29(8):1430018, 2014.

[160] D. Abanin, W. De Roeck, W. W. Ho, and F. Huveneers. A Rigorous Theory of Many-Body Prethermalization for Periodically Driven and Closed Quantum Systems. *Commun. Math. Phys.,*, 354(3):809, 2017.

[161] M. C. Tran, A. Ehrenberg, A. Y. Guo, P. Titum, D. A. Abanin, and A. V. Gorshkov. Locality and heating in periodically driven, power-law-interacting systems. *Phys. Rev. A*, 100:052103, 2019.

[162] F. Machado, D. V. Else, G. D. Kahanamoku-Meyer, C. Nayak, and N. Y. Yao. Long-range prethermal phases of nonequilibrium matter. *Phys. Rev. X*, 10:011043, 2020.

[163] F. H. L. Essler, S. Kehrein, S. R. Manmana, and N. J. Robinson. Quench dynamics in a model with tuneable integrability breaking. *Phys. Rev. B*, 89:165104, 2014.

[164] J. I. Cirac and P. Zoller. Goals and opportunities in quantum simulation. *Nat. Phys.*, 8(4):264, 2012.

[165] C. Gogolin and J. Eisert. Equilibration, thermalisation, and the emergence of statistical mechanics in closed quantum systems. *Rep. Prog. Phys.*, 79(5):056001, 2016.

[166] J. Preskill. Simulating quantum field theory with a quantum computer. In *The 36th Annual International Symposium on Lattice Field Theory. 22-28 July*, 2018.

[167] S. P. Jordan, K. S. M. Lee, and J. Preskill. Quantum Computation of Scattering in Scalar Quantum Field Theories. *Quantum Inf. Comput.*, 2:1014, 2014.

[168] S. P. Jordan, H. Krovi, K. S. M. Lee, and J. Preskill. BQP-completeness of scattering in scalar quantum field theory. *Quantum*, 2:44, 2018.

[169] J. B. Kogut. An introduction to lattice gauge theory and spin systems. *Rev. Mod. Phys.*, 51:659, 1979.

[170] B. M. McCoy and T. T. Wu. Speculations on quark observation. *Phys. Lett. B*, 72(2):219, 1977.

[171] F. M. Surace, A. Russomanno, M. Dalmonte, A. Silva, R. Fazio, and F. Iemini. Floquet time crystals in clock models. *Phys. Rev. B*, 99:104303, 2019.

[172] H. Weimer, M. Müller, I. Lesanovsky, P. Zoller, and H. P. Büchler. A Rydberg quantum simulator. *Nat. Phys.*, 6(5):382, 2010.

[173] S. Notarnicola, M. Collura, and S. Montangero. Real-time-dynamics quantum simulation of $(1 + 1)$-dimensional lattice QED with Rydberg atoms. *Phys. Rev. Research*, 2:013288, 2020.

[174] W. L. Tan, P. Becker, F. Liu, G. Pagano, K. S. Collins, A. De, L. Feng, H. B. Kaplan, A. Kyprianidis, R. Lundgren, W. Morong, S. Whitsitt, A. V. Gorshkov, and C. Monroe. Domain-wall confinement and dynamics in a quantum simulator. *Nat. Phys.*, pages 1–6, 2021.

[175] I. Bloch, J. Dalibard, and S. Nascimbène. Quantum simulations with ultracold quantum gases. *Nat. Phys.*, 8(4):267, 2012.

[176] Á. Rapp, G. Zaránd, C. Honerkamp, and W. Hofstetter. Color superfluidity and "baryon" formation in ultracold fermions. *Phys. Rev. Lett.*, 98(16):1, 2007.

[177] P. Fendley, K. Sengupta, and S. Sachdev. Competing density-wave orders in a one-dimensional hard-boson model. *Phys. Rev. B*, 69:075106, 2004.

[178] N. Chepiga and F. Mila. Floating phase versus chiral transition in a 1d hard-boson model. *Phys. Rev. Lett.*, 122:017205, 2019.

[179] S. Ostlund. Incommensurate and commensurate phases in asymmetric clock models. *Phys. Rev. B*, 24(1):398, 1981.

[180] D. A. Huse and M. E. Fisher. Domain walls and the melting of commensurate surface phases. *Phys. Rev. Lett.*, 49(11):793, 1982.

[181] A. B. Zamolodchikov. Integrals of motion and s-matrix of the (scaled) t = tc ising model with magnetic field. *Int. J. Mod. Phys. A*, 04(16):4235, 1989.

[182] A. Omran, H. Levine, A. Keesling, G. Semeghini, T. T. Wang, S. Ebadi, H. Bernien, A. S. Zibrov, H. Pichler, S. Choi, J. Cui, M. Rossignolo, P. Rembold, S. Montangero, T. Calarco, M. Endres, M. Greiner, V. Vuletić, and M. D. Lukin. Generation and manipulation of schrödinger cat states in rydberg atom arrays. *Science*, 365(6453):570, 2019.

[183] S. Elitzur, R. B. Pearson, and J. Shigemitsu. Phase structure of discrete abelian spin and gauge systems. *Phys. Rev. D*, 19:3698, 1979.

[184] M. B. Einhorn, R. Savit, and E. Rabinovici. A physical picture for the phase transitions in zn symmetric models. *Nucl. Phys. B*, 170(1):16, 1980.

[185] S. Coleman, R. Jackiw, and L. Susskind. Charge shielding and quark confinement in the massive schwinger model. *Ann. Phys.*, 93(1):267, 1975.

[186] S. Coleman. More about the massive schwinger model. *Ann. Phys.*, 101(1):239, 1976.

[187] G. Delfino and G. Mussardo. Non-integrable aspects of the multi-frequency sine-gordon model. *Nucl. Phys. B*, 516(3):675, 1998.

[188] R. Shankar and G. Murthy. Deconfinement in $d = 1$: Asymptotic and half-asymptotic particles. *Phys. Rev. B*, 72:224414, 2005.

[189] Z.-C. Yang, F. Liu, A. V. Gorshkov, and T. Iadecola. Hilbert-space fragmentation from strict confinement. *Phys. Rev. Lett.*, 124:207602, 2020.

[190] R. Samajdar, W. W. Ho, H. Pichler, M. D. Lukin, and S. Sachdev. Complex density wave orders and quantum phase transitions in a model of square-lattice rydberg atom arrays. *Phys. Rev. Lett.*, 124:103601, 2020.

[191] L. D'Alessio, Y. Kafri, A. Polkovnikov, and M. Rigol. From quantum chaos and eigenstate thermalization to statistical mechanics and thermodynamics. *Adv. Phys.*, 65(3):239, 2016.

[192] J. M. Deutsch. Quantum statistical mechanics in a closed system. *Phys. Rev. A*, 43:2046, 1991.

[193] M. Srednicki. Chaos and quantum thermalization. *Phys. Rev. E*, 50:888–901, 1994.

[194] C. J. Turner, A. A. Michailidis, D. A. Abanin, M. Serbyn, and Z. Papić. Quantum scarred eigenstates in a rydberg atom chain: Entanglement, breakdown of thermalization, and stability to perturbations. *Phys. Rev. B*, 98:155134, 2018.

[195] C. Chamon. Quantum glassiness in strongly correlated clean systems: An example of topological overprotection. *Phys. Rev. Lett.*, 94:040402, 2005.

[196] C. Castelnovo and C. Chamon. Topological quantum glassiness. *Philos. Mag.*, 92(1-3):304, 2012.

[197] J. Haah. Local stabilizer codes in three dimensions without string logical operators. *Phys. Rev. A*, 83:042330, 2011.

[198] S. Vijay, J. Haah, and L. Fu. Fracton topological order, generalized lattice gauge theory, and duality. *Phys. Rev. B*, 94:235157, 2016.

[199] M. Pretko. Subdimensional particle structure of higher rank $U(1)$ spin liquids. *Phys. Rev. B*, 95:115139, 2017.

[200] M. Pretko. Generalized electromagnetism of subdimensional particles: A spin liquid story. *Phys. Rev. B*, 96:035119, 2017.

[201] S. Pai, M. Pretko, and R. M. Nandkishore. Localization in fractonic random circuits. *Phys. Rev. X*, 9:021003, 2019.

[202] V. Khemani, M. Hermele, and R. Nandkishore. Localization from hilbert space shattering: From theory to physical realizations. *Phys. Rev. B*, 101:174204, 2020.

[203] P. Sala, T. Rakovszky, R. Verresen, M. Knap, and F. Pollmann. Ergodicity breaking arising from hilbert space fragmentation in dipole-conserving hamiltonians. *Phys. Rev. X*, 10:011047, 2020.

[204] S. Moudgalya, A. Prem, R. Nandkishore, N. Regnault, and B A. Bernevig. Thermalization and its absence within krylov subspaces of a constrained hamiltonian. *arXiv:1910.14048*, 2019.

[205] T. Rakovszky, P. Sala, R. Verresen, M. Knap, and F. Pollmann. Statistical localization: From strong fragmentation to strong edge modes. *Phys. Rev. B*, 101:125126, 2020.

[206] O. Sikora, N. Shannon, F. Pollmann, K. Penc, and P. Fulde. Extended quantum $U(1)$-liquid phase in a three-dimensional quantum dimer model. *Phys. Rev. B*, 84:115129, 2011.

[207] M. Žnidarič. Coexistence of diffusive and ballistic transport in a simple spin ladder. *Phys. Rev. Lett.*, 110:070602, 2013.

[208] M. Iadecola, T.and Žnidari č. Exact localized and ballistic eigenstates in disordered chaotic spin ladders and the fermi-hubbard model. *Phys. Rev. Lett.*, 123:036403, 2019.

[209] P. Patil and A. W. Sandvik. Hilbert space fragmentation and Ashkin-Teller criticality in fluctuation coupled Ising models. *Phys. Rev. B*, 101:014453, 2020.

[210] G. De Tomasi, D. Hetterich, P. Sala, and F. Pollmann. Dynamics of strongly interacting systems: From fock-space fragmentation to many-body localization. *Phys. Rev. B*, 100:214313, 2019.

[211] A. Hudomal, I. Vasić, N. Regnault, and Z. Papić. Quantum scars of bosons with correlated hopping. *Commun. Phys.*, 3(1):1, 2020.

[212] S. Pai and M. Pretko. Fractons from confinement in one dimension. *Phys. Rev. Research*, 2:013094, 2020.

[213] Y.-Z. Chou, R. M. Nandkishore, and L. Radzihovsky. Mott glass from localization and confinement. *Phys. Rev. B*, 97:184205, 2018.

[214] F. Hebenstreit, J. Berges, and D. Gelfand. Real-time dynamics of string breaking. *Phys. Rev. Lett.*, 111:201601, 2013.

[215] T. Iadecola and M. Schecter. Quantum many-body scar states with emergent kinetic constraints and finite-entanglement revivals. *Phys. Rev. B*, 101:024306, 2020.

[216] D. N. Page. Average entropy of a subsystem. *Phys. Rev. Lett.*, 71:1291–1294, 1993.

[217] A. Pal and D. A. Huse. Many-body localization phase transition. *Phys. Rev. B*, 82:174411, 2010.

[218] F. C. Alcaraz and R. Z. Bariev. An exactly solvable constrained XXZ chain. *arXiv:cond-mat/9904042*, 1999.

[219] T. Iadecola, L. H. Santos, and C. Chamon. Stroboscopic symmetry-protected topological phases. *Phys. Rev. B*, 92:125107, 2015.

[220] L. Barbiero, C. Schweizer, M. Aidelsburger, E. Demler, N. Goldman, and F. Grusdt. Coupling ultracold matter to dynamical gauge fields in optical lattices: From flux attachment to Z_2 lattice gauge theories. *Sci. Adv.*, 5(10):eaav7444, 2019.

[221] M. Rigol, V. Dunjko, and M. Olshanii. Thermalization and its mechanism for generic isolated quantum systems. *Nature*, 452(7189):854, 2008.

[222] V. Khemani, M. Hermele, and R. Nandkishore. Localization from hilbert space shattering: From theory to physical realizations. *Phys. Rev. B*, 101:174204, 2020.

[223] P. W. Anderson. Absence of Diffusion in Certain Random Lattices. *Phys. Rev.*, 109(5):1492, 1958.

[224] P. A. Lee. Disordered electronic systems. *Rev. Mod. Phys.*, 57(2):287, 1985.

[225] I. V. Gornyi, A. D. Mirlin, and D. G. Polyakov. Interacting Electrons in Disordered Wires: Anderson Localization and Low-T Transport. *Phys. Rev. Lett.*, 95(20):206603, 2005.

[226] D.M. Basko, I.L. Aleiner, and B.L. Altshuler. Metal–insulator transition in a weakly interacting many-electron system with localized single-particle states. *Ann. Phys.*, 321(5):1126, 2006.

[227] M. Serbyn, Z. Papić, and Dmitry A. Abanin. Local Conservation Laws and the Structure of the Many-Body Localized States. *Phys. Rev. Lett.*, 111(12):127201, 2013.

[228] D. A. Huse, R. Nandkishore, and V. Oganesyan. Phenomenology of fully many-body-localized systems. *Phys. Rev. B*, 90(17):174202, 2014.

[229] Dmitry A. Abanin, Ehud Altman, Immanuel Bloch, and Maksym Serbyn. Colloquium: Many-body localization, thermalization, and entanglement. *Rev. Mod. Phys.*, 91(2):021001, 2019.

[230] S. Iyer, V. Oganesyan, G. Refael, and D. A. Huse. Many-body localization in a quasiperiodic system. *Phys. Rev. B*, 87(13):134202, 2013.

[231] T. Grover and M. P. A. Fisher. Quantum disentangled liquids. *J. Stat. Mech.: Theory Exp.*, 2014(10):P10010, 2014.

[232] N. Y. Yao, C. R. Laumann, J. I. Cirac, M. D. Lukin, and J. E. Moore. Quasi-Many-Body Localization in Translation-Invariant Systems. *Phys. Rev. Lett.*, 117(24):240601, 2016.

[233] F. Alet and N. Laflorencie. Many-body localization: An introduction and selected topics. *C. R. Phys.*, 19(6):498, 2018.

[234] G. H. Wannier. Dynamics of Band Electrons in Electric and Magnetic Fields. *Rev. Mod. Phys.*, 34(4):645, 1962.

[235] E. Van Nieuwenburg, Y. Baum, and G. Refael. From Bloch oscillations to many-body localization in clean interacting systems. *Proc. Natl. Acad. Sci. U.S.A.*, 116(19):9269, 2019.

[236] M. Schulz, C. A. Hooley, R. Moessner, and F. Pollmann. Stark Many-Body Localization. *Phys. Rev. Lett.*, 122(4):040606, 2019.

[237] M. Taylor, S. R.and Schulz, F. Pollmann, and R. Moessner. Experimental probes of Stark many-body localization. *Phys. Rev. B*, 102(5):054206, 2020.

[238] A. Kshetrimayum, J. Eisert, and D. M. Kennes. Stark time crystals: Symmetry breaking in space and time. *Phys. Rev. B*, 102(19):195116, 2020.

[239] L. Zhang, Y. Ke, W. Liu, and C. Lee. Mobility edge of stark many-body localization. *Phys. Rev. A*, 103:023323, 2021.

[240] T. Chanda, R. Yao, and J. Zakrzewski. Coexistence of localized and extended phases: Many-body localization in a harmonic trap. *Phys. Rev. Research*, 2(3):032039, 2020.

[241] D. S. Bhakuni and A. Sharma. Stability of electric field driven many-body localization in an interacting long-range hopping model. *Phys. Rev. B*, 102(8):085133, 2020.

[242] E. V. H. Doggen, I. V. Gornyi, and D. G. Polyakov. Stark many-body localization: Evidence for hilbert-space shattering. *Phys. Rev. B*, 103:L100202, 2021.

[243] E. Guardado-Sanchez, A. Morningstar, B. M. Spar, P. T. Brown, D. A. Huse, and W. S. Bakr. Subdiffusion and Heat Transport in a Tilted Two-Dimensional Fermi-Hubbard System. *Phys. Rev. X*, 10(1):011042, 2020.

[244] S. Scherg, T. Kohlert, P. Sala, F. Pollmann, H. M. Bharath, I. Bloch, and M. Aidelsburger. Observing non-ergodicity due to kinetic constraints in tilted fermi-hubbard chains. *arXiv:2010.12965*, 2020.

[245] Q. Guo, C. Cheng, H. Li, S. Xu, P. Zhang, Z. Wang, C. Song, W. Liu, W. Ren, H. Dong, et al. Stark many-body localization on a superconducting quantum processor. *arXiv:2011.13895*, 2020.

[246] B. Chiaro, C. Neill, A. Bohrdt, M. Filippone, F. Arute, K. Arya, R. Babbush, D. Bacon, J. Bardin, R. Barends, et al. Direct measurement of non-local interactions in the many-body localized phase. *arXiv:1910.06024*, 2019.

[247] A. Lukin, M. Rispoli, R. Schittko, M. E. Tai, A. M. Kaufman, S. Choi, V. Khemani, J. Léonard, and M. Greiner. Probing entanglement in a many-body-localized system. *Science*, 364(6437):256, 2019.

[248] T. Brydges, A. Elben, P. Jurcevic, B. Vermersch, C. Maier, B. P. Lanyon, P. Zoller, R. Blatt, and C. F. Roos. Probing Rényi entanglement entropy via randomized measurements. *Science*, 364(6437):260, 2019.

[249] V. Oganesyan and D. A. Huse. Localization of interacting fermions at high temperature. *Phys. Rev. B*, 75(15):155111, 2007.

[250] Y.-L. Wu and S. Das Sarma. Understanding analog quantum simulation dynamics in coupled ion-trap qubits. *Phys. Rev. A*, 93(2):022332, 2016.

[251] M. Pino. Entanglement growth in many-body localized systems with long-range interactions. *Phys. Rev. B*, 90(17):174204, 2014.

[252] M. Serbyn, M. Knap, S. Gopalakrishnan, Z. Papić, N. Y. Yao, C. R. Laumann, D. A. Abanin, M. D. Lukin, and E. A. Demler. Interferometric Probes of Many-Body Localization. *Phys. Rev. Lett.*, 113(14):147204, 2014.

[253] W. De Roeck and F. Huveneers. Stability and instability towards delocalization in many-body localization systems. *Phys. Rev. B*, 95(15):155129, 2017.

[254] J. Léonard, M. Rispoli, Al. Lukin, R. Schittko, S. Kim, J. Kwan, D. Sels, E. Demler, and M. Greiner. Signatures of bath-induced quantum avalanches in a many-body–localized system. *arXiv:2012.15270*, 2020.

[255] S. S. Kondov, W. R. McGehee, W. Xu, and B. DeMarco. Disorder-Induced Localization in a Strongly Correlated Atomic Hubbard Gas. *Physical Review Letters*, 114(8):083002, 2015.

[256] D. V. Else, C. Monroe, C. Nayak, and N. Y. Yao. Discrete Time Crystals. *Annu. Rev. Condens. Matter Phys.*, 11(1):467, 2020.

[257] K. Agarwal, E. Altman, E. Demler, S. Gopalakrishnan, D. A. Huse, and M. Knap. Rare-region effects and dynamics near the many-body localization transition. *Ann. Phys. (Berl.)*, 529(7):1600326, 2017.

[258] E. Guardado-Sanchez, P. T Brown, D. Mitra, T. Devakul, D. A Huse, P. Schauß, and W. S Bakr. Probing the quench dynamics of antiferromagnetic correlations in a 2D quantum Ising spin system. *Phys. Rev. X*, 8(2):021069, 2018.

[259] K. Sun, Z. Gu, H. Katsura, and S. D. Sarma. Nearly Flatbands with Nontrivial Topology. *Phys. Rev. Lett.*, 106:236803, 2011.

[260] E. Tang, J.-W. Mei, and X.-G. Wen. High-Temperature Fractional Quantum Hall States. *Phys. Rev. Lett.*, 106:236802, 2011.

[261] T. Neupert, L. Santos, C. Chamon, and C. Mudry. Fractional Quantum Hall States at Zero Magnetic Field. *Phys. Rev. Lett.*, 106:236804, 2011.

[262] N. Y. Yao, C. R. Laumann, A. V. Gorshkov, S. D. Bennett, E. Demler, P. Zoller, and M. D. Lukin. Topological Flat Bands from Dipolar Spin Systems. *Phys. Rev. Lett.*, 109:266804, 2012.

[263] E. H. Lieb. Two theorems on the Hubbard model. *Phys. Rev. Lett.*, 62:1201, 1989.

[264] A. Mielke. Ferromagnetism in the Hubbard model on line graphs and further considerations. *J. Phys. A*, 24(14):3311, 1991.

[265] D. Leykam, A. Andreanov, and S. Flach. Artificial flat band systems: from lattice models to experiments. *Adv. Phys.:X*, 3(1):1473052, 2018.

[266] N. Regnault and B. A. Bernevig. Fractional Chern Insulator. *Phys. Rev. X*, 1:021014, 2011.

[267] E. J Bergholtz and Z. Liu. Topological flat band models and fractional Chern insulators. *Int. J. Mod. Phys. B*, 27(24):1330017, 2013.

[268] Z. Liu, E. J. Bergholtz, H. Fan, and A. M. Läuchli. Fractional Chern Insulators in Topological Flat Bands with Higher Chern Number. *Phys. Rev. Lett.*, 109:186805, 2012.

[269] N. Y. Yao, A. V. Gorshkov, C. R. Laumann, A. M. Läuchli, J. Ye, and M. D. Lukin. Realizing Fractional Chern Insulators in Dipolar Spin Systems. *Phys. Rev. Lett.*, 110:185302, 2013.

[270] Y. Cao, V. Fatemi, A. Demir, S. Fang, S. L. Tomarken, J. Y. Luo, J. D. Sanchez-Yamagishi, K. Watanabe, T. Taniguchi, E. Kaxiras, R. C. Ashoori, and P. Jarillo-Herrero. Correlated insulator behaviour at half-filling in magic-angle graphene superlattices. *Nature*, 556(7699):80, 2018.

[271] Y. Cao, V. Fatemi, S. Fang, K. Watanabe, T. Taniguchi, E. Kaxiras, and P. Jarillo-Herrero. Unconventional superconductivity in magic-angle graphene superlattices. *Nature*, 556(7699):43, 2018.

[272] M. Yankowitz, S. Chen, H. Polshyn, Y. Zhang, K. Watanabe, T. Taniguchi, D. Graf, A. F Young, and C. R Dean. Tuning superconductivity in twisted bilayer graphene. *Science*, 363(6431):1059, 2019.

[273] H. C. Po, L. Zou, A. Vishwanath, and T. Senthil. Origin of mott insulating behavior and superconductivity in twisted bilayer graphene. *Phys. Rev. X*, 8:031089, 2018.

[274] A. J. Kollar, M. Fitzpatrick, and A. A. Houck. Hyperbolic lattices in circuit quantum electrodynamics. *Nature*, 571:45, 2019.

[275] Alicia J Kollár, Mattias Fitzpatrick, Peter Sarnak, and Andrew A Houck. Line-Graph Lattices: Euclidean and Non-Euclidean Flat Bands, and Implementations in Circuit Quantum Electrodynamics. *Commun. Math. Phys.*, 44:1601, 2019.

[276] J. T. Chalker, T. S. Pickles, and P. Shukla. Anderson localization in tight-binding models with flat bands. *Phys. Rev. B*, 82:104209, 2010.

[277] D. Leykam, S. Flach, O. Bahat-Treidel, and A. S. Desyatnikov. Flat band states: Disorder and nonlinearity. *Phys. Rev. B*, 88:224203, 2013.

[278] M. Goda, S. Nishino, and H. Matsuda. Inverse Anderson Transition Caused by Flatbands. *Phys. Rev. Lett.*, 96:126401, 2006.

[279] J. H. Wilson, Y. Fu, S. D. Sarma, and J. H. Pixley. Disorder in twisted bilayer graphene. *Phys. Rev. Research*, 2(2):023325, 2020.

[280] J. H. Wilson, D. A. Huse, S. D. Sarma, and J. H. Pixley. Avoided quantum criticality in exact numerical simulations of a single disordered Weyl cone. *Phys. Rev. B*, 102(10):100201, 2020.

[281] Yixing Fu, Justin H Wilson, and JH Pixley. Flat topological bands and eigenstate criticality in a quasiperiodic insulator. *arXiv:2003.00027*, 2020.

[282] M. Mattioli, A. W. Glätzle, and W. Lechner. From classical to quantum nonequilibrium dynamics of Rydberg excitations in optical lattices. *New J. Phys.*, 17(11):113039, 2015.

[283] M. Marcuzzi, J. Minář, D. Barredo, S. de Léséleuc, H. Labuhn, T. Lahaye, A. Browaeys, E. Levi, and I. Lesanovsky. Facilitation Dynamics and Localization Phenomena in Rydberg Lattice Gases with Position Disorder. *Phys. Rev. Lett.*, 118:063606, 2017.

[284] M. Ostmann, M. Marcuzzi, J. Minář, and I. Lesanovsky. Synthetic lattices, flat bands and localization in Rydberg quantum simulators. *Quantum Sci. Technol.*, 4(2):02LT01, 2019.

[285] S. Mukherjee, A. Spracklen, D. Choudhury, N. Goldman, P. Öhberg, E. Andersson, and R. R. Thomson. Observation of a Localized Flat-Band State in a Photonic Lieb Lattice. *Phys. Rev. Lett.*, 114:245504, 2015.

[286] R. A. Vicencio, C. Cantillano, L. Morales-Inostroza, B. Real, C. Mejía-Cortés, S. Weimann, A. Szameit, and M. I. Molina. Observation of Localized States in Lieb Photonic Lattices. *Phys. Rev. Lett.*, 114:245503, 2015.

[287] F. Diebel, D. Leykam, S. Kroesen, C. Denz, and A. S. Desyatnikov. Conical Diffraction and Composite Lieb Bosons in Photonic Lattices. *Phys. Rev. Lett.*, 116:183902, 2016.

[288] D. Guzmán-Silva, C. Mejía-Cortés, M. A. Bandres, M. C. Rechtsman, S. Weimann, S. Nolte, M. Segev, A. Szameit, and R. A. Vicencio. Experimental observation of bulk and edge transport in photonic Lieb lattices. *New J. Phys.*, 16(6):063061, 2014.

[289] S. Xia, Y. Hu, D. Song, Y. Zong, L. Tang, and Z. Chen. Demonstration of flat-band image transmission in optically induced Lieb photonic lattices. *Opt. Lett.*, 41(7):1435, 2016.

[290] S. Taie, H. Ozawa, T. Ichinose, T. Nishio, S. Nakajima, and Y. Takahashi. Coherent driving and freezing of bosonic matter wave in an optical Lieb lattice. *Sci. Adv.*, 1(10):e1500854, 2015.

[291] F. Baboux, L. Ge, T. Jacqmin, M. Biondi, E. Galopin, A. Lemaître, L. Le Gratiet, I. Sagnes, S. Schmidt, H. E. Türeci, A. Amo, and J. Bloch. Bosonic Condensation and Disorder-Induced Localization in a Flat Band. *Phys. Rev. Lett.*, 116:066402, 2016.

[292] M. R Slot, T. S Gardenier, P. H Jacobse, G. CP v. Miert, S. N Kempkes, S. JM Zevenhuizen, C. M. Smith, D. Vanmaekelbergh, and I. Swart. Experimental realization and characterization of an electronic Lieb lattice. *Nat. Phys.*, 13(7):672, 2017.

[293] Doron L. Bergman, Congjun Wu, and Leon Balents. Band touching from real-space topology in frustrated hopping models. *Phys. Rev. B*, 78:125104, 2008.

[294] J.-W. Rhim and B.-J. Yang. Classification of flat bands according to the band-crossing singularity of Bloch wave functions. *Phys. Rev. B*, 99:045107, 2019.

[295] In (a)-(c), each point represents an average over eigenstates in an energy window containing 1/24 of the total number of eigenstates. All data shown in (a)-(d) are averaged over 800 realizations of disorder.

[296] F. Evers and A. D. Mirlin. Anderson transitions. *Rev. Mod. Phys.*, 80:1355, 2008.

[297] D. J. Luitz, F. Alet, and N. Laflorencie. Universal Behavior beyond Multifractality in Quantum Many-Body Systems. *Phys. Rev. Lett.*, 112:057203, 2014.

[298] N. Macé, F. Alet, and N. Laflorencie. Multifractal Scalings Across the Many-Body Localization Transition. *Phys. Rev. Lett.*, 123:180601, 2019.

[299] J. Lindinger, A. Buchleitner, and A. Rodríguez. Many-Body Multifractality throughout Bosonic Superfluid and Mott Insulator Phases. *Phys. Rev. Lett.*, 122:106603, 2019.

[300] R. Menu and T. Roscilde. Anomalous Diffusion and Localization in a Positionally Disordered Quantum Spin Array. *Phys. Rev. Lett.*, 124:130604, 2020.

[301] B. L. Altshuler, E. Cuevas, L. B. Ioffe, and V. E. Kravtsov. Nonergodic Phases in Strongly Disordered Random Regular Graphs. *Phys. Rev. Lett.*, 117:156601, 2016.

[302] A. De Luca, B. L. Altshuler, V. E. Kravtsov, and A. Scardicchio. Anderson Localization on the Bethe Lattice: Nonergodicity of Extended States. *Phys. Rev. Lett.*, 113:046806, 2014.

[303] S. Nishino, H. Matsuda, and M. Goda. Flat-band localization in weakly disordered system. *J. Phys. Soc. Jpn*, 76(2):024709, 2007.

[304] B. I. Shklovskii, B. Shapiro, B. R. Sears, P. Lambrianides, and H. B. Shore. Statistics of spectra of disordered systems near the metal-insulator transition. *Phys. Rev. B*, 47:11487, 1993.

[305] Y. Huang and B. I. Shklovskii. Anderson transition in three-dimensional systems with non-hermitian disorder. *Phys. Rev. B*, 101:014204, 2020.

[306] X. Deng, B. L. Altshuler, G. V. Shlyapnikov, and L. Santos. Quantum Levy Flights and Multifractality of Dipolar Excitations in a Random System. *Phys. Rev. Lett.*, 117:020401, 2016.

[307] P. Shukla. Disorder perturbed flat bands. II. Search for criticality. *Phys. Rev. B*, 98:184202, 2018.

[308] M. Hilke. Localization properties of the periodic random Anderson model. *J. Phys. A*, 30(11):L367, 1997.

[309] W. Jiang, H. Huang, and F. Liu. A Lieb-like lattice in a covalent-organic framework and its Stoner ferromagnetism. *Nat. Commun.*, 10:2207, 2019.

[310] Y. Kuno, T. Orito, and I. Ichinose. Flat-band many-body localization and ergodicity breaking in the creutz ladder. *New J. Phys.*, 22(1):013032, 2020.

[311] C. Danieli, A. Andreanov, and S. Flach. Many-body flatband localization. *Phys. Rev. B*, 102:041116, 2020.

[312] N. Roy, A. Ramachandran, and A. Sharma, "Compact, flat-band based, Anderson and many-body localization in a diamond chain," arXiv:1912.09951.

[313] J. M. Leinaas and J. Myrheim. On the theory of identical particles. *Il Nuovo Cimento B (1971-1996)*, 37(1):1, 1977.

[314] G. A. Goldin, R. Menikoff, and D. H. Sharp. Representations of a local current algebra in nonsimply connected space and the Aharonov–Bohm effect. *J. Math. Phys*, 22(8):1664, 1981.

[315] F. Wilczek. Magnetic Flux, Angular Momentum, and Statistics. *Phys. Rev. Lett.*, 48:1144, 1982.

[316] D. C. Tsui, H. L. Stormer, and A. C. Gossard. Two-Dimensional Magnetotransport in the Extreme Quantum Limit. *Phys. Rev. Lett.*, 48:1559, 1982.

[317] R. B. Laughlin. Anomalous Quantum Hall Effect: An Incompressible Quantum Fluid with Fractionally Charged Excitations. *Phys. Rev. Lett.*, 50:1395, 1983.

[318] B. I. Halperin. Statistics of Quasiparticles and the Hierarchy of Fractional Quantized Hall States. *Phys. Rev. Lett.*, 52:1583, 1984.

[319] D. Arovas, J. R. Schrieffer, and F. Wilczek. Fractional Statistics and the Quantum Hall Effect. *Phys. Rev. Lett.*, 53:722, 1984.

[320] A. Kitaev. Anyons in an exactly solved model and beyond. *Ann. Phys.*, 321(1):2, 2006.

[321] H. Yao and S. A. Kivelson. Exact Chiral Spin Liquid with Non-Abelian Anyons. *Phys. Rev. Lett.*, 99:247203, 2007.

[322] B. Bauer, L. Cincio, B. P. Keller, M. Dolfi, G. Vidal, S. Trebst, and A. W. W. Ludwig. Chiral spin liquid and emergent anyons in a Kagome lattice Mott insulator. *Nat. Commun.*, 5:5137, 2014.

[323] A. Y. Kitaev. Fault-tolerant quantum computation by anyons. *Ann. Phys.*, 303:2, 2003.

[324] S. Das Sarma, M. Freedman, and C. Nayak. Topologically Protected Qubits from a Possible Non-Abelian Fractional Quantum Hall State. *Phys. Rev. Lett.*, 94:166802, 2005.

[325] P. Bonderson, A. Kitaev, and K. Shtengel. Detecting Non-Abelian Statistics in the $\nu = 5/2$ Fractional Quantum Hall State. *Phys. Rev. Lett.*, 96:016803, 2006.

[326] A. Stern and B. I. Halperin. Proposed Experiments to Probe the Non-Abelian $\nu = 5/2$ Quantum Hall State. *Phys. Rev. Lett.*, 96:016802, 2006.

[327] C. Nayak, S. H. Simon, A. Stern, M. Freedman, and S. Das Sarma. Non-Abelian anyons and topological quantum computation. *Rev. Mod. Phys.*, 80:1083, 2008.

[328] J. Alicea, Y. Oreg, G. Refael, F. von Oppen, and M. P. A. Fisher. Non-Abelian statistics and topological quantum information processing in 1D wire networks. *Nat. Phys.*, 7:412, 2011.

[329] A. Stern and N. H. Lindner. Topological Quantum Computation—From Basic Concepts to First Experiments. *Science*, 339:1179, 2013.

[330] F. D. M. Haldane. 'Fractional statistics' in arbitrary dimensions: A generalization of the Pauli principle. *Phys. Rev. Lett.*, 67:937, 1991.

[331] F. D. M. Haldane. 'Spinon gas' description of the $S = 1/2$ Heisenberg chain with inverse-square exchange: Exact spectrum and thermodynamics. *Phys. Rev. Lett.*, 66:1529, 1991.

[332] Z. N. C. Ha. Exact Dynamical Correlation Functions of Calogero-Sutherland Model and One-Dimensional Fractional Statistics. *Phys. Rev. Lett.*, 73:1574, 1994.

[333] M. V. N. Murthy and R. Shankar. Thermodynamics of a One-Dimensional Ideal Gas with Fractional Exclusion Statistics. *Phys. Rev. Lett.*, 73:3331, 1994.

[334] Y.-S. Wu and Y. Yu. Bosonization of One-Dimensional Exclusons and Characterization of Luttinger Liquids. *Phys. Rev. Lett.*, 75:890, 1995.

[335] L. Amico, A. Osterloh, and U. Eckern. One-dimensional XXZ model for particles obeying fractional statistics. *Phys. Rev. B*, 58:R1703, 1998.

[336] A. Kundu. Exact Solution of Double δ Function Bose Gas through an Interacting Anyon Gas. *Phys. Rev. Lett.*, 83:1275, 1999.

[337] M. T. Batchelor, X.-W. Guan, and N. Oelkers. One-Dimensional Interacting Anyon Gas: Low-Energy Properties and Haldane Exclusion Statistics. *Phys. Rev. Lett.*, 96:210402, 2006.

[338] M. D. Girardeau. Anyon-Fermion Mapping and Applications to Ultracold Gases in Tight Waveguides. *Phys. Rev. Lett.*, 97:100402, 2006.

[339] A. del Campo. Fermionization and bosonization of expanding one-dimensional anyonic fluids. *Phys. Rev. A*, 78:045602, 2008.

[340] P. Calabrese and M. Mintchev. Correlation functions of one-dimensional anyonic fluids. *Phys. Rev. B*, 75:233104, 2007.

[341] M. Greiter. Statistical phases and momentum spacings for one-dimensional anyons. *Phys. Rev. B*, 79(6):064409, 2009.

[342] Y. Hao, Y. Zhang, and S. Chen. Ground-state properties of one-dimensional anyon gases. *Phys. Rev. A*, 78:023631, 2008.

[343] Y. Hao, Y. Zhang, and S. Chen. Ground-state properties of hard-core anyons in one-dimensional optical lattices. *Phys. Rev. A*, 79:043633, 2009.

[344] G. Tang, S. Eggert, and A. Pelster. Ground-state properties of anyons in a one-dimensional lattice. *New J. Phys.*, 17(12):123016, 2015.

[345] Y. Hao and S. Chen. Dynamical properties of hard-core anyons in one-dimensional optical lattices. *Phys. Rev. A*, 86:043631, 2012.

[346] T. Keilmann, S. Lanzmich, I. McCulloch, and M. Roncaglia. Statistically induced phase transitions and anyons in 1D optical lattices. *Nat. Commun.*, 2:361, 2011.

[347] S. Greschner and L. Santos. Anyon Hubbard Model in One-Dimensional Optical Lattices. *Phys. Rev. Lett.*, 115(5):053002, 2015.

[348] F. Lange, S. Ejima, and H. Fehske. Anyonic Haldane Insulator in One Dimension. *Phys. Rev. Lett.*, 118:120401, 2017.

[349] C. Sträter, S. C. L. Srivastava, and A. Eckardt. Floquet Realization and Signatures of One-Dimensional Anyons in an Optical Lattice. *Phys. Rev. Lett.*, 117:205303, 2016.

[350] L. W. Clark, B. M. Anderson, L. Feng, A. Gaj, K. Levin, and C. Chin. Observation of Density-Dependent Gauge Fields in a Bose-Einstein Condensate Based on Micromotion Control in a Shaken Two-Dimensional Lattice. *Phys. Rev. Lett.*, 121:030402, 2018.

[351] L. Yuan, M. Xiao, S. Xu, and S. Fan. Creating anyons from photons using a nonlinear resonator lattice subject to dynamic modulation. *Phys. Rev. A*, 96(4):043864, 2017.

[352] M. Greiner, O. Mandel, T. Esslinger, T. W. Hänsch, and I. Bloch. Quantum phase transition from a superfluid to a Mott insulator in a gas of ultracold atoms. *Nature*, 415:39, 2002.

[353] M. Lewenstein, A. Sanpera, V. Ahufinger, B. Damski, A. Sen, and U. Sen. Ultracold atomic gases in optical lattices: mimicking condensed matter physics and beyond. *Adv. Phys.*, 56:243, 2007.

[354] I. Bloch, J. Dalibard, and W. Zwerger. Many-body physics with ultracold gases. *Rev. Mod. Phys.*, 80:885, 2008.

[355] U. Schneider, L. Hackermüller, J. P. Ronzheimer, S. Will, S. Braun, T. Best, I. Bloch, E. Demler, S. Mandt, D. Rasch, and A. Rosch. Fermionic transport and out-of-equilibrium dynamics in a homogeneous Hubbard model with ultracold atoms. *Nat. Phys.*, 8:213, 2012.

[356] J. P. Ronzheimer, M. Schreiber, S. Braun, S. S. Hodgman, S. Langer, I. P. McCulloch, F. Heidrich-Meisner, I. Bloch, and U. Schneider. Expansion Dynamics of Interacting Bosons in Homogeneous Lattices in One and Two Dimensions. *Phys. Rev. Lett.*, 110:205301, 2013.

[357] D. Pertot, A. Sheikhan, E. Cocchi, L. A. Miller, J. E. Bohn, M. Koschorreck, M. Köhl, and C. Kollath. Relaxation Dynamics of a Fermi Gas in an Optical Superlattice. *Phys. Rev. Lett.*, 113:170403, 2014.

[358] C.-L. Hung, V. Gurarie, and C. Chin. From Cosmology to Cold Atoms: Observation of Sakharov Oscillations in a Quenched Atomic Superfluid. *Science*, 341:1213, 2013.

[359] A. M. Kaufman, M. E. Tai, A. Lukin, M. Rispoli, R. Schittko, P. M. Preiss, and M. Greiner. Quantum thermalization through entanglement in an isolated many-body system. *Science*, 353:794, 2016.

[360] N. Fläschner, D. Vogel, M. Tarnowski, B. S. Rem, D.-S. Lühmann, M. Heyl, J. C. Budich, L. Mathey, K. Sengstock, and C. Weitenberg. Observation of a dynamical topological phase transition. *Nat. Phys.*, 14(3):265, 2018.

[361] F. Meinert, M. J. Mark, K. Lauber, A. J. Daley, and H.-C. Nägerl. Floquet Engineering of Correlated Tunneling in the Bose-Hubbard Model with Ultracold Atoms. *Phys. Rev. Lett.*, 116:205301, 2016.

[362] A. I. Larkin and Y. N. Ovchinnikov. Quasiclassical Method in the Theory of Superconductivity. *J. Exp. Theor. Phys.*, 28:1200, 1969.

[363] T. M. Wright, M. Rigol, M. J. Davis, and K. V. Kheruntsyan. Nonequilibrium Dynamics of One-Dimensional Hard-Core Anyons Following a Quench: Complete Relaxation of One-Body Observables. *Phys. Rev. Lett.*, 113:050601, 2014.

[364] S. C. Morampudi, A. M. Turner, F. Pollmann, and F. Wilczek. Statistics of Fractionalized Excitations through Threshold Spectroscopy. *Phys. Rev. Lett.*, 118:227201, 2017.

[365] F. Wilczek. *Fractional statistics and anyon superconductivity*, volume 5. World Scientific, 1990.

[366] J. Yu, N. Sun, and H. Zhai. Symmetry Protected Dynamical Symmetry in the Generalized Hubbard Models. *Phys. Rev. Lett.*, 119(22):225302, 2017.

[367] A. M. Läuchli and C. Kollath. Spreading of correlations and entanglement after a quench in the one-dimensional Bose Hubbard model. *J. Stat. Mech. Theory Exp.*, 5:05018, 2008.

[368] A. Bohrdt, C. B. Mendl, M. Endres, and M. Knap. Scrambling and thermalization in a diffusive quantum many-body system. *New J. Phys.*, 19(6):063001, 2017.

[369] H. Shen, P. Zhang, R. Fan, and H. Zhai. Out-of-time-order correlation at a quantum phase transition. *Phys. Rev. B*, 96:054503, 2017.

[370] A. Nahum, S. Vijay, and J. Haah. Operator Spreading in Random Unitary Circuits. *Phys. Rev. X*, 8(2):021014, 2018.

[371] Y. Huang, Y.-L. Zhang, and X. Chen. Out-of-time-ordered correlators in many-body localized systems. *Ann. Phys. (Berlin)*, 529:1600318, 2017.

[372] R.-Q. He and Z.-Y. Lu. Characterizing many-body localization by out-of-time-ordered correlation. *Phys. Rev. B*, 95(5):054201, 2017.

[373] R. Fan, P. Zhang, H. Shen, and H. Zhai. Out-of-time-order correlation for many-body localization. *Sci. Bull.*, 62(10):707, 2017.

[374] Y. Chen. Universal logarithmic scrambling in many body localization. *arXiv:1608.02765*, 2016.

[375] B. Swingle and D. Chowdhury. Slow scrambling in disordered quantum systems. *Phys. Rev. B*, 95(6):060201, 2017.

[376] E. Leviatan, F. Pollmann, J. H. Bardarson, D. A. Huse, and E. Altman. Quantum thermalization dynamics with matrix-product states. *arXiv:1702.08894*, 2017.

[377] S. Xu and B. Swingle. Accessing scrambling using matrix product operators. *Nat. Phys.*, 16(2):199, 2020.

[378] Y.-L. Zhang and X. Huang, Y.and Chen. Information scrambling in chaotic systems with dissipation. *Phys. Rev. B*, 99:014303, 2019.

[379] B. Swingle and N. Yunger Halpern. Resilience of scrambling measurements. *Phys. Rev. A*, 97(6):062113, 2018.

[380] N. Y. Yao, F. Grusdt, B. Swingle, M. D. Lukin, D. M. Stamper-Kurn, J. E. Moore, and E. A. Demler. Interferometric approach to probing fast scrambling. *arXiv:1607.01801*, 2016.

[381] G. Zhu, M. Hafezi, and T. Grover. Measurement of many-body chaos using a quantum clock. *Phys. Rev. A*, 94:062329, 2016.

[382] B. Swingle, G. Bentsen, M. Schleier-Smith, and P. Hayden. Measuring the scrambling of quantum information. *Phys. Rev. A*, 94:040302, 2016.

[383] D. J. Clarke, J. Alicea, and K. Shtengel. Exotic non-Abelian anyons from conventional fractional quantum Hall states. *Nat. Commun.*, 4:1348, 2013.

[384] M. Cheng. Superconducting proximity effect on the edge of fractional topological insulators. *Phys. Rev. B*, 86:195126, 2012.

[385] R. S. K. Mong, D. J. Clarke, J. Alicea, N. H. Lindner, P. Fendley, C. Nayak, Y. Oreg, A. Stern, E. Berg, K. Shtengel, and M. P. A. Fisher. Universal Topological Quantum Computation from a Superconductor-Abelian Quantum Hall Heterostructure. *Phys. Rev. X*, 4:011036, 2014.

[386] J. Watrous. *Quantum Computational Complexity*, pages 7174–7201. Springer New York, New York, NY, 2009.

[387] S. Aaronson. The complexity of quantum states and transformations: from quantum money to black holes. *arXiv:1607.05256*, 2016.

[388] M. A. Nielsen. A geometric approach to quantum circuit lower bounds. *arXiv:quant-ph/0502070*, 2005.

[389] M. A. Nielsen, M. R. Dowling, M. Gu, and A. C. Doherty. Quantum Computation as Geometry. *Science*, 311:1133, 2006.

[390] M. R. Dowling and M. A. Nielsen. The geometry of quantum computation. *Quantum Information & Computation*, 8(10):861, 2008.

[391] R. A. Jefferson and R. C. Myers. Circuit complexity in quantum field theory. *J. High Energy Phys.*, 10:107, 2017.

[392] R.-Q. Yang. Complexity for quantum field theory states and applications to thermofield double states. *Phys. Rev. D*, 97:066004, 2018.

[393] M. Guo, J. Hernandez, R. C. Myers, and S.-M. Ruan. Circuit complexity for coherent states. *J. High Energy Phys.*, 10:11, 2018.

[394] H. A. Camargo, P. Caputa, D. Das, M. P. Heller, and R. Jefferson. Complexity as a novel probe of quantum quenches: Universal scalings and purifications. *Phys. Rev. Lett.*, 122:081601, 2019.

[395] D. W. F. Alves and G. Camilo. Evolution of complexity following a quantum quench in free field theory. *J. High Energy Phys.*, 6:29, 2018.

[396] S. Chapman, J. Eisert, L. Hackl, M. P. Heller, R. Jefferson, H. Marrochio, and R. C. Myers. Complexity and entanglement for thermofield double states. *SciPost physics*, 6, 2019.

[397] L. Hackl and R. C. Myers. Circuit complexity for free fermions. *J. High Energy Phys.*, 7:139, 2018.

[398] R. Khan, C. Krishnan, and S. Sharma. Circuit complexity in fermionic field theory. *Phys. Rev. D*, 98(12):126001, 2018.

[399] A. P. Reynolds and S. F. Ross. Complexity of the AdS soliton. *Class. Quantum Grav*, 35(9):095006, 2018.

[400] J. Jiang, J. Shan, and J. Yang. Circuit complexity for free fermion with a mass quench. *Nuclear Physics B*, 954:114988, 2020.

[401] R. Q. Yang, Y. S. An, C. Niu, C. Y. Zhang, and K. Y. Kim. Principles and symmetries of complexity in quantum field theory. *Eur. Phys. J. C*, 79(2):109, 2019.

[402] R. Q. Yang, Y. S. An, C. Niu, C. Y. Zhang, and K. Y. Kim. More on complexity of operators in quantum field theory. *J. High Energy Phys.*, 2019(3):161, 2019.

[403] R. Q. Yang and K. Y. Kim. Complexity of operators generated by quantum mechanical Hamiltonians. *J. High Energy Phys.*, 2019(3):10, 2019.

[404] D. Stanford and L. Susskind. Complexity and shock wave geometries. *Phys. Rev. D*, 90(12):126007, 2014.

[405] L. Susskind. Computational complexity and black hole horizons. *Fortschritte der Physik*, 64(1):24–43, 2016.

[406] A. R. Brown, D. A. Roberts, L. Susskind, B. Swingle, and Y. Zhao. Holographic complexity equals bulk action? *Phys. Rev. Lett.*, 116:191301, 2016.

[407] A. R. Brown, D. A. Roberts, L. Susskind, B. Swingle, and Y. Zhao. Complexity, action, and black holes. *Phys. Rev. D*, 93(8):086006, 2016.

[408] S. Chapman, M. P. Heller, H. Marrochio, and F. Pastawski. Toward a Definition of Complexity for Quantum Field Theory States. *Phys. Rev. Lett*, 120(12):121602, 2018.

[409] P. Caputa and J. M. Magan. Quantum computation as gravity. *Phys. Rev. Lett.*, 122:231302, 2019.

[410] M. Vojta. Quantum phase transitions. *Rep. Prog. Phys*, 66:2069, 2003.

[411] T. Caneva, R. Fazio, and G. E. Santoro. Adiabatic quantum dynamics of a random Ising chain across its quantum critical point. *Phys. Rev. B*, 76:144427, 2007.

[412] A. S. Sørensen, E. Altman, M. Gullans, J. V. Porto, M. D. Lukin, and E. Demler. Adiabatic preparation of many-body states in optical lattices. *Phys. Rev. A*, 81(6):061603, 2010.

[413] A. Y. Kitaev. Unpaired Majorana fermions in quantum wires. *Phys.-Uspekhi*, 44(10S):131, 2001.

[414] J. Alicea. New directions in the pursuit of Majorana fermions in solid state systems. *Rep. Prog. Phys*, 75(7):076501, 2012.

[415] J. D. Sau, R. M. Lutchyn, S. Tewari, and S. Das Sarma. Generic new platform for topological quantum computation using semiconductor heterostructures. *Phys. Rev. Lett.*, 104:040502, 2010.

[416] Y. Oreg, G. Refael, and F. von Oppen. Helical Liquids and Majorana Bound States in Quantum Wires. *Phys. Rev. Lett.*, 105:177002, 2010.

[417] R. M. Lutchyn, J. D. Sau, and S. Das Sarma. Majorana fermions and a topological phase transition in semiconductor-superconductor heterostructures. *Phys. Rev. Lett.*, 105:077001, 2010.

[418] S. Bravyi, M. B. Hastings, and F. Verstraete. Lieb-robinson bounds and the generation of correlations and topological quantum order. *Phys. Rev. Lett.*, 97:050401, 2006.

[419] X. Chen, Z.-C. Gu, and X.-G. Wen. Local unitary transformation, long-range quantum entanglement, wave function renormalization, and topological order. *Phys. Rev. B*, 82:155138, 2010.

[420] Y. Huang and X. Chen. Quantum circuit complexity of one-dimensional topological phases. *Phys. Rev. B*, 91:195143, 2015.

[421] M. Heyl and J. C. Budich. Dynamical topological quantum phase transitions for mixed states. *Phys. Rev. B*, 96:180304, 2017.

[422] L. D'Alessio and M. Rigol. Dynamical preparation of Floquet Chern insulators. *Nat. Commun*, 6:8336, 2015.

[423] M. D. Caio, N. R. Cooper, and M. J. Bhaseen. Quantum Quenches in Chern Insulators. *Phys. Rev. Lett.*, 115:236403, 2015.

[424] S. Vajna and B. Dóra. Topological classification of dynamical phase transitions. *Phys. Rev. B*, 91(15):155127, 2015.

[425] J. H. Wilson, J. C. W. Song, and G. Refael. Remnant Geometric Hall Response in a Quantum Quench. *Phys. Rev. Lett*, 117(23):235302, 2016.

[426] C. Wang, P. Zhang, X. Chen, J. Yu, and H. Zhai. Scheme to Measure the Topological Number of a Chern Insulator from Quench Dynamics. *Phys. Rev. Lett.*, 118:185701, 2017.

[427] M. D. Caio, G. Möller, N. R. Cooper, and M. J. Bhaseen. Topological marker currents in chern insulators. *Nat. Phys.*, 15(3):257, 2019.

[428] M. Heyl, F. Pollmann, and B. Dóra. Detecting Equilibrium and Dynamical Quantum Phase Transitions in Ising Chains via Out-of-Time-Ordered Correlators. *Phys. Rev. Lett.*, 121:016801, 2018.

[429] S. Roy, R. Moessner, and A. Das. Locating topological phase transitions using nonequilibrium signatures in local bulk observables. *Phys. Rev. B*, 95:041105, 2017.

[430] P. Titum, J. T. Iosue, J. R. Garrison, A. V. Gorshkov, and Z.-X. Gong. Probing ground-state phase transitions through quench dynamics. *Phys. Rev. Lett.*, 123:115701, 2019.

[431] H. T. Quan, Z. Song, X. F. Liu, P. Zanardi, and C. P. Sun. Decay of Loschmidt Echo Enhanced by Quantum Criticality. *Phys. Rev. Lett.*, 96:140604, 2006.

[432] G. Kells, D. Sen, J. K. Slingerland, and S. Vishveshwara. Topological blocking in quantum quench dynamics. *Phys. Rev. B*, 89:235130, 2014.

[433] D. Vodola, L. Lepori, E. Ercolessi, A. V. Gorshkov, and G. Pupillo. Kitaev Chains with Long-Range Pairing. *Phys. Rev. Lett*, 113(15):156402, 2014.

[434] D. Vodola, L. Lepori, E. Ercolessi, and G. Pupillo. Long-range Ising and Kitaev models: phases, correlations and edge modes. *New J. Phys*, 18(1):015001, 2016.

[435] K. Patrick, T. Neupert, and J. K. Pachos. Topological Quantum Liquids with Long-Range Couplings. *Phys. Rev. Lett*, 118(26):267002, 2017.

[436] L. Pezzè, M. Gabbrielli, L. Lepori, and A. Smerzi. Multipartite entanglement in topological quantum phases. *Phys. Rev. Lett.*, 119:250401, 2017.

[437] Z. Xiong, D.-X. Yao, and Z. Yan. Nonanalyticity of circuit complexity across topological phase transitions. *Phys. Rev. B*, 101:174305, 2020.

[438] M. Z. Hasan and C. L. Kane. Colloquium: Topological insulators. *Rev. Mod. Phys.*, 82:3045, 2010.

[439] X.-L. Qi and S.-C. Zhang. Topological insulators and superconductors. *Rev. Mod. Phys.*, 83:1057, 2011.

[440] K. Hyatt, J. R. Garrison, and B. Bauer. Extracting entanglement geometry from quantum states. *Phys. Rev. Lett.*, 119:140502, 2017.

[441] D. Girolami. How difficult is it to prepare a quantum state? *Phys. Rev. Lett.*, 122:010505, 2019.

[442] E. Lieb, T. Schultz, and D. Mattis. Two soluble models of an antiferromagnetic chain. *Ann. Phys.*, 16(3):407, 1961.

[443] S. Katsura. Statistical Mechanics of the Anisotropic Linear Heisenberg Model. *Phys. Rev.*, 127:1508, 1962.

[444] J. H. H. Perk, H. W. Capel, M. J. Zuilhof, and Th. J. Siskens. On a soluble model of an antiferromagnetic chain with alternating interactions and magnetic moments. *Physica A*, 81(3):319, 1975.

[445] F. D. M. Haldane. 'Luttinger liquid theory'of one-dimensional quantum fluids. I. Properties of the Luttinger model and their extension to the general 1D interacting spinless Fermi gas. *J. Phys. Condens. Matter*, 14(19):2585, 1981.

[446] J. Voit. One-dimensional Fermi liquids. *Rep. Prog. Phys*, 58:977, 1995.

[447] A. Rahmani and C. Chamon. Optimal Control for Unitary Preparation of Many-Body States: Application to Luttinger Liquids. *Phys. Rev. Lett.*, 107:016402, 2011.

[448] Pablo Sala, Tibor Rakovszky, Ruben Verresen, Michael Knap, and Frank Pollmann. Ergodicity Breaking Arising from Hilbert Space Fragmentation in Dipole-Conserving Hamiltonians. *Physical Review X*, 10(1):011047, 2020.

[449] Vedika Khemani, Michael Hermele, and Rahul Nandkishore. Localization from Hilbert space shattering: From theory to physical realizations. *Physical Review B*, 101(17):174204, 2020.

[450] R. Samajdar, S. Choi, H. Pichler, M. D. Lukin, and S. Sachdev. Numerical study of the chiral $\mathbb{Z}_3$ quantum phase transition in one spatial dimension. *Phys. Rev. A*, 98:023614, 2018.

[451] S. Whitsitt, R. Samajdar, and S. Sachdev. Quantum field theory for the chiral clock transition in one spatial dimension.

[452] D. J. Wineland, C. Monroe, W. M. Itano, D. Leibfried, B. E King, and D. M. Meekhof. Experimental issues in coherent quantum-state manipulation of trapped atomic ions. *J. Res. Natl. Inst. Stand. Technol.*, 103(3):259, 1998.

[453] B. Neyenhuis, J. Zhang, P. W. Hess, J. Smith, A. C. Lee, P. Richerme, Z.-X. Gong, A. V. Gorshkov, and C. Monroe. Observation of prethermalization in long-range interacting spin chains. *Sci. Adv.*, 3(8):e1700672, 2017.

[454] C.-C. J. Wang and J. K. Freericks. Intrinsic phonon effects on analog quantum simulators with ultracold trapped ions. *Phys. Rev. A*, 86:032329, 2012.

[455] Y. Wu. *Quantum Computation in Large Ion Crystals*. PhD thesis, 2019.

[456] M. Kac and C. J Thompson. Critical behavior of several lattice models with long-range interaction. *J. Math. Phys.*, 10(8):1373, 1969.

[457] J. R. Schrieffer and P. A. Wolff. Relation between the anderson and kondo hamiltonians. *Phys. Rev.*, 149:491, 1966.

[458] S. Bravyi, D. P. DiVincenzo, and D. Loss. Schrieffer–wolff transformation for quantum many-body systems. *Ann. Phys. (N. Y.)*, 326(10):2793, 2011.

[459] K. Slagle and Y. B. Kim. Fracton topological order from nearest-neighbor two-spin interactions and dualities. *Phys. Rev. B*, 96:165106, 2017.

[460] R. Islam, E. E. Edwards, K. Kim, S. Korenblit, C. Noh, H. Carmichael, G. D. Lin, L. M. Duan, C. C. Joseph Wang, J. K. Freericks, and C. Monroe. Onset of a quantum phase transition with a trapped ion quantum simulator. *Nat. Commun.*, 2(1):1, 2011.

[461] B. P. Lanyon, C. Hempel, D. Nigg, M. Muller, R. Gerritsma, F. Zahringer, P. Schindler, J. T. Barreiro, M. Rambach, G. Kirchmair, M. Hennrich, P. Zoller, R. Blatt, and C. F. Roos. Universal Digital Quantum Simulation with Trapped Ions. *Science*, 334(6052):57, 2011.

[462] P. Ponte, Z. Papić, F. Huveneers, and D. A. Abanin. Many-Body Localization in Periodically Driven Systems. *Phys. Rev. Lett.*, 114(14):140401, 2015.

[463] Y. Y. Atas, E. Bogomolny, O. Giraud, and G. Roux. Distribution of the Ratio of Consecutive Level Spacings in Random Matrix Ensembles. *Phys. Rev. Lett.*, 110(8):084101, 2013.

[464] X. Wei, C. Cheng, G. Xianlong, and R. Mondaini. Investigating many-body mobility edges in isolated quantum systems. *Phys. Rev. B*, 99(16):165137, 2019.

[465] Q. Guo, C. Cheng, Z. H. Sun, Z. Song, H. Li, Z. Wang, W. Ren, H. Dong, D. Zheng, Y. R. Zhang, R. Mondaini, H. Fan, and H. Wang. Observation of energy-resolved many-body localization. *Nat. Phy.*, 2020.

[466] P. Hyllus, W. Laskowski, R. Krischek, C. Schwemmer, W. Wieczorek, H. Weinfurter, L. Pezzé, and A. Smerzi. Fisher information and multiparticle entanglement. *Phys. Rev. A*, 85(2):022321, 2012.